İSTANBUL TECHNICAL UNIVERSITY ★ INSTITUTE OF SCIENCE AND TECHNOLOGY

VISCOELASTOPLASTIC MODELING OF ARTERIAL TISSUE

Ph.D. Thesis by

Emin SÜNBÜLOĞLU, Mech. Eng.

Department : Mechanical Engineering

Programme: Design

DECEMBER 2007

İSTANBUL TECHNICAL UNIVERSITY ★ INSTITUTE OF SCIENCE AND TECHNOLOGY

VISCOELASTOPLASTIC MODELING OF ARTERIAL TISSUE

Ph.D. Thesis by

Emin SÜNBÜLOĞLU, Mech. Eng.

503012050

Date of submission : 3 September 2007

Date of defence examination: 4 December 2007

Supervisor (Chairman): Prof. Dr. Tuncer TOPRAK

Members of the Examining Committee Prof. Dr. Kadir KIRKKÖPRÜ

Prof. Dr. Civan IŞLAK (İÜ.)

Prof. Dr. Alaeddin ARPACI

Prof. Dr. Murat HANCI (İÜ.)

DECEMBER 2007

İSTANBUL TEKNİK ÜNİVERSİTESİ ★ FEN BİLİMLERİ ENSTİTÜSÜ

DAMAR DOKUSUNUN VİSKOELASTOPLASTİK MODELLENMESİ

DOKTORA TEZİ

Mak. Müh. Emin SÜNBÜLOĞLU

503012050

Tezin Enstitüye Verildiği Tarih: 3 Eylül 2007

Tezin Savunulduğu Tarih: 4 Aralık 2007

Tez Danışmanı: Prof. Dr. Tuncer TOPRAK

Diğer Jüri Üyeleri Prof. Dr. Kadir KIRKKÖPRÜ

Prof. Dr. Civan IŞLAK (İÜ.)

Prof. Dr. Alaeddin ARPACI

Prof. Dr. Murat HANCI (İÜ.)

ARALIK 2007

PREFACE

I would like to express my thanks to my professors, colleagues, friends and especially to:

My Mother, who is "all of everything" here and everywhere, every time;

Dr. Ergün BOZDAĞ for guiding, redirecting and promoting me in tasks throughout this thesis, and all other studies we have conducted;

Dr. Tuncer TOPRAK, for his great support in laying out the most well equipped laboratory (of Turkey, maybe) on experimental solid mechanics and biomechanics;

Dr. Civan IŞLAK, for his introduction on this subject and laying out the initiation for this phenomenon as a Ph.D. Thesis to me;

Med. Dr. Burçak ERDİNÇ for her invaluable technical surgical assistance in specimen preparation during my experimental studies on arteries,

Dr. Saim AKYÜZ for his very in-depth and addicted contributions on viscoelasticity and its application to my studies,

Dr. Kadir KIRKKÖPRÜ for his valuable helpings in scientific leadings and moral support during my studies;

Dr. Alaeddin ARPACI for injecting to my soul the methodology of theoretical scientific research;

Dr. A. Nilüfer EĞRİCAN, who introduced to me "the academic life" and ensured its continuity with her invaluable helpings and always "being there";

Burak YAZICI and *Levent KIRKAYAK* for their invaluable help at initiating the experimental setup with optical systems, and their moral support throughout my studies and their ongoing invaluable friendship;

Dr. Ata MUGAN for his kind helpings in issues when I got stuck in numerics;

Dr. Murat HANCI for letting us enjoy and get keen on Biomechanics;

Family of ITU Faculty of Mech. Eng., and Dept. of Strength of Materials for their assistance, coaching and friendship every now and then I have been there;

Orhan KAMBUROĞLU and *Mehmet SÖNMEZ* for their great technical assistance and innovative ideas in setting up and creating the parts of my experimental setup;

Gökhan BAYSAL for his "life-saving existence" during my last year of studies;

Emin Et Sanayi, Tuzla for letting us obtain the specimens everytime we wanted to;

All my friends who have beared me during my tempered times.

September 2007 **Emin SÜNBÜLOĞLU**

TABLE OF CONTENTS

PREFACE i
TABLE OF CONTENTS ii
LIST OF TABLES vi
LIST OF FIGURES vii
NOMENCLATURE xv
SUMMARY xvii
ÖZET xix

1. INTRODUCTION 1

2. THE CIRCULATORY SYSTEM AND ARTERIAL PHYSIOLOGY 3
2.1. The Artery: Anatomical Basics 3
2.2. Mechanical Basics on Arterial Physiology 6
2.2.1. Mechanics of Arterial Wall 7
2.2.2. Mechanical Tests on Arterial Tissue 8
2.2.3. Mechanical Response of Arterial Tissue to External Loads 9

3. BASICS OF NON-LINEAR CONTINUUM MECHANICS 12
3.1. Kinematics Preliminaries 12
3.2. The Concept of Stress 15
3.3. Basic Postulates of Continuum Mechanics [22-24] 18
3.3.1. Conservation of Mass 18
3.3.2. Balance of Linear Momentum 19
3.3.3. Conservation of Angular Momentum 21
3.3.4. Conservation of Energy 21
3.3.5. Entropy Inequality 22

4. THE VISCOELASTIC MODEL FOR TRACING PASSIVE ARTERIAL DEFORMATIONS 23
4.1.1. Some Previous Studies on Arterial Material Models 23
4.2. General Assumptions of proposed Material Model: 27
4.3. Kinematics for Materials Exhibiting Intermediate Configurations 28
4.4. The Fiber Orientation Matrix 31

4.4.1. The Representation of Reference Configuration 31
4.4.2. The Stretch of Fibers 32
4.5. The Constitutive Layout 33
4.5.1. Thermodynamics 33
4.6. The Material-Specific Constitutive Laws 40
4.6.1. General Considerations 40
4.6.2. The Specific Material Model 43
4.6.3. The "Constitutive Derivatives" 45
4.6.4. The "Flow Rule" 46

5. EXPRESSIONS FOR THICK-WALLED TUBE MODEL OF ARTERIAL STRUCTURE 51
5.1. The Basic Kinematics 51
5.2. The Strain Expressions 53
5.3. External Quantities 56
5.3.1. The Equations of Equilibrium 56
5.3.2. An Addendum to the Functional Form of Ψ 58
5.3.3. The Explicit Terms of Cauchy Stress Tensor 59
5.3.4. The Internal Pressure – Stress Relations 60
5.3.5. The Axial Force – Stress Relations 61
5.3.6. The Torque – Stress Relations 63
5.4. Scalar Equations of State 63
5.4.1. An Alternative Formulation 64

6. BASICS OF PLASTICITY 66
6.1. Introduction 66
6.2. Crystal Plasticity 67
6.2.1. The Slip Directions 70
6.2.2. The Resolved Shear Stress (Schmid's Law) 70
6.2.3. The Yield 71
6.2.4. Plastic Hardening of Material 71
6.2.5. The shear Rate and Normality of Flow 73
6.2.6. The Accumulated Shear Angle 74
6.3. The Specific Plasticity Material Model for Arterial Tissue: 74
6.3.1. The Kinematics of Crystal Plasticity 76
6.4. Numerical Approximation to Analytical Expressions: 78
6.5. Addendum for Cylindrical Coordinates: 79

7. THE SOFTENING OF TISSUE AND THE "DAMAGE RULE" 82

8. THE ELASTOPLASTIC FRAMEWORK FOR ARTERIAL TISSUE 85

9. MODELING PRE-STRESS IN ARTERIAL TISSUE 90
9.1. Introduction 90
9.2. Application to Constitutive Framework 90

10. SUMMARY OF CONSIDERATIONS STATED 96

11. SOME SOLUTIONS TO PROPOSED MATERIAL MODEL 99
11.1. Analysis without Plastic Deformations 99
11.1.1. Pure Elasticity 99
11.1.2. Pure Elasticity with Softening 103
11.1.3. Isotropic Viscoelasticity 106
11.1.4. Nonlinear Viscoelasticity 110
11.1.5. Isotropic Viscoelasticity with Softening 114
11.1.6. Isotropic Viscoelasticity with Softening and Static Torsion. 118
11.1.7. Isotropic Viscoelasticity with Softening and Dynamic Torsion over Static Pressure and Axial Force 122
11.1.8. Isotropic Viscoelasticity with Softening and Under Dynamic Inflation and Torsion with Static Axial Load 126
11.2. Analysis Incorporating Plastic Deformations 130
11.2.1. Elastoplasticity 130
11.2.2. Viscoelastoplasticity with Isotropic Damping 134

12. EXPERIMENTAL METHOD FOR PARAMETER ESTIMATION 137
12.1. The Experimental Setup 137
12.1.1. Layout of the Setup and Measurement Principles 137
12.1.2. Specimen Preperation 140
12.1.3. Experimental Loading Protocols for Specimens 144
12.2. Numerical Data Evaluation 146
12.2.1. Algorithm 149
12.3. Experimental Loading Protocols for Elastic Parameter Estimation 155
12.3.1. Summary of Tests Performed 155
12.3.2. In-Phase Static Extension and Inflation for Elastic Parameter Estimation 155
12.3.3. In-Phase Extension, Torsion Inflation for Elastic Parameter Estimation 159
12.3.4. Out-of-Phase Static Extension, Inflation and Torsion for Elastic Parameter Estimation 162

12.3.5. Out-of-Phase Static Extension, Inflation and Torsion for Elastic Parameter Estimation 166
12.3.6. Summary 170
12.4. Experimental Loading Protocols for Viscoelastic Parameter Estimation 171
12.5. Parameter Estimation Regarding Plastic Deformations and Damage Evolution 175
12.6. Comments on Parameter Estimation 176

13. CONCLUSIONS 177

REFERENCES 180

ADDENDUM-A:STRESS AND STRAIN DISTRIBUTION IN VESSEL WALL 184
A-1. Pure Elastic Material Model (due to Section 11.1.1) 184
A-2. Pure Elastic Material Model with Softening (due to Section 11.1.2) 188
A-3. Isotropic Viscoelasticity Model (due to Section 11.1.3) 191
A-4. Nonlinear Viscoelasticity Model (due to Section 11.1.4) 194
A-5. Isotropic Viscoelasticity Model with Softening (due to Section 11.1.5) 197
A-6. Isotropic Viscoelasticity Model with Softening and Static Torsion (due to Section 11.1.6) 200
A-7. Isotropic Viscoelasticity Model with Softening and Dynamic Torsion over Static Pressure and Axial Force (due to Section 11.1.7) 204
A-8. Isotropic Viscoelasticity Model with Softening and Under Dynamic Inflation and Torsion with Static Axial Load (due to Section 11.1.8) 208
A-9. Elastoplasticity Material Model (due to Section 11.2.1) 212
A-10. Viscoelastoplasticity Material Model with Isotropic Damping (due to Section 11.2.2) 217

CURRICULUM VITAE 222

LIST OF TABLES

Table 2.1: Characteristics of various types of blood vessels 6
Table 10.1: The Equations of State 96
Table 10.2: The Equations of Plasticity and Damage Evolution 97
Table 10.3: Physical and Derived Quantities 98
Table 11.1: Material Properties Used for Pure Elasticity Material Model Analysis in Section 11.1.1 99
Table 11.2: Material Properties Used for Pure Elasticity with Softening Effect in Section 11.1.2 104
Table 11.3: Material Properties Used for Isotropic Viscoelasticity Model Analysis in Section 11.1.3 106
Table 11.4: Material Properties Used for Nonlinear Viscoelasticity Analysis in Section 11.1.4 110
Table 11.5: Material Properties Used for Pure Isotropic Viscoelasticity Analysis with Softening Effect in Section 11.1.5 114
Table 11.6: Material Properties Used for Pure Isotropic Viscoelasticity Analysis with Softening Effect in Section 11.1.6 120
Table 11.7: Material Properties Used for Pure Isotropic Viscoelasticity Analysis with Softening Effect in Section 11.1.7 123
Table 11.8: Material Properties Used for Pure Isotropic Viscoelasticity Analysis with Softening Effect in Section 11.1.8 127
Table 11.9: Material Properties Used for Elastoplasticity Material Model Analysis in Section 11.2.1 130
Table 11.10: Material Properties Used for Isotropic Viscoelasticity and Anisotropic Plasticity Analysis 135
Table 12.1: Material Properties Obtained for Pure Elastic Model 170
Table 12.2: Material Properties Obtained for Pure Elastic Model 171
Table 12.3: Material Properties Obtained for Viscoelastic Model 171

LIST OF FIGURES

Figure 2.1 : The cross section schema of a healthy young artery [4] 5
Figure 2.2 : The cross section of a healthy lamb pulmonary artery..... 5
Figure 2.3 : Classification of blood vessels according to their size and pressure they carry [5]..... 6
Figure 2.4 : Schematic illustration of blood circulation (A) and a layout of the arterial system in the human body (B) [5] 7
Figure 2.5 : Schematic diagram of typical uniaxial stress-strain curves for circumferential arterial strips (taken from [16])..... 10
Figure 3.1 : The Deformation Gradient [21]..... 14
Figure 3.2 : Visual representation of Traction Vectors..... 15
Figure 4.1 : The Multiplicative decomposition [21]..... 29
Figure 4.2 : The 3-Element Solid Model (Poynting-Thomson Viscoelastic Solid)..... 34
Figure 4.3 : The In-Plane Shear 47
Figure 6.1 : Illustration of Crystal Plasticity theory based on multiplicative decomposition. The terminology here is due to [35] 68
Figure 6.2 : The experimentally obtainable elasto-plastic loading/unloading curve for a material and the visualization of the multiplicative decomposition concept..... 69
Figure 6.3 : The slip directions in single crystal [42] 70
Figure 6.4 : Visual Representation of Different Material Constitutive Models under Plastic Deformations. [35] 72
Figure 6.5 : Representative Behaviour of Selected Plastic Hardening Model..... 76
Figure 8.1 : The 1D Analogy to Elastoplastic Constitutive Model..... 85
Figure 9.1 : The 1D Analogy of the Prestrained Viscoelastoplastic Model. 91
Figure 11.1 : Pure Elastic Strain vs. Time Graphs under Cyclic Loading at 1Hz..... 100
Figure 11.2 : Pure Elastic Strain vs. Load Graphs under Cyclic Loading at 1Hz..... 101
Figure 11.3 : Pure Elastic Load vs. Time Graphs under Cyclic Loading at 1Hz..... 102
Figure 11.4 : Strain vs. Time Graphs under Cyclic Loading at 1Hz under Pure Elasticity with Softening Effects..... 103
Figure 11.5 : Strain vs. Load Graphs under Cyclic Loading at 1Hz under Pure Elasticity with Softening Effect 104
Figure 11.6 : Load vs. Time Graphs under Cyclic Loading at 1Hz under Pure Elasticity with Softening Effect 105
Figure 11.7 : Strain vs. Time Graphs under Cyclic Loading at 1Hz under Isotropic Viscoelasticity..... 107
Figure 11.8 : Strain vs. Load Graphs under Cyclic Loading at 1Hz under Isotropic Viscoelasticity..... 108
Figure 11.9 : Load vs. Time Graphs under Cyclic Loading at 1Hz under Isotropic Viscoelasticity..... 109

Figure 11.10 :–Strain vs. Time Graphs under Cyclic Loading at 1Hz using NonLinear Viscoelasticity Model 111
Figure 11.11 :–Strain vs. Load Graphs under Cyclic Loading at 1Hz using NonLinear Viscoelasticity Model 112
Figure 11.12 : Load vs. Time Graphs under Cyclic Loading at 1Hz using NonLinear Viscoelasticity Model 113
Figure 11.13 : Strain vs. Time Graphs under Cyclic Loading at 1Hz using Isotropic Viscoelasticity Model with Softening Effects 115
Figure 11.14 : Strain vs. Load Graphs under Cyclic Loading at 1Hz using Isotropic Viscoelasticity Model with Softening Effects 116
Figure 11.15 : Load vs. Time Graphs under Cyclic Loading at 1Hz using Isotropic Viscoelasticity Model with Softening Effects 117
Figure 11.16 : Strain vs. Time Graphs under Cyclic Loading at 1Hz over Static Torsion using Isotropic Viscoelasticity Model with Softening Effects 118
Figure 11.17 : Strain vs. Load Graphs under Cyclic Loading at 1Hz over Static Torsion using Isotropic Viscoelasticity Model with Softening Effects 119
Figure 11.18 : Load vs. Time Graphs under Cyclic Loading at 1Hz over Static Torsion using Isotropic Viscoelasticity Model with Softening Effects 121
Figure 11.19 : Strain vs. Time Graphs under Cyclic Loading at 1Hz with Torsion using Isotropic Viscoelasticity Model with Softening Effects" 122
Figure 11.20 : Strain vs. Load Graphs under Cyclic Loading at 1Hz with Torsion using Isotropic Viscoelasticity Model with Softening Effects 124
Figure 11.21 : Load vs. Time Graphs under Cyclic Loading at 1Hz with Torsion using Isotropic Viscoelasticity Model with Softening Effects 125
Figure 11.22 : Strain vs. Time Graphs under Cyclic Loading at 1Hz with Torsion using Isotropic Viscoelasticity Model with Softening Effects 126
Figure 11.23 : Strain vs. Load Graphs under Cyclic Loading at 1Hz with Torsion using Isotropic Viscoelasticity Model with Softening Effects 128
Figure 11.24 : Load vs. Time Graphs under Cyclic Loading at 1Hz with Torsion using Isotropic Viscoelasticity Model with Softening Effects 129
Figure 11.25 : Strain Components During an Elastoplastic Analysis of Axisymetric Tube as to details provided Section 11.2.1 131
Figure 11.26 : Load-Deformation Curves During an Elastoplastic Analysis of Axisymetric Tube as to details provided Section 11.2.1 132
Figure 11.27 : Load-Deformation Curves During an Elastoplastic Analysis of Axisymetric Tube as to details provided Section 11.2.1 133
Figure 11.28 : Strain Components During a Viscoelastoplastic Analysis of Axisymetric Tube as to details provided Section 11.2.2 134
Figure 11.29 : Load-Deformation Curves During anViscoelastoplastic Analysis of Axisymetric Tube as to details provided Section 11.2.2 135

Figure 11.30 : Load-Deformation Curves During anViscoelastoplastic Analysis of Axisymetric Tube as to details provided Section 11.2.2 136
Figure 12.1 : Laboratory of Strength of Materials and Biomechanics, Istanbul Technical University, Faculty of Mechanical Engineering..... 137
Figure 12.2 : Layout of the Experimental Setup 139
Figure 12.3 : View of Testing System During Set-up with the High Speed Cameras 140
Figure 12.4 : View of Testing System with Illumination and Artery Mounted..... 141
Figure 12.5 : Harvesting of Pulmonary Arteries by author..... 141
Figure 12.6: The secondary branches on the lamb pulmonary artery that have been closed with the aid of Plastic Surgeon Burcak ERDINC, M.D. 142
Figure 12.7 : The Speckled Artery Connected to the Testing System. 143
Figure 12.8 : A demonstration of PreStress in Arterial Tissue. 143
Figure 12.9 : Sample pictures from a loading protocol and respective Axial Lagrangian Strain values superposed over deformed arterial specimen..... 145
Figure 12.10 : Sample pictures from the loading protocol same in Figure 12.9 and respective Tangential Lagrangian Strain values superposed onto..... 145
Figure 12.11 : Sample pictures from the loading protocol same in Figure 12.9 and respective Shearing Lagrangian Strain values superposed onto..... 146
Figure 12.12 : Simple layout of algorithm 150
Figure 12.13 : The flowchart of parameter estimation algorithm 154
Figure 12.14 : Demonstration of Deformation Gradient Components, Comparison of Experimental and Theoretical Data at Initial Iteration as to 12.3.2 156
Figure 12.15 : Demonstration of Deformation Gradient Components, Comparison of Experimental and Theoretical Data at an Intermediate Iteration as to 12.3.2 157
Figure 12.16 : Demonstration of Deformation Gradient Components, Comparison of Experimental and Theoretical Data at Convergence Iteration as to 12.3.2..... 158
Figure 12.17 : Demonstration of Deformation Gradient Components, Comparison of Experimental and Theoretical Data at Initial Iteration as to 12.3.3..... 159
Figure 12.18 : Demonstration of Deformation Gradient Components, Comparison of Experimental and Theoretical Data at an Intermediate Iteration as to 12.3.3 160
Figure 12.19 : Demonstration of Deformation Gradient Components, Comparison of Experimental and Theoretical Data at Convergence Iteration as to 12.3.3..... 161
Figure 12.20 : Demonstration of Deformation Gradient Components, Comparison of Experimental and Theoretical Data at Initial Iteration as to 12.3.4..... 163
Figure 12.21 : Demonstration of Deformation Gradient Components, Comparison of Experimental and Theoretical Data at an Intermediate Iteration as to 12.3.4 164

Figure 12.22 : Demonstration of Deformation Gradient Components, Comparison of Experimental and Theoretical Data at Convergence Iteration as to 12.3.4 165
Figure 12.23 : Demonstration of Deformation Gradient Components, Comparison of Experimental and Theoretical Data at Initial Iteration as to 12.3.5 167
Figure 12.24 : Demonstration of Deformation Gradient Components, Comparison of Experimental and Theoretical Data at an Intermediate Iteration as to 12.3.5 168
Figure 12.25 : Demonstration of Deformation Gradient Components, Comparison of Experimental and Theoretical Data at Convergence Iteration as to 12.3.5 169
Figure 12.26 : Demonstration of Deformation Gradient Components, Comparison of Experimental and Theoretical Data at Convergence Iteration for as to 12.4.1 172
Figure 12.27 : Demonstration of Deformation Gradient Components, Comparison of Experimental and Theoretical Data at Convergence Iteration as to 12.4.2 173
Figure 12.28 : Demonstration of Deformation Gradient Components, Comparison of Experimental and Theoretical Data at Convergence Iteration as to 12.4.3 174
Figure A-1.1: Variation of Tangential Stress with Time and within Wall Thickness under Cyclic Loading at 1Hz 184
Figure A-1.2: Variation of Axial Stress with Time and within Wall Thickness under Cyclic Loading at 1Hz 185
Figure A-1.3: Variation of Radial Stress with Time and within Wall Thickness under Cyclic Loading at 1Hz 185
Figure A-1.4: Variation of Axial Total Strain with Time and within Wall Thickness under Cyclic Loading at 1Hz 186
Figure A-1.5: Variation of Tangential Total Strain with Time and within Wall Thickness under Cyclic Loading at 1Hz 186
Figure A-1.6: Variation of Radial Total Strain with Time and within Wall Thickness under Cyclic Loading at 1Hz 187
Figure A-2.1: Variation of Tangential Stress with Time and within Wall Thickness under Pure Elasticity with Softening Effect 188
Figure A-2.2: Variation of Axial Stress with Time and within Wall Thickness under Pure Elasticity with Softening Effect 188
Figure A-2.3: Variation of Radial Stress with Time and within Wall Thickness under Pure Elasticity with Softening Effect 189
Figure A-2.4: Variation of Axial Total Strain with Time and within Wall Thickness under Pure Elasticity with Softening Effect 189
Figure A-2.5: Variation of Tangential Total Strain with Time and within Wall Thickness under Pure Elasticity with Softening Effect 190
Figure A-2.6: Variation of Radial Total Strain with Time and within Wall Thickness under Pure Elasticity with Softening Effect 190
Figure A-3.1: Variation of Tangential Stress with Time and within Wall Thickness under Isotropic Viscoelasticity 191
Figure A-3.2: Variation of Axial Stress with Time and within Wall Thickness under Isotropic Viscoelasticity 191

Figure A-3.3: Variation of Radial Stress with Time and within Wall Thickness under Isotropic Viscoelasticity 192
Figure A-3.4: Variation of Axial Total Strain with Time and within Wall Thickness under Isotropic Viscoelasticity 192
Figure A-3.5: Variation of Tangential Total Strain with Time and within Wall Thickness under Isotropic Viscoelasticity 193
Figure A-3.6: Variation of Radial Total Strain with Time and within Wall Thickness under Isotropic Viscoelasticity 193
Figure A-4.1: Variation of Tangential Stress with Time and within Wall Thickness under Cyclic Loading at 1Hz using NonLinear Viscoelasticity Model..... 194
Figure A-4.2: Variation of Axial Stress with Time and within Wall Thickness under Cyclic Loading at 1Hz using NonLinear Viscoelasticity Model 194
Figure A-4.3: Variation of Radial Stress with Time and within Wall Thickness under Cyclic Loading at 1Hz using NonLinear Viscoelasticity Model..... 195
Figure A-4.4: Variation of Axial Total Strain with Time and within Wall Thickness under Cyclic Loading at 1Hz using NonLinear Viscoelasticity Model..... 195
Figure A-4.5: Variation of Tangential Total Strain with Time and within Wall Thickness under Cyclic Loading at 1Hz using NonLinear Viscoelasticity Model..... 196
Figure A-4.6: Variation of Radial Total Strain with Time and within Wall Thickness under Cyclic Loading at 1Hz using NonLinear Viscoelasticity Model..... 196
Figure A-5.1: Variation of Tangential Stress with Time and within Wall Thickness under Cyclic Loading at 1Hz using Isotropic Viscoelasticity Model and Softening 197
Figure A-5.2: Variation of Axial Stress with Time and within Wall Thickness under Cyclic Loading at 1Hz using Isotropic Viscoelasticity Model and Softening" 197
Figure A-5.3: Variation of Radial Stress with Time and within Wall Thickness under Cyclic Loading at 1Hz using Isotropic Viscoelasticity Model and Softening 198
Figure A-5.4: Variation of Axial Total Strain with Time and within Wall Thickness under Cyclic Loading at 1Hz using Isotropic Viscoelasticity Model and Softening 198
Figure A-5.5: Variation of Tangnt. Total Strain with Time and within Wall Thickness under Cyclic Loading at 1Hz using Isotropic Viscoelasticity Model and Softening 199
Figure A-5.6: Variation of Radial Total Strain with Time and within Wall Thickness under Cyclic Loading at 1Hz using Isotropic Viscoelasticity Model and Softening 199
Figure A-6.1: Variation of Shear Stress with Time and within Wall Thickness under Cyclic Loading at 1Hz over Static Torsion using Isotropic Viscoelasticity Model with Softening Effects"..... 200
Figure A-6.2: Variation of Tangential Stress with Time and within Wall Thickness under Cyclic Loading at 1Hz over Static Torsion using Isotropic Viscoelasticity Model with Softening Effects..... 200

Figure A-6.3: Variation of Axial Stress with Time and within Wall Thickness under Cyclic Loading at 1Hz over Static Torsion using Isotropic Viscoelasticity Model with Softening Effects..... 201
Figure A-6.4: Variation of Radial Stress with Time and within Wall Thickness under Cyclic Loading at 1Hz over Static Torsion using Isotropic Viscoelasticity Model with Softening Effects..... 201
Figure A-6.5: Variation of Total Shear Strain with Time and within Wall Thickness under Cyclic Loading at 1Hz over Static Torsion using Isotropic Viscoelasticity Model with Softening Effects..... 202
Figure A-6.6: Variation of Axial Total Strain with Time and within Wall Thickness under Cyclic Loading at 1Hz over Static Torsion using Isotropic Viscoelasticity Model with Softening Effects..... 202
Figure A-6.7: Variation of Tangential Total Strain with Time and within Wall Thickness under Cyclic Loading at 1Hz over Static Torsion using Isotropic Viscoelasticity Model with Softening Effects..... 203
Figure A-6.8: Variation of Radial Total Strain with Time and within Wall Thickness under Cyclic Loading at 1Hz over Static Torsion using Isotropic Viscoelasticity Model with Softening Effects..... 203
Figure A-7.1: Variation of Shear Stress with Time and within Wall Thickness under Cyclic Loading at 1Hz with Torsion using Isotropic Viscoelasticity Model with Softening Effects..... 204
Figure A-7.2: Variation of Tangential Stress with Time and within Wall Thickness under Cyclic Loading at 1Hz with Torsion using Isotropic Viscoelasticity Model with Softening Effects 204
Figure A-7.3: Variation of Axial Stress with Time and within Wall Thickness a under Cyclic Loading at 1Hz with Torsion using Isotropic Viscoelasticity Model with Softening Effects..... 205
Figure A-7.4: Variation of Radial Stress with Time and within Wall Thickness under Cyclic Loading at 1Hz with Torsion using Isotropic Viscoelasticity Model with Softening Effects 205
Figure A-7.5: Variation of Total Shear Strain with Time and within Wall Thickness under Cyclic Loading at 1Hz with Torsion using Isotropic Viscoelasticity Model with Softening Effects 206
Figure A-7.6: Variation of Axial Total Strain with Time and within Wall Thickness under Cyclic Loading at 1Hz with Torsion using Isotropic Viscoelasticity Model with Softening Effects 206
Figure A-7.7: Variation of Tangential Total Strain with Time and within Wall Thickness under Cyclic Loading at 1Hz with Torsion using Isotropic Viscoelasticity Model with Softening Effects 207
Figure A-7.8: Variation of Radial Total Strain with Time and within Wall Thickness under Cyclic Loading at 1Hz with Torsion using Isotropic Viscoelasticity Model with Softening Effects" 207
Figure A-8.1: Variation of Shear Stress with Time and within Wall Thickness under Cyclic Loading at 1Hz with Torsion using Isotropic Viscoelasticity Model with Softening Effects..... 208
Figure A-8.2: Variation of Tangential Stress with Time and within Wall Thickness under Cyclic Loading at 1Hz with Torsion using Isotropic Viscoelasticity Model with Softening Effects" 208

Figure A-8.3: Variation of Axial Stress with Time and within Wall Thickness under Cyclic Loading at 1Hz with Torsion using Isotropic Viscoelasticity Model with Softening Effects..... 209
Figure A-8.4: Variation of Radial Stress with Time and within Wall Thickness under Cyclic Loading at 1Hz with Torsion using Isotropic Viscoelasticity Model with Softening Effects 209
Figure A-8.5: Variation of Total Shear Strain with Time and within Wall Thickness under Cyclic Loading at 1Hz with Torsion using Isotropic Viscoelasticity Model with Softening Effects 210
Figure A-8.6: Variation of Axial Total Strain with Time and within Wall Thickness under Cyclic Loading at 1Hz with Torsion using Isotropic Viscoelasticity Model with Softening Effects 210
Figure A-8.7: Variation of Tangential Total Strain with Time and within Wall Thickness under Cyclic Loading at 1Hz with Torsion using Isotropic Viscoelasticity Model with Softening Effects 211
Figure A-8.8: Variation of Radial Total Strain with Time and within Wall Thickness under Cyclic Loading at 1Hz with Torsion using Isotropic Viscoelasticity Model with Softening Effects 211
Figure A-9.1: Variation of Axial Stress with Time and within Wall Thickness During an Elastoplastic Analysis of Axisymetric Tube as to details provided Section 11.2.1 212
Figure A-9.2: Variation of Tangential Stress with Time and within Wall Thickness During an Elastoplastic Analysis of Axisymetric Tube as to details provided Section 11.2.1..... 212
Figure A-9.3: Variation of Radial Stress with Time and within Wall Thickness During an Elastoplastic Analysis of Axisymetric Tube as to details provided Section 11.2.1..... 213
Figure A-9.4: Variation of Axial Plastic Strain with Time and within Wall Thickness During an Elastoplastic Analysis of Axisymetric Tube as to details provided Section 11.2.1..... 213
Figure A-9.5: Variation of Tangential Plastic Strain with Time and within Wall Thickness During an Elastoplastic Analysis of Axisymetric Tube as to details provided Section 11.2.1 214
Figure A-9.6: Variation of Radial Plastic Strain with Time and within Wall Thickness During an Elastoplastic Analysis of Axisymetric Tube as to details provided Section 11.2.1..... 214
Figure A-9.7: Variation of Axial Total Strain with Time and within Wall Thickness During an Elastoplastic Analysis of Axisymetric Tube as to details provided Section 11.2.1..... 215
Figure A-9.8: Variation of Tangential Total Strain with Time and within Wall Thickness During an Elastoplastic Analysis of Axisymetric Tube as to details provided Section 11.2.1..... 215
Figure A-9.9: Variation of Radial Total Strain with Time and within Wall Thickness During an Elastoplastic Analysis of Axisymetric Tube as to details provided Section 11.2.1..... 216
Figure A-10.1: Variation of Axial Stress with Time and within Wall Thickness During anViscoelastoplastic Analysis of Axisymetric Tube as to details provided Section 11.2.2 217

Figure A-10.2: Variation of Tangential Stress with Time and within Wall Thickness During anViscoelastoplastic Analysis of Axisymetric Tube as to details provided Section 11.2.2 217
Figure A-10.3: Variation of Radial Stress with Time and within Wall Thickness During anViscoelastoplastic Analysis of Axisymetric Tube as to details provided Section 11.2.2 218
Figure A-10.4: Variation of Axial Plastic Strain with Time and within Wall Thickness During anViscoelastoplastic Analysis of Axisymetric Tube as to details provided Section 11.2.2 218
Figure A-10.5: Variation of Tangential Plastic Strain with Time and within Wall Thickness During anViscoelastoplastic Analysis of Axisymetric Tube as to details provided Section 11.2.2..... 219
Figure A-10.6: Variation of Radial Plastic Strain with Time and within Wall Thickness During anViscoelastoplastic Analysis of Axisymetric Tube as to details provided Section 11.2.2 219
Figure A-10.7: Variation of Axial Total Strain with Time and within Wall Thickness During anViscoelastoplastic Analysis of Axisymetric Tube as to details provided Section 11.2.2 220
Figure A-10.8: Variation of Tangential Total Strain with Time and within Wall Thickness During anViscoelastoplastic Analysis of Axisymetric Tube as to details provided Section 11.2.2..... 220
Figure A-10.9: Variation of Radial Total Strain with Time and within Wall Thickness During anViscoelastoplastic Analysis of Axisymetric Tube as to details provided Section 11.2.2 221

NOMENCLATURE

$\mathbf{F}$, $\mathbf{F}_e$, $\mathbf{F}_v$	The Total, Elastic And Viscous Deformation Gradient Tensors
$\mathbf{F}_0$, $\mathbf{F}_m$, $\mathbf{F}_p$	The Prestrain-Related, Elastic Mechanical And Plastic Deformation Gradient Tensors
J	Volumetric Ratio
$\mathbf{E}$	Total Lagrangian Strain Tensor
$\mathbf{E}_v$	Viscous Lagrangian Strain Tensor
$\mathbf{\Gamma}_e$	Elastic Lagrangian Strain Tensor
$\mathbf{C}_e$	Elastic Right Cauchy-Green Stretch Tensor
$\mathbf{L}$, $\mathbf{L}_e$, $\mathbf{L}_v$, $\mathbf{L}_p$	The Total, Elastic, Viscous and PlasticVelocity Gradient Tensors
$\mathbf{I}$	Identity Tensor
$I_1,...,I_9$	(Pseudo) Strain Invariants
Ψ, Ψ_e, Ψ_v	Total, Elastic and Viscous Strain Energy Density Function
Ψ_v^∞	Undamaged Viscous Strain Energy Density Function
$\dot{\mathbf{E}}$, $\dot{\mathbf{E}}_v$	Material Time Derivative of Total and Viscous Lagr Strain Tensor
ε	Resolved Normal Strain
γ, $\dot{\gamma}$	Resolved Shear Strain and Its Material Time Derivative
$\mathbf{S}$	II. Piola-Kirchhoff Stress Tensor
$\mathbf{P}$	I. Piola-Kirchhoff Stress Tensor
$\boldsymbol{\sigma}$	Cauchy Stress Tensor
$\boldsymbol{\Sigma}$	Mandel Stress Tensor
$\boldsymbol{\tau}$	Kirchoff Stress Tensor
Φ	Dissipation Potential
φ_4, φ_6	Fiber Orientation Helix Angles with respect to Tube Axis
$\mathbf{m}_4^0$, $\mathbf{m}_6^0$	Vectors Indicating the Fiber Orientation Helix Direction
$\mathbf{n}_4^0$, $\mathbf{n}_6^0$	Normal Vectors to Orientation of Fiber Helix Directions
$\mathbf{M}_4^0$, $\mathbf{M}_6^0$	Fiber Orientation Structural Tensors in Reference Configuration
$\mathbf{M}_4^v$, $\mathbf{M}_6^v$	Fiber Orientation Structural Tensors in Intermediate Configuration
$\mathbf{D}_4^0$, $\mathbf{D}_6^0$	Dilatational Shear Resolving Tensors in Reference Configuration
$\mathbf{\Omega}_4^0$, $\mathbf{\Omega}_6^0$	Spin Tensors in Reference Configuration
η, η_f, η_{GS}	Viscosity Coefficient
α_f	Nonlinear Dissipation Exponent
Q	Damage Variable
s	Damage Evolution Surface
D	Damage Variable
δ, Q_∞	Damage Saturation and Critical Damage Values as Material

	Constants
(R,Θ,Z)	Cylindrical Coordinates in Reference Configuration
(ρ,ν,ζ)	Cylindrical Coordinates in Intermediate Configuration
(r,θ,z)	Cylindrical Coordinates in Final Configuration
φ , ϕ	Unit Twist Angles in Reference and Intermediate Configurations
Λ , λ	Axial Stretch Ratios in Reference and Intermediate Configurations
A_0 , B_0	Inner and Outer Radius of Tube in Un-Prestressed Configuration
A , B	Inner and Outer Radius of Tube in Reference Configuration
α , β	Inner and Outer Radius of Tube in Intermediate Configuration
a , b	Inner and Outer Radius of Tube in Final Configuration
C_1^e, C_2^e, C_3^e	Material Parameters for Ψ_e
C_1^v, C_2^v, C_3^v	Material Parameters for Ψ_v^∞
g_0 , g_∞ , h_0 , k, $\dot{a}$	Material Parameters Referring to the Rate-Dependent Plasticity Model
τ_α	Resolved Shear Stress on Active Slip Direction
P_i	Internal Pressure
p	Hydrostatic Pressure (Incompressibility Lagrange Multiplier)
F_{ax}	Axial Force exerted on Arterial Segment
N	Net Axial Force acquired from Transducer
M_b	Torque
R_T	Testing Machine Rigid Connection Radius for Arterial Segment

VISCOELASTOPLASTIC MODELING OF ARTERIAL TISSUE

SUMMARY

The great majority of diseases in the (western) world, such as atherosclerosis and degeneration of intervertebral discs are diseases of soft tissues. Hence, the multidisciplinary field of soft tissue research is of crucial scientific, medical and socioeconomic importance. The fast progress in the developments of hardware and software facilities makes it possible to thoroughly investigate biological soft tissues and their pathologies on a computational basis. Since soft tissues are biological materials, which fulfill mechanical purposes and adapt to their mechanical environment (growth, remodeling and morphogenesis), it is of fundamental importance to identify the complex interactions of mechanical and biological responses.

This work has aimed at setting the foundations of a non-linear material model for arterial viscoelastoplasticity. The model accounts for the composite structure of the vessel and its complex passive mechanical response to loading conditions. Long term property changes of arterial structure have been modeled with a damage model. It can easily be extended to remodeling phenomenon which also accounts for adaptation of the structure to long-term steady-state changes in the loading conditions such as chronic hypertension. Much work has been done in the literature, but hardly few have been extensively studied with diverse experimental data.

The initiation of the study has been pointed out to be a section where the basics of arterial anatomy, the cardiovascular system have been presented. The important facts about the arterial structure, such as its collagenous fibrous composite structure, layered composition and its consequences have been presented. Some examples from previous work on the subject have been presented and the current work has been positioned over the intention that the others have not presented.

A brief of continuum mechanics has been presented to make the terminology clear. Then, the material models have been proposed from simple viscoelastic formulations to a damage-softening viscoelastoplastic formulation, where the prestress effects have also been considered within the constitutive framework. Demonstrative analysis with estimate material parameters have been presented to inspect in detail whether the proposed model behaves in accordance with the expectations and with full compatibility with solid mechanics basics and thermodynamic restrictions on constitutive modeling.

The study has been enhanced with an extensive testing system for controlled synchronous and discrete application of combined inflation/extension/torsion loads on tubular specimens, enhanced with high speed optical deformation measurement systems. The test setup has been implemented in the Strength of Materials and

Biomechanics Laboratory at Istanbul Technical University, Faculty of Mechanical Engineering.

Analytical formulations suitable to application of parameter estimation studies for specimens under combined inflation/extension/torsion loads on thick-walled cylindrical tubes have been presented. In vitro experiments have been carried out with lamb arterial segments, which have been treated by plastic surgeons, and with looping the secondary branches, a watertight (quasi) cylindrical test specimen has been obtained. Parameter fitting procedures have been carried out on experimental data to the extent that the experimental system allowed reasonable and useful data to feed into the optimization algorithm for parameter estimation.

The work concludes with a summary of basic outcomes of the material's models abilities and comments on the outcomes and data obtained from the parameter estimation studies. It has been commented that the model is very compatible for determining viscoelastoplastic behavior of arterial segments, and more generally for estimating behavior of fibrous composites that exhibit geometrical and material nonlinearity to the extent that the loading conditions are in-phase. Based on the outcomes of the studies, some comments on future research topics have also been presented.

DAMAR DOKUSUNUN VİSKOELASTOPLASTİK MODELLENMESİ

ÖZET

Dünyadaki ekonomik, bilimsel ve tıp açısından oldukça önemli ve gözlemlenme oranı yüksek olan arteroskleroz ve disk dejenerasyonu gibi hastalıklar, temelde yumuşak doku hastalıkları olarak adlandırılabilirler. Bu bağlamda, disiplinler arası bir araştırma konusu olan yumuşak dokularda araştırma, sosyoekonomik olarak gittikçe büyüyen bir önem arz etmektedir. Donanım ve yazılım olanaklarındaki hızlı gelişmeler, yumuşak dokuların ve ilgili patolojilerin sayısal olarak detaylı şekilde modellenebilmesine olanak tanımaktadır. Yumuşak dokular da, çeşitli mekanik özellikleri haiz ve mekanik dış ortam uyaranlarına göre (büyüme, yeniden modelleme, morfojenez) kendilerini uyarlabilindiklerinden dolayı, biyolojik ve mekanik etkileşimlerin bilinmesi ve belirtilmesi çok büyük önem taşımaktadır.

Bu çalışma kapsamında, damar dokusu için viskoelastoplastik bir malzeme modelinin temellerinin oluşturulması amaçlanmıştır. Model, damar cidar yapısının kompozit özelliklerini içermekte ve çok eksenli yükleme durumlarına göre karmaşık pasif mekanik cevap mekanizmasını kapsamaktadır. Bir (elastik) hasar (damage) mekanizması ile malzemenin zamanla mekanik özelliklerinin değiştiği (yumuşama gösterdiği) dikkate alınmıştır. Model, kronik hipertansiyon gibi yüklenme şartlarındaki uzun vadeli değişimlere uyumu tasvir eden "yeniden yapılanma" (remodeling) özelliklerinin eklenebileceği modüler bir şekilde tasarlanmıştır. Literatürde bu konuda oldukça fazla sayıda çalışma olmasına rağmen, deneysel verilerle desteklenen modeller yok denecek kadar azdır.

Çalışmanın başlangıcı olarak, kardiyovasküler sistem ve damar anatomisi hakkında bilgiler sunulmuştur. Bu esnada, yapının kollajen fibrillerden oluşan sarmal kompozit ve katmanlı yapısı hakkında ayrıntılar sunulmuş ve bu yapının katı mekaniği açısından getirdiği sonuçlar hakkında yorumlar yapılmıştır. Literatürde bulunan daha önceki çalışmalardan örnekler verilmiştir. Böylelikle, bu çalışmada sunulan modelin diğer modellerin zayıf taraflarına göre konumlandırılması yapılmıştır.

Daha sonraki bölümlerde, ilk olarak terminoloji ve temel kavramları açıklamak için kısa bir sürekli ortamlar mekaniği özeti sunulmuştur. Daha sonra, temel viskoelastik bir malzeme formülasyonundan başlayarak adım adım en genel hal olan hasar mekanizmalı viskoelastoplastik malzeme modelinin elde edilmesi gerçekleştirilmiştir. Bu model elde edilirken, damar yapısı üzerindeki öngerilmelerin de modele konulması hakkında gerekli altyapı hazırlanmıştır. Yaklaşık malzeme parametreleri ile örnek yükleme koşulları ile analizler gerçekleştirilmiş ve öngörülen modelin beklentilerle ve katı mekaniğinin temelleri ve termodinamik sınırlamaları ile uyumlu olup olmadığı incelenmiştir.

Çalışma daha sonra deneysel bir sistem kurulumu, tanıtımı ve bu sistemle gerçekleştirilmiş deneysel çalışmalarla geliştirilmiştir. İstanbul Teknik Üniversitesi

Makina Fakültesi Mukavemet ve Biyomekanik Laboratuarı kapsamında bir test düzeneği kurulmuştur. Bu düzenekle, silindirik test numunelerine senkron yükleme yapabilecek, fakat bağımsız kontrollu bir iç basınç/eksenel kuvvet/burulma momenti uygulama imkanı sağlanmıştır. Deney düzeneği, yüksek hızlı optik deformasyon ölçüm sistemi ile desteklenmiştir.

Testlerden elde edilen verilerin incelenmesine yönelik olarak analitik formülasyonlarla elde edilmiş ve kalın cidarlı eksenel simetrik tüp olarak modellenen damar üzerinde birleşik iç basınç, eksenel zorlanma ve burulma zorlanması yüklenmeleri için genel yüklenme/deformasyon ilişkileri çıkartılmıştır. Koyun pulmoner arterleri ile in-vitro deneysel çalışmalar gerçekleştirilmiştir. Bu numunelerin, plastik cerrah yardımı ile ikincil branşman damarları dikilerek su sızdırmazlığı sağlanmış ve neredeyse eksenel simetrik hale getirilmiştir. Çeşitli optimizasyon teknikleri kullanılarak, parametre tahmini yapmaya uygun olan deneysel verilerden malzeme katsayıları tahmini gerçekleştirilmiştir.

Çalışma, öngörülen malzeme modelinin ve deneysel çalışmalardan elde edilen bilgilerin bir özeti ile sonuçlanmaktadır. Burada ortaya konmaktadır ki, yüklenmeler aynı fazda olduğu müddetçe, sözkonusu model, yeterli başarı ile deneysel verilere uygunluk sağlamaktadır. Elde edilen sonuçlar ışığında ayrıca ileriye yönelik araştırma konuları hakkında kısa bir yol gösterme ortaya konulmuştur.

1. INTRODUCTION

The great majority of diseases in the (western) world, such as atherosclerosis and degeneration of intervertebral discs can be classified as problems with soft tissues. Thus, the soft tissue research is of crucial scientific, medical and socioeconomic importance as one of the most complex multidisciplinary field of science. The fast development in hardware and software resources now makes it possible to thoroughly investigate biological soft tissues and their pathologies on a computational basis. As being biological materials, which fulfill mechanical purposes and adapt to their mechanical environment (growth, remodeling, etc…), it is of fundamental importance to identify the complex interactions of mechanical and biological responses.

In order to achieve clinically meaningful results to contribute to development of clinical techniques and devices as well as engineering skills, focusing an engineering "eye" to biological structures requires:

- A comprehensive experimental database of the material to be modeled,
- A mathematical model that captures the essential mechanical characteristics
- An efficient numerical model with the aim to study the effects of medical treatments subject to certain procedural parameters in a robust and reliable way since as in other fields of applied mechanics the computational approach offers an essential alternative in situations where experiments are either too costly or even impossible.

This work has aimed at setting the foundations of a non-linear material model for arterial viscoelastoplasticity with damage softening. The model accounts for the composite structure of the vessel and its complex passive mechanical response to loading conditions. Long term failure of arterial structure has been modeled with a rate-dependent plasticity model. The strain (and respectively, time) dependent

softening is also accounted for, by means of a damage accumulation model. Both characteristics have been modeled to capture the anisotropic response at all stages. The model, thus, can easily be extended to remodeling phenomenon which also accounts for adaptation of the structure to long-term steady-state changes in the loading conditions such as chronic hypertension. Much work has been done in the literature, but hardly few have been extensively studied with diverse experimental data.

The study proposed within this work also aims to be a guide to non-linear experimental data evaluation and conducting experiments with large-deforming composite materials under multi-axial loading conditions. Also, viscoelasticity has been considered and dynamical tests have been conducted for parameter estimation. By now, many of the methods employed within this thesis have not been applied to problems in fields of either engineering or biomechanics.

2. THE CIRCULATORY SYSTEM AND ARTERIAL PHYSIOLOGY

2.1. The Artery: Anatomical Basics

This study is concerned with the in vitro passive behavior of arteries. Hence, in vivo effects such as the vasa vasorum, nerve control, humoral control, interferences due to perivascular connective tissue etc. and effects through boundaries of neighboring organs are not discussed.

By composition, arteries are roughly subdivided into two types: elastic and muscular. Elastic arteries have relatively large diameters and are located close to the heart (e.g., the aorta and the carotid and iliac arteries), while muscular arteries are more peripheral (for example, femoral, celiac, cerebral arteries). Some arteries exhibit morphological structures of both types. Attention is focused on the microscopic structure of arterial walls composed of three distinct layers, the intima (tunica intima), the media (tunica media) and the adventitia (tunica externa). The constituents of arterial walls, which are important to researchers interested in constitutive issues from a mechanical perspective, are discussed and emphasized. Figure 2.1 shows a sketch of a healthy elastic artery.

The intima is the innermost layer of the artery. It is just a single layer of endothelial cells lining the arterial wall and resting on basal lamina. The subendothelial layer, whose thickness varies with topography, age and health condition is almost not present in healthy young muscular arteries. In healthy young individuals, the intima is very thin and is assumed not to be of negligible importance to the solid mechanical properties of the arterial wall. However, its the mechanical contribution may become significant with age, in the form arteriosclerosis; the deposition of fatty substances, calcium, collagen fibers, cellular waste products and fibrin.

The media is the middle layer of the artery (see Figure 2.1). It is a complex three-dimensional network of smooth muscle cells, elastin and collagen fibrils. According to [1] the fenestrated elastic lamina separates the media into a varying number of

well-defined concentrically fiber-reinforced medial layers. This structure is important in generating assumptions during constitutive modeling. It is separated from the intima and adventitia by the internal elastic lamina and external elastic lamina, respectively. Existence of elastic lamina decreases toward the periphery (as the size of the vessels decreases) so that elastic lamina is hardly present in muscular arteries. Consequently, this structure is not present in cerebral blood vessels, where aneurysm development is a major problem. The orientation of and close interconnection between the elastic and collagen fibrils, elastic lamina, and smooth muscle cells together constitute a "composite material structure" with a continuous fibrous helix [2] with a small pitch angle with respect to the tangential horizon. Thus the fibrils in the media are almost circumferentially oriented, and give the media its high strength, resilience and the ability to resist loads in both the longitudinal and circumferential directions.

The adventitia is the outermost layer of the artery (see again figure 2.1) and consists mainly of fibroblasts and fibrocytes (cells that produce collagen and elastin), a ground substance and thick bundles of collagen fibrils forming a complex fibrous tissue. It is surrounded continuously by loose connective tissue. The thickness of the adventitia depends strongly on the type (elastic or muscular) and the physiological function of the blood vessel and its topographical site. In cerebral blood vessels there is virtually no adventitia. The wavy collagen fibrils are arranged in helical structures and serve to reinforce the wall. They contribute significantly to the stability and strength of the arterial wall at high blood pressure levels than normal situation. Consequently, the adventitia is much less stiff in the load-free configuration [3].

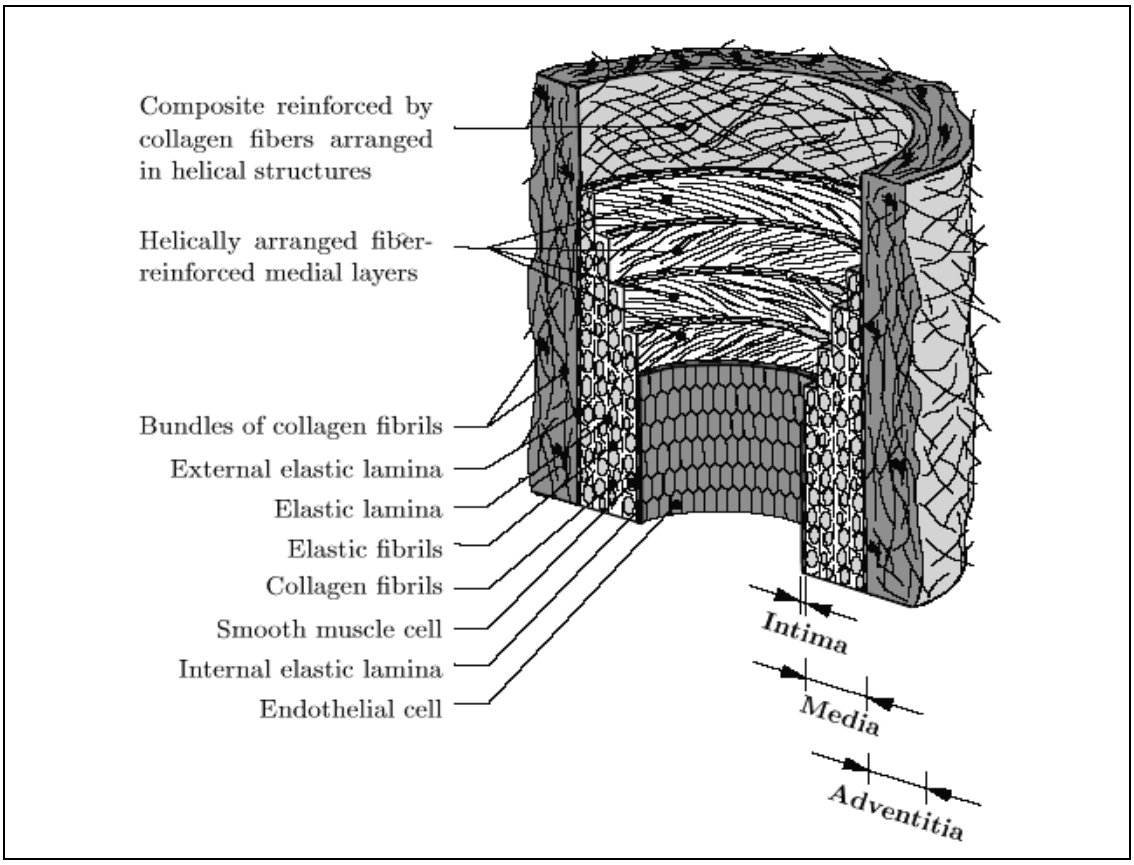

Figure 2.1 : The cross section schema of a healthy young artery [4]

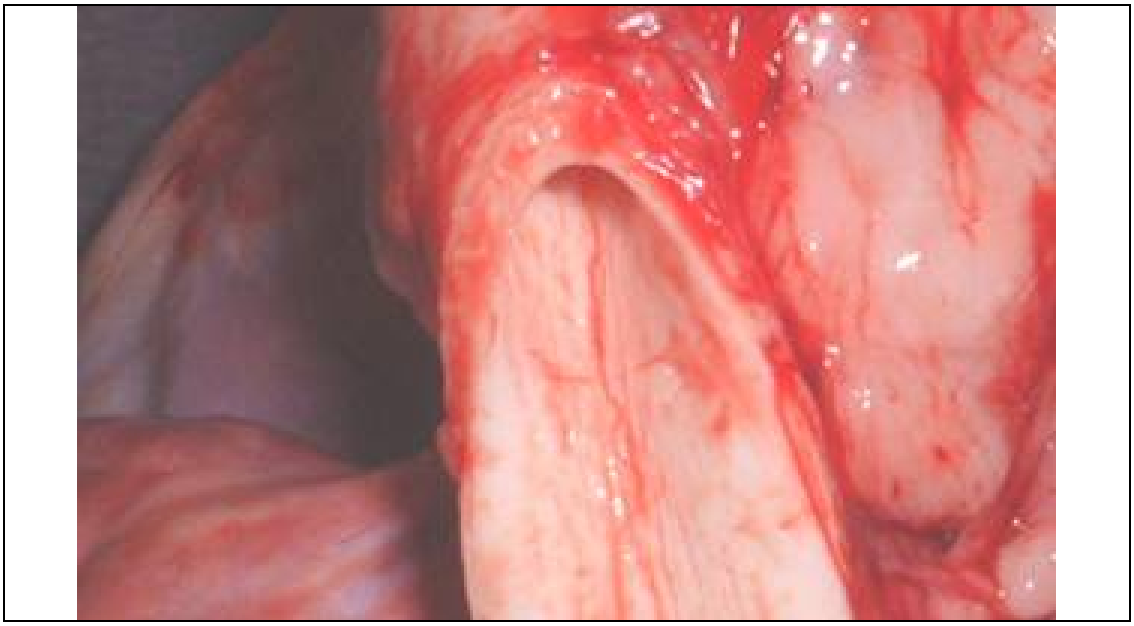

Figure 2.2 : The cross section of a healthy lamb pulmonary artery

2.2. Mechanical Basics on Arterial Physiology

The cardiovascular network is a complex architecture of blood vessels that carry blood to and from various organs. The blood vessels may be named based on their sizes, function and proximity to the heart.A typical classification discriminates these structures into one of the 7 categories as listed in Table 2.1 and visualized in Figure 2.3. A scheme of the path of blood flow is as shown in the Figure 2.4 [5].

Table 2.1: Characteristics of various types of blood vessels

Vessel	Aorta	Artery	Arteriole	Capillary	Venule	Vein	V.Cava
Wall Thickness	2mm	1mm	20µm	1µm	2µm	0.5mm	1.5mm
Lumen Diameter	25mm	4mm	30µm	8µm	20µm	5mm	30mm

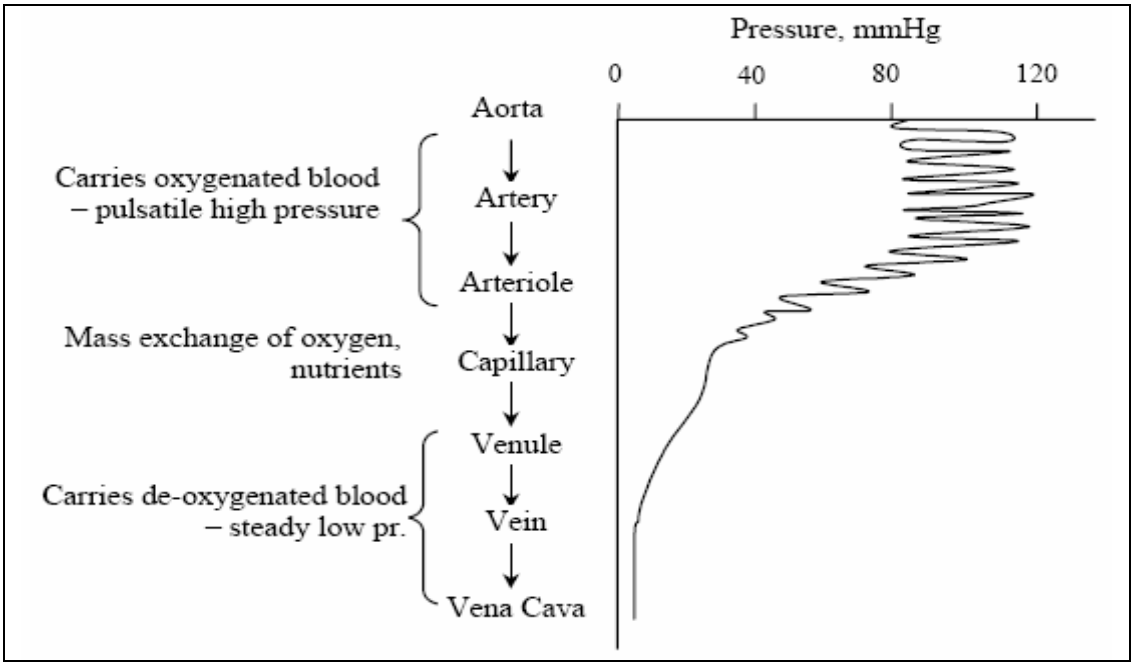

Figure 2.3 : Classification of blood vessels according to their size and pressure they carry [5]

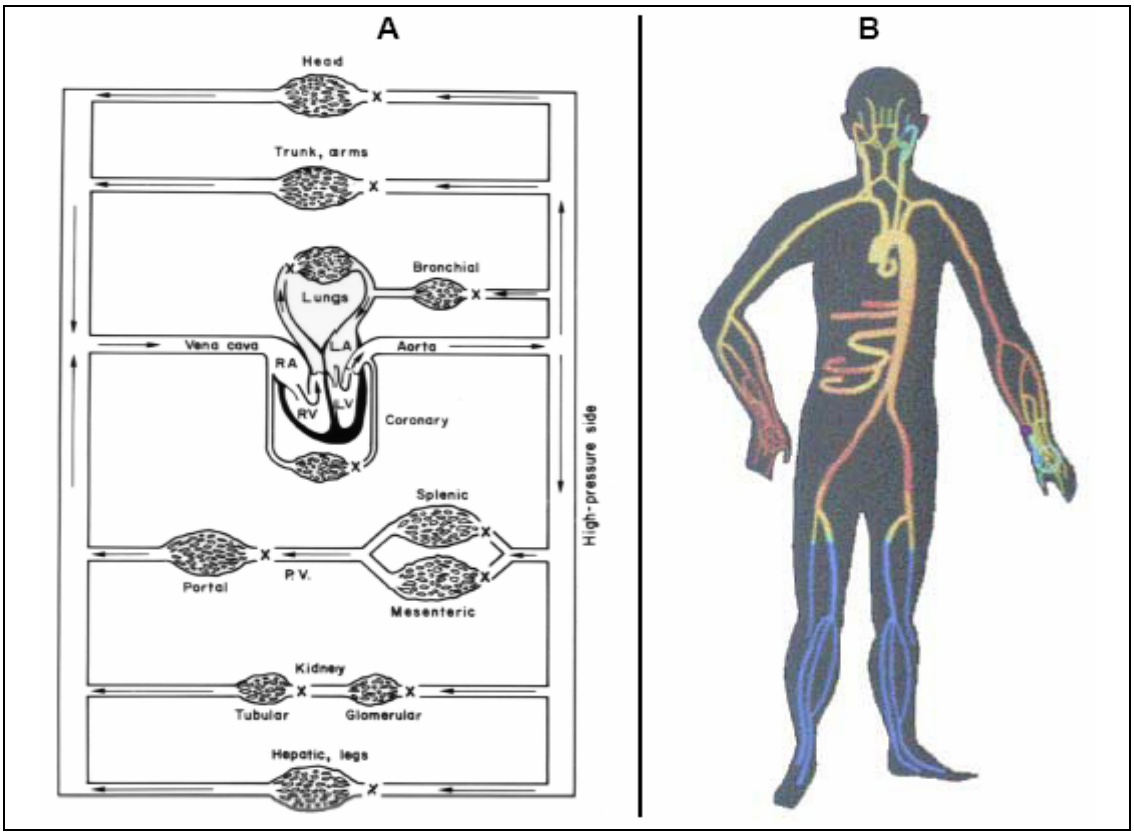

Figure 2.4 : Schematic illustration of blood circulation (A) and a layout of the arterial system in the human body (B) [5]

2.2.1. Mechanics of Arterial Wall

Each constitutive framework and determination of its associated set of material parameters in biological structures require detailed studies on the particular material of interest, since the model's reliability is strongly correlated to the completeness of available experimental data, which may have been obtained via appropriate in vivo tests or from in vitro tests that simulate the real loading conditions in a corresponding physiological environment. In practice, in vivo tests are much more preferable because the vessel is observed under real life conditions. However, in vivo tests have major limitations because of, for example, the influence of hormones and neural control or non-applicability of engineering techniques required. Data sets from the complex material response of arterial walls subject to simultaneous (or discrete) cyclic inflation, axial extension and twist can only be measured in an in vitro experiment. Only with such data sets can the anisotropic mechanical behavior of arterial walls be described completely [6]. In addition, in in-vitro experiments the

contraction state (active or passive) of the muscular media has to be determined, mostly with the aid of appropriate chemical agents.

2.2.2. Mechanical Tests on Arterial Tissue

The early work [7] is one of the best examples for pure inflation tests of straight artery tubes, which is the most common two dimensional test, where shear deformations are not considered. Since arteries do not change their volume (within the physiological range of deformation [8]), they can be regarded as incompressible materials.

Based on the works done by then is that, by means of the incompressibility constraint it is possible to determine the mechanical properties of three-dimensional specimens from two-dimensional tests. Uniaxial extension tests on arterial patches (strips) provide basic information about the material, but they are certainly not sufficient to quantify completely the anisotropic behavior of arterial walls, nor the uniaxial extension tests on small arterial rings [9,10].

In general, a segment of vessel shortens on removal from the body, as was first reported in [11]. Each non-axisymmetric arterial segment (such as a bifurcation or a segment with sclerotic changes) under combined inflation and axial extension develops significant shear stresses (in the θZ plane, namely) in the wall. This yields the result that, in order to properly mimic the shear properties of arterial walls shear tests are required. In shear tests either the angle of twist of an arterial tube subjected to transmural pressure, longitudinal force and torque [12] or the shear deformation of a rectangular arterial wall specimen subjected to shear forces is measured.

Another classification over mechanical tests might be developed with respect to the strain rates applied (quasi-static or dynamic) and to whether the loading is performed cyclically or discontinuously (such as creep tests).

It has been known for many years that the load-free configuration of an artery is not a stress-free state [12,13], and a load-free arterial ring contains inherent residual stresses (and strains). It is of crucial importance to incorporate such effects in order to predict reliably the state of stress in an arterial wall. This issue has been the aim of many experimental investigations such as bending tests on blood vessel walls in [14].

Disregarding for a moment the loading conditions, the mechanical behavior of arteries depends on physical and chemical environmental factors, such as temperature, osmotic pressure, pH, partial pressure of CO_2 and O_2, ionic and monosaccharide concentration. In ex vivo conditions the mechanical properties are altered due to biological degradation. These issues should also be considered during in-vitro testing conditions to the extent that they are thought to be important in the model created to examine a specific phenomenon. Details on environment-controlled tests are summarized in [15].

2.2.3. Mechanical Response of Arterial Tissue to External Loads

Circumferential strip of the media subjected to uniaxial cyclic loading and unloading demonstrates stress softening, which occurs during the first few load cycles and diminishes with increasing number of cycles. Limit is a nearly repeatable cyclic behavior, when the biological material is said to be 'pre-conditioned'. Depending on the type of artery considered, the material behavior may be regarded as (perfectly) elastic (proximal)or viscoelastic (distal).

Figure 2.6 demonstrates a schematic of a typical uniaxial stress-strain curve for circumferentially dissected arterial strips (from the media) in passive condition[16] From the figure one can conclude that the cyclic loading and unloading, associated with softening effects, lead to a pre-conditioned material which behaves (perfectly) elastical or viscoelastical around an equilibrium (nearly repeatable cyclic behavior).up to point I. Loading up to point II leads to inelastic deformations. Additional loading and unloading cycles display softening again until point III is reached. Then, the material again exhibits (perfectly) elastic or viscoelastic response. The thick solid line indicates the (approximate) engineering response of the material.

It should be noted that, in strip tests, the continuity of the collagen fibrils are destroyed, and care should be taken while considering the plastic deformations regarding fiber slip within base ground material, which might be an artificial issue imposed by the test method.

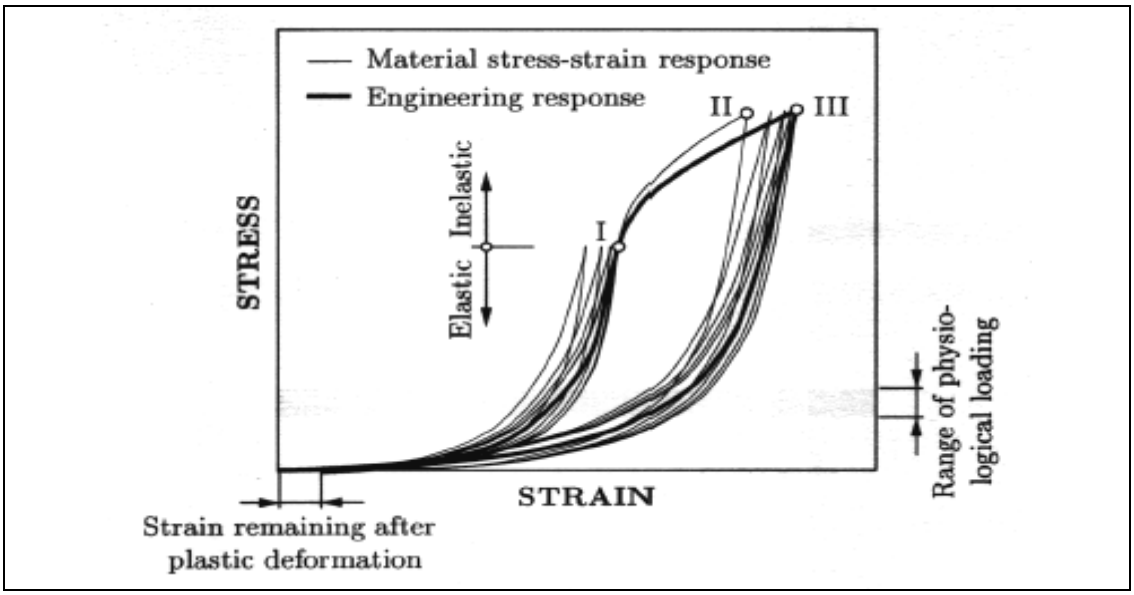

Figure 2.5 : Schematic diagram of typical uniaxial stress-strain curves for circumferential arterial strips (taken from [16])

As indicated in Section 2.2.1 the composition of arterial walls varies along the arterial tree, which is sure to induce a systematic dependence of the shape of the stress-strain curve for a blood vessel depending on its location over the cardiovascular network [17]. But, the general mechanical characteristics exhibited by arterial walls are more or less the same and in order to explain the typical stress-strain response of an arterial wall of smooth muscles in the passive state (i.e. when the resistance of wall is purely governed by elastin and collagen fibers), Figure 2.5 is more than sufficient. Note that the curves in Figure 2.5 are schematic, but based on experimental tension tests performed as to [16]).

Referring to Figure 2.5 again, it can be stated that, arteries are highly deformable composite structures and show the nonlinear stress-strain response with a typical (exponential) stiffening effect at higher pressures. This stiffening effect, almost common to all biological tissues, is based on the rearrangement of wavy collagen fibrils, which also leads to the characteristic anisotropic mechanical behavior of arteries. Early works on arterial anisotropy (see, for example, [8]) considered arterial walls to be cylindrically orthotropic. Loading beyond the viscoelastic domain (indicated by point I in Figure 2.5), far outside the physiological range of deformation, often occurs during mechanical treatments such as percutaneous transluminal angioplasty (see [20]), or natural cases where material degeneration is

accompanied by, for example, hypertension. In the strain range up to point II in Figure 2.5, the viscoelastic deformation in an arterial layer is accompanied with inelastic effects (elastoplastic and/or damage mechanisms) leading to significant changes in the mechanical behavior, where overstretching involves dissipation, captured by the area between the loading and unloading curves. Hence, starting from point II, additional cyclic loading and unloading again displays softening, which again vanishes with the number of load cycles. At point III the material exhibits a (perfectly) elastic or viscoelastic behavior. However, unloading initiated from point III returns the arterial (medial) strip to an unstressed state with non-vanishing strains remaining, these being responsible for the change of shape. [19,20]

3. BASICS OF NON-LINEAR CONTINUUM MECHANICS

3.1. Kinematics Preliminaries

In finite deformation continuum mechanics, the main kinematic quantity is the deformation gradient tensor, which is the local mapping of a differential line element $d\mathbf{X}$ in the reference configuration to the element in the deformed configuration $d\mathbf{x}$. Thus, by using the definition $\mathbf{x} = \mathbf{x}(\mathbf{X}, t)$

$$d\mathbf{x} = \mathbf{F} d\mathbf{X} \tag{3-1}$$

and if there is no deformation,

$$\mathbf{F} = \mathbf{I} \tag{3-2}$$

where $\mathbf{I}$ is the second-order identity tensor:

$$\mathbf{I} = \begin{bmatrix} 1 & 0 & 0 \\ 0 & 1 & 0 \\ 0 & 0 & 1 \end{bmatrix} \tag{3-3}$$

When a deformation step, say, (1) is followed by say, step(2), then step(2) takes the deformed line segment of step(1) as reference. Thus as the gradient for the total deformation (process)

$$d\mathbf{x} = \mathbf{F}_2 (\mathbf{F}_1 d\mathbf{X}) \tag{3-4}$$

$$d\mathbf{x} = \mathbf{F}_2 \mathbf{F}_1 d\mathbf{X} \tag{3-5}$$

$$\mathbf{F} = \mathbf{F}_2 \mathbf{F}_1 \tag{3-6}$$

is obtained. Loosely speaking, the tensor of the preceding deformation step is placed to the right of the following.

Any deformation can be considered to be a combination of

a) An orthogonal rigid body rotation followed by some stretch $\mathbf{F} = \mathbf{VR}$

b) Some stretch following some orthogonal rigid body rotation $\mathbf{F} = \mathbf{RU}$

These decompositions enable the evolution of so-called left ($\mathbf{V}$) and right ($\mathbf{U}$) stretch tensors.

In the (total) Lagrangian concept, the Right Cauchy-Green stretch tensor ($\mathbf{F}$ is to the right of $\mathbf{F}^T$) is defined as

$$\mathbf{C} = \mathbf{F}^T\mathbf{F} \tag{3-7}$$

which is, equivalent to

$$\mathbf{C} = \mathbf{U}^T\mathbf{R}^T\mathbf{R}\mathbf{U} = \mathbf{U}^T\mathbf{U} \tag{3-8}$$

Thus, the Right Cauchy-Green stretch tensor is independent of rigid body rotations, and is an objective measure of deformations at a point, since

$$\mathbf{R}^T\mathbf{R} = \mathbf{I}$$

Identically satisfied for orthogonal rotations. Notice also that

$$\mathbf{C} = \mathbf{I} \tag{3-9}$$

if there is no deformation. The Lagrangian Strain is defined as

$$\mathbf{E} = \frac{1}{2}(\mathbf{C} - \mathbf{I}) \tag{3-10}$$

In the limit of complete volumetric collapse,

$$\mathbf{E} \to \frac{1}{2}(-\mathbf{I}) \tag{3-11}$$

can be obtained as the limit.

The volumetric change of a differential volume element is defined as the volume ratio, denoted as

$$J = \det(\mathbf{F}) \tag{3-12}$$

or

$$J^2 = \det(\mathbf{C}) \tag{3-13}$$

since

$$\det(\mathbf{R}) = 1 \tag{3-14}$$

identically.

Setting $J = 1$ during some deformation process imposes the incompressibility constraint on the deformation.

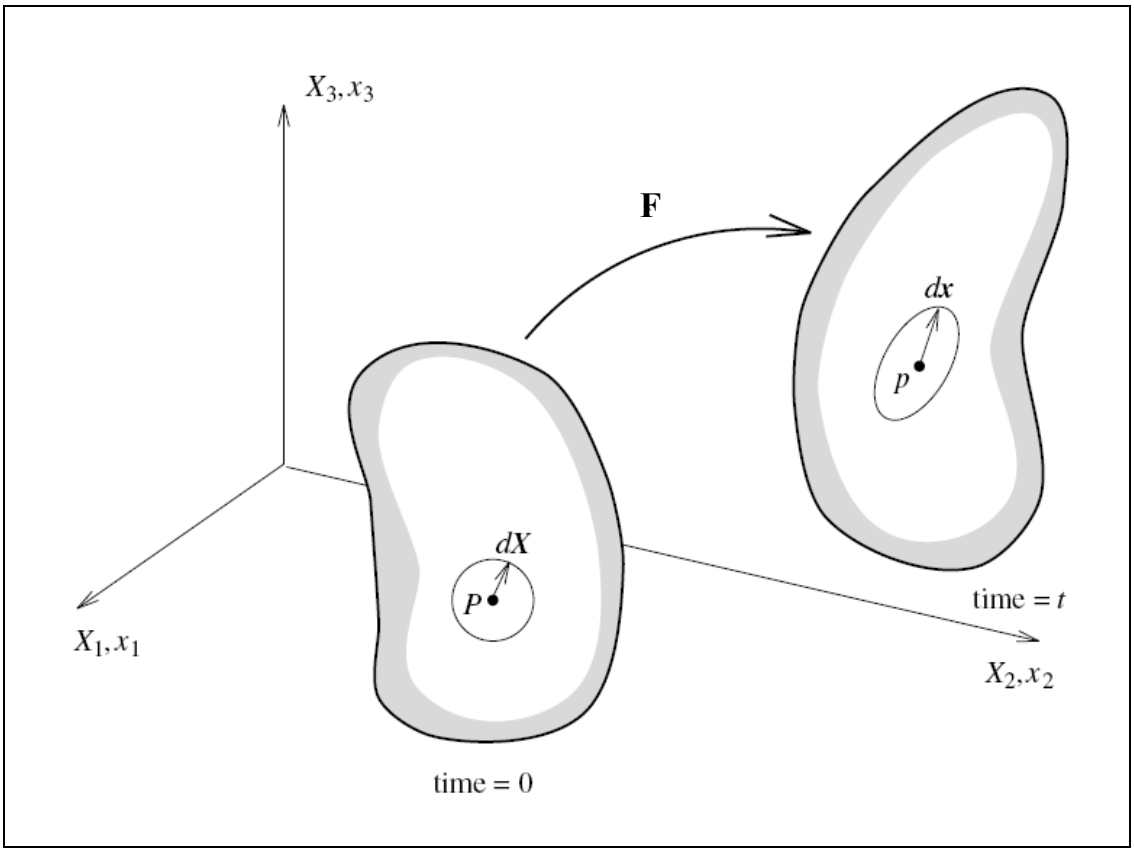

Figure 3.1 : The Deformation Gradient [21]

3.2. The Concept of Stress

Force is considered by many to be an intuitive concept. Its precise definition is not quite straightforward. Force, within this study, is considered to simply be the action of one body on another, thus a vectorial push or pull. There are two general types of forces of utmost interest:

- Body forces, such as gravity or electromagnetic forces, which act on all material particles in a body without physical contact,
- Surface forces, such as a pressure or frictional forces, which act through physical contact on a body through its bounding surface.

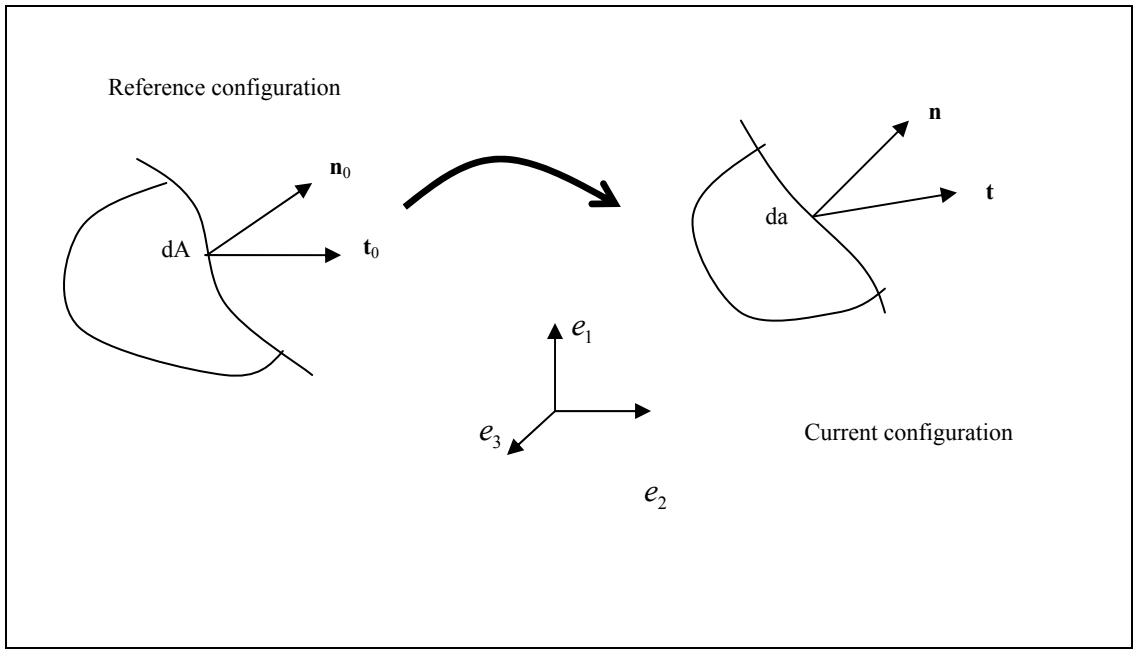

Figure 3.2 : Visual representation of Traction Vectors

Many forces act on a material through a surface area, it is very useful to define a traction vector $\mathbf{T}^{(n)}$ as follows;

$$\mathbf{t}^{(n)} = \lim_{\Delta a \to 0}\left(\frac{\Delta f}{\Delta a}\right) = \frac{df}{da} \qquad \textbf{(3-15)}$$

Where df is a differential force vector and da a differential area, both defined in β_t, with da having an orientation given by the outward unit normal vector **n**. The term

$df = \mathbf{t}^{(n)} da$ will prove convenient below in the definition of multiple measure of stress. Now Cauchy's postulate can be introduced in the form

$$\mathbf{t} = \mathbf{t}(\mathbf{x}, t, \mathbf{n}) \tag{3-16}$$

$$\mathbf{t}_0 = \mathbf{t}_0(\mathbf{X}, t, \mathbf{N}) \tag{3-17}$$

In these expressions,

- **t** represents the Cauchy traction vector (force measured per unit surface area defined in the current configuration) with **n** as the unit outward normal.
- $\mathbf{t_0}$ represents the first Piola-Kirchhoff traction vector which represents a force measured per unit surface area defined in the reference configuration.

Using the introduced traction vectors Cauchy's stress theorem can be stated as

$$\mathbf{t}(x, t, n) = \boldsymbol{\sigma}(x, t)\mathbf{n} \tag{3-18}$$

$$\mathbf{t}_0(X, t, N) = \mathbf{P}(X, t)\mathbf{n}_0 \tag{3-19}$$

There $\boldsymbol{\sigma}$ denotes a symmetric spatial tensor field called the Cauchy stress tensor. **P** is called the first Piola-Kirchhoff stress tensor. Newton's third law of action can thus be stated as

$$\mathbf{t}(\mathbf{x}, t, \mathbf{n}) = -\mathbf{t}(\mathbf{x}, t, -\mathbf{n}) \tag{3-20}$$

$$\mathbf{t}_0(\mathbf{X}, t, \mathbf{n}_0) = -\mathbf{t}_0(\mathbf{X}, t, -\mathbf{n}_0) \tag{3-21}$$

which leads directly to relating between $\boldsymbol{\sigma}$ to **P**, using Nanson's formula connecting line elements in the different configurations expressed as

$$da = J\mathbf{F}^{-T} dA \tag{3-22}$$

Combining **(3-18)** to **(3-22)** leads to the following relations:

$$\mathbf{t}(\mathbf{x}, t, \mathbf{n})da = \mathbf{t}_0(\mathbf{X}, t, \mathbf{n}_0)dA, \tag{3-23}$$

$$\boldsymbol{\sigma}(\mathbf{x},t)\mathbf{n}da = \mathbf{P}(\mathbf{X},t)\mathbf{n}_0 dA\,, \tag{3-24}$$

$$\boldsymbol{\sigma}(\mathbf{x},t)da = \mathbf{P}(\mathbf{X},t)dA\,, \tag{3-25}$$

$$\boldsymbol{\sigma} = J^{-1}\mathbf{P}\mathbf{F}^{T}\,, \tag{3-26}$$

$$\mathbf{P} = J\boldsymbol{\sigma}\mathbf{F}^{-T}\,. \tag{3-27}$$

It can be shown that $\boldsymbol{\sigma}$ is symmetric (with the aid of balance laws) and $\mathbf{P}$ is not symmetric in general and follows the rule

$$\mathbf{P}\mathbf{F}^{T} = \mathbf{F}\mathbf{P}^{T} \tag{3-28}$$

In nonlinear analysis, in general two more definitions of stress tensors are frequently used. These are the Kirchhoff stress tensor $\boldsymbol{\tau}$ which differs from the Cauchy stress tensor by the volume ratio J and is defined by

$$\boldsymbol{\tau} = J\boldsymbol{\sigma} \tag{3-29}$$

and the second Piola-Kirchhoff stress tensor $\mathbf{S}$ which does not admit a physical interpretation in terms of surface tractions, but is defined in the reference (fixed) configuration enabling a position suitable for the formulation of constitutive equations, especially for solid materials. The second Piola-Kirchhoff stress tensor can be obtained "pull-back" operation and is expressed as

$$\mathbf{S} = \mathbf{F}^{-1}\boldsymbol{\tau}\mathbf{F}^{-T} \tag{3-30}$$

Other relations also hold between $\mathbf{S}$, $\boldsymbol{\sigma}$ and $\mathbf{P}$ like

$$\mathbf{S} = \mathbf{F}^{-1}\boldsymbol{\sigma}\mathbf{F}^{-T} = \mathbf{F}^{-1}\mathbf{P} = \mathbf{S}^{T} \tag{3-31}$$

$$\boldsymbol{\sigma} = J^{-1}\mathbf{F}\mathbf{S}\mathbf{F}^{T} \tag{3-32}$$

$$\mathbf{P} = \mathbf{F}\mathbf{S}\,. \tag{3-33}$$

3.3. Basic Postulates of Continuum Mechanics [22-24]

There are five basic postulates in continuum mechanics:

1. Conservation of mass
2. Conservation of linear momentum
3. Conservation of angular momentum
4. Conservation of energy
5. The entropy inequality

3.3.1. Conservation of Mass

In non-relativistic physics, which is concerned here, mass cannot be produced or destroyed. Thus, it is assumed that during a motion there are either mass sources or mass sinks, so that the mass m of a body is a conserved quantity. Hence, if a particle has certain mass in the reference configuration it must stay the same during a motion

$$\int_{\beta_0} \rho_0 dV = \int_{\beta_t} \rho dv \qquad \textbf{(3-34)}$$

where β_0 and β_t denote reference and current domains (volumes). ρ_0 is called the reference mass density and ρ is called the spatial mass density. The spatial mass density, also known as the density in the motion, depends on coordinate and time throughout the body. In contrary, ρ_0 is time-independent and is only associated with the reference configuration of the body. If the density does not depend on geometrical position, the configuration is said to be homogeneous.

Using the relation,

$$dv = JdV = \det \mathbf{F} dV \qquad \textbf{(3-35)}$$

the local formulation of the conservation of mass can be written as

$$\rho_0 = J\rho = \rho \det \mathbf{F} \qquad \textbf{(3-36)}$$

(3-36) deals with the reference density as a time independent quantity. Then, the continuity equation can be derived as

$$\frac{D}{Dt}(J\rho) = \dot{\rho} + \rho div\mathbf{v} = 0 \qquad \textbf{(3-37)}$$

where $\mathbf{v} = \dot{\mathbf{x}}$ denotes the velocity and $\dot{J} = Jdiv\mathbf{v}$

3.3.2. Balance of Linear Momentum

Conservation of linear momentum requires that the time rate of change of the linear momentum (i.e., mass times velocity for all particles) of a body must balance all the forces (body plus surface) that act on the body. Inferred from this definition, it is concluded that forces act on a deformed (current) configuration. Accordingly, the linear momentum equation is, in common practice, derived using spatial approach, though referential form of many equations are preferred in constitutive formulations. The spatial form is then given as

$$\frac{d}{dt}\int_{\beta_t} \rho\mathbf{v}dv = \int_{\beta_t} \rho\mathbf{b}dv + \int_{\partial\beta_t} \mathbf{t}^{(n)}da \qquad \textbf{(3-38)}$$

where **v** is the velocity, and **b** and **t** are the actual body force (defined per unit mass since mass remains constant) and traction vector that act on the body in the current configuration. To get a form $\int(...)dv = 0$ for all (deformed) configurations, which yields a local form, the order of the time differentiation and volume integration on the left hand side are interchanged and the current differential volume is eliminated in favor of JdV . Thus

$$\frac{d}{dt}\int_{\beta_t} \rho\mathbf{v}dv = \int_{\beta_0} \frac{d}{dt}(\rho\mathbf{v}J)dV = \int_{\beta_t} \rho\mathbf{a}dv \qquad \textbf{(3-39)}$$

and following is acquired.

$$\int_{\beta_0}\left(\frac{d\rho}{dt}\mathbf{v}J + \rho\mathbf{v}\frac{dJ}{dt}\right)dV = \int_{\beta_0}\left(\frac{d\rho}{dt} + \rho tr\mathbf{L}\right)\mathbf{v}JdV = 0 \qquad \textbf{(3-40)}$$

Applying the divergence theorem to **(3.38)**,

$$\int_{\partial\beta_t} \mathbf{t}^{(n)} da = \int_{\partial\beta_t} \mathbf{n}\mathbf{t} da = \int_{\beta_t} \nabla\boldsymbol{\sigma} dv \,. \tag{3-41}$$

the spatial form of the linear momentum equation becomes

$$\int_{\beta_t} (\rho\mathbf{a} - \nabla\boldsymbol{\sigma} - \rho\mathbf{b}) dv = 0 \qquad \forall \quad \beta_t \tag{3-42}$$

And thereby the point wise field equation, in direct and Cartesian notation, is

$$\nabla\boldsymbol{\sigma} + \rho\mathbf{b} = \rho\mathbf{a}\,, \qquad \frac{\partial\sigma_{ij}}{\partial x_i} + \rho b_j = \rho a_j \,. \tag{3-43}$$

This is the most natural and thus the most familiar form of the linear momentum equation; called the equation of motion. If the acceleration is zero (or negligible), then the equation above is called the equilibrium equation.

Configuring everytihing in the reference configuration yields

$$\frac{d}{dt}\int_{\beta_0} \rho_0 \mathbf{v} dV = \int_{\beta_0} \rho_0 \mathbf{b} dV + \int_{\partial\beta_0} \mathbf{t}_0{}^{(N)} dA\,, \tag{3-44}$$

where $\mathbf{t}_0{}^{(N)}$ is the traction vector defined in reference configuration in terms of the actual surface forces that act on the body in the current configuration. This time, the differentiation and integration can be interchanged directly because the reference volume dV is constant. Hence, using the definition for the first Piola-Kirchoff stress tensor and the divergence theorem, equation 3-43 can be written as

$$\int_{\beta_0} (\rho_0\mathbf{a} - \nabla_0\mathbf{P} - \rho_0\mathbf{b}) dV = 0 \qquad \forall \quad \beta_0 \tag{3-45}$$

from which the local form of the equation is gathered as

$$\nabla_0\mathbf{P} + \rho_0\mathbf{b} = \rho_0\mathbf{a}\,, \qquad \frac{\partial P_{Aj}}{\partial X_A} + \rho_0 b_j = \rho_0 a_j \tag{3-46}$$

It is not hard to infer that the referential form is not as “natural” as the spatial form, but the formulation is simpler since the reference configuration does not change with time. The two relations are similar and, of course, can be obtained one from the other.

3.3.3. Conservation of Angular Momentum

Conservation of angular momentum requires that the time rate of change of the total momentum of the body must balance the applied moments. Hence, in referential form,

$$\frac{d}{dt}\int_{\beta_0}\left(\mathbf{x}\times\rho_0\mathbf{v}\right)dV=\int_{\beta_0}\left(\mathbf{x}\times\rho_0\mathbf{v}\right)dV+\int_{\partial\beta_0}\left(\mathbf{x}\times\mathbf{T}^{(N)}\right)dA \qquad \textbf{(3-47)}$$

is given. Following details in the literature, the balance of angular momentum ensures that

$$\mathbf{F}.\mathbf{P}=\mathbf{P}^T\mathbf{F}^T \qquad \textbf{(3-48)}$$

i.e., the Cauchy stress tensor is a symmetric quantity.

$$\boldsymbol{\sigma}=\boldsymbol{\sigma}^T \qquad \textbf{(3-49)}$$

Following the definition of the second Piola-Kirchhoff stress tensor **S** in equation **(3-32)**.

$$\mathbf{S}=\mathbf{S}^T \qquad \textbf{(3-50)}$$

can also be gathered. Contrary to the above definitions, the first Piola-Kirchhoff stress tensor **P** is not symmetric in general as can be inferred from equation 3-33

In practice, balance of angular momentum provides little information for the formulation of a boundary value problem, but restrictions on constitutive relations in terms of $\mathbf{P},\boldsymbol{\sigma}$ or $\mathbf{S}$; in the form of enforced symmetries.

3.3.4. Conservation of Energy

This is namely "the first law of thermodynamics". This law asserts that the time rate of change of the total energy of a body (kinetic plus potential being accounted for via body forces) must balance the rate at which work is done on the body (via volumetric and/or surface heating). Since this work is aimed at isothermal processes throughout this work, one shall not need to invoke the energy equation. Nevertheless, for completeness the referential form of the energy equation is

$$\rho_0 \frac{d\varepsilon}{dt} = \mathbf{P}^T : \frac{d\mathbf{F}}{dt} - \nabla_0 \mathbf{q}_0 + \rho_0 g \qquad \textbf{(3-51)}$$

where ε is the internal energy density (defined per unit mass), ∇_0 denotes the referential gradient, q_0 the referential heat flux vector, and g heat addition defined per unit mass.

3.3.5. Entropy Inequality

Entropy inequality is also known as the second law of thermodynamics. The referential form of the equation is

$$-\left(\frac{d\Psi}{dt} + \mu \frac{dT}{dt}\right) + \mathbf{P}^T : \frac{d\mathbf{F}}{dt} - \frac{1}{\rho_0} \mathbf{q}_0 \nabla_0 T \geq 0 \qquad \textbf{(3-52)}$$

where

Ψ is the stored energy per unit volume

T is the temperature

ρ_0 is the mass density in reference configuration

μ is the specific heat

q_0 is the referential heat flux vector

For an isothermal process with no heat transfer, the equation above degenerates to

$$-\rho_0 \frac{d\Psi}{dt} + \mathbf{P}^T : \frac{d\mathbf{F}}{dt} \geq 0 \qquad \textbf{(3-53)}$$

This reveals that the second law of thermodynamics can provide important information even for isothermal, mechanical processes. A material model should exactly behave compatible to the second law of thermodynamics. This ensures the constitutive equations be stable (and realistic). The second law of thermodynamics is essential to the development of constitutive relations for all hyperelastic, viscohyperelastic and viscohyperelastoplastic materials.

4. THE VISCOELASTIC MODEL FOR TRACING PASSIVE ARTERIAL DEFORMATIONS

4.1.1. Some Previous Studies on Arterial Material Models

An adequate constitutive model for arteries which incorporates the active state (contraction of smooth muscles) was proposed recently by Rachev and Hayashi [25], but such behavior is quite out of the scope of this study. The active mechanical behavior of arterial walls is governed mainly by the intrinsic properties of elastin and collagen fibers and by the degree of activation of smooth muscles..

The passive mechanical behavior of arterial walls is quite different than the aforementioned active and is governed mainly by the elastin and collagen fibers. The passive state of the smooth muscles may also contribute to the passive arterial behavior but the extent of this contribution is not yet known, and is completely disregarded. Most constitutive models proposed for arteries describe the artery as a macroscopic system. Furthermore, most of these models are designed to capture the response near the physiological state and in this respect they have been successfully applied in fitting experimental data. The most common potentials (strain-energy density functions) are of exponential type, although polynomial and logarithmic forms are also used.

Some of the constitutive models proposed use the biphasic theory to describe arterial walls as hydrated soft tissues[26]. Less frequently, models account for the specific morphological structure of arterial walls. One attempt to model the helically wound fibrous structure is provided by Tozeren [27], which is based on the idea that the only wall constituent is the fiber structure. However, this is a significant simplification of histology.

A model byWuyts et al. [28] assumes that the artery is only composed of media, and wavy collagen fibrils are embedded in concentrically arranged elastin/smooth-muscle membranes, in agreement with the histology with collagen fibrils having a statistically

distributed initial length which may be stretched initially with a very low force but then is linearly elastic. Though the model in [28] incorporates some histological information, the artery is considered as a tube reinforced by circularly oriented collagen and elastin fibers, which does not model the real histological situation.

Most of the constitutive models treat the arterial wall as a single layer, but a number of two-layer models have been proposed in the literature. Two-layer models which include anisotropy are those due to, for example, Von Maltzahn et al. [29], Demiray [30] and Rachev [31]. However, the emphasis of the latter paper is on stress-dependent remodeling.

The Mooney-type and Ogden-type models are first isotropic hyperelastic models which are commonly used for elastomers and soft tissues. These models are also widely integrated within commercial finite element software. Ogden and Mooney type models are based on stretch ratios. However, for arterial tissues, these models are failed to determine fiber-reinforced material behavior. The Mooney materials used in soft tissue modeling is of the form

$$\psi = c_0(I_1 - 3) + c_1(I_2 - 3) + c_2(I_1 - 3)(I_2 - 3) \quad \textbf{(4-1)}$$

$$I_1 = \lambda_1^{\,2} + \lambda_2^{\,2} + \lambda_3^{\,2} \quad \textbf{(4-2)}$$

$$I_2 = \lambda_1^{\,-2} + \lambda_2^{\,-2} + \lambda_3^{\,-2} \quad \textbf{(4-3)}$$

and the Ogden model is in the form;

$$\psi = \sum_{i=i}^{n} \left(\lambda_1^{\,\alpha_i} + \lambda_2^{\,\alpha_i} + \lambda_3^{\,\alpha_i} - 3 \right) \quad \textbf{(4-4)}$$

where, ψ stands for the strain energy density functional, I for the strain invariants and λ for the principal stretch ratios, the other symbols being indices or material coefficients. Details to these models can be found in literature, since they have been extensively captured in modeling of rubber structures and similar.

Vaishnav et al [32] proposed and compared three different multi-axial forms of strain energy density function ψ to describe the 3D anisotropic behavior of canine thoracic

aorta. They explicitly enforce incompressibility rather than via a Lagrange multiplier embedding. Briefly, each ψ is taken to be a polynomial function of the Green strains, but contained different number of material parameters. Overall a seven parameter relation was discussed to yield the best. It is of the form

$$W = c_1 E_{\Theta\Theta}{}^2 + c_2 E_{\Theta\Theta} E_{ZZ} + c_3 E_{ZZ}{}^2 + c_4 E_{\Theta\Theta}{}^3 + c_5 E_{\Theta\Theta}{}^2 E_{ZZ} + c_6 E_{\Theta\Theta} E_{ZZ}{}^2 + c_7 E_{ZZ}{}^3 \quad \textbf{(4-5)}$$

In their paper they determined the values from global equilibrium and thereby accounted for transmural variations in stress and strains. Differences in the two sets of parameter values prompted Vaishnav and colleagues to conclude that the thick walled approach was preferred, a conclusion that is generally held today.

Another proposal by Holzapfel and Wiezsacker [33] promotes a combined polynomial exponential form of ψ for passive aorta. Specifically, they suggested that

$$\psi = c_0(I_C - 3) + \frac{1}{2}c\left(e^Q - 1\right) \quad \textbf{(4-6)}$$

$$I_C = tr\mathbf{C} = 2tr\mathbf{E} + 3 \quad \textbf{(4-7)}$$

$$Q = c_1 E_{RR}{}^2 + c_2 E_{\Theta\Theta}{}^2 + c_3 E_{\Theta\Theta}{}^2 + 2c_4 E_{RR} E_{\Theta\Theta} + 2c_5 E_{\Theta\Theta} E_{ZZ} + 2c_6 E_{ZZ} E_{RR} \quad \textbf{(4-8)}$$

Here c_0 and c values are parameters having the units of stress, whereas the other parameters are non-dimensionless.

Demiray and Vito [30] also presented such results for passive aorta. Using a Lagrange multiplier approach and based on biaxial data, they suggested the following form of ψ

$$\psi_{Media} = \frac{c}{2}(\exp[c_1(C_{11} - 1) + c_2(C_{22} - 1) + c_3(C_{33} - 1)] - 1) \quad \textbf{(4-9)}$$

for the media, where the subscripts 1 and 2 on the components of C denote in-plane components (Θ, Z) however, the third one denotes the out of plane component R.

In contrast they suggested

$$\psi_{Adv} = \frac{\beta}{2\alpha}(\exp[\alpha(I_C - 3)] - 1) \tag{4-10}$$

For the adventitia, where α, β are material parameters and

$$I_C = tr\mathbf{C} = 2tr\mathbf{E} + 3 \tag{4-11}$$

Choung and Fung [34] suggested a 3D exponential form of ψ. It is

$$\psi = \frac{1}{2}ce^{Q} \tag{4-12}$$

where ψ is defined per unit initial volume and Q is

$$\begin{aligned} Q = {} & c_1 E_{RR}^{\ 2} + c_2 E_{\Theta\Theta}^{\ 2} + c_3 E_{ZZ}^{\ 3} + 2c_4 E_{RR}E_{\Theta\Theta} + 2c_5 E_{\Theta\Theta}E_{ZZ} + 2c_6 E_{ZZ}E_{RR} \\ & + c_7\left(E_{R\Theta}^{\ 2} + E_{\Theta R}^{\ 2}\right) + c_8\left(E_{\Theta Z}^{\ 2} + E_{Z\Theta}^{\ 2}\right) + c_9\left(E_{ZR}^{\ 2} + E_{RZ}^{\ 2}\right) \end{aligned} \tag{4-13}$$

notice that this postulate does not satisfy $\psi = 0$ at the state of zero strain.

Takamizawa and Hayashi [9] reported that Fung type exponential forms of ψ describe better the passive behavior of carotid arteries than polynomial forms. Also including residual stresses in their data analysis, In [9] a logarithmic form of ψ has been suggested

$$\psi = -c\ln(1 - Q) \tag{4-14}$$

$$Q = \frac{1}{2}c_1 E_{\Theta\Theta}^{\ 2} + \frac{1}{2}c_2 E_{ZZ}^{\ 2} + c_3 E_{\Theta\Theta}E_{ZZ} \tag{4-15}$$

as a slightly better descriptor of carotid behavior than an exponential form.

Von Malzahn et al [29] showed that the following exponential pseudo strain-energy function described well the behavior of both the adventitia and media of bovine carotid arteries

$$\psi = \frac{1}{2}c(\exp[c_1 E_{\Theta\Theta}^{\ 2} + c_2 E_{ZZ}^{\ 2} + 2c_3 E_{\Theta\Theta}E_{ZZ}] - 1) \tag{4-16}$$

Kasyanov and Rachev [25] present the mechanical behavior of human carotid arteries tested via finite inflation, extension and torsion. Following Vaishnav, incompressibility has been directly enforced and postulated

$$\psi = c_1[e^Q - 1] + [c_7 E_{\Theta\Theta} e^{c_8 E_{\Theta\Theta}} + c_9 E_{ZZ} + c_{10}({E_{\Theta Z}}^2 + {E_{Z\Theta}}^2)] \quad \textbf{(4-17)}$$

$$Q = c_2 {E_{ZZ}}^2 + c_3 E_{\Theta\Theta} E_{ZZ} + c_4 {E_{\Theta\Theta}}^2 + c_5 E_{\Theta\Theta} {E_{ZZ}}^2 + c_6 {E_{\Theta\Theta}}^2 E_{ZZ} \quad \textbf{(4-18)}$$

G.A. Holzapfel, T.C. Gasser and R. W. Ogden [3] proposed a multilayer material model including fiber orientations. Details of this model is also applied in section 4.6 of this thesis, but in short, they state that the total strain energy can be decomposed into a homogeneous (due to ground elastin) and fiber (due to helically wound collagen fibers) component, for which a different behavior models can be adopted.

$$\psi(\mathbf{C}, \mathbf{A}_1, \mathbf{A}_2) = \psi_{iso}(I_1) + \psi_{aniso}(I_4, I_6) \quad \textbf{(4-19)}$$

$$\psi_{iso} = \frac{c}{2}(I_1 - 3) \quad \textbf{(4-20)}$$

$$\psi_{aniso} = \frac{k_1}{2k_2} \sum_{i=4,6} \{\exp[k_2 (I_i - 1)^2] - 1\} \quad \textbf{(4-21)}$$

4.2. General Assumptions of proposed Material Model:

1) The artery is a mono-layer (orthotropic) fiber-reinforced thick-walled tube

2) This orthotropic behavior is due to two families of collagen fibers in elastin matrix.

3) Both the viscoelastic and pure elastic kinematics are finite

4) The structure is viscoelastic, thus dissipative.

5) The deformation procedure followed is purely isothermal.

6) The structure exhibits long-term damage behavior

7) Only passive mechanical properties are modeled

8) The elastic properties are in form of HyperElasticity

9) The material is incompressible.

10) Permanent (plastic) deformations are due to fiber slip within ground material

11) Plasticity is rate-dependent.

4.3. Kinematics for Materials Exhibiting Intermediate Configurations

If some "known" or "assumed" intermediate configuration can be mentioned during the deformation, the deformation gradient can be assumed to get multiplicatively split over two phases, as to general applied practice in finite plasticity, where the "intermediate stress free configuration" is the main point of many theories:

$$\mathbf{F} = \mathbf{F}_e \mathbf{F}_v \qquad \textbf{(4-22)}$$

where $\mathbf{F}_e$ is the elastic deformation after some evolving (viscous / viscoelastic) deformation $\mathbf{F}_v$, which can be regarded as an intermediate (and fictious) (stress-free) configuration within here. The phrases in parenthesis imply that those terms can be valid or invalid as to the theoretical layout of the model. In applications of multiplicative decomposition of the deformation gradient to plasticity, the intermediate configuration is assumed to be "stress-free" after unloading the material, whereas in a 3-element viscoelastic solid similar to one in Figure 4.2, this might not be the case unless stress-relaxation experiments are carried out. However, the "evolving" character of this configuration is similar in both assumptions. A scheme of the hypothesis is given in Figure 4.1

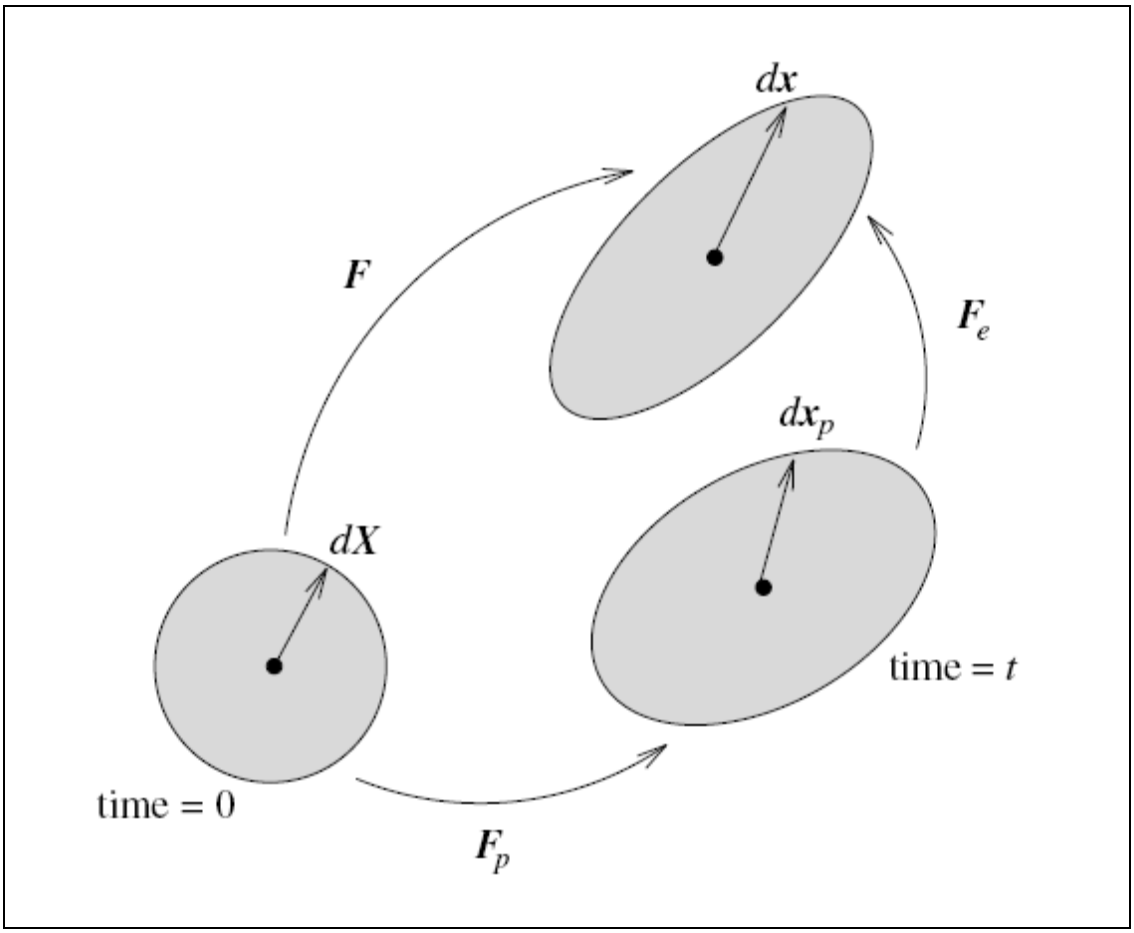

Figure 4.1 : The Multiplicative decomposition [21]

The material time-rate of each deformation gradient tensor is defined as

$$\dot{\mathbf{F}} = \mathbf{L}\mathbf{F} \tag{4-23}$$

$$\dot{\mathbf{F}}_v = \mathbf{L}_v\mathbf{F}_v \tag{4-24}$$

$$\dot{\mathbf{F}}_e = \mathbf{F}_e\mathbf{L}_e \tag{4-25}$$

where "$\mathbf{L}$" are the velocity gradient tensors that relate the material time rates of deformation gradients to each, respectively. Thus,

$$\dot{\mathbf{F}} = \mathbf{L}\mathbf{F} = \mathbf{L}\mathbf{F}_e\mathbf{F}_v = \dot{\mathbf{F}}_e\mathbf{F}_v + \mathbf{F}_e\dot{\mathbf{F}}_v = \mathbf{F}_e\mathbf{L}_e\mathbf{F}_v + \mathbf{F}_e\mathbf{L}_v\mathbf{F}_v \tag{4-26}$$

$$\mathbf{L}\mathbf{F}_e = \mathbf{F}_e\mathbf{L}_e + \mathbf{F}_e\mathbf{L}_v = \mathbf{F}_e\left(\mathbf{L}_e + \mathbf{L}_v\right) \tag{4-27}$$

$$\mathbf{L} = \mathbf{F}_e\left(\mathbf{L}_e + \mathbf{L}_v\right)\mathbf{F}_e^{-1} \tag{4-28}$$

is obtained. This enables transformations among deformation rate gradient tensorial variables appropriately as required.

One important concept that rises with the multiplicative decomposition is the so-called "plastic" spin, in multiplicative plasticity. In the notation represented here for viscoelastic deformations,

$$\mathbf{\Omega}_v = \frac{1}{2}\left[\mathbf{F}_e\mathbf{L}_v\mathbf{F}_e^{-1} - \mathbf{F}_e^{-T}\mathbf{L}_v^{T}\mathbf{F}_e^{T}\right] \tag{4-29}$$

reads, which is defined as the spin of the substructure defined on the intermediate configuration with respect to the reference configuration. The reason that this quantity is named here as "plastic spin" is that it is a very common concept in plasticity and the notion is straightforwardly the same. Other variables to be defined are the Total Lagrangian Strain

$$\mathbf{E} = \frac{1}{2}\left(\mathbf{F}^T\mathbf{F} - \mathbf{I}\right) \tag{4-30}$$

and the Lagrangian Viscous (intermediate) Strain

$$\mathbf{E}_v = \frac{1}{2}\left(\mathbf{F}_v^{T}\mathbf{F}_v - \mathbf{I}\right) \tag{4-31}$$

Transformations among each quantity is possible:

$$\mathbf{E} = \frac{1}{2}\left(\mathbf{F}_v^{T}\mathbf{F}_e^{T}\mathbf{F}_e\mathbf{F}_v - \mathbf{I}\right) = \frac{1}{2}\left(\mathbf{F}_v^{T}\left(2\mathbf{\Gamma}_e + \mathbf{I}\right)\mathbf{F}_v - \mathbf{I}\right) \tag{4-32}$$

$$\mathbf{E} = \mathbf{F}_v^{T}\mathbf{\Gamma}_e\mathbf{F}_v + \mathbf{E}_v \tag{4-33}$$

The elastic strain, defined with reference to the viscously-deformed (intermediate) state is shifted along with the viscous deformation. Thus, with respect to the intermediate configuration, the strains are simply summed up, in spite the viscous strain turns Eulerian.

$$\mathbf{F}_v^{-T}\mathbf{E}\mathbf{F}_v^{-1} = \mathbf{\Gamma}_e + \mathbf{\Gamma}_v \tag{4-34}$$

$$\boldsymbol{\Gamma}_e = \frac{1}{2}\left(\mathbf{F}_e{}^T\mathbf{F}_e - \mathbf{I}\right) = \frac{1}{2}\left(\mathbf{C}_e - \mathbf{I}\right) \tag{4-35}$$

$$\boldsymbol{\Gamma}_v = \frac{1}{2}\left(\mathbf{I} - \mathbf{F}_v{}^{-T}\mathbf{F}_v{}^{-1}\right) = \frac{1}{2}\left(\mathbf{I} - \mathbf{B}_v{}^{-1}\right) \tag{4-36}$$

4.4. The Fiber Orientation Matrix

A broad range of composite materials can be regarded as fiber-reinforced continua, where, at least the cross-sectional dimensions of the fibers are of orders lower scale than the model of interest (similar to continuum definition in fluid dynamics). Considering the fiber types, various sub-types can be defined as long-fiber composites and short fiber composites. The latter can also be subdivided into anisotropic and isotropic types, but is beyond the concept of arterial physiology, where, helically wound long collagen fibrils are of main interest. In such models, the main input to material models are the fiber orientations in a reference state. Following [37], the mathematical representation of fiber-related quantities have developed rapidly, as in his study a method that enabled mathematical isotropy to model anisotropic materials have been developed.

4.4.1. The Representation of Reference Configuration

Let the two sets of fibers be aligned with respect to the (R,Θ,Z) undeformed coordinates of the tube as

$$\mathbf{m}_4^0 = \begin{bmatrix} 0 & Sin\varphi_4 & Cos\varphi_4 \end{bmatrix} \tag{4-37}$$

$$\mathbf{m}_6^0 = \begin{bmatrix} 0 & Sin\varphi_6 & Cos\varphi_6 \end{bmatrix} \tag{4-38}$$

with $\mathbf{a}_4$ and $\mathbf{a}_6$ defining the direction of the fiber sets 4 and 6 respectively. (The reason for naming families as "4" and "6" will be made clear later.)

The angles "φ" are given with respect to the longitudinal axis of the hollow cylinder.

The normals to these directions are defined as

$$\mathbf{n}_4^0 = \begin{bmatrix} 0 & -Cos\varphi_4 & Sin\varphi_4 \end{bmatrix} \tag{4-39}$$

$$\mathbf{n}_6^0 = \begin{bmatrix} 0 & -Cos\varphi_6 & Sin\varphi_6 \end{bmatrix} \tag{4-40}$$

The director's matrix for each family of fibers, can be defined as the dyads [37,4]:

$$\mathbf{M}_4^0 = \mathbf{m}_4^0 \otimes \mathbf{m}_4^0 = \begin{bmatrix} 0 & 0 & 0 \\ 0 & (Sin\varphi_4)^2 & Cos\varphi_4 Sin\varphi_4 \\ 0 & Cos\varphi_4 Sin\varphi_4 & (Cos\varphi_4)^2 \end{bmatrix} \tag{4-41}$$

$$\mathbf{M}_6^0 = \mathbf{m}_6^0 \otimes \mathbf{m}_6^0 = \begin{bmatrix} 0 & 0 & 0 \\ 0 & (Sin\varphi_6)^2 & Cos\varphi_6 Sin\varphi_6 \\ 0 & Cos\varphi_6 Sin\varphi_6 & (Cos\varphi_6)^2 \end{bmatrix} \tag{4-42}$$

Remember that these tensor quantities are defined with respect to the reference configuration, with superscript "0" indicating that they are defined in the reference configuration, and their norms are unity.

4.4.2. The Stretch of Fibers

As the material is subjected to some state of stress, it will (hopefully) deform. Thus, the fibers will be re-aligned. This shifts the director's matrices:

$$\mathbf{M}_4^v = \mathbf{F}_v \mathbf{m}_4^0 \otimes \mathbf{F}_v \mathbf{m}_4^0 \tag{4-43}$$

$$\left(\mathbf{M}_4^v\right)_{ab} = \left(\mathbf{F}_v \mathbf{m}_4^0\right)_a \left(\mathbf{F}_v \mathbf{m}_4^0\right)_b \tag{4-44}$$

$$= \left(\mathbf{F}_v\right)_{ak} \left(\mathbf{m}_4^0\right)_k \left(\mathbf{F}_v\right)_{bm} \left(\mathbf{m}_4^0\right)_m \tag{4-45}$$

$$= \left(\mathbf{F}_v\right)_{ak} \left(\mathbf{m}_4^0\right)_k \left(\mathbf{m}_4^0\right)_m \left(\mathbf{F}_v^{\,T}\right)_{mb} \tag{4-46}$$

$$\mathbf{M}_4^v = \mathbf{F}_v \mathbf{M}_4^0 \mathbf{F}_v^{\,T} \tag{4-47}$$

Similar tensor algebra can be carried out for other quantities.

Thus, the fiber directions with respect to reference configuration, after some viscous deformation $\mathbf{F}_v$ is given by

$$\mathbf{M}_4^v = \mathbf{F}_v \mathbf{M}_4^0 \mathbf{F}_v^T \tag{4-48}$$

$$\mathbf{M}_6^v = \mathbf{F}_v \mathbf{M}_6^0 \mathbf{F}_v^T \tag{4-49}$$

The fiber directions with respect to reference configuration, after some total deformation $\mathbf{F}$ is given by

$$\mathbf{M}_4^x = \mathbf{F}_e \mathbf{M}_4^v \mathbf{F}_e^T = \mathbf{F}_e \mathbf{F}_v \mathbf{M}_4^0 \mathbf{F}_v^T \mathbf{F}_e^T = \mathbf{F} \mathbf{M}_4^0 \mathbf{F}^T \tag{4-50}$$

$$\mathbf{M}_6^x = \mathbf{F}_e \mathbf{M}_6^v \mathbf{F}_e^T = \mathbf{F}_e \mathbf{F}_v \mathbf{M}_6^0 \mathbf{F}_v^T \mathbf{F}_e^T = \mathbf{F} \mathbf{M}_6^0 \mathbf{F}^T \tag{4-51}$$

Note that, the norms of $\mathbf{M}^v$ and $\mathbf{M}^x$ are no more unity.

In general, the initial directions of fiber families (in the arterial tissue) are known from material. The others are tracked with the deformation, with the aid of the formulations presented.

4.5. The Constitutive Layout

4.5.1. Thermodynamics

For isothermal processes, the entropy inequality is expressed as (recall from section 3.3.5):

$$\mathbf{S} : \dot{\mathbf{E}} - \dot{\Psi} \geq 0 \tag{4-52}$$

where, $\mathbf{S}$ is the II. Piola – Kirchhoff Stress Tensor, $\dot{\mathbf{E}}$ is the Lagrangian strain rate (work conjugate to stress) and $\dot{\Psi}$ is the rate of energy stored per volume within the body.

Now a model for the material behavior is to be chosen for accurate application of the general concepts to special case. A 3-element non-linear viscoelastic solid is assumed:

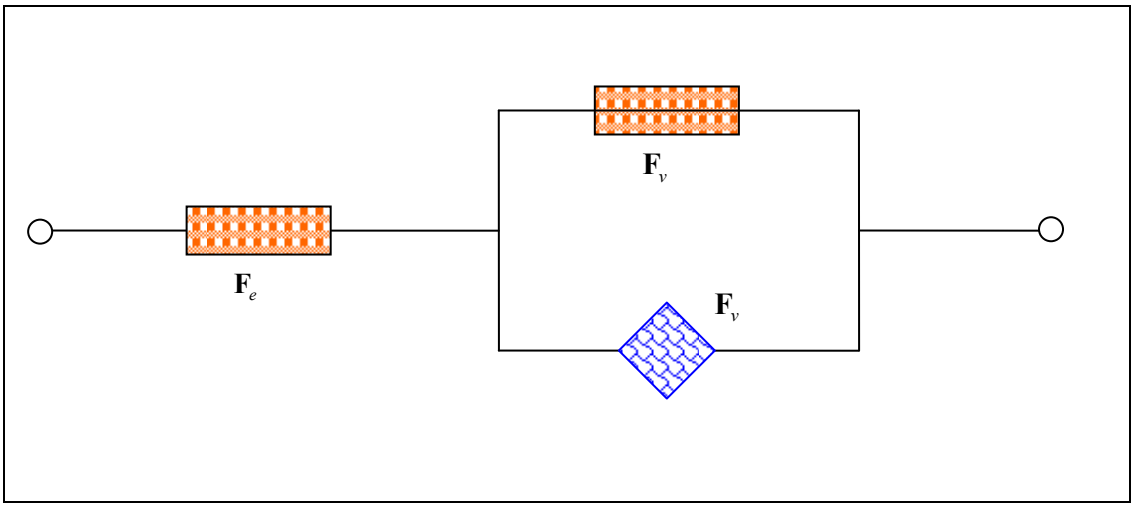

Figure 4.2 : The 3-Element Solid Model (Poynting-Thomson Viscoelastic Solid)

where the orange hatches denote spring elements and the blue box represent the dissipative dashpot. According to this model,

- The strain energy can be summed up to be due to the pure elastic part and the viscoelastic part,
- The deformation is two-fold, thus the model behaves compatible with the multiplicative decomposition assumption,
- The dissipation is incorporated within the context of the dashpot element (blue).

Due to the natural decomposition $\mathbf{F} = \mathbf{F}_e\mathbf{F}_v$, one is free to choose 2 variables among 3. Possible choices are to select $\mathbf{F}$ and $\mathbf{F}_e$; $\mathbf{F}$ and $\mathbf{F}_v$; and $\mathbf{F}_e$ and $\mathbf{F}_v$. The 1st choice is not useful, since for pure elasticity, one will have two (identical) quantities that differ from unity during deformation; it is not liked to have very-dependent variables in equations. The 2nd choice is in practice good, but the equations get cumbersome when total deformations are involved. Thus, choosing $\mathbf{F}_e$ as the main and $\mathbf{F}_v$ as the evolving deformation is (among the three choices) seems the most logical. This means that, in terms of strains, the Lagrangian elastic strain with respect to the intermediate configuration and the Lagrangian Viscous (Internal Variable Like) Strain with respect to the original configuration will be used as the variables.

$$\mathbf{E} = \mathbf{F}_v^{\,T}\boldsymbol{\Gamma}_e\mathbf{F}_v + \mathbf{E}_v \tag{4-53}$$

$$\dot{\mathbf{E}} = \dot{\mathbf{E}}_v + \mathbf{F}_v^{\,T}\mathbf{L}_v^{\,T}\boldsymbol{\Gamma}_e\mathbf{F}_v + \mathbf{F}_v^{\,T}\boldsymbol{\Gamma}_e\mathbf{L}_v\mathbf{F}_v + \mathbf{F}_v^{\,T}\dot{\boldsymbol{\Gamma}}_e\mathbf{F}_v \tag{4-54}$$

Furthermore, the total energy stored in the material can be assumed to be the sum of energies stored in the springs. Thus, based on the additive decomposition of the total strain energy,

$$\Psi = \Psi_e\left(\boldsymbol{\Gamma}_e\right) + \Psi_v\left(\mathbf{E}_v\right) \tag{4-55}$$

$$\dot{\Psi} = \frac{\partial\Psi}{\partial\boldsymbol{\Gamma}_e} : \dot{\boldsymbol{\Gamma}}_e + \frac{\partial\Psi}{\partial\mathbf{E}_v} : \dot{\mathbf{E}}_v + \frac{\partial\Psi}{\partial Q} : \dot{Q} \tag{4-56}$$

$$\mathbf{S} : \dot{\mathbf{E}} - \left(\frac{\partial\Psi}{\partial\boldsymbol{\Gamma}_e} : \dot{\boldsymbol{\Gamma}}_e + \frac{\partial\Psi}{\partial\mathbf{E}_v} : \dot{\mathbf{E}}_v + \frac{\partial\Psi}{\partial Q} : \dot{Q} \right) \geq 0 \tag{4-57}$$

where Q is any arbitrary parameter. It will be made clear later that, it is associated to internal damage variable that will be correlated to softening effects and variables related to plastic deformations.

Leaving the Q parameter aside for now, using the total Lagrangian strain rate from definition for the stress power in detail,

$$\mathbf{S} : \left(\dot{\mathbf{E}}_v + \mathbf{F}_v^{\,T}\dot{\boldsymbol{\Gamma}}_e\mathbf{F}_v + \mathbf{F}_v^{\,T}\mathbf{L}_v^{\,T}\boldsymbol{\Gamma}_e\mathbf{F}_v + \mathbf{F}_v^{\,T}\boldsymbol{\Gamma}_e\mathbf{L}_v\mathbf{F}_v\right) - \dot{\Psi} \geq 0 \tag{4-58}$$

$$tr\left(\mathbf{S}\dot{\mathbf{E}}_v + \mathbf{S}\mathbf{F}_v^{\,T}\dot{\boldsymbol{\Gamma}}_e\mathbf{F}_v + \mathbf{S}\mathbf{F}_v^{\,T}\mathbf{L}_v^{\,T}\boldsymbol{\Gamma}_e\mathbf{F}_v + \mathbf{S}\mathbf{F}_v^{\,T}\boldsymbol{\Gamma}_e\mathbf{L}_v\mathbf{F}_v\right) - \dot{\Psi} \geq 0 \tag{4-59}$$

$$tr\left(\mathbf{F}_v\mathbf{S}\mathbf{F}_v^{\,T}\mathbf{D}_v + \mathbf{F}_v\mathbf{S}\mathbf{F}_v^{\,T}\dot{\boldsymbol{\Gamma}}_e + \boldsymbol{\Gamma}_e\mathbf{F}_v\mathbf{S}\mathbf{F}_v^{\,T}\mathbf{L}_v^{\,T} + \mathbf{F}_v\mathbf{S}\mathbf{F}_v^{\,T}\boldsymbol{\Gamma}_e\mathbf{L}_v\right) - \dot{\Psi} \geq 0 \tag{4-60}$$

The procedure in the paper [38] uses a different rate formulation other than employed here, and they presumably incorporate that traces of $\mathbf{F}_v\mathbf{S}\mathbf{F}_v^{\,T}\mathbf{L}_v^{\,T}\boldsymbol{\Gamma}_e$ and $\mathbf{F}_v\mathbf{S}\mathbf{F}_v^{\,T}\mathbf{L}_v\boldsymbol{\Gamma}_e$ are equal. But to that extent, the underlying assumptions are not laid. For the most general case, this is only satisfied if it is said that the viscoelastic intermediate deformation is spin-free. That is, the intermediate deformation is assumed to have a kinematic constraint over:

$$\boldsymbol{\Omega}_v = \frac{1}{2}\left[\mathbf{F}_e\mathbf{L}_v\mathbf{F}_e^{-1} - \mathbf{F}_e^{-T}\mathbf{L}_v^{T}\mathbf{F}_e^{T}\right] \tag{4-61}$$

This concept has been adopted in many areas in multiplicative deformation plasticity, as stated before, and many details can be found in the book by Lubarda [35]. Setting the "spin" to zero

$$\boldsymbol{\Omega}_v = \mathbf{0} = \frac{1}{2}\left[\mathbf{F}_e\mathbf{L}_v\mathbf{F}_e^{-1} - \mathbf{F}_e^{-T}\mathbf{L}_v^{T}\mathbf{F}_e^{T}\right] \tag{4-62}$$

Rearranging,

$$\mathbf{0} = \mathbf{F}_e^{T}\left(\mathbf{F}_e\mathbf{L}_v\mathbf{F}_e^{-1} - \mathbf{F}_e^{-T}\mathbf{L}_v^{T}\mathbf{F}_e^{T}\right)\mathbf{F}_e \tag{4-63}$$

one obtains

$$\mathbf{0} = \mathbf{C}_e\mathbf{L}_v - \mathbf{L}_v^{T}\mathbf{C}_e \tag{4-64}$$

The following steps are rather straightforward arrangement of the variables

$$tr\left(\mathbf{S}\dot{\mathbf{E}}_v + \mathbf{S}\mathbf{F}_v^{T}\dot{\mathbf{\Gamma}}_e\mathbf{F}_v + \mathbf{S}\mathbf{F}_v^{T}\mathbf{L}_v^{T}\frac{1}{2}(\mathbf{C}_e - \mathbf{I})\mathbf{F}_v + \mathbf{S}\mathbf{F}_v^{T}\frac{1}{2}(\mathbf{C}_e - \mathbf{I})\mathbf{L}_v\mathbf{F}_v\right) - \dot{\Psi} \geq 0 \tag{4-65}$$

$$tr\left(\mathbf{S}\dot{\mathbf{E}}_v + \mathbf{S}\mathbf{F}_v^{T}\dot{\mathbf{\Gamma}}_e\mathbf{F}_v + \mathbf{F}_v\mathbf{S}\mathbf{F}_v^{T}\mathbf{L}_v^{T}\frac{1}{2}(\mathbf{C}_e - \mathbf{I}) + \mathbf{F}_v\mathbf{S}\mathbf{F}_v^{T}\frac{1}{2}(\mathbf{C}_e - \mathbf{I})\mathbf{L}_v\right) - \dot{\Psi} \geq 0 \tag{4-66}$$

$$tr\left(\mathbf{S}\dot{\mathbf{E}}_v + \mathbf{S}\mathbf{F}_v^{T}\dot{\mathbf{\Gamma}}_e\mathbf{F}_v\right) + tr\left(\frac{1}{2}\left\{\mathbf{F}_v\mathbf{S}\mathbf{F}_v^{T}\mathbf{L}_v^{T}\mathbf{C}_e + \mathbf{F}_v\mathbf{S}\mathbf{F}_v^{T}\mathbf{C}_e\mathbf{L}_v\right\} - \frac{1}{2}\left\{\mathbf{F}_v\mathbf{S}\mathbf{F}_v^{T}\mathbf{L}_v^{T} + \mathbf{F}_v\mathbf{S}\mathbf{F}_v^{T}\mathbf{L}_v\right\}\right) - \dot{\Psi} \geq 0 \tag{4-67}$$

$$tr\left(\mathbf{S}\mathbf{F}_v^{T}\mathbf{D}_v\mathbf{F}_v + \mathbf{S}\mathbf{F}_v^{T}\dot{\mathbf{\Gamma}}_e\mathbf{F}_v\right) + tr\left(\frac{1}{2}\left\{\mathbf{F}_v\mathbf{S}\mathbf{F}_v^{T}\mathbf{L}_v^{T}\mathbf{C}_e + \mathbf{F}_v\mathbf{S}\mathbf{F}_v^{T}\mathbf{C}_e\mathbf{L}_v\right\} - \left\{\mathbf{S}\mathbf{F}_v^{T}\mathbf{D}_v^{T}\mathbf{F}_v\right\}\right) - \dot{\Psi} \geq 0 \tag{4-68}$$

After canceling relevant terms

$$tr\left(\mathbf{S}\mathbf{F}_v^{T}\dot{\mathbf{\Gamma}}_e\mathbf{F}_v\right) + tr\left(\frac{1}{2}\left\{\mathbf{F}_v\mathbf{S}\mathbf{F}_v^{T}\mathbf{L}_v^{T}\mathbf{C}_e + \mathbf{F}_v\mathbf{S}\mathbf{F}_v^{T}\mathbf{C}_e\mathbf{L}_v\right\}\right) - \dot{\Psi} \geq 0 \tag{4-69}$$

and using the vanishing spin

$$tr\left(\mathbf{S}\mathbf{F}_v^{\,T}\dot{\mathbf{\Gamma}}_e\mathbf{F}_v\right)+tr\left(\frac{1}{2}\left\{\mathbf{F}_v\mathbf{S}\mathbf{F}_v^{\,T}\mathbf{C}_e\mathbf{L}_v+\mathbf{F}_v\mathbf{S}\mathbf{F}_v^{\,T}\mathbf{C}_e\mathbf{L}_v\right\}\right)-\dot{\Psi}\geq 0 \qquad \textbf{(4-70)}$$

which reads

$$tr\left(\mathbf{F}_v\mathbf{S}\mathbf{F}_v^{\,T}\dot{\mathbf{\Gamma}}_e+\mathbf{F}_v\mathbf{S}\mathbf{F}_v^{\,T}\mathbf{C}_e\mathbf{L}_v\right)-\dot{\Psi}\geq 0 \qquad \textbf{(4-71)}$$

Now one can return to more primitive formulations, for better understanding of the issue. Rather than the decomposition **(4.56)**, let

$$\dot{\Psi}=\frac{\partial\Psi_e}{\partial\dot{\mathbf{\Gamma}}_e}:\dot{\mathbf{\Gamma}}_e+\frac{\partial\Psi_v}{\partial\mathbf{F}_v^{\,T}}:\dot{\mathbf{F}}_v^{\,T} \qquad \textbf{(4-72)}$$

For the second term involving Ψ_v

$$\frac{\partial\Psi_v}{\partial\mathbf{F}_v^{\,T}}:\dot{\mathbf{F}}_v^{\,T}=tr\left(\frac{\partial\Psi_v}{\partial\mathbf{F}_v^{\,T}}\dot{\mathbf{F}}_v\right)=tr\left(\frac{\partial\Psi_v}{\partial\mathbf{F}_v^{\,T}}\mathbf{L}_v\mathbf{F}_v\right)=tr\left(\mathbf{F}_v\frac{\partial\Psi_v}{\partial\mathbf{F}_v^{\,T}}\mathbf{L}_v\right) \qquad \textbf{(4-73)}$$

Then

$$tr\left(\mathbf{F}_v\mathbf{S}\mathbf{F}_v^{\,T}\dot{\mathbf{\Gamma}}_e+\mathbf{F}_v\mathbf{S}\mathbf{F}_v^{\,T}\mathbf{C}_e\mathbf{L}_v-\frac{\partial\Psi_e}{\partial\dot{\mathbf{\Gamma}}_e}\dot{\mathbf{\Gamma}}_e-\mathbf{F}_v\frac{\partial\Psi_v}{\partial\mathbf{F}_v^{\,T}}\mathbf{L}_v\right)\geq 0 \qquad \textbf{(4-74)}$$

Using the identity

$$\frac{\partial\Psi_v}{\partial\mathbf{F}_v^{\,T}}=\frac{\partial\Psi_v}{\partial\mathbf{E}_v}\mathbf{F}_v^{\,T} \qquad \textbf{(4-75)}$$

$$tr\left(\left(\mathbf{F}_v\mathbf{S}\mathbf{F}_v^{\,T}-\frac{\partial\Psi_e}{\partial\dot{\mathbf{\Gamma}}_e}\right)\dot{\mathbf{\Gamma}}_e+\left(\mathbf{F}_v\mathbf{S}\mathbf{F}_v^{\,T}\mathbf{C}_e-\mathbf{F}_v\frac{\partial\Psi_v}{\partial\mathbf{E}_v}\mathbf{F}_v\right)\mathbf{L}_v\right)\geq 0 \qquad \textbf{(4-76)}$$

is obtained. Using the argument that in pure elasticity no dissipation occurs and the deformation is path-independent and reversible [23]

$$\mathbf{F}_v\mathbf{S}\mathbf{F}_v^{\,T}=\frac{\partial\Psi_e}{\partial\dot{\mathbf{\Gamma}}_e} \qquad \textbf{(4-77)}$$

and the dissipation inequality is

$$tr\left(\left(\mathbf{F}_v\mathbf{S}\mathbf{F}_v{}^T\mathbf{C}_e-\mathbf{F}_v\frac{\partial\Psi_v}{\partial\mathbf{E}_v}\mathbf{F}_v\right)\mathbf{L}_v\right)\geq 0 \qquad \textbf{(4-78)}$$

Let the dissipation be related to some potential, and turn the system into an equality

$$tr\left(\left(\mathbf{F}_v\mathbf{S}\mathbf{F}_v{}^T\mathbf{C}_e-\mathbf{F}_v\frac{\partial\Psi_v}{\partial\mathbf{E}_v}\mathbf{F}_v\right)\mathbf{L}_v\right)-\frac{\partial\Phi}{\partial\mathbf{L}_v}:\mathbf{L}_v{}^T=0 \qquad \textbf{(4-79)}$$

Arranging the last term

$$\frac{\partial\Phi}{\partial\mathbf{L}_v}:\mathbf{L}_v{}^T=tr\left(\frac{\partial\Phi}{\partial\mathbf{L}_v}\mathbf{L}_v\right)\frac{\partial\Phi}{\partial(\mathbf{L}_v)_{ij}}(\mathbf{L}_v)_{ji}=\frac{\partial\Phi}{\partial(\dot{\mathbf{F}}_v)_{ab}}\frac{\partial(\dot{\mathbf{F}}_v)_{ab}}{\partial(\mathbf{L}_v)_{ij}}(\mathbf{L}_v)_{ij}=\frac{\partial\Phi}{\partial(\dot{\mathbf{F}}_v)_{ab}}\left[\frac{\partial}{\partial(\mathbf{L}_v)_{ij}}((\mathbf{L}_v)_{ak}(\mathbf{F}_v)_{kb})\right](\mathbf{L}_v)_{ji} \qquad \textbf{(4-80)}$$

$$\frac{\partial\Phi}{\partial\mathbf{L}_v}:\mathbf{L}_v{}^T=\frac{\partial\Phi}{\partial(\dot{\mathbf{F}}_v)_{ab}}(\delta_{ia}\delta_{jk})(\mathbf{F}_v)_{kb}(\mathbf{L}_v)_{ji}=\frac{\partial\Phi}{\partial(\dot{\mathbf{F}}_v)_{ib}}(\mathbf{F}_v)_{jb}(\mathbf{L}_v)_{ji}=\frac{\partial\Phi}{\partial(\dot{\mathbf{F}}_v)_{ib}}(\mathbf{F}_v{}^T)_{bj}(\mathbf{L}_v)_{ji} \qquad \textbf{(4-81)}$$

$$\frac{\partial\Phi}{\partial\mathbf{L}_v}:\mathbf{L}_v{}^T=\frac{\partial\Phi}{\partial\dot{\mathbf{F}}_v}\mathbf{F}_v{}^T:\mathbf{L}_v{}^T=tr\left(\frac{\partial\Phi}{\partial\dot{\mathbf{F}}_v}\mathbf{F}_v{}^T\mathbf{L}_v\right) \qquad \textbf{(4-82)}$$

The result then reads

$$tr\left(\left(\mathbf{F}_v\mathbf{S}\mathbf{F}_v{}^T\mathbf{C}_e-\mathbf{F}_v\frac{\partial\Psi_v}{\partial\mathbf{E}_v}\mathbf{F}_v{}^T-\frac{\partial\Phi}{\partial\dot{\mathbf{F}}_v}\mathbf{F}_v{}^T\right)\mathbf{L}_v\right)=0 \qquad \textbf{(4-83)}$$

Investigating further,

$$\frac{\partial\Phi}{\partial\dot{\mathbf{F}}_v}=\frac{\partial\Phi}{\partial\dot{\mathbf{E}}_v}:\frac{\partial\dot{\mathbf{E}}_v}{\partial\dot{\mathbf{F}}_v}=\frac{\partial\Phi}{\partial(\dot{\mathbf{E}}_v)_{ab}}\frac{\partial(\dot{\mathbf{E}}_v)_{ab}}{\partial(\dot{\mathbf{F}}_v)_{ij}}=\frac{\partial\Phi}{\partial(\dot{\mathbf{E}}_v)_{ab}}\frac{\partial}{\partial(\dot{\mathbf{F}}_v)_{ij}}\frac{1}{2}\left[(\dot{\mathbf{F}}_v{}^T)_{ak}(\mathbf{F}_v)_{kb}+(\mathbf{F}_v{}^T)_{aq}(\dot{\mathbf{F}}_v)_{qb}\right] \qquad \textbf{(4-84)}$$

$$\frac{\partial\Phi}{\partial\dot{\mathbf{F}}_v}=\frac{\partial\Phi}{\partial(\dot{\mathbf{E}}_v)_{ab}}\frac{\partial}{\partial(\dot{\mathbf{F}}_v)_{ij}}\frac{1}{2}\left[(\dot{\mathbf{F}}_v)_{ka}(\mathbf{F}_v)_{kb}+(\mathbf{F}_v)_{qa}(\dot{\mathbf{F}}_v)_{qb}\right]=\frac{\partial\Phi}{\partial(\dot{\mathbf{E}}_v)_{ab}}\frac{1}{2}\left(\delta_{ik}\delta_{ja}(\mathbf{F}_v)_{kb}+\delta_{qi}\delta_{jb}(\mathbf{F}_v)_{qa}\right) \qquad \textbf{(4-85)}$$

$$\frac{\partial\Phi}{\partial\dot{\mathbf{F}}_v}=\frac{1}{2}\left[\frac{\partial\Phi}{\partial(\dot{\mathbf{E}}_v)_{jb}}(\mathbf{F}_v)_{ib}+\frac{\partial\Phi}{\partial(\dot{\mathbf{E}}_v)_{aj}}(\mathbf{F}_v)_{ia}\right]=\frac{1}{2}\left[\mathbf{F}_v\left(\frac{\partial\Phi}{\partial\dot{\mathbf{E}}_v}\right)^T+\mathbf{F}_v\frac{\partial\Phi}{\partial\dot{\mathbf{E}}_v}\right]=\mathbf{F}_v\frac{\partial\Phi}{\partial\dot{\mathbf{E}}_v}$$

$$tr\left(\left(\mathbf{F}_v\mathbf{S}\mathbf{F}_v{}^T\mathbf{C}_e-\mathbf{F}_v\frac{\partial\Psi_v}{\partial\mathbf{E}_v}\mathbf{F}_v{}^T-\mathbf{F}_v\frac{\partial\Phi}{\partial\dot{\mathbf{E}}_v}\mathbf{F}_v{}^T\right)\mathbf{L}_v\right)=0 \qquad \textbf{(4-86)}$$

$$tr\left(\left(\frac{\partial \Psi_e}{\partial \boldsymbol{\Gamma}_e}\mathbf{C}_e - \mathbf{F}_v\frac{\partial \Psi_v}{\partial \mathbf{E}_v}\mathbf{F}_v^{\,T} - \mathbf{F}_v\frac{\partial \Phi}{\partial \dot{\mathbf{E}}_v}\mathbf{F}_v^{\,T}\right)\mathbf{L}_v\right) = 0 \qquad \textbf{(4-87)}$$

Now it is obvious that, the last two terms in the parenthesis are symmetrical, while first is not. Decomposing it into symmetrical and anti-symmetrical parts leads

$$tr\left(\frac{\partial \Psi_e}{\partial \boldsymbol{\Gamma}_e}\mathbf{C}_e\mathbf{L}_v\right) = tr\left[\frac{1}{2}\left(\frac{\partial \Psi_e}{\partial \boldsymbol{\Gamma}_e}\mathbf{C}_e\mathbf{L}_v + \frac{\partial \Psi_e}{\partial \boldsymbol{\Gamma}_e}\mathbf{L}_v^{\,T}\mathbf{C}_e\right) + \frac{1}{2}\left(\frac{\partial \Psi_e}{\partial \boldsymbol{\Gamma}_e}\mathbf{C}_e\mathbf{L}_v - \frac{\partial \Psi_e}{\partial \boldsymbol{\Gamma}_e}\mathbf{L}_v^{\,T}\mathbf{C}_e\right)\right] \textbf{(4-88)}$$

$$tr\left(\frac{\partial \Psi_e}{\partial \boldsymbol{\Gamma}_e}\mathbf{C}_e\mathbf{L}_v\right) = tr\left[\frac{1}{2}\left(\frac{\partial \Psi_e}{\partial \boldsymbol{\Gamma}_e}\mathbf{C}_e\mathbf{L}_v + \mathbf{C}_e\frac{\partial \Psi_e}{\partial \boldsymbol{\Gamma}_e}\mathbf{L}_v^{\,T}\right) + \frac{1}{2}\frac{\partial \Psi_e}{\partial \boldsymbol{\Gamma}_e}\left(\mathbf{C}_e\mathbf{L}_v - \mathbf{L}_v^{\,T}\mathbf{C}_e\right)\right] \qquad \textbf{(4-89)}$$

Using that plastic spin is zero again, the term in the right hand side vanishes identically, which leads

$$tr\left(\frac{\partial \Psi_e}{\partial \boldsymbol{\Gamma}_e}\mathbf{C}_e\mathbf{L}_v\right) = tr\left[\frac{1}{2}\left(\frac{\partial \Psi_e}{\partial \boldsymbol{\Gamma}_e}\mathbf{C}_e\mathbf{L}_v + \mathbf{C}_e\frac{\partial \Psi_e}{\partial \boldsymbol{\Gamma}_e}\mathbf{L}_v^{\,T}\right)\right] \qquad \textbf{(4-90)}$$

Then,

$$tr\left[\left(\frac{\partial \Psi_e}{\partial \boldsymbol{\Gamma}_e}\mathbf{C}_e - \mathbf{F}_v\frac{\partial \Psi_v}{\partial \mathbf{E}_v}\mathbf{F}_v^{\,T} - \mathbf{F}_v\frac{\partial \Phi}{\partial \dot{\mathbf{E}}_v}\mathbf{F}_v^{\,T}\right)\mathbf{L}_v\right] = 0 \qquad \textbf{(4-91)}$$

$$tr\left[\left(\frac{1}{2}\left(\frac{\partial \Psi_e}{\partial \boldsymbol{\Gamma}_e}\mathbf{C}_e\mathbf{L}_v + \mathbf{C}_e\frac{\partial \Psi_e}{\partial \boldsymbol{\Gamma}_e}\mathbf{L}_v^{\,T}\right) - \mathbf{F}_v\frac{\partial \Psi}{\partial \mathbf{E}_v}\mathbf{F}_v^{\,T} - \mathbf{F}_v\frac{\partial \Phi}{\partial \dot{\mathbf{E}}_v}\mathbf{F}_v^{\,T}\right)\mathbf{L}_v\right] = 0 \qquad \textbf{(4-92)}$$

Since the negative-signed terms are symmetrical and trace of a tensor equals trace of its transpose

$$tr\left[\mathbf{F}_v\left(\frac{\partial \Psi}{\partial \mathbf{E}_v} + \frac{\partial \Phi}{\partial \dot{\mathbf{E}}_v}\right)\mathbf{F}_v^{\,T}\mathbf{L}_v\right] = tr\left[\mathbf{L}_v^{\,T}\mathbf{F}_v\left(\frac{\partial \Psi_v}{\partial \mathbf{E}_v} + \frac{\partial \Phi}{\partial \dot{\mathbf{E}}_v}\right)\mathbf{F}_v^{\,T}\right] = tr\left[\mathbf{F}_v\left(\frac{\partial \Psi}{\partial \mathbf{E}_v} + \frac{\partial \Phi}{\partial \dot{\mathbf{E}}_v}\right)\mathbf{F}_v^{\,T}\mathbf{L}_v^{\,T}\right] \textbf{(4-93)}$$

$$tr\left[\left(\frac{1}{2}\left(\frac{\partial \Psi_e}{\partial \boldsymbol{\Gamma}_e}\mathbf{C}_e\mathbf{L}_v + \mathbf{C}_e\frac{\partial \Psi_e}{\partial \boldsymbol{\Gamma}_e}\mathbf{L}_v^{\,T}\right) - \frac{1}{2}\left(\mathbf{F}_v\frac{\partial \Psi_v}{\partial \mathbf{E}_v}\mathbf{F}_v^{\,T} + \mathbf{F}_v\frac{\partial \Phi}{\partial \dot{\mathbf{E}}_v}\mathbf{F}_v^{\,T}\right)\left(\mathbf{L}_v + \mathbf{L}_v^{\,T}\right)\right)\right] = 0 \textbf{(4-94)}$$

Arranging terms in groups of $\mathbf{L}_v$ and $\mathbf{L}_v^{\,T}$ reads

$$tr\left[\left(\frac{\partial\Psi_e}{\partial\boldsymbol{\Gamma}_e}\mathbf{C}_e-\mathbf{F}_v\left(\frac{\partial\Psi}{\partial\mathbf{E}_v}+\frac{\partial\Phi}{\partial\dot{\mathbf{E}}_v}\right)\mathbf{F}_v^{\,T}\right)\mathbf{L}_v+\left(\mathbf{C}_e\frac{\partial\Psi_e}{\partial\boldsymbol{\Gamma}_e}-\mathbf{F}_v\left(\frac{\partial\Psi_v}{\partial\mathbf{E}_v}+\frac{\partial\Phi}{\partial\dot{\mathbf{E}}_v}\right)\mathbf{F}_v^{\,T}\right)\mathbf{L}_v^{\,T}\right]=0 \quad \textbf{(4-95)}$$

As to the most general case, the leading terms of $\mathbf{L}_v$ and $\mathbf{L}_v^{\,T}$ should be independently equal to zero, which implies their sum is also zero. Then,

$$\frac{1}{2}\left(\frac{\partial\Psi_e}{\partial\boldsymbol{\Gamma}_e}\mathbf{C}_e+\mathbf{C}_e\frac{\partial\Psi_e}{\partial\boldsymbol{\Gamma}_e}\right)-\mathbf{F}_v\left(\frac{\partial\Psi_v}{\partial\mathbf{E}_v}+\frac{\partial\Phi}{\partial\dot{\mathbf{E}}_v}\right)\mathbf{F}_v^{\,T}=\mathbf{0} \quad \textbf{(4-96)}$$

is obtained, as the evolution equation for the model proposed.

4.6. The Material-Specific Constitutive Laws

4.6.1. General Considerations

For examining one structure's behavior using mathematical models, the constitutive laws should be stated. For the statements proposed in Section 4.5 and related, there is a hidden fact that the strain energy Ψ should be an isotropic function of its arguments. For anisotropic materials, this requirement is generally not obtainable at hand and is a strong restriction over the form of Ψ. However, for the case where fiber reinforced materials are represented by means of structural "alignment" tensors for specific families of fibers, this strong requirement holds [23, 37].

For any isotropic material, it is known that, the strain energy density function can be represented by the function

$$\Psi=\Psi\left(I_1,I_2,I_3\right) \quad \textbf{(4-97)}$$

where, the I_1,I_2,I_3 are invariants of the deformation field, and can be represented as the eingenvalue polynomial's coefficients for deformation:

$$\lambda^3-I_1\lambda^2-I_2\lambda-I_3=0 \quad \textbf{(4-98)}$$

Since it has been stated that the arterial tissue is incompressible

$$I_3=\det\left(\mathbf{C}\right)=1 \quad \textbf{(4-99)}$$

and a Lagrange multiplier is introduced into the equations of stress. Thus,

$$\Psi = \Psi(I_1, I_2) \tag{4-100}$$

holds for isotropic materials. Details can be sought for basics within the Mooney-Rivlin materials concept widely discussed in literature, such as [23].

The addition of the (symmetric) structural tensors into the behavior of the system brings in additional invariants that account for fiber stretches, fiber-matrix interactions and fiber-fiber interactions. The whole list of invariants is then [3,37]:

$$I_1 = tr(\mathbf{C}) = tr(2\mathbf{E} + \mathbf{I}) \tag{4-101}$$

$$I_2 = (tr(\mathbf{C}))^2 - tr(\mathbf{C}^2), \tag{4-102}$$

with $\mathbf{C} = 2\mathbf{E} + \mathbf{I}$ hereafter and

$$I_3 = \det(\mathbf{C}) = 1 \tag{4-103}$$

for incompressible materials

$$I_4 = \mathbf{M}_4^0 : \mathbf{C} \tag{4-104}$$

for the square of stretch of fibers aligned in direction $\mathbf{m}_4^0 = [0 \quad Sin\varphi_4 \quad Cos\varphi_4]$

$$I_5 = \mathbf{M}_4^0 : \mathbf{C}^2 \tag{4-105}$$

due to interactions between fiber and ground matrix

$$I_6 = \mathbf{M}_6^0 : \mathbf{C} \tag{4-106}$$

for the square of stretch of fibers aligned in direction $\mathbf{m}_6^0 = [0 \quad Sin\varphi_6 \quad Cos\varphi_6]$

$$I_7 = \mathbf{M}_6^0 : \mathbf{C}^2 \tag{4-107}$$

due to interactions between fiber and ground matrix

$$I_8 = \mathbf{M}_4^0 : \mathbf{M}_6^0 \tag{4-108}$$

due to cross-fiber interaction and

$$I_9 = tr\left(\mathbf{C}\mathbf{M}_4^0\mathbf{M}_6^0\right) \tag{4-109}$$

tripled-interaction among every constituent

Notice that $\mathbf{C}$ here is of no relation to statements above, it just demonstrates the stretch for any given $\mathbf{F}$.

When coordinate frame indifference is of interest also for the strain-rates, which is the basis for viscoelastic formulations, additional set of invariants can be introduced. For the sake of simplicity and to have an idea of broadness of choices, the following is a list of invariants that are related with the deformation rates, in groups with respect to

a) Pure effects of rate of deformation

$$J_1 = tr\left(\dot{\mathbf{C}}\right) \tag{4-110}$$

$$J_2 = \frac{1}{2}tr\left(\dot{\mathbf{C}}^2\right) \tag{4-111}$$

$$J_3 = \det\left(\dot{\mathbf{C}}\right) \tag{4-112}$$

b) Effects of rate of deformation over fibers

$$J_4 = \mathbf{M}^0 : \dot{\mathbf{C}} \tag{4-113}$$

$$J_5 = \mathbf{M}^0 : \dot{\mathbf{C}}^2 \tag{4-114}$$

c) Coupling of isotropic deformation with deformation rate

$$J_6 = tr\left(\mathbf{C}\dot{\mathbf{C}}\right) \tag{4-115}$$

$$J_7 = tr\left(\mathbf{C}\dot{\mathbf{C}}^2\right) \tag{4-116}$$

$$J_8 = tr\left(\mathbf{C}^2\dot{\mathbf{C}}\right) \tag{4-117}$$

$$J_9 = tr\left(\mathbf{C}^2\dot{\mathbf{C}}^2\right) \tag{4-118}$$

d) Coupling of anisotropic deformation with deformation rate

$$J_{10} = tr\left(\mathbf{M}^0\mathbf{C}\dot{\mathbf{C}}\right) \tag{4-119}$$

$$J_{11} = tr\left(\mathbf{M}^0\mathbf{C}\dot{\mathbf{C}}^2\right) \tag{4-120}$$

$$J_{12} = tr\left(\mathbf{M}^0\mathbf{C}^2\dot{\mathbf{C}}\right) \tag{4-121}$$

Notice that in these expressions $\dot{\mathbf{C}}$, $\mathbf{C}$ and $\mathbf{M}^0$ refer to arbitrary rate of right Cauchy-Green Tensor, right Cauchy-Green Tensor and Fiber Orientation Tensor respectively, which are not related to tensors somewhere within this text.

It is worth mentioning that, the rate-related invariants listed above are valid for transversely isotropic materials where only one preferred direction (family of fibers) exists. In the case of (orthotropic) anisotropy with two families of fibers, additional invariants that include coupling effects among fibers are to exists, but are beyond the scope of this text.

Notice that these invariants are obtained using the fiber direction tensors that are "stretch" related. It will, in section 4.6.4 be shown that a "shearing" related formulation is also possible exhibiting the same mathematical properties.

As a concluding remark, then, the strain energy density function for such a composite is then a function of all these invariants, in general.

4.6.2. The Specific Material Model

However, for the sake of simplicity, and not to diversify much from the literature, it is assumed, in this study, that

$$\Psi = \Psi\left(I_1, I_2, I_4, I_6\right) \tag{4-122}$$

only.

More specifically, the pure elastic and viscoelastic stored energies are assumed to be of the form:

$$\Psi_e = C_1^e\left(I_1^e - 3\right) + \frac{C_2^e}{\alpha^e}\left[e^{\alpha^e\left(I_4^e-1\right)^n} + e^{\alpha^e\left(I_6^e-1\right)^n} - 2\right] \tag{4-123}$$

$$\Psi_v = C_1^v\left(I_1^v - 3\right) + \frac{C_2^v}{\alpha^v}\left[e^{\alpha^v\left(I_4^v-1\right)^n} + e^{\alpha^v\left(I_6^v-1\right)^n} - 2\right] \tag{4-124}$$

where, the material constants are C_1^e, C_2^e and α^e for the pure elastic deformations and C_1^v, C_2^v and α^v for internal state variable evolutionary model. The two sets of constants can be chosen to be the same, but the deformation invariants cannot be equalized. To cope with the partial derivatives, the chain rule is always applied.

$$\frac{\partial\Psi_e}{\partial\boldsymbol{\Gamma}_e} = \frac{\partial\Psi_e}{\partial I_1^e}\frac{\partial I_1^e}{\boldsymbol{\Gamma}_e} + \frac{\partial\Psi_e}{\partial I_4^e}\frac{\partial I_4^e}{\boldsymbol{\Gamma}_e} + \frac{\partial\Psi_e}{\partial I_6^e}\frac{\partial I_6^e}{\boldsymbol{\Gamma}_e} \tag{4-125}$$

$$\frac{\partial\Psi_v}{\partial\mathbf{E}_v} = \frac{\partial\Psi_v}{\partial I_1^v}\frac{\partial I_1^v}{\mathbf{E}_v} + \frac{\partial\Psi_v}{\partial I_4^v}\frac{\partial I_4^v}{\mathbf{E}_v} + \frac{\partial\Psi_v}{\partial I_6^v}\frac{\partial I_6^v}{\mathbf{E}_v} \tag{4-126}$$

This motivation implies that any constitutive relation in finite elasticity has a "constitutive derivative" followed by a "kinematic derivative".

By definition,

$$I_4^v = \mathbf{M}_4^0 : \mathbf{C}^v = \mathbf{M}_4^0 : \left(2\mathbf{E}_v + \mathbf{I}\right) = 2\mathbf{E}_v : \mathbf{M}_4^0 + 1 \tag{4-127}$$

$$I_6^v = \mathbf{M}_6^0 : \mathbf{C}^v = \mathbf{M}_6^0 : \left(2\mathbf{E}_v + \mathbf{I}\right) = 2\mathbf{E}_v : \mathbf{M}_6^0 + 1 \tag{4-128}$$

holds. Since, the elastic deformation is imposed upon (viscoelastic) intermediate deformation (configuration), the fiber stretches are no more identified by $\mathbf{M}_i^0$ tensors with having norm of unity. Thus one has to normalize these directors to unity norm to get the effective stretch:

$$I_4^e = \frac{\mathbf{M}_4^v}{\left\|\mathbf{M}_4^v\right\|} : \mathbf{C}^e = \frac{\mathbf{M}_4^v}{\left\|\mathbf{M}_4^v\right\|} : \left(2\boldsymbol{\Gamma}_e + \mathbf{I}\right) = \frac{2}{\left\|\mathbf{M}_4^v\right\|}\mathbf{M}_4^v : \boldsymbol{\Gamma}_e + 1 \tag{4-129}$$

$$I_6^e = \frac{\mathbf{M}_6^v}{\left\|\mathbf{M}_6^v\right\|} : \mathbf{C}^e = \frac{\mathbf{M}_6^v}{\left\|\mathbf{M}_6^v\right\|} : \left(2\boldsymbol{\Gamma}_e + \mathbf{I}\right) = \frac{2}{\left\|\mathbf{M}_6^v\right\|} \mathbf{M}_6^v : \boldsymbol{\Gamma}_e + 1 \qquad \textbf{(4-130)}$$

Thus, it can be re-written

$$2\varepsilon_i^e + 1 = 2\frac{\mathbf{M}_i^v : \boldsymbol{\Gamma}_e}{\left\|\mathbf{M}_i^v\right\|} + 1 \qquad \textbf{(4-131)}$$

and may get furbished to

$$I_i^e - 1 = 2\varepsilon_i^e \qquad \textbf{(4-132)}$$

and similarly

$$2\varepsilon_i^v + 1 = 2\mathbf{E}_v : \mathbf{M}_i^0 + 1 \qquad \textbf{(4-133)}$$

$$I_i^v - 1 = 2\varepsilon_i^v \qquad \textbf{(4-134)}$$

Thus, the fourth and sixth invariants, in structural mechanics point of view, can be regarded as twice the normal strain in the (preferred) direction of alignment (of fibers).

4.6.3. The "Constitutive Derivatives"

For the proposed material constitutive equation, the required constitutive derivatives can be obtained as follows:

$$\frac{\partial I_1^v}{\partial \mathbf{E}_\mathbf{v}} = 2 \;;\; \frac{\partial I_4^v}{\partial \mathbf{E}_\mathbf{v}} = 2\mathbf{M}_4^0 \;;\; \frac{\partial I_6^v}{\partial \mathbf{E}_\mathbf{v}} = 2\mathbf{M}_6^0 \qquad \textbf{(4-135)}$$

$$\frac{\partial I_1^e}{\partial \boldsymbol{\Gamma}_e} = 2 \;;\; \frac{\partial I_4^e}{\partial \boldsymbol{\Gamma}_e} = 2\frac{\mathbf{M}_4^v}{\left\|\mathbf{M}_4^v\right\|} \;;\; \frac{\partial I_6^e}{\partial \boldsymbol{\Gamma}_e} = 2\frac{\mathbf{M}_6^v}{\left\|\mathbf{M}_6^v\right\|} \qquad \textbf{(4-136)}$$

Now one can rewrite the equations:

$$\Psi_e = C_1^e\left(I_1^e - 3\right) + \frac{C_2^e}{\alpha^e}\left[e^{\alpha^e\left(I_4^e - 1\right)^n} + e^{\alpha^e\left(I_6^e - 1\right)^n} - 2\right] \qquad \textbf{(4-137)}$$

$$\frac{\partial \Psi_e}{\partial \boldsymbol{\Gamma}_e} = \frac{\partial \Psi_e}{\partial I_1^e}\frac{\partial I_1^e}{\boldsymbol{\Gamma}_e} + \frac{\partial \Psi_e}{\partial I_4^e}\frac{\partial I_4^e}{\boldsymbol{\Gamma}_e} + \frac{\partial \Psi_e}{\partial I_6^e}\frac{\partial I_6^e}{\boldsymbol{\Gamma}_e} \tag{4-138}$$

$$\frac{\partial \Psi_e}{\partial \boldsymbol{\Gamma}_e} = 2\frac{\partial \Psi_e}{\partial I_1^e} + 2\frac{\partial \Psi_e}{\partial I_4^e}\frac{\mathbf{M}_4^v}{\left\|\mathbf{M}_4^v\right\|} + 2\frac{\partial \Psi_e}{\partial I_6^e}\frac{\mathbf{M}_6^v}{\left\|\mathbf{M}_6^v\right\|} \tag{4-139}$$

$$\frac{\partial \Psi_e}{\partial \boldsymbol{\Gamma}_e} = 2C_1^e + 2(n)C_2^e\left[e^{\alpha^e\left(I_4^e-1\right)^n}\left(I_4^e-1\right)^{n-1}\frac{\mathbf{M}_4^v}{\left\|\mathbf{M}_4^v\right\|} + e^{\alpha^e\left(I_6^e-1\right)^n}\left(I_6^e-1\right)^{n-1}\frac{\mathbf{M}_6^v}{\left\|\mathbf{M}_6^v\right\|}\right] \tag{4-140}$$

$$\frac{\partial \Psi_v}{\partial \mathbf{E}_v} = \frac{\partial \Psi_v}{\partial I_1^v}\frac{\partial I_1^v}{\mathbf{E}_v} + \frac{\partial \Psi_v}{\partial I_4^v}\frac{\partial I_4^v}{\mathbf{E}_v} + \frac{\partial \Psi_v}{\partial I_6^v}\frac{\partial I_6^v}{\mathbf{E}_v} \tag{4-141}$$

$$\frac{\partial \Psi_v}{\partial \mathbf{E}_v} = 2\frac{\partial \Psi_v}{\partial I_1^v} + \frac{\partial \Psi_v}{\partial I_4^v}\mathbf{M}_4^0 + \frac{\partial \Psi_v}{\partial I_6^v}\mathbf{M}_6^0 \tag{4-142}$$

$$\frac{\partial \Psi_v}{\partial \mathbf{E}_v} = 2C_1^v + 2(n)C_2^v\left[e^{\alpha^v\left(I_4^v-1\right)^n}\left(I_4^v-1\right)^{n-1}\mathbf{M}_4^0 + e^{\alpha^v\left(I_6^v-1\right)^n}\left(I_6^v-1\right)^{n-1}\mathbf{M}_6^0\right] \tag{4-143}$$

4.6.4. The "Flow Rule"

Considering the equation of evolution

$$\frac{1}{2}\left(\frac{\partial \Psi_e}{\partial \boldsymbol{\Gamma}_e}\mathbf{C}_e + \mathbf{C}_e\frac{\partial \Psi_e}{\partial \boldsymbol{\Gamma}_e}\right) - \mathbf{F}_v\left(\frac{\partial \Psi_v}{\partial \mathbf{E}_v} + \frac{\partial \Phi}{\partial \dot{\mathbf{E}}_v}\right)\mathbf{F}_v^{\,T} = \mathbf{0} \tag{4-144}$$

it is explixit that the model is closed since

$$\frac{\partial \Phi}{\partial \dot{\mathbf{E}}_v} : \dot{\mathbf{E}}_v \geq 0 \tag{4-145}$$

for any deformation rate $\dot{\mathbf{E}}_v$. As long as the dissipation inequality is satisfied, the choice of the potential function Φ is arbitrary.

Considering the effects due to anisotropy, a choice for the potential can be such that it is related to the resolved shear over the fibers, where due to this shear some flow occurs between the matrix and the fiber. This is a similar concept that is first used in single crystal plasticity theory, which indicates the Schmid resolved shear stress over

an active slip system. Letting the fiber directions are known, one can calculate the in-plane shear (strain) as:

$$\gamma_4 = \mathbf{n}_4^0 \mathbf{E}_v \mathbf{m}_4^0 \tag{4-146}$$

for fiber layout 4, which is a scalar. A visual representation of the concept layout here is schematically provided in Figure 4.3.

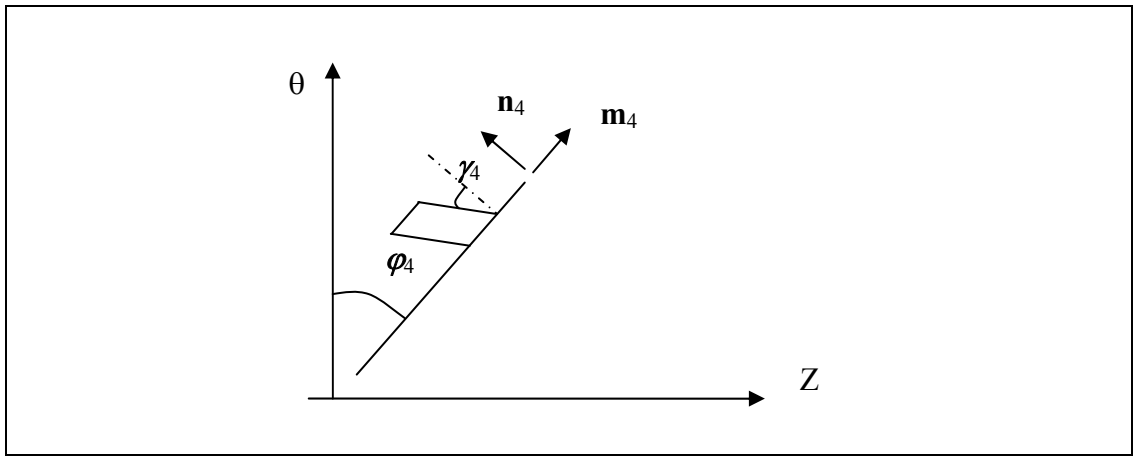

Figure 4.3 : The In-Plane Shear

On the other hand, shear deformation is not, in general case, a symmetrical quantity. Thus, decomposition into symmetric and anti-symmetric components is possible. Rewriting

$$\gamma_4 = \mathbf{E}_v : \left(\mathbf{n}_4^0 \otimes \mathbf{m}_4^0\right) \tag{4-147}$$

and decomposing

$$\gamma_4 = \frac{1}{2}\left[\mathbf{E}_v : \left(\mathbf{m}_4^0 \otimes \mathbf{n}_4^0\right) + \mathbf{E}_v : \left(\mathbf{n}_4^0 \otimes \mathbf{m}_4^0\right)\right] + \frac{1}{2}\left[\mathbf{E}_v : \left(\mathbf{m}_4^0 \otimes \mathbf{n}_4^0\right) - \mathbf{E}_v : \left(\mathbf{n}_4^0 \otimes \mathbf{m}_4^0\right)\right] \tag{4-148}$$

is obtained. Defining

$$\mathbf{D}_4^0 = \frac{1}{2}\left[\left(\mathbf{m}_4^0 \otimes \mathbf{n}_4^0\right) + \left(\mathbf{n}_4^0 \otimes \mathbf{m}_4^0\right)\right] \tag{4-149}$$

$$\mathbf{D}_4^0 = \frac{1}{2}\begin{bmatrix} 0 & 0 & 0 \\ 0 & -\left(Cos\varphi_4 Sin\varphi_4 + Cos\varphi_4 Sin\varphi_4\right) & \left(Sin^2\varphi_4 - Cos^2\varphi_4\right) \\ 0 & \left(Sin^2\varphi_4 - Cos^2\varphi_4\right) & \left(Cos\varphi_4 Sin\varphi_4 + Cos\varphi_4 Sin\varphi_4\right) \end{bmatrix} \quad \textbf{(4-150)}$$

$$\mathbf{D}_4^0 = \frac{1}{2}\begin{bmatrix} 0 & 0 & 0 \\ 0 & -Sin(2\varphi_4) & -Cos(2\varphi_4) \\ 0 & -Cos(2\varphi_4) & Sin(2\varphi_4) \end{bmatrix} \quad \textbf{(4-151)}$$

$$\mathbf{\Omega}_4^0 = \frac{1}{2}\left[\left(\mathbf{m}_4^0 \otimes \mathbf{n}_4^0\right) - \left(\mathbf{n}_4^0 \otimes \mathbf{m}_4^0\right)\right] \quad \textbf{(4-152)}$$

$$\mathbf{\Omega}_4^0 = \frac{1}{2}\begin{bmatrix} 0 & 0 & 0 \\ 0 & 0 & 1 \\ 0 & -1 & 0 \end{bmatrix} \quad \textbf{(4-153)}$$

$$\gamma_4 = \mathbf{E}_v : \mathbf{D}_4^0 + \mathbf{E}_v : \mathbf{\Omega}_4^0 \quad \textbf{(4-154)}$$

is refurbished. The rate of shear is then

$$\dot{\gamma}_4 = \dot{\mathbf{E}}_v : \left(\mathbf{D}_4^0 + \mathbf{\Omega}_4^0\right) \quad \textbf{(4-155)}$$

with respect to the reference configuration. Since $\dot{\mathbf{E}}_v$ is symmetric, and for the aforementioned special choice of the shear rate calculation, $\mathbf{\Omega}_4^0$ has the special form

$$\dot{\mathbf{E}}_v : \mathbf{\Omega}_4^0 = 0 \quad \textbf{(4-156)}$$

is identically ensured, thus it readily follows

$$\dot{\gamma}_4 = \dot{\mathbf{E}}_v : \mathbf{D}_4^0 \quad \textbf{(4-157)}$$

Notice that the initial orientations are not to be updated, as the formulation is Lagrangian with respect to the reference configuration. Letting this assumption to be valid for both families of fibers, one can let a postulate for dissipation potential to be

$$\Phi = \frac{1}{2}\eta_f\left(\dot{\gamma}_4^{\,2} + \dot{\gamma}_6^{\,2}\right) = \frac{1}{2}\eta_f\left[\left(\dot{\mathbf{E}}_v : \mathbf{D}_4^0\right)^2 + \left(\dot{\mathbf{E}}_v : \mathbf{D}_6^0\right)^2\right] \quad \textbf{(4-158)}$$

where $\mathbf{D}_4^0$ and $\mathbf{D}_6^0$ are the symmetric tensors denoting dilatational shear, and η is viscosity parameter. These are a-priori known quantities. Thus the derivative is captured as

$$\frac{\partial \Phi}{\partial \dot{\mathbf{E}}_v} = \frac{\partial \Phi}{\partial \dot{\gamma}_4}\frac{\partial \dot{\gamma}_4}{\partial \dot{\mathbf{E}}_v} + \frac{\partial \Phi}{\partial \dot{\gamma}_6}\frac{\partial \dot{\gamma}_6}{\partial \dot{\mathbf{E}}_v} = \eta_f\left[\dot{\gamma}_4 \mathbf{D}_4^0 + \dot{\gamma}_6 \mathbf{D}_6^0\right] \tag{4-159}$$

which indicates a behavior similar to that of a linear viscous fluid if η is constant. Recalling the evolution equation,

$$\frac{\partial \Psi_v}{\partial \mathbf{E}_v} - \mathbf{F}_v^{-1}\left(\mathbf{I} + 2\boldsymbol{\Gamma}_e\right)\frac{\partial \Psi_e}{\partial \boldsymbol{\Gamma}_e}\mathbf{F}_v^{-T} = -\frac{\partial \Phi}{\partial \dot{\mathbf{E}}_v} \tag{4-160}$$

the form can then be expressed as

$$\frac{\partial \Psi_v}{\partial \mathbf{E}_v} - \mathbf{F}_v^{-1}\left(\mathbf{I} + 2\boldsymbol{\Gamma}_e\right)\frac{\partial \Psi_e}{\partial \boldsymbol{\Gamma}_e}\mathbf{F}_v^{-T} = -\eta_f\left[\dot{\gamma}_4 \mathbf{D}_4^0 + \dot{\gamma}_6 \mathbf{D}_6^0\right] \tag{4-161}$$

the structural matrices being defined in **(4-149).** Under these assumptions laid out so far, Φ and $\frac{\partial \Phi}{\partial \dot{\mathbf{E}}_v}$ are (again) isotropic functions of their arguments; thus symmetry properties are still valid, though our material (and flow rule) is anisotropic (orthotropic)!

On the other hand, since the stress is a tensorial variable, and anisotropy in the sense of structural tensors yield "coupled" terms of tensor components, including the effect of base material within the model is a mathematical workaround for well-posedness of the problem, besides the fact that it is mostly the muscular base that contributes to the viscous effects.

Assuming additive contribution of each effect over the potential Φ, such effects can be easily accounted for. One can modify

$$\Phi = \frac{1}{2}\eta_f\left(\dot{\gamma}_4^{\,2} + \dot{\gamma}_6^{\,2}\right) \tag{4-162}$$

to include terms related to dissipation within base material itself. To avoid the interference of the Lagrange multiplier to the evolution equation, an assumption that is also consistent with the known postulate that incompressible flows are in nature deviatoric, the potential can be extended as

$$\Phi = \frac{1}{2}\eta_f\left(\dot{\gamma}_4^{\,2} + \dot{\gamma}_6^{\,2}\right) + \frac{1}{2}\eta_{GS}\left[dev\left(\dot{\mathbf{E}}_v\right) : dev\left(\dot{\mathbf{E}}_v\right)\right] \tag{4-163}$$

which is quite straight forward. The shear-rate expressions due to fiber orientations are deviatoric in nature since

$$tr\left(\mathbf{D}_4^0\right) = tr\left(\mathbf{D}_6^0\right) = 0 \tag{4-164}$$

Explorations with non-linear anisotropy are also possible with the proposed model. A similar choice to that of the forms postulated for the strain energy functional would be an exponential form as

$$\Phi = \frac{1}{2}\frac{\eta_f}{\alpha_f}\left(e^{\alpha_f(\dot{\gamma}_4)^n} + e^{\alpha_f(\dot{\gamma}_6)^n} - 2\right) + \frac{1}{2}\eta_{GS}\left[dev\left(\dot{\mathbf{E}}_v\right) : dev\left(\dot{\mathbf{E}}_v\right)\right] \tag{4-165}$$

where rate-stiffening or softening can easily get modeled. Notice that with

$$dev(\mathbf{A}) : dev(\mathbf{A}) = tr\left[\left(\mathbf{A} - \frac{1}{3}tr(\mathbf{A})\mathbf{I}\right)\left(\mathbf{A} - \frac{1}{3}tr(\mathbf{A})\mathbf{I}\right)^T\right] \tag{4-166}$$

$$= \left(\mathbf{A} - \frac{1}{3}tr(\mathbf{A})\mathbf{I}\right)_{ij}\left(\mathbf{A} - \frac{1}{3}tr(\mathbf{A})\mathbf{I}\right)_{ij} = \left(A_{ij} - \frac{1}{3}A_{kk}\delta_{ij}\right)\left(A_{ij} - \frac{1}{3}A_{kk}\delta_{ij}\right) \tag{4-167}$$

$$= A_{ij}A_{ij} - \frac{2}{3}A_{kk}A_{ij}\delta_{ij} + \frac{1}{9}A_{kk}A_{kk}\delta_{ij}\delta_{ij} = A_{ij}A_{ij} - \frac{2}{3}A_{kk}A_{ii} + \frac{3}{9}A_{kk}A_{kk} \tag{4-168}$$

$$= A_{ij}A_{ij} - \frac{1}{3}A_{kk}A_{kk} \tag{4-169}$$

$$\frac{\partial\left(2dev(\mathbf{A}) : dev(\mathbf{A})\right)}{\partial\mathbf{A}} = 2\left(A_{ij} - \frac{1}{3}A_{kk}\delta_{ij}\right) = 2dev(\mathbf{A}) \tag{4-170}$$

the required derivative for substitution of the potential expression can be obtained.

5. EXPRESSIONS FOR THICK-WALLED TUBE MODEL OF ARTERIAL STRUCTURE

5.1. The Basic Kinematics

In non-linear mechanics, the common practice for obtaining closed-form analytical expressions for quantities is by assuming a deformation mode, a method which is named as "Prescribed Kinematics Approach".

Regarding that the structure is NOT prestressed for the beginning, (Prestress can also be incorporated within the damage model by some way, as it will be made clear in Section 9) the kinematics for axial tension, inflation and simple torsion of a thick walled tube as follows.

As the first step, the first mapping is due to the viscoelastic deformations, that maps the reference coordinates (R,Θ,Z) to intermediate configuration (ρ,ν,ζ) as

$$\rho=\rho(R)\,;\,\nu=\Theta+\varphi Z\,;\;\zeta=\Lambda Z \qquad \textbf{(5-1)}$$

Things to notice are that the radial distribution of radius deformation is not uniform, thus the model is thick-walled. But the axial stretch is, as that of a tensile test at a universal testing machine, is uniform throughout the wall thickness. The deformation gradient is then obtained as follows:

$$\mathbf{F}_v=\begin{bmatrix}\dfrac{\partial\rho}{\partial R} & 0 & 0\\ 0 & \dfrac{\rho}{R} & \rho\varphi\\ 0 & 0 & \Lambda\end{bmatrix} \qquad \textbf{(5-2)}$$

The mapping from intermediate (ρ,ν,ζ) to final configuration (r,θ,z) is as follows:

$$r=r(\rho);\;\theta=\nu+\phi\zeta\,;\;z=\lambda\zeta$$

The deformation gradient for this step is then obtained as follows:

$$\mathbf{F}_e = \begin{bmatrix} \dfrac{\partial r}{\partial \rho} & 0 & 0 \\ 0 & \dfrac{r}{\rho} & r\phi \\ 0 & 0 & \lambda \\ \end{bmatrix} \tag{5-3}$$

after laying out the major quantities, it is possible to obtain all the others:

$$\mathbf{F} = \mathbf{F}_e\mathbf{F}_v = \begin{bmatrix} \dfrac{\partial r}{\partial \rho}\dfrac{\partial \rho}{\partial R} & 0 & 0 \\ 0 & \dfrac{r}{\rho}\dfrac{\rho}{R} & \left(\dfrac{r}{\rho}\rho\varphi + \Lambda r\phi\right) \\ 0 & 0 & \Lambda\lambda \\ \end{bmatrix} = \begin{bmatrix} \dfrac{\partial r}{\partial R} & 0 & 0 \\ 0 & \dfrac{r}{R} & \left(r\varphi + \Lambda r\phi\right) \\ 0 & 0 & \Lambda\lambda \\ \end{bmatrix} \tag{5-4}$$

Setting the incompressibility constraints

$$\det(\mathbf{F}) = \det(\mathbf{F}_e) = \det(\mathbf{F}_v) = 1 \tag{5-5}$$

$$\frac{\partial \rho}{\partial R}\frac{\rho}{R}\Lambda = 1 \tag{5-6}$$

$$\frac{\partial \rho}{\partial R} = \frac{R}{\rho\Lambda} \tag{5-7}$$

$$\beta^2 - \rho^2 = \frac{1}{\Lambda}\left(B^2 - R^2\right) \tag{5-8}$$

and similarly

$$\frac{\partial r}{\partial \rho} = \frac{\rho}{\lambda r} \tag{5-9}$$

$$b^2 - r^2 = \frac{1}{\lambda}\left(\beta^2 - \rho^2\right) \tag{5-10}$$

Thus, one can obtain the radial coordinate transformations.

The legend is as follows:

B is the outer radius at the initial configuration

β is the outer radius at the intermediate (viscously deformed) configuration

Λ is the axial stretch at the intermediate (viscously deformed) configuration

b is the outer radius at the final configuration

λ is the axial stretch at the final configuration with respect to the intermediate one.

The formulae **(5-5)** to **(5-10)** imply that, due to the incompressibility constraint, a point's radial travel to deformed coordinates is known, if its position with respect to the outer diameter at the current and previous configurations, along with the axial stretch is known.

5.2. The Strain Expressions

Recalling

$$\mathbf{F}_v = \begin{bmatrix} \dfrac{R}{\rho\Lambda} & 0 & 0 \\ 0 & \dfrac{\rho}{R} & \rho\varphi \\ 0 & 0 & \Lambda \end{bmatrix} \tag{5-11}$$

the Lagrangian strain components can be calculated.

$$\mathbf{E}_v = \frac{1}{2}\left(\mathbf{F}_v{}^T\mathbf{F}_v - \mathbf{I}\right) = \frac{1}{2}\begin{bmatrix} \left(\dfrac{R}{\rho\Lambda}\right)^2 - 1 & 0 & 0 \\ 0 & \left(\dfrac{\rho}{R}\right)^2 - 1 & \dfrac{\rho}{R}\rho\varphi \\ 0 & \dfrac{\rho}{R}\rho\varphi & (\rho\varphi)^2 + \Lambda^2 - 1 \end{bmatrix} \tag{5-12}$$

Notice the nonlinear correlation among torsion and the axial strain. Thus our model is able to detect second order effects as desired. Also this implies that a torsional load has some effects in the axial stress / strain, whichever is not controlled.

In the formulations above, based on the special properties of the decomposition of total deformation gradient and the specific material model, ρ, Λ and φ are the parameters to evolve; they cannot be directly measured. The total strain, on the other hand is more complex:

$$\mathbf{F} = \mathbf{F}_e \mathbf{F}_v = \begin{bmatrix} \frac{R}{\Lambda\lambda r} & 0 & 0 \\ 0 & \frac{r}{R} & \left(\frac{r}{\rho}\rho\varphi + \Lambda r\phi\right) \\ 0 & 0 & \Lambda\lambda \end{bmatrix} \tag{5-13}$$

$$\mathbf{E} = \frac{1}{2}\left(\mathbf{F}^T\mathbf{F} - \mathbf{I}\right) \tag{5-14}$$

$$\mathbf{E} = \frac{1}{2}\begin{bmatrix} \left(\frac{R}{\rho}\frac{\rho}{r}\frac{1}{\Lambda\lambda}\right)^2 - 1 & 0 & 0 \\ 0 & \left(\frac{r}{\rho}\frac{\rho}{R}\right)^2 - 1 & \left(\frac{r}{\rho}\frac{\rho}{R}\right)\left(\frac{r}{\rho}\rho\varphi + \Lambda r\phi\right) \\ 0 & \left(\frac{r}{\rho}\frac{\rho}{R}\right)\left(\frac{r}{\rho}\rho\varphi + \Lambda r\phi\right) & \left(\frac{r}{\rho}\rho\varphi + \Lambda r\phi\right)^2 + (\Lambda\lambda)^2 - 1 \end{bmatrix} \tag{5-15}$$

$$\mathbf{E} = \frac{1}{2}\begin{bmatrix} \left(\frac{R}{\Lambda\lambda r}\right)^2 - 1 & 0 & 0 \\ 0 & \left(\frac{r}{R}\right)^2 - 1 & \frac{r}{R}(r\varphi + \Lambda r\phi) \\ 0 & \frac{r}{R}(r\varphi + \Lambda r\phi) & (r\varphi + \Lambda r\phi)^2 + (\Lambda\lambda)^2 - 1 \end{bmatrix} \tag{5-16}$$

The coupling between different parameters gets, as seen, much more complicated. However, they are still second order, since torsion angles are of order "0" while stretches are of order "1".

The elastic strain is obtained similarly. The formulae read

$$\boldsymbol{\Gamma}_e = \frac{1}{2}\left\{\begin{bmatrix} \frac{\rho}{r\lambda} & 0 & 0 \\ 0 & \frac{r}{\rho} & 0 \\ 0 & r\phi & \lambda \end{bmatrix}\begin{bmatrix} \frac{\rho}{r\lambda} & 0 & 0 \\ 0 & \frac{r}{\rho} & r\phi \\ 0 & 0 & \lambda \end{bmatrix} - \begin{bmatrix} 1 & 0 & 0 \\ 0 & 1 & 0 \\ 0 & 0 & 1 \end{bmatrix}\right\} \tag{5-17}$$

$$\boldsymbol{\Gamma}_e = \frac{1}{2}\begin{bmatrix} \left(\frac{\rho}{r\lambda}\right)^2 - 1 & 0 & 0 \\ 0 & \left(\frac{r}{\rho}\right)^2 - 1 & \frac{r}{\rho} r\phi \\ 0 & \frac{r}{\rho} r\phi & (r\phi)^2 + \lambda^2 - 1 \end{bmatrix} \tag{5-18}$$

in matrix notation.

The strain-rate for the intermediate configuration is also obtained via

$$\dot{\mathbf{E}}_v = \frac{1}{2}\left(\mathbf{F}_v{}^T\mathbf{F}_v - \mathbf{I}\right)^{\bullet} = \frac{1}{2}\left(\dot{\mathbf{F}}_v{}^T\mathbf{F}_v + \mathbf{F}_v{}^T\dot{\mathbf{F}}_v\right) \tag{5-19}$$

which is also symmetric, and in the form of $\mathbf{E}_v$, since it is the material time derivative of the intermediate deformation with respect to the fixed undeformed configuration.

$$\dot{\mathbf{E}}_v = \begin{bmatrix} -\frac{R^2}{\rho^2\Lambda^2}\left(\frac{\dot{\rho}}{\rho} + \frac{\dot{\Lambda}}{\Lambda}\right) & 0 & 0 \\ 0 & \frac{\rho^2}{R^2}\frac{\dot{\rho}}{\rho} & \frac{\rho}{R}\left(\varphi\dot{\rho} + \frac{1}{2}\rho\dot{\varphi}\right) \\ 0 & \frac{\rho}{R}\left(\varphi\dot{\rho} + \frac{1}{2}\rho\dot{\varphi}\right) & \Lambda\dot{\Lambda} + \rho\varphi\left(\varphi\dot{\rho} + \rho\dot{\varphi}\right) \end{bmatrix} \tag{5-20}$$

The same result can also be obtained via using the velocity gradient $\mathbf{L}_v$, though $\mathbf{L}_v$ has extra terms due to the non-vanishing material derivatives of the base vectors in cylindrical coordinates [39].

5.3. External Quantities

In any experimental system, besides recording the deformations, the loading condition is also known. The parameter identification process thus can be carried out for a given material model, as long as the stress-external load relations are known, so that there is a common base of meeting two branches of "numbers": The measurement branch with loads & deformations is matched with the theory & parameters branch.

In the model of thick walled tube for a segment of artery within the scope of this study is subjected to three (independent) external loads, namely: (1) the internal hydraulic pressure; (2) the axial stretching force on the segment and (3) the torque applied on the segment. Thus, these quantities have to be identified using stress components obtained from theory.

Since the structure deforms as loads are applied, one now has to switch to Eulerian framework, where real quantities of stress values are tracked, unlike the way done while deriving the constitutive framework, where the strain energy functionals were expressed in terms of Lagrangian quantities mainly (for sake of simplicity there).

5.3.1. The Equations of Equilibrium

From the balance of linear momentum, well-known for (incompressible) materials is the equation of motion recalled from Section 3.3.2

$$\nabla\boldsymbol{\sigma} + \rho\mathbf{b} = \rho\mathbf{a} \qquad \textbf{(5-21)}$$

in Eulerian frame. In case that the body forces (applied acceleration, gravity, other magnetic & centrifugal components) are negligible, the tensorial form of equation of equilibrium reads

$$\nabla\boldsymbol{\sigma} = 0 \qquad \textbf{(5-22)}$$

where the gradient is also with respect to the deformed coordinates. Transformations between Lagrangian and Eulerian expressions are always possible, but the simplicity then blows up.

Knowing what has been neglected (the body forces), and as to the kinematics' and symmetry assumptions, it can said that the strain and the stress field, is now only a function of r (or R). Thus, the scalar expressions for the tensorial equation of equilibrium are

$$\frac{\partial \sigma_{rr}}{\partial r} + \frac{\sigma_{rr} - \sigma_{\theta\theta}}{r} = 0 \qquad \textbf{(5-23)}$$

$$\frac{1}{r^2}\frac{\partial}{\partial r}\left(r^2 \sigma_{r\theta}\right) = 0 \qquad \textbf{(5-24)}$$

$$\frac{1}{r}\frac{\partial}{\partial r}\left(r \sigma_{rz}\right) = 0 \qquad \textbf{(5-25)}$$

with the non-zero components. Integrating the last two equations yield

$$\sigma_{r\theta} = \frac{d_1}{r^2} \qquad \textbf{(5-26)}$$

$$\sigma_{rz} = \frac{d_2}{r} \qquad \textbf{(5-27)}$$

where d_1 and d_2 are constants. Since the current framework is based on "prescribed kinematics", these equations determine what tractions are required on the faces to maintain the prescribed deformation. Or, if the circumferential and axial components of the tractions on the inner and outer surface of the are known, then the associated values of these shear components can be calculated. Whereas it is nearly impossible to ascertain the tractions on the adventitial surface in vivo, which result from perivascular coupling, the tractions on the intimal surface can be calculated from the hemodynamics. Indeed, at the intima σ_{rz} must be equal and opposite of the axially directed shear stress in the blood at the wall, a quantity that is known to be very important in vascular mechanics. Conversely, tractions on the intimal surface due to endovascular balloon catheters are problematic to evaluate. To the luck devoted to researchers, in most in vitro experiments designed to study wall properties, (since there is no considerable flow) the shearing components of the traction vector are negligible, hence

$$d_1 = 0 \tag{5-28}$$

$$d_2 = 0 \tag{5-29}$$

and the only "non-identically-zero" equation of equilibrium is

$$\frac{\partial \sigma_{rr}}{\partial r} + \frac{\sigma_{rr} - \sigma_{\theta\theta}}{r} = 0 \tag{5-30}$$

5.3.2. An Addendum to the Functional Form of Ψ

The above statements **(5-26)** to **(5-29)** also impose an indirect restriction on the form of the strain energy density functions to be proposed for the arterial tissue. Consider a polynomial type expression of Ψ in terms of strain components:

$$\Psi = aE_{\theta\theta}{}^3 + bE_{zz}{}^3 + cE_{\theta\theta}E_{zz} + dE_{\theta z}{}^2 + \ldots \tag{5-31}$$

As long as Ψ is formed as the sum of an explicit expression for each component, and the parameter for each strain component appearing in the functional form of Ψ is not (experimentally) determined, the validity of that specific form of Ψ is restricted to the state where that term does not dominate or exist for the deformation thus occurrence of the relevant stress component(s); i.e. it works under the strict assumptions of the experimental setup.

A formulation in terms of different invariants, thus enables complex coupling effects on different loading conditions, that can occur (for example in a finite element analysis) to get reflected as a contribution to the change of strain energy of structure. Thus, unlike polynomial formulations, which are of course more explicit to solve, invariant formulations are much more useful for generalization into modeling of complex phenomenon.

Following this approach, for our model, despite incorporating this ability for generalization, imposes another type of restriction on form. Setting σ_{rz} and $\sigma_{r\theta}$ to be identically zero, implies that

$$\sigma_{r\theta} = \sigma_{r\theta}\left(\frac{\partial \Psi}{\partial E_{R\Theta}}, \frac{\partial \Psi}{\partial E_{RZ}}\right) \tag{5-32}$$

$$\sigma_{rz} = \sigma_{rz}\left(\frac{\partial \Psi}{\partial E_{RZ}}\right) \tag{5-33}$$

to be identically zero. Thus, for the model to work in the general case, Ψ should not explicitly depend on $E_{R\Theta}$ and E_{RZ} [39]. This setting, in physical world, has an explicit meaning: The model implies that, arterial tissue behaves like layers of very thin tubes, among which shear stress is not transferred, thus does not occur, in the $r\theta$ and rz directions. These frictionless layers form a network forming the tissue, and any shearing load (i.e. the hemodynamic intimal shear) is beared in terms of (axial) strain and stress components.

at this stage, it is also useful to recall the anatomical properties of the arterial tissue provided briefly in Section 2.1.

5.3.3. The Explicit Terms of Cauchy Stress Tensor

Since, most of the stuff following is based on the statements above, it should be of great interest to visualize the components of the Cauchy Stress tensor in terms of components of $\frac{\partial \psi_e}{\partial \mathbf{\Gamma}_e}$.

Let

$$\mathbf{\Gamma}_e = \begin{bmatrix} \Gamma_{\rho\rho} & 0 & 0 \\ 0 & \Gamma_{\theta\theta} & \Gamma_{\theta Z} \\ 0 & \Gamma_{\theta Z} & \Gamma_{ZZ} \end{bmatrix} \tag{5-34}$$

Then,

$$\boldsymbol{\tau}_e = \frac{\partial \psi_e}{\partial \mathbf{\Gamma}_e} = \begin{bmatrix} \tau_{\rho\rho} & 0 & 0 \\ 0 & \tau_{\theta\theta} & \tau_{\theta Z} \\ 0 & \tau_{\theta Z} & \tau_{ZZ} \end{bmatrix} \tag{5-35}$$

Excluding the p terms of incompressibility, since

$$\boldsymbol{\sigma} = \mathbf{F}_e \frac{\partial \psi_e}{\partial \boldsymbol{\Gamma}_e} \mathbf{F}_e^T \tag{5-36}$$

it readily follows

$$\boldsymbol{\sigma} = \begin{bmatrix} \frac{R^2}{r^2\lambda^2}\tau_{\rho\rho} - p & 0 & 0 \\ 0 & \frac{r}{R}\left(r\tau_{\theta\theta} + r\phi\tau_{\theta Z}\right) - p & \lambda\left(\frac{r}{R}\tau_{\theta Z} + r\phi\tau_{ZZ}\right) \\ 0 & \lambda\left(\frac{r}{R}\tau_{\theta Z} + r\phi\tau_{ZZ}\right) & \lambda^2\tau_{ZZ} - p \end{bmatrix} \tag{5-37}$$

where "–p" terms in diagonal denote the incompressibility constraint being introduced.

It is worth to note that members of $\boldsymbol{\sigma}$ and $\boldsymbol{\tau}$ fully depend on r for a thick-walled formulation.

5.3.4. The Internal Pressure – Stress Relations

Internal pressure is the boundary condition to stress components in the inner radius: Knowing that it is the negative radial stress at the inner surface of the tube wall, the equilibrium equation in the radial direction, namely;

$$\frac{\partial \sigma_{rr}}{\partial r} + \frac{\sigma_{rr} - \sigma_{\theta\theta}}{r} = 0 \tag{5-38}$$

can be used to find internal pressure. Integrating by r,

$$\sigma_{rr}(r) - \sigma_{rr}(a) = \int_a^r (\sigma_{\theta\theta} - \sigma_{rr}) \frac{1}{r} dr \tag{5-39}$$

is obtained where r is the radial coordinate and a is the inner radius in the final configuration of the artery. With $\sigma_{rr}(a) = -P_i$ and $\sigma_{rr}(b) = 0$,

$$P_i = \int_a^b (\sigma_{\theta\theta} - \sigma_{rr}) \frac{1}{r} dr \tag{5-40}$$

is gathered as the first explicit expression between geometric measures and applied loads. It should be noted that due to incompressibility, the geometric relations

$$\beta^2 - \rho^2 = \frac{1}{\Lambda}\left(B^2 - R^2\right) \tag{5-41}$$

$$b^2 - r^2 = \frac{1}{\lambda}\left(\beta^2 - \rho^2\right) \tag{5-42}$$

hold, which state that a and b are not independent.

5.3.5. The Axial Force – Stress Relations

In general, the net axial force is given by

$$F_{AX} = 2\pi\int_a^b \sigma_{zz} r dr \tag{5-43}$$

which is the integral (signed arithmetic total) of axial stress over the cross section. Knowing that, due to incompressibility,

$$\sigma_{zz} = -p + \overline{\sigma}_{zz} \tag{5-44}$$

is imposed. Thus substituting this expression into the axial force equation

$$F_{AX} = 2\pi\left\{\int_a^b \left(-p + \overline{\sigma}_{zz}\right) r dr\right\} = 2\pi\left\{\int_a^b \left(-p\right) r dr + \int_a^b \left(\overline{\sigma}_{zz}\right) r dr\right\} \tag{5-45}$$

$$F_{AX} = 2\pi\left\{\left(-p\frac{r^2}{2}\right)\Bigg|_a^b - \int_a^b \frac{r^2}{2}\left(-\frac{dp}{dr}\right) dr + \int_a^b \left(\overline{\sigma}_{zz}\right) r dr\right\} \tag{5-46}$$

$$F_{AX} = -0 + P_i \pi a^2 + \pi\int_a^b \frac{dp}{dr} r^2 dr + 2\pi\int_a^b \left(\overline{\sigma}_{zz}\right) r dr \tag{5-47}$$

Using the equation of equilibrium in the radial direction, and decoupling the Lagrange multipliers,

$$\frac{d\left(-p + \overline{\sigma}_{rr}\right)}{dr} + \frac{\left(-p + \overline{\sigma}_{rr}\right) - \left(-p + \overline{\sigma}_{\theta\theta}\right)}{r} = 0 \tag{5-48}$$

$$\frac{dp}{dr} = \frac{d\overline{\sigma}_{rr}}{dr} - \frac{\overline{\sigma}_{\theta\theta} - \overline{\sigma}_{rr}}{r} \tag{5-49}$$

Substituting yields

$$F_{AX} - P_i \pi a^2 = \pi \int_a^b \left(\frac{d\overline{\sigma}_{rr}}{dr} - \frac{\overline{\sigma}_{\theta\theta} - \overline{\sigma}_{rr}}{r} \right) r^2 dr + 2\pi \int_a^b (\overline{\sigma}_{zz}) r dr \tag{5-50}$$

$$F_{AX} - P_i \pi a^2 = \pi \int_a^b \left(\frac{d\overline{\sigma}_{rr}}{dr} \right) r^2 dr + \pi \int_a^b (2\overline{\sigma}_{zz} - \overline{\sigma}_{\theta\theta} + \overline{\sigma}_{rr}) r dr \tag{5-51}$$

$$F_{AX} - P_i \pi a^2 = \pi \left[\left(r^2 \overline{\sigma}_{rr} \right)_a^b - \int_a^b 2\overline{\sigma}_{rr} r dr \right] + \pi \int_a^b (2\overline{\sigma}_{zz} - \overline{\sigma}_{\theta\theta} + \overline{\sigma}_{rr}) r dr \tag{5-52}$$

Since $\overline{\sigma}_{rr}(a) = 0$ since $\sigma_{rr}(a) = -P_i$ and $\overline{\sigma}_{rr}(b) = 0$ since on outer surface $\sigma_{rr}(b) = 0$ and pressure is identically 0,

$$\left(r^2 \overline{\sigma}_{rr} \right)_a^b = 0 \tag{5-53}$$

and

$$F_{AX} - P_i \pi a^2 = \pi \int_a^b (2\overline{\sigma}_{zz} - \overline{\sigma}_{\theta\theta} - \overline{\sigma}_{rr}) r dr \tag{5-54}$$

or identically

$$F_{AX} - P_i \pi a^2 = \pi \int_a^b (2\sigma_{zz} - \sigma_{\theta\theta} - \sigma_{rr}) r dr \tag{5-55}$$

since the Lagrangian multiplier (pressure) term vanishes within the parenthesis. Setting

$$N = F_{AX} - P_i \pi a^2 \tag{5-56}$$

and call N the "reduced axial force". In fact, what is read from an axial thrust transducer connected to an end of the arterial segment is some sort of "reduced axial force", but not with respect to the deformed diameter of the artery but considering the diameter of the inner connection interface. Thus, the revised the formula is:

$$F_{AX} - P_i \pi R_T{}^2 = \pi \left[\left(a^2 - R_T{}^2 \right) P_i + \int_a^b \left(2\sigma_{zz} - \sigma_{\theta\theta} - \sigma_{rr} \right) r dr \right] \quad \textbf{(5-57)}$$

where R_T is introduced as the diameter of the rigid connection of the arterial segment to axial thrust transducer. Then, recalling

$$N = F_{AX} - P_i \pi R_T{}^2 \quad \textbf{(5-58)}$$

one have the expression

$$N = \pi \left[\left(a^2 - R_T{}^2 \right) P_i + \int_a^b \left(2\sigma_{zz} - \sigma_{\theta\theta} - \sigma_{rr} \right) r dr \right] \quad \textbf{(5-59)}$$

for relating what is read from the axial thrust transducer to stress components. Notice that this equation, to our knowledge, is not given explicitly in the literature by now. The term $\left(a^2 - R_T{}^2 \right)$, at the beginning of an experimental sequence, might not be of importance, since it tends to zero as pressure vanishes, but with the large deformation of artery under inflation, it becomes quite sound.

5.3.6. The Torque – Stress Relations

Since for shear components, not much is related to issues with incompressibility, the torque formulation is rather straightforward

$$M_b = 2\pi \int_a^b \sigma_{z\theta} r^2 dr \quad \textbf{(5-60)}$$

indicating the torque as the distance-weighted total of shear stress in the $z\theta$ (cross-section of artery) plane. Notice again that a and b are not independent.

5.4. Scalar Equations of State

Using these expressions; the evolution laws and the stress equation can be transformed into scalar equations.

5.4.1. An Alternative Formulation

Having for the II.Piola-Kirchhoff stress:

$$\mathbf{S} = \mathbf{F}_v^{-1} \frac{\partial \Psi_e}{\partial \boldsymbol{\Gamma}_e} \mathbf{F}_v^{-T} \tag{5-61}$$

Since all the quantities have been obtained in terms of Cauchy stress components in the previous section, a conversion is required. For the incompressible case,

$$\boldsymbol{\sigma} = \mathbf{F}\mathbf{S}\mathbf{F}^T = \mathbf{F}_e\mathbf{F}_v\left(\mathbf{F}_v^{-1} \frac{\partial \Psi_e}{\partial \boldsymbol{\Gamma}_e} \mathbf{F}_v^{-T} \right)\mathbf{F}_v^{\,T}\mathbf{F}_e^{\,T} = \mathbf{F}_e \frac{\partial \Psi_e}{\partial \boldsymbol{\Gamma}_e} \mathbf{F}_e^{\,T} \tag{5-62}$$

$$\boldsymbol{\sigma} = \mathbf{F}_e \frac{\partial \Psi_e}{\partial \boldsymbol{\Gamma}_e} \mathbf{F}_e^{\,T} \tag{5-63}$$

The equation of evolution is

$$\frac{\partial \Psi_v^{\infty}}{\partial \mathbf{E}_v} - \mathbf{F}_v^{-1}\left(\mathbf{I} + 2\boldsymbol{\Gamma}_e\right)\frac{\partial \Psi_e}{\partial \boldsymbol{\Gamma}_e} \mathbf{F}_v^{-T} = -\frac{\partial \Phi}{\partial \dot{\mathbf{E}}_v} \tag{5-64}$$

This equation can be used as the evolution tracker; one can use it for deriving the viscous deformation $\mathbf{F}_v$ (intermediate configuration), with known inputs from total deformation. Eliminating $\frac{\partial \Psi_e}{\partial \boldsymbol{\Gamma}_e}$ in between is another possibility:

$$\left(\mathbf{I} + 2\boldsymbol{\Gamma}_e\right)\frac{\partial \Psi_e}{\partial \boldsymbol{\Gamma}_e} = \mathbf{F}_v\left(\frac{\partial \Psi_v}{\partial \mathbf{E}_v} + \frac{\partial \Phi}{\partial \dot{\mathbf{E}}_v} \right)\mathbf{F}_v^{\,T} \tag{5-65}$$

$$\frac{\partial \Psi_e}{\partial \boldsymbol{\Gamma}_e} = \left(\mathbf{I} + 2\boldsymbol{\Gamma}_e\right)^{-1}\left[\mathbf{F}_v\left(\frac{\partial \Psi_v}{\partial \mathbf{E}_v} + \frac{\partial \Phi}{\partial \dot{\mathbf{E}}_v} \right)\mathbf{F}_v^{\,T} \right] \tag{5-66}$$

Recalling

$$\left(\mathbf{I} + 2\boldsymbol{\Gamma}_e\right)^{-1} = \left(\mathbf{F}_e^{\,T}\mathbf{F}_e\right)^{-1} = \mathbf{F}_e^{-1}\mathbf{F}_e^{-T} \tag{5-67}$$

one substitutes all into the Cauchy stress equation

$$\boldsymbol{\sigma} = \mathbf{F}_e\left(\mathbf{F}_e^{-1}\mathbf{F}_e^{-T}\right)\left[\mathbf{F}_v\left(\frac{\partial\Psi_v}{\partial\mathbf{E}_v}+\frac{\partial\Phi}{\partial\dot{\mathbf{E}}_v}\right)\mathbf{F}_v^{T}\right]\mathbf{F}_e^{T} \tag{5-68}$$

Finally the two identical equations are derived, with $\mathbf{F}_e^{-T} = \mathbf{F}^{-T}\mathbf{F}_v^{T}$;

$$\boldsymbol{\sigma} = \mathbf{F}^{-T}\mathbf{F}_v^{T}\mathbf{F}_v\left(\frac{\partial\Psi_v}{\partial\mathbf{E}_v}+\frac{\partial\Phi}{\partial\dot{\mathbf{E}}_v}\right)\mathbf{F}^{T} \tag{5-69}$$

$$\boldsymbol{\sigma} = \mathbf{F}_e\frac{\partial\Psi_e}{\partial\boldsymbol{\Gamma}_e}\mathbf{F}_e^{T} \tag{5-70}$$

for the Cauchy Stress Tensor. Since these two equations are identical, one can also interpret the coefficients among different parts of the formulae. Notice that the viscous effects and the elastic effects are decoupled if the former formulation (**5-63**, **5-64**) is readopted.

6. BASICS OF PLASTICITY

6.1. Introduction

The materials that go beyond some limit of a comparison parameter (strain, stress) may exhibit irreversible deformations, as the loading condition reverts to original state where the observations have begun. This phenomenon is called as "plastic deformations" of a (solid) body in continuum mechanics [35]. In classical plasticity, macroscopic variables play the key role in initiation of plastic deformation, i.e. the stress state at a point, or the stress state, etc … Thus, no motivation is captured from the internal substructure of the material. These internal substructures can be said to be the dislocation distribution in metallic materials, the crystal orientations and orientation of inter-crystal surfaces at the micro-scale, deformation-related orientation of initially-homogeneous structures, such as dislocation and crystal arrangement in sheet metal forming.

In biological structures, the macro-scale theory of plasticity is more pleasant in the sense of finding a geometrical guide form micro-scale, since, especially in soft tissues, the materials are predominantly fiber-reinforced, continuum-to-macroscale organizations. Thus, non-local theories may apply to them.

The non-local theories are mostly related to the single crystal plasticity theories developed in the literature, where, in classical engineering materials, the slip is assumed to take place over some preferred slip directions, in the form of smooth shearing [35]. In fiber reinforced (biological) materials, the slip directions are assumed to be that of the fibers, thus enabling preferred permanent shearing due to some criteria.

In a recent paper by Holzapfel [40], this has been indicated that failure of soft biological tissue is not accompanied with non-recoverable deformations only. Such examples include (damage based) softening of the left ventricular myocardium of a rat but no changes in the unloaded segment length after overstretching the material.

A hypothetical explanation of these two contrary mechanical behaviors of soft biological tissues under failure (i.e. yielding and softening) was given by two competing factors of a connective tissue:

(i) if collagen fibrils have to carry high tensile stress they need to be large in diameter in order to maximize the density of inter-fiber covalent cross links, and

(ii) in order to capture non-recoverable creep after removal of the load, the tissue needs sufficient inter-fiber cross links. This can be achieved by numerous collagen fibrils small in diameter such that the surface area per unit mass increases.

which has been reported in [40] to yield

(i) that damage in connective tissue incorporating thick collagen fibrils, is mainly governed by a relative sliding mechanism of collagen fibrils, and non-recoverable creep evolves. Hence, it is suggested that the matrix material is responsible for the plastic deformation. In this case the mechanical response may be described by the theory of plasticity, which is one goal of the present work.

(ii) damage evolves in connective tissue incorporating thin collagen fibrils due to breakage of collagen and collagen cross-links. This failure pattern is clearly addressed to damage mechanics, and is another goal of this work.

The mechanics of evolving damage has been addressed in Section 7, and this section is devoted to the permanent deformations that (arterial) fiber-reinforced continuum exhibits under different circumstances.

6.2. Crystal Plasticity

In the crystal plasticity theory, slip is assumed to occur before the material exhibits any elastic deformation that bears the applied stress. Thus, the multiplicative decomposition, in the formal manner, is assumed to hold. The demonstrative sketch in Figure 6.1 [35] assumes a such decomposition, and illustrates how the mechanism

works. Figure 6.2 demonstrates the path of loading and unloading curves for an elasto-plastic deformation, and the mechanism hypothetical multiplicative decomposition is assumed to occur, which is in the sense completely different than the real world.

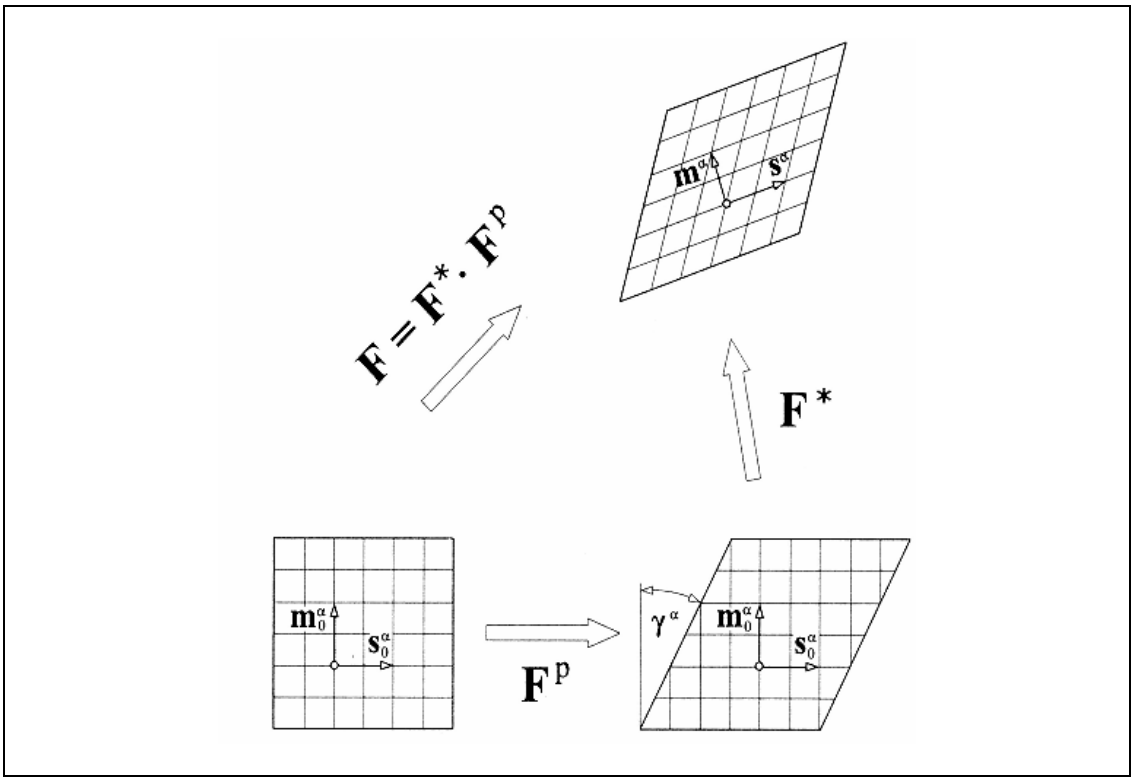

Figure 6.1 : Illustration of Crystal Plasticity theory based on multiplicative decomposition. The terminology here is due to [35]

Mostly in engineering, the concept of "intermediate stress-free configuration" is not traceable by a typical loading/unloading experiment. That is because, the intermediate configuration is assumed to evolve before the structure bears load, but in a tensile experiment, let's say, the path is vice versa: the plastic deformation takes place after some elastic deformation happens and a "limit value" is violated. Thus, in real world, the apparent intermediate configuration is Eulerian (as it follows the current deformation and stress state) and not stress-free. The theory, turns the procedure vice versa, and traces the unloading path. [41] recalls both formulations, and comments on the duality (equivalency) of each with respect to the other for a wide spectrum of material configurations.

In crystal plasticity to be adopted here, the parameters to mention to completely describe a (phenomenological) model are

a) The slip directions
b) The accumulated shearing angle
c) The resolved shear stress (Schmid's Law)
d) The shear rate and normality of flow
e) The yield condition and its evolution (hardening, etc..)

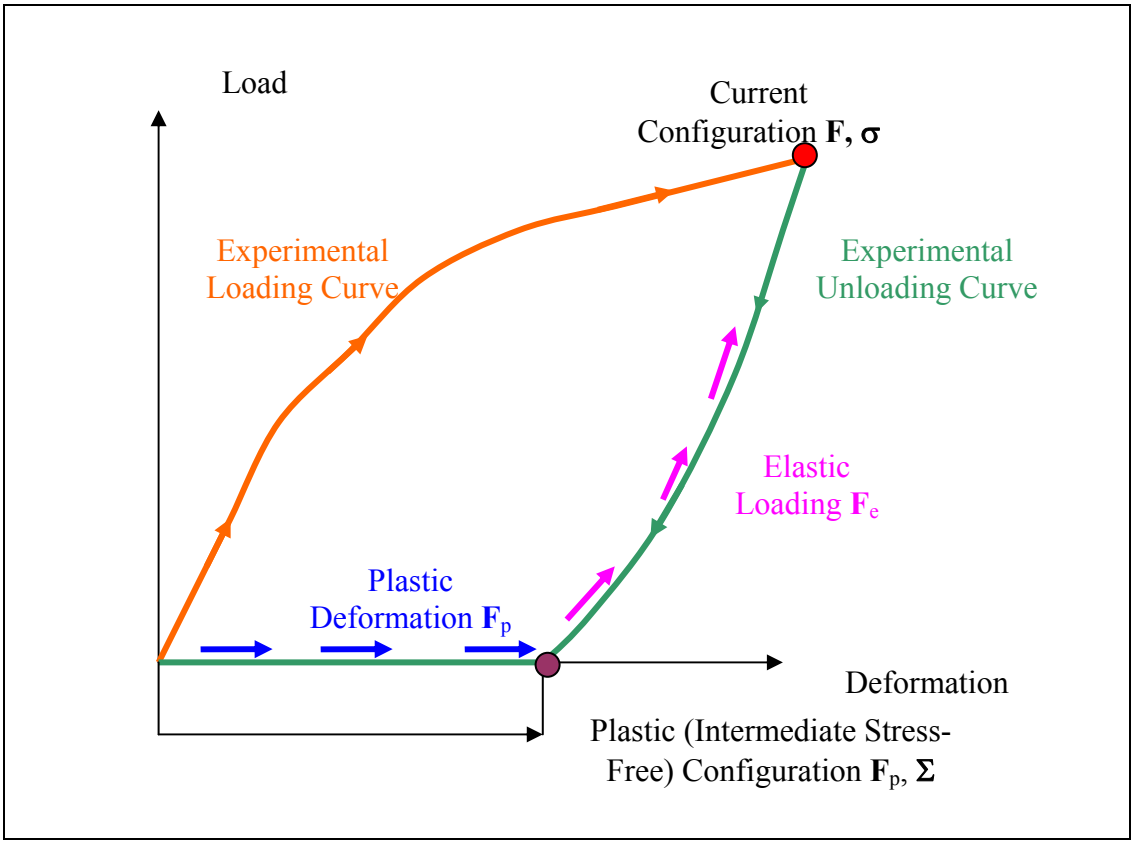

Figure 6.2 : The experimentally obtainable elasto-plastic loading/unloading curve for a material and the visualization of the multiplicative decomposition concept.

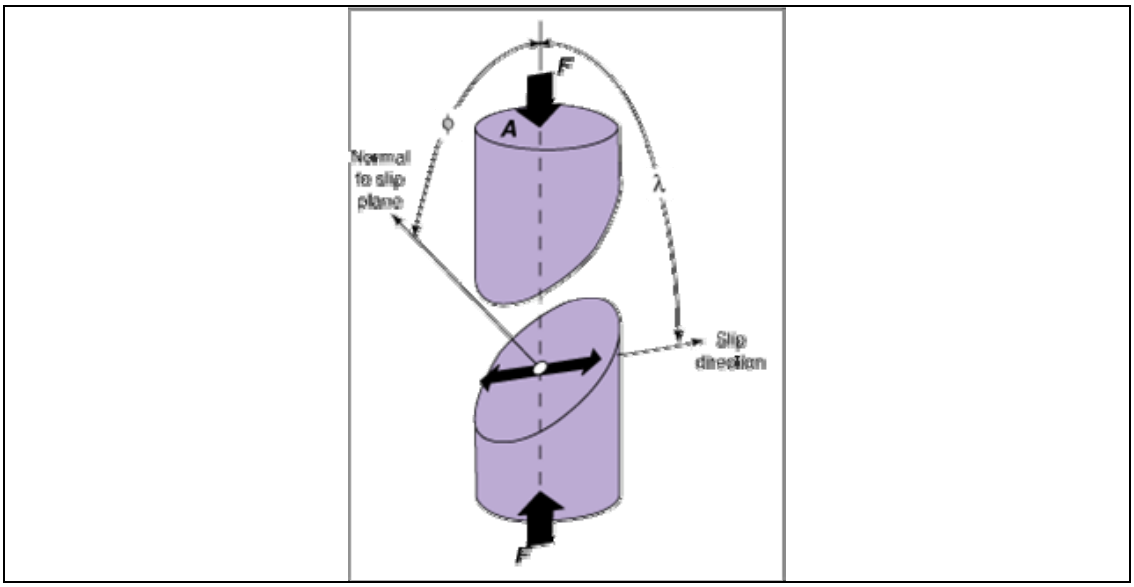

Figure 6.3 : The slip directions in single crystal [42]

6.2.1. The Slip Directions

The assumption within this thesis is that the plastic deformation occurs between the ground substance (elastin) and the collagen fibrils that bear tensile loads within the arterial structure. Thus, the normal to the slip direction is fiber direction, and its normal is the normal of fiber being the in plane (θZ) component. This assumption is valid due to the facts that, the constitutive restrictions defined in Section 6.3 enforce such a shearing to occur, as well as that the fibers are in plane, and no radial component is expected to occur.

6.2.2. The Resolved Shear Stress (Schmid's Law)

This law states that for a given axial load in a sample, as long as the slip direction and the normal to the slip plane is known, the shear in that slip system can be defined to be, as in Figure 6.3,

$$\tau_\alpha = \sigma \cos\phi \cos\lambda \qquad \textbf{(6-1)}$$

In tensorial notation, the resolved shear is given by the inner trace of the stress tensor

$$\tau_\alpha = \boldsymbol{\sigma} : (\mathbf{m} \otimes \mathbf{n}) \qquad \textbf{(6-2)}$$

where **m** and **n** indicate the fiber direction and the slip normal respectively

Normally, in plasticity theory, $\boldsymbol{\sigma}$, the Cauchy Stress is not used due to thermodynamics. The stress quantity that is resolved to shear stress to check for yield conditions is called the Mandel Stress tensor. This tensor arises as another quantity through (which is in general not a symmetric tensor) the entropy equation, and for thermodynamic rules to be satisfied (positive entropy production, or positive dissipation), the yield should follow the Mandel Stress and relevant quantities.

6.2.3. The Yield

Plasticity theory assumes that there is some criteria that prohibits permanent deformation before some limit condition is triggered or violated. In stress-space theories, this condition is a stress surface in the (stress) space.

If the resolved shear on a specific slip system goes beyond the yield stress, plastic flow occurs. In rate-independent theories, the flow is resistance-free, i.e. it takes place and goes on without any resistance. Mathematically speaking, the rate-independent theories the plastic arc length (the path plastic deformation has followed) are differential equation systems of order one in time with respect to the post-yield stress state, resulting in explicit equations of evolution in time. In rate-dependent theories, the relation is not as simple, and some formulations do not explicitly include a yield condition, but a rather smooth transition zone. The rate-dependency in plastic flow rate, on the other hand due to inclusion of viscosity-like parameters in formulations, include a "length-scale" in formulations, that avoid artificial geometry dependence. The latter effect is observed in finite-element analysis as "mesh-size sensitivity", which is an issue discussed in detail in [43].

6.2.4. Plastic Hardening of Material

The yield condition is said to be isotropic if it is independent of any direction. The most well-known yield conditions of Tresca (maximum-shear) and Von-Mises (maximum distortion energy) criterion are the best to achieve an illustrative example.

If the aforementioned yield surface moves within plastic deformation in the stress space, (i.e., the yield condition / yield stress changes with ongoing plastic deformation) then the material's behavior is said to change with the deformation history. This motion influences a constitutive hardening or softening with ongoing

increasing plastic deformation. It is worth to mention that, damage models incorporate only “elastic” softening of structure. As the accumulation of damage increases (by some quantitiy), the material constitutive behavior changes and it gets less resistant to external loads. Plastic hardening/softening is neither geometric softening, where due to geometrical relations the load /deflection behavior of a structure gets instable (consider a self-inflating balloon under constant pressure) nor damage related softening where the internal structure of the material changes and responds different within the elastica. Simple paraphrases of various hardening rules have been stated in the following titles. Details on the model can be sought in [35] and references therein.

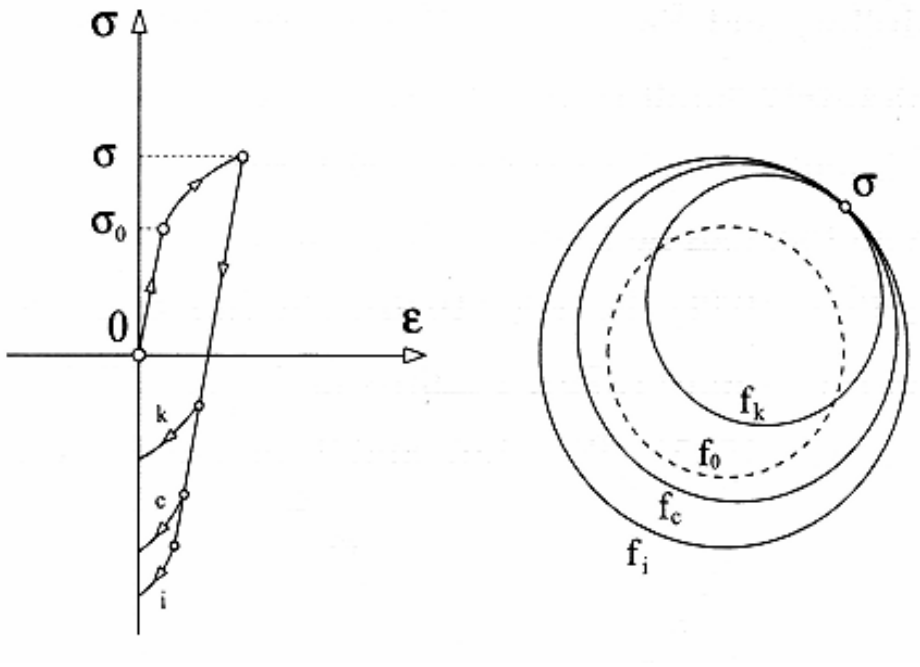

The material is loaded up point s. Then as hardening occurs, follows the path “k” if kinematic hardening occurs, “i” if isotropic hardening occurs and “c” if combined hardening occurs. The relevant representations of the yield surface in stress space is given on the right as f_k, f_i and f_c respectively, with f_0 indicating the initial yield surface.

Figure 6.4 : Visual Representation of Different Material Constitutive Models under Plastic Deformations. [35]

No Hardening: If the initial yield surface (f_0 in Figure 6.4) in the stress space does neither translate nor scale with accumulating plastic deformations, the material is said not exhibiting any hardening behavior.

Isotropic Hardening: If the yield surface in the stress space expands symmetrically with accumulating plastic deformation, then the material is said to exhibit isotropic hardening behavior (See Figure 6.4).

Kinematic Hardening: If the yield surface in the stress space translates with accumulating plastic deformation, then the material is said to exhibit isotropic hardening behavior (See Figure 6.4). This concept mainly is formulated using back-stress variables, and is best observed in "Bauschinger Effect" of metal tests.

Combined Hardening: This is a mixed case where isotropic and kinematic hardening effects are coupled. In Figure 6.4, the yield surface after a mixed / combined hardening is recalled with f_c.

In the plasticity of fiber reinforced material of interest within the scope of this thesis, it has been assumed that the "plastic" constitutive behavior each family of fiber is independent of each other, and does not have correlation in terms of hardening behaviors. Thus, a multisurface plasticity model with no latent hardening is adopted, as detailed in Section 6.3

6.2.5. The shear Rate and Normality of Flow

After some yield condition occurs, it should be noted that the yield occurs in the direction of pulling. The statement in a more legal terminology would be "in the normal of the yield surface". This is called the "consistency condition" and ensures that the plastic flow maximizes the dissipation (which is also automatically said to be positive by this assumption).

The shear rate, under the formulations presented here, is related to the stress state for the rate dependent plasticity, counterpart of the Kuhn-Tucker consistency conditions for rate-independent plasticity.

6.2.6. The Accumulated Shear Angle

Plasticity is a dynamical process, which accumulates in time. For rate-independent plasticity, where the shear angle over the preferred directions are only functions of the current (local) stress (or strain) state, the evolution of accumulated plastic deformation can be correlated to a (monotonically increasing) component (such as force, pressure, etc..). Nevertheless, especially for rate dependent models, these assumptions cannot easily verified. Thus, the accumulated shear on each slip system

$$\gamma_\alpha = \int_0^t \dot{\gamma}_\alpha dt \tag{6-3}$$

has to be evaluated for all active slip systems. The accumulated shear on a slip system, besides being for tracking the deformation, is also important in tracking the evolution of hardening and tracking of the yield condition.

6.3. The Specific Plasticity Material Model for Arterial Tissue:

In investigating the plastic deformations of arterial tissue, a rate-dependent two-surface anisotropic model has been adopted with combined hardening. The model has been verified to be stable in the sense of geometrical inputs (for example, finite element mesh dependence). Details of the model have been presented in [43]

The rate dependency of the proposed model is based on the relation

$$\dot{\gamma}_\alpha = \dot{a}\ \mathrm{sgn}(\tau_\alpha)\left[\frac{\|\tau_\alpha\|}{g_\alpha}\right]^k \tag{6-4}$$

where $\dot{a}$ is the proportionality material coefficient to shear rate, τ_α is the resolved shear stress over the slip direction, g_α is stress-counterpart estimate of the relevant slip system strain hardness, or in other words reference yield stress as a function of accumulated shearing and k is the rate-dependence sensitivity exponent, as which tends to infinity, guides the model to become less and less rate dependent, and at the limit lets the model resolves to rate-independent plasticity.

The slip system strain hardness can be given with a formula

$$g_\alpha = g_0 + (g_\infty - g_0)\tanh\left(\frac{h_0}{g_\infty - g_0}|\gamma_\alpha|\right) \quad \textbf{(6-5)}$$

where

- g_0 is the initial hardness
- g_∞ is the maximum hardness when $\frac{\partial g_\alpha}{\partial \gamma_\alpha} = 0$
- h_0 is the initial hardening, at $\gamma_\alpha = 0$
- $\gamma_\alpha = \int_0^t \dot{\gamma}_\alpha dt$ the accumulated shearing on the slip system
- $g_\alpha > 0$, $\dot{a} > 0$, $h_0 > 0$ are the bounds to material parameters.

In the above expressions and the following ones throughout the plasticity considerations, α index stands for each active slip system, or more explicitly the fiber families as noted by “4” and “6” throughout this text. The model features that

- the inter-fiber hardening is not present (no latent hardening is considered)
- the overall behavior is anisotropic multisurface plasticity
- the flow rule always ensures positive dissipation for each slip system.

A sample visualization of the strain-hardening model is provided in figure X. The sample data has been prepared the material parameters $g_0 = 15kPa$, $g_\infty = 45kPa$ and $h = 150kPa$. The model resolves into a no hardening model with g_∞ is being set to g_0, or a linear hardening model for proper estimates of h_0.

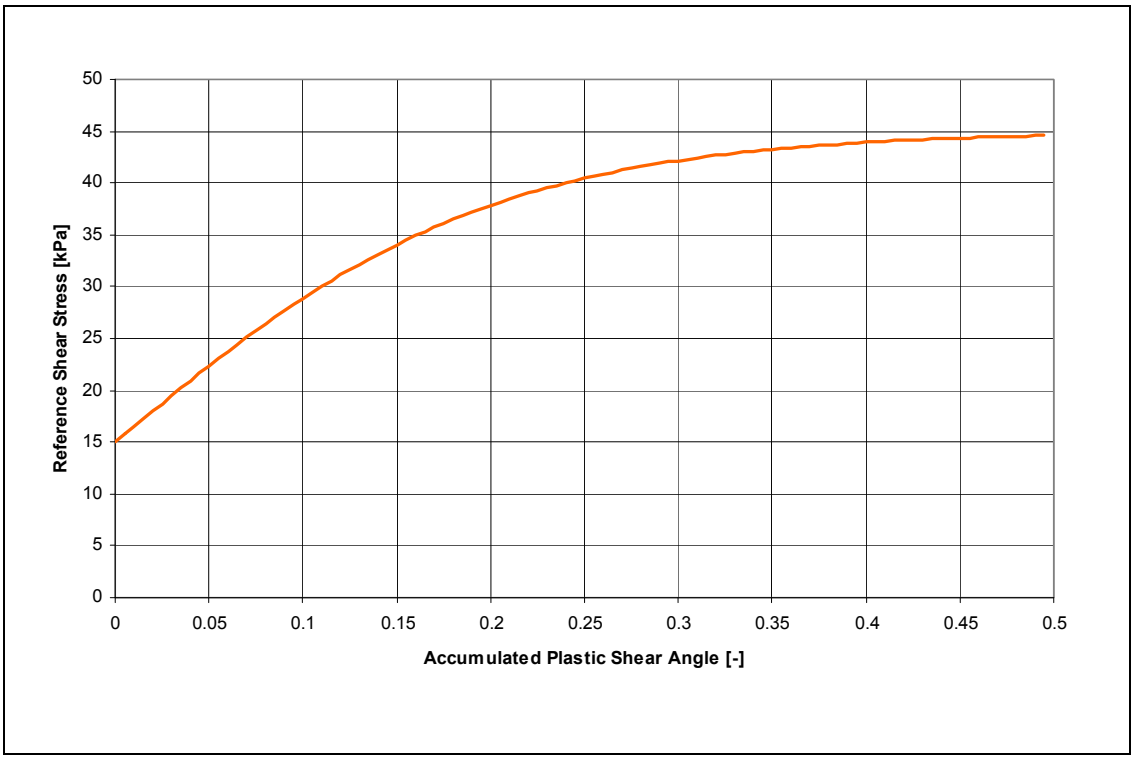

Figure 6.5 : Representative Behaviour of Selected Plastic Hardening Model

6.3.1. The Kinematics of Crystal Plasticity

In crystal plasticity, the relation between the overall deformation and the slip in each slip system is proposed in the form

$$\mathbf{L}_p = \sum_{\alpha} \dot{\gamma}_{\alpha} \left(\mathbf{m}_{\alpha} \otimes \mathbf{n}_{\alpha} \right) \tag{6-6}$$

where

$$\dot{\mathbf{F}}_p = \mathbf{L}_p \mathbf{F}_p \tag{6-7}$$

or

$$\mathbf{L}_p = \dot{\mathbf{F}}_p \left(\mathbf{F}_p \right)^{-1} \tag{6-8}$$

is the plastic velocity gradient, $\mathbf{F}_p$ is the deformation gradient due to plastic deformation, $\dot{\mathbf{F}}_p$ is its material time rate and the (-1) in the power standing for the inverse.

In rate-independent plasticity models, the expression (S) above should be accompanied by the Kuhn-Tucker consistency conditions, or its equivalent equality, but for rate-dependent model proposed above, there is no explicit need for such "conditions" as they are embedded in the accumulation of shear (rate).

The resolved shear stress on each fiber family, namely τ_α is calculated at the Eulerian configuration with respect to the plastic deformation. Thus, assuming the multiplicative decomposition

$$\mathbf{F} = (\mathbf{F}^*)\mathbf{F}_p \tag{6-9}$$

where $\mathbf{F}^*$ stands for any other deformation that follows over the configuration generated (fictive) plastic deformation. Letting $\boldsymbol{\Sigma}$ denote the Mandel Stress tensor is defined the resolved shear stress is defined as

$$\tau_\alpha = dev(\boldsymbol{\Sigma}) : (\mathbf{n}_\alpha \otimes \mathbf{m}_\alpha) \tag{6-10}$$

where $\mathbf{n}_\alpha$ is the fiber normal (slip normal) in the θZ plane and $\mathbf{m}_\alpha$ is the fiber direction (slip direction). It is worth to note that the slip directions should be updated with ongoing plastic deformation. Thus, the system is Eulerian with respect to plasticity in sense. Naming

$$\mathbf{S}_\alpha^0 = \mathbf{n}_\alpha \otimes \mathbf{m}_\alpha \tag{6-11}$$

as the initial slip directions in the material (before plastic deformation, in the reference configuration)

$$\mathbf{S}_\alpha^p = \mathbf{F}_p(\mathbf{n}_\alpha \otimes \mathbf{m}_\alpha)\mathbf{F}_p^T \tag{6-12}$$

$$\tau_\alpha = dev(\boldsymbol{\Sigma}) : \mathbf{S}_\alpha^p \tag{6-13}$$

reads. The similar thoughts can be applied to the velocity gradient, so

$$\mathbf{L}_p = \sum_\alpha \dot{\gamma}_\alpha \mathbf{S}_\alpha^p = \sum_\alpha \dot{\gamma}_\alpha \mathbf{F}_p(\mathbf{n}_\alpha \otimes \mathbf{m}_\alpha)\mathbf{F}_p^T \tag{6-14}$$

6.4. Numerical Approximation to Analytical Expressions:

The main problem with classical plasticity applications is that, most formulations require explicit formulation of the problem when analytical solutions are not obtainable and numerical calculations become a "must". However, within the proposed concept, there is the option of forming an implicit algorithm for updating the plastic deformations.

Recalling

$$\mathbf{L}_p = \dot{\mathbf{F}}_p \left(\mathbf{F}_p\right)^{-1} \tag{6-15}$$

and

$$\mathbf{L}_p = \sum_\alpha \dot{\gamma}_\alpha \mathbf{S}_\alpha^p = \sum_\alpha \dot{\gamma}_\alpha \mathbf{F}_p \left(\mathbf{m}_\alpha^0 \otimes \mathbf{n}_\alpha^0\right) \mathbf{F}_p{}^T \tag{6-16}$$

and letting the backward approximation

$$\dot{\mathbf{F}}_p = \frac{\left(\mathbf{F}_p\right)_n - \left(\mathbf{F}_p\right)_{n-1}}{\Delta t} \tag{6-17}$$

hold, where subscript "n" denotes the current time step, "n-1" denotes the previous time step. Thus, for the velocity gradient at the current time step,

$$\left(\mathbf{L}_p\right)_n = \frac{\left(\mathbf{F}_p\right)_n - \left(\mathbf{F}_p\right)_{n-1}}{\Delta t} \left(\mathbf{F}_p{}^{-1}\right)_n \tag{6-18}$$

is obtained. Then the following reads:

$$\left(\dot{\gamma}_\alpha\right)_n = \dot{a}\ \mathrm{sgn}\left(\left(\tau_\alpha\right)_n\right) \left[\frac{\left\|\left(\tau_\alpha\right)_n\right\|}{\left(g_\alpha\right)_n}\right]^k \tag{6-19}$$

$$\left(g_\alpha\right)_n = g_\infty + \left(g_\infty - g_0\right) \tanh\left(\frac{h_0}{g_\infty - g_0} \left[\left(\gamma_\alpha\right)_{n-1} + \Delta t \left(\dot{\gamma}_\alpha\right)_n\right]\right) \tag{6-20}$$

$$\left(\tau_\alpha\right)_n = dev\left(\mathbf{\Sigma}_n\right) : \left(\mathbf{F}_p\right)_n \left(\mathbf{m}_\alpha^0 \otimes \mathbf{n}_\alpha^0\right) \left(\mathbf{F}_p{}^T\right)_n \tag{6-21}$$

Combining

$$\frac{\left(\mathbf{F}_p\right)_n-\left(\mathbf{F}_p\right)_{n-1}}{\Delta t}\left(\mathbf{F}_p^{-1}\right)_n = \sum_\alpha \left\{ \dot{a}\,\mathrm{sgn}\left(\left(\tau_\alpha\right)_n\right)\left[\frac{\left|dev\left(\boldsymbol{\Sigma}_n\right):\left(\mathbf{F}_p\right)_n\left(\mathbf{m}_\alpha^0\otimes\mathbf{n}_\alpha^0\right)\left(\mathbf{F}_p^{\,T}\right)_n\right|}{g_\infty+\left(g_\infty-g_0\right)\tanh\left(\frac{h_0}{g_\infty-g_0}\left|\left(\gamma_\alpha\right)_{n-1}+\Delta t\left(\dot{\gamma}_\alpha\right)_n\right|\right)}\right]^k \right\}\left\{\left(\mathbf{F}_p\right)_n\left(\mathbf{m}_\alpha^0\otimes\mathbf{n}_\alpha^0\right)\left(\mathbf{F}_p^{\,T}\right)_n\right\} \tag{6-22}$$

is obtained. Rearranging the update equation

$$\frac{\left(\mathbf{F}_p\right)_n-\left(\mathbf{F}_p\right)_{n-1}}{\Delta t}\left(\mathbf{F}_p^{-1}\right)_n = \frac{\mathbf{I}-\left(\mathbf{F}_p\right)_{n-1}\left(\mathbf{F}_p^{-1}\right)_n}{\Delta t} \tag{6-23}$$

$$\mathbf{I}-\left(\mathbf{F}_p\right)_{n-1}\left(\mathbf{F}_p^{-1}\right)_n = \Delta t\sum_\alpha\left(\dot{\gamma}_\alpha\right)_n\left\{\left(\mathbf{F}_p\right)_n\left(\mathbf{m}_\alpha^0\otimes\mathbf{n}_\alpha^0\right)\left(\mathbf{F}_p^{\,T}\right)_n\right\}\ \text{(shortened)} \tag{6-24}$$

is obtained.

This equation is fully dependent on the current plastic deformation gradient $\left(\mathbf{F}_p\right)_n$, thus $\left(\dot{\gamma}_\alpha\right)_n$ and the previous *known* variables $\left(\mathbf{F}_p\right)_{n-1}$ and $\left(\gamma_\alpha\right)_{n-1}$. The formulation is obtained in a fully implicit manner, which is required for experimental data evaluation, where the time step Δt is prescribed to an extent which in general not as low as an explicit method would be able to handle, and for unconditional stability.

6.5. Addendum for Cylindrical Coordinates:

The expressions provided above hold exactly for any Cartesian coordinate system.

For cylindrical coordinates, some details should be made clear.

Let the plastic deformation gradient be

$$\mathbf{F}_p = \begin{bmatrix} \dfrac{\partial r}{\partial R} & 0 & 0 \\ 0 & \dfrac{r}{R} & r\phi \\ 0 & 0 & \lambda \end{bmatrix} \tag{6-25}$$

in physical terms. (Basis $(\mathbf{e}_r, \mathbf{e}_\theta, \mathbf{e}_z) \otimes (\mathbf{e}_R, \mathbf{e}_\Theta, \mathbf{e}_Z)$) Notice that the terminology of mapping is general and not related to that represented in Section 5.

Differentiating in the usual manner, for cylindrical coordinates does not hold since, $\dot{\mathbf{e}}_r = \dot{\theta}\mathbf{e}_\theta$ and $\dot{\mathbf{e}}_\theta = -\dot{\theta}\mathbf{e}_r$. Thus, tensor notation and curvilinear base vectors $(\mathbf{g}_r, \mathbf{g}_\theta, \mathbf{g}_z)$ should be used instead. Details can be found in [39] , but the important parts are summarized as follows.

Using the tensor derivative rules using Christoffel Symbols, it is obtained that

$$\dot{\mathbf{F}}_p = \begin{bmatrix} \frac{\partial \dot{r}}{\partial r}\frac{\partial r}{\partial R} & -\frac{r}{R}\dot{\phi}Z & r\phi\dot{\phi}Z \\ \frac{\partial r}{\partial R}\dot{\phi}Z & \frac{\dot{r}}{R} & \left(r\dot{\phi} + \dot{r}\phi\right) \\ 0 & 0 & \dot{\lambda} \end{bmatrix} \tag{6-26}$$

and

$$\mathbf{L}_p = \begin{bmatrix} \frac{\partial \dot{r}}{\partial r} & -\dot{\phi}Z & 0 \\ \dot{\phi}Z & \frac{\dot{r}}{r} & \left(r\dot{\phi} + \dot{r}\phi\right) \\ 0 & 0 & \frac{\dot{\lambda}}{\lambda} \end{bmatrix} \tag{6-27}$$

in physical terms (Basis $(\mathbf{e}_r, \mathbf{e}_\theta, \mathbf{e}_z) \otimes (\mathbf{e}_R, \mathbf{e}_\Theta, \mathbf{e}_Z)$).

Remembering equation **(6-16)** above, the flow rule proposed only relates $\frac{\dot{r}}{R}$, $\dot{\lambda}$ and $\left(r\dot{\phi} + \dot{r}\phi\right)$ terms from $\dot{\mathbf{F}}_p$ via $\mathbf{L}_p$ to plastic flow. But there is the problem with the term in $\mathbf{F}_p$ (and $\mathbf{L}_p$) that, $\frac{\partial z}{\partial \Theta}$ is not identically zero. It can be shown that, under the assumptions aforementioned, the deviator of unsymmetrical Mandel Stress tensor, in the most general case, can be given as

$$dev(\boldsymbol{\Sigma}) = \begin{bmatrix} \Sigma_{RR} & 0 & 0 \\ 0 & \Sigma_{\Theta\Theta} & \Sigma_{\Theta Z} \\ 0 & \Sigma_{Z\Theta} & \Sigma_{ZZ} \end{bmatrix} \tag{6-28}$$

Moreover, the shear strain velocity gradient is, explicitly

$$\dot{\gamma}_4 \left(\mathbf{F}_p\right)\left(\mathbf{n}_4^0 \otimes \mathbf{m}_4^0\right)\left(\mathbf{F}_p{}^T\right) + \dot{\gamma}_6 \left(\mathbf{F}_p\right)\left(\mathbf{n}_4^0 \otimes \mathbf{m}_4^0\right)\left(\mathbf{F}_p{}^T\right) = \begin{bmatrix} 0 & 0 & 0 \\ 0 & L_a & L_b \\ 0 & L_c & L_d \end{bmatrix}$$

where $L_b = 0$, $L_c = 0$ is only satisfied if the conditions

$$\dot{\gamma}_4 = -\dot{\gamma}_6 = \dot{\gamma} \tag{6-29}$$

$$\mathbf{F}_p(2,3) = 0 \tag{6-30}$$

is identically satisfied. Otherwise, non-axisymmetrical deformations (due to $\frac{\partial z}{\partial \Theta}$ terms that will arise from the expansion **(6-6)**) will arise enforcedly. Thus, for the $\frac{\partial z}{\partial \Theta}$ term to vanish, the only way is to prevent any shear loading within the scope of this study.

Considering the shear-loading case above, that bears a necessity for disturbing the axisymmetry assumption, which is one of the main underlying assumptions of the analytical formulation for data evaluation and performance testing of a material model that has been developed elastoplastic framework, there is no torsion in the axisymmetric tube model hereafter considered regarding plastic deformations. Under these circumstances, the governing system again gets independent of Z, and is solved accordingly.

It is worth to note that the aforementioned shear plasticity introduces warping in the cross section of the arterial tissue.

7. THE SOFTENING OF TISSUE AND THE "DAMAGE RULE"

Recalling Figure 2.5 in Section 2.2.3, which is a schematic of load-deformation curve for a circumferential strip of the media subjected to uniaxial cyclic loading and unloading. The pronounced stress softening is evident during the first few load cycles which diminishes with the number of load cycles, when the biological material is said to be 'pre-conditioned'

Now if one returns to the main dissipation inequality, that has been presented for pure viscoelastic behavior,

$$\mathbf{S} : \dot{\mathbf{E}} - \left(\frac{\partial \Psi}{\partial \boldsymbol{\Gamma}_e} : \dot{\boldsymbol{\Gamma}}_e + \frac{\partial \Psi}{\partial \mathbf{E}_v} : \dot{\mathbf{E}}_v + \frac{\partial \Psi}{\partial Q} : \dot{Q} \right) \geq 0 \qquad \textbf{(7-1)}$$

one can no more bother the aim of the parameter Q. For the case presented, Q is the measure of damage accumulated.

For damage to occur, loosely speaking, some springs should not be able to resist as much to the applied load onto as they should, getting extrapolated from their initial characteristics of constitutive behavior. This phenomenon can be incorporated into the proposed material model by letting the "evolving" part (the spring of the Kelvin element) of the material behave in some softening way. Thus, the accumulating deformation described by $\mathbf{E}_v$, or more preliminarily $\mathbf{F}_v$, will exhibit viscoelastic behavior with damage accumulation, or in other words "elastic softening".

Summing up all, it is postulated that there is damage associated with Ψ_v:

$$\Psi_v = (1 - Q)\Psi_v^{\infty} \qquad \textbf{(7-2)}$$

where Q stands for the damage accumulated in the model so far, and Q<1.

This formulation results in

$$\frac{\partial \Psi}{\partial Q} = \frac{\partial \Psi_v}{\partial Q} = \frac{\partial}{\partial Q}\left[(1-Q)\Psi_v^{\infty}\right] = -\Psi_v^{\infty} \tag{7-3}$$

This represents some sort of decoupled representation for damage. Following common practice in damage mechanics,(see, for example [44]) , a damage evolution surface is introduced:

$$s\left(\Psi_v^{\infty}, D\right) = -\Psi_v^{\infty} - D = \Psi_v^{\infty} + D = 0 \tag{7-4}$$

This recalls the evolution of the yield surface in plasticity. D is the measure of damage accumulated. Now, for increasing Ψ_v^{∞}, the damage accumulates if the (yield) surface is "touched". That, in mathematical terms, says

$$\dot{D} = \begin{Bmatrix} \dot{\Psi}_v^{\infty} \,@\left(s = \Psi_v^{\infty} + D = 0\right) \cup \left(\dot{\Psi}_v^{\infty} > 0\right) \\ 0 \,@\, Otherwise \end{Bmatrix} \tag{7-5}$$

This means that damage follows $\dot{\Psi}_v^{\infty}$ for $\dot{\Psi}_v^{\infty} > 0$ and otherwise nothing happens. Following [44], let

$$D = -\frac{1}{\delta}\ln\left(1 - \frac{Q}{Q_{\infty}}\right) \tag{7-6}$$

as the damage accumulation rule. This leads to

$$\dot{D} = \frac{\partial D}{\partial Q}\dot{Q} \tag{7-7}$$

and

$$\frac{1}{Q_{\infty}}\dot{D} = \frac{1}{\delta}\frac{\dot{Q}}{Q_{\infty} - Q} \tag{7-8}$$

which, after rearranging yields

$$Q = Q_{\infty}\left(1 - e^{-\delta D}\right) \tag{7-9}$$

In this model, δ and Q_∞ are the only material parameters, where Q_∞ denotes the maximum possible damage the material can bear, where δ signifies a "damage saturation" parameter.

Going back to the original evolution equation, one obtains, after re-arranging the formulation with respect to strain rate

$$\frac{\partial(1-Q)\Psi_v}{\partial \mathbf{E}_v} = (1-Q)\frac{\partial \Psi_v^\infty}{\partial \boldsymbol{\Gamma}_v} - \frac{\partial Q}{\partial \boldsymbol{\Gamma}_v}\Psi_v^\infty \tag{7-10}$$

and the equation of evolution **(7-1)** is refurbished to

$$\frac{1}{2}\left(\frac{\partial \Psi_e}{\partial \boldsymbol{\Gamma}_e}\mathbf{C}_e + \mathbf{C}_e\frac{\partial \Psi_e}{\partial \boldsymbol{\Gamma}_e}\right) - \mathbf{F}_v\left((1-Q)\frac{\partial \Psi_v^\infty}{\partial \boldsymbol{\Gamma}_v} - \frac{\partial Q}{\partial \boldsymbol{\Gamma}_v}\Psi_v^\infty + \frac{\partial \Phi}{\partial \dot{\mathbf{E}}_v}\right)\mathbf{F}_v^{\,T} = \mathbf{0} \tag{7-11}$$

and nothing else in the formulation is altered. Since one has $\dot{Q} \geq 0$ and $\Psi_v^\infty \geq 0$ always, this model satisfies the dissipation inequality. The remaining is to choose how to set the evolution equation for Q. It can be set such that it behaves like a von-Mises-like equivalent strain parameter per fiber direction. Thus,

$$D(t) = \max\left\{\left(I_\alpha^v - 1\right), D\left(t^-\right)\right\};\ D(0) = 0 \tag{7-12}$$

is a suitable evolution model. The stated model above

- is anisotropic and multi-criteria based
- does not incorporate latent effects within softening
- can easily be extended to include non-linearity in the damage evolution

Notice once more that, I_α^v is only related to the deformation of the Kelvin element. Altering the value of $\left(I_\alpha^v - \Delta\right)$ would result in different aspects. In a manner like

$$\left(I_\alpha^v - \Delta\right);\ \Delta > 1 \tag{7-13}$$

the damage accumulation is triggered only after some pre-deformation.

8. THE ELASTOPLASTIC FRAMEWORK FOR ARTERIAL TISSUE

It is of best practical importance to set again a 1-D layout of analogy for the visualization of material's behavior, as in Figure 8.1.

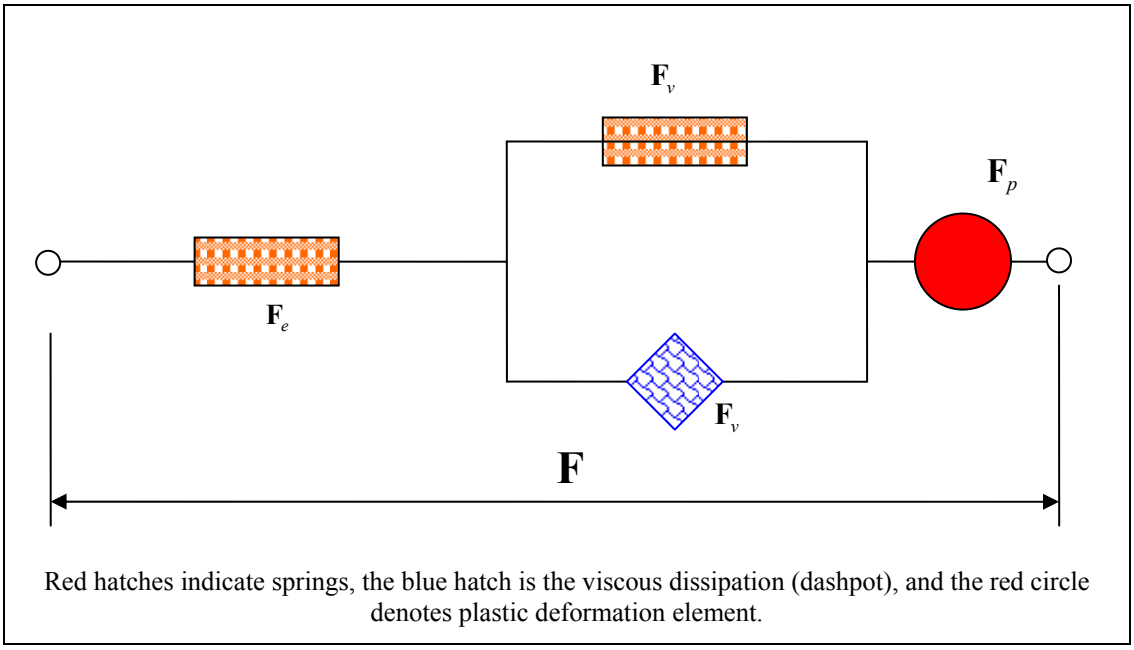

Figure 8.1 : The 1D Analogy to Elastoplastic Constitutive Model.

Applying the multiplicative decomposition again as it can be gathered from the figure, and one can write

$$\mathbf{F} = \mathbf{F}_e \mathbf{F}_v \mathbf{F}_p \tag{8-1}$$

where $\mathbf{F}_p$ denotes for the plastic deformations, $\mathbf{F}_v$ for viscoelastic properties and $\mathbf{F}_e$ for elastic components. Setting the dissipation inequality

$$\mathbf{S} : \dot{\mathbf{E}} - \dot{\psi} > 0 \tag{8-2}$$

and letting the time rate of strain energy

$$\dot{\psi} = \frac{\partial \psi_e}{\partial \boldsymbol{\Gamma}_e} : \dot{\boldsymbol{\Gamma}}_e + \left[(1-Q) \frac{\partial \psi_v}{\partial \boldsymbol{\Gamma}_v} - \frac{\partial Q}{\partial \boldsymbol{\Gamma}_v} \psi_v \right] : \dot{\boldsymbol{\Gamma}}_v + \frac{\partial \psi_p}{\partial \boldsymbol{\Gamma}_p} : \dot{\boldsymbol{\Gamma}}_p \tag{8-3}$$

along with

$$\mathbf{E} = \frac{1}{2}\left(\mathbf{F}^T\mathbf{F} - \mathbf{I}\right) \tag{8-4}$$

and its decomposition into components as

$$\mathbf{E} = \frac{1}{2}\left(\mathbf{F}_p{}^T\mathbf{F}_v{}^T\mathbf{F}_e{}^T\mathbf{F}_e\mathbf{F}_v\mathbf{F}_p - \mathbf{I}\right) \tag{8-5}$$

$$\mathbf{E} = \frac{1}{2}\left(\mathbf{F}_p{}^T\mathbf{F}_v{}^T\boldsymbol{\Gamma}_e\mathbf{F}_v\mathbf{F}_p + \mathbf{F}_p{}^T\boldsymbol{\Gamma}_v\mathbf{F}_p + \mathbf{E}_p\right) \tag{8-6}$$

with the rate defined as

$$\dot{\mathbf{E}} = \frac{1}{2}\frac{d}{dt}\left(\mathbf{F}^T\mathbf{F} - \mathbf{I}\right) \tag{8-7}$$

$$\dot{\mathbf{E}} = \begin{bmatrix} \mathbf{F}_p{}^T\mathbf{F}_v{}^T\dot{\boldsymbol{\Gamma}}_e\mathbf{F}_v\mathbf{F}_p + \mathbf{F}_p{}^T\dot{\boldsymbol{\Gamma}}_v\mathbf{F}_p + \dot{\mathbf{E}}_p \\ + \mathbf{F}_p{}^T\left(\mathbf{L}_p{}^T\mathbf{F}_v{}^T\boldsymbol{\Gamma}_e\mathbf{F}_v + \mathbf{F}_v{}^T\boldsymbol{\Gamma}_e\mathbf{F}_v\mathbf{L}_p\right)\mathbf{F}_p \\ + \mathbf{F}_p{}^T\mathbf{F}_v{}^T\left(\mathbf{L}_v{}^T\boldsymbol{\Gamma}_e + \boldsymbol{\Gamma}_e\mathbf{L}_v\right)\mathbf{F}_v\mathbf{F}_p \\ + \mathbf{F}_p{}^T\left(\mathbf{L}_p{}^T\boldsymbol{\Gamma}_v + \boldsymbol{\Gamma}_v\mathbf{L}_p\right)\mathbf{F}_p \end{bmatrix} \tag{8-8}$$

$$\dot{\mathbf{E}} = \begin{bmatrix} \mathbf{F}_p{}^T\mathbf{F}_v{}^T\dot{\boldsymbol{\Gamma}}_e\mathbf{F}_v\mathbf{F}_p + \mathbf{F}_p{}^T\dot{\boldsymbol{\Gamma}}_v\mathbf{F}_p + \dot{\mathbf{E}}_p \\ + \mathbf{F}_p{}^T\left(\mathbf{L}_p{}^T\left(\mathbf{F}_v{}^T\boldsymbol{\Gamma}_e\mathbf{F}_v + \boldsymbol{\Gamma}_v\right) + \left(\mathbf{F}_v{}^T\boldsymbol{\Gamma}_e\mathbf{F}_v + \boldsymbol{\Gamma}_v\right)\mathbf{L}_p\right)\mathbf{F}_p \\ + \mathbf{F}_p{}^T\mathbf{F}_v{}^T\left(\mathbf{L}_v{}^T\boldsymbol{\Gamma}_e + \boldsymbol{\Gamma}_e\mathbf{L}_v\right)\mathbf{F}_v\mathbf{F}_p \end{bmatrix} \tag{8-9}$$

incorporating

$$\dot{\boldsymbol{\Gamma}}_e = \mathbf{F}_e{}^T\mathbf{D}_e\mathbf{F}_e\,,\ \dot{\boldsymbol{\Gamma}}_v = \mathbf{F}_v{}^T\mathbf{D}_v\mathbf{F}_v\,,\ \dot{\mathbf{E}}_p = \mathbf{F}_p{}^T\mathbf{D}_p\mathbf{F}_p \tag{8-10}$$

finally reads initially as

$$tr\left\{\mathbf{S}\dot{\mathbf{E}}-\left[\mathbf{F}_e\frac{\partial\psi_e}{\partial\boldsymbol{\Gamma}_e}\mathbf{F}_e{}^T\mathbf{D}_e+\mathbf{F}_v\left[(1-Q)\frac{\partial\psi_v}{\partial\boldsymbol{\Gamma}_v}-\frac{\partial Q}{\partial\boldsymbol{\Gamma}_v}\psi_v\right]\mathbf{F}_v{}^T\mathbf{D}_v+\mathbf{F}_p\frac{\partial\psi_p}{\partial\boldsymbol{\Gamma}_p}\mathbf{F}_p{}^T\mathbf{D}_p\right]\right\} \quad \textbf{(8-11)}$$

and followed by

$$tr\left\{\begin{array}{l}\mathbf{S}\left[\begin{array}{l}\mathbf{F}_p{}^T\mathbf{F}_v{}^T\dot{\boldsymbol{\Gamma}}_e\mathbf{F}_v\mathbf{F}_p+\mathbf{F}_p{}^T\dot{\boldsymbol{\Gamma}}_v\mathbf{F}_p+\dot{\mathbf{E}}_p\\+\mathbf{F}_p{}^T\left(\mathbf{L}_p{}^T\left(\mathbf{F}_v{}^T\boldsymbol{\Gamma}_e\mathbf{F}_v+\boldsymbol{\Gamma}_v\right)+\left(\mathbf{F}_v{}^T\boldsymbol{\Gamma}_e\mathbf{F}_v+\boldsymbol{\Gamma}_v\right)\mathbf{L}_p\right)\mathbf{F}_p\\+\mathbf{F}_p{}^T\mathbf{F}_v{}^T\left(\mathbf{L}_v{}^T\boldsymbol{\Gamma}_e+\boldsymbol{\Gamma}_e\mathbf{L}_v\right)\mathbf{F}_v\mathbf{F}_p\end{array}\right]\\-\left[\mathbf{F}_e\frac{\partial\psi_e}{\partial\boldsymbol{\Gamma}_e}\mathbf{F}_e{}^T\mathbf{D}_e+\mathbf{F}_v\left[(1-Q)\frac{\partial\psi_v}{\partial\boldsymbol{\Gamma}_v}-\frac{\partial Q}{\partial\boldsymbol{\Gamma}_v}\psi_v\right]\mathbf{F}_v{}^T\mathbf{D}_v+\mathbf{F}_p\frac{\partial\psi_e}{\partial\boldsymbol{\Gamma}_p}\mathbf{F}_p{}^T\mathbf{D}_p\right]\end{array}\right\}\geq 0 \quad \textbf{(8-12)}$$

or more precisely

$$tr\left\{\begin{array}{l}\left[\begin{array}{l}\mathbf{F}_v\mathbf{F}_p\mathbf{S}\mathbf{F}_p{}^T\mathbf{F}_v{}^T\mathbf{F}_e{}^T\mathbf{D}_e\mathbf{F}_e+\mathbf{S}\mathbf{F}_p{}^T\mathbf{F}_v{}^T\mathbf{D}_v\mathbf{F}_v\mathbf{F}_p+\mathbf{S}\mathbf{F}_p{}^T\mathbf{D}_p\mathbf{F}_p\\+\mathbf{S}\mathbf{F}_p{}^T\left(\mathbf{L}_p{}^T\left(\mathbf{F}_v{}^T\boldsymbol{\Gamma}_e\mathbf{F}_v+\boldsymbol{\Gamma}_v\right)+\left(\mathbf{F}_v{}^T\boldsymbol{\Gamma}_e\mathbf{F}_v+\boldsymbol{\Gamma}_v\right)\mathbf{L}_p\right)\mathbf{F}_p\\+\mathbf{S}\mathbf{F}_p{}^T\mathbf{F}_v{}^T\left(\mathbf{L}_v{}^T\boldsymbol{\Gamma}_e+\boldsymbol{\Gamma}_e\mathbf{L}_v\right)\mathbf{F}_v\mathbf{F}_p\end{array}\right]\\-\left[\mathbf{F}_e\frac{\partial\psi_e}{\partial\boldsymbol{\Gamma}_e}\mathbf{F}_e{}^T\mathbf{D}_e+\mathbf{F}_v\left[(1-Q)\frac{\partial\psi_v}{\partial\boldsymbol{\Gamma}_v}-\frac{\partial Q}{\partial\boldsymbol{\Gamma}_v}\psi_v\right]\mathbf{F}_v{}^T\mathbf{D}_v+\mathbf{F}_p\frac{\partial\psi_e}{\partial\boldsymbol{\Gamma}_p}\mathbf{F}_p{}^T\mathbf{D}_p\right]\end{array}\right\}\geq 0 \quad \textbf{(8-13)}$$

as the main dissipation inequality. Knowing (postulating) that

$$\psi=\psi_e\left(\boldsymbol{\Gamma}_e\right)+\psi_v\left(\boldsymbol{\Gamma}_v\right) \quad \textbf{(8-14)}$$

only the plastic rate of stored energy diminishes, thus

$$\frac{\partial\psi}{\partial\boldsymbol{\Gamma}_p}=\frac{\partial\psi_p}{\partial\boldsymbol{\Gamma}_p}=0 \quad \textbf{(8-15)}$$

is obtained.

Following the spin-free configurations at intermediate steps to let the equations be of symmetric tensorial quantities as a kinematic constraint,

$$\boldsymbol{\Omega}_p=\mathbf{0},\ \boldsymbol{\Omega}_v=\mathbf{0} \quad \textbf{(8-16)}$$

is applied.

The steps follow in a fashionable manner:

$$tr\left\{\begin{array}{l}\left(\mathbf{F}_e\mathbf{F}_v\mathbf{F}_p\mathbf{S}\mathbf{F}_p{}^T\mathbf{F}_v{}^T\mathbf{F}_e{}^T-\mathbf{F}_e\frac{\partial\psi_e}{\partial\boldsymbol{\Gamma}_e}\mathbf{F}_e{}^T\right)\mathbf{D}_e\\+\left(\mathbf{F}_v\mathbf{F}_p\mathbf{S}\mathbf{F}_p{}^T\mathbf{F}_v{}^T-\mathbf{F}_v\left[(1-Q)\frac{\partial\psi_v}{\partial\boldsymbol{\Gamma}_v}-\frac{\partial Q}{\partial\boldsymbol{\Gamma}_v}\psi_v\right]\mathbf{F}_v{}^T\right)\mathbf{D}_v\\+\mathbf{F}_p\mathbf{S}\mathbf{F}_p{}^T\mathbf{D}_p+2\left(\mathbf{F}_v{}^T\boldsymbol{\Gamma}_e\mathbf{F}_v+\boldsymbol{\Gamma}_v\right)\mathbf{F}_p\mathbf{S}\mathbf{F}_p{}^T\left(\mathbf{L}_p{}^T\right)\\+2\boldsymbol{\Gamma}_e\mathbf{F}_v\mathbf{F}_p\mathbf{S}\mathbf{F}_p{}^T\mathbf{F}_v{}^T\left(\mathbf{L}_v{}^T\right)\end{array}\right\}\geq 0 \qquad \textbf{(8-17)}$$

$$tr\left\{\begin{array}{l}\left(\boldsymbol{\sigma}-\mathbf{F}_e\frac{\partial\psi_e}{\partial\boldsymbol{\Gamma}_e}\mathbf{F}_e{}^T\right)\mathbf{D}_e\\+\left(\left\{\left[2\boldsymbol{\Gamma}_e+\mathbf{I}\right]\mathbf{F}_v\mathbf{F}_p\mathbf{S}\mathbf{F}_p{}^T\mathbf{F}_v{}^T\right\}_{sym}-\mathbf{F}_v\left[(1-Q)\frac{\partial\psi_v}{\partial\boldsymbol{\Gamma}_v}-\frac{\partial Q}{\partial\boldsymbol{\Gamma}_v}\psi_v\right]\mathbf{F}_v{}^T\right)\mathbf{D}_v\\+\left\{\left[2\left(\mathbf{F}_v{}^T\boldsymbol{\Gamma}_e\mathbf{F}_v+\boldsymbol{\Gamma}_v\right)+\mathbf{I}\right]\mathbf{F}_p\mathbf{S}\mathbf{F}_p{}^T\right\}\mathbf{L}_p{}^T\end{array}\right\}\geq 0 \qquad \textbf{(8-18)}$$

These arrangements lead to the following quantities:

$$\boldsymbol{\sigma}=\mathbf{F}_e\frac{\partial\psi_e}{\partial\boldsymbol{\Gamma}_e}\mathbf{F}_e{}^T \qquad \textbf{(8-19)}$$

for the Cauchy Stress component, or its II. Piola – Kirchhoff equivalent

$$\mathbf{F}_v\mathbf{F}_p\mathbf{S}\mathbf{F}_p{}^T\mathbf{F}_v{}^T=\frac{\partial\psi_e}{\partial\boldsymbol{\Gamma}_e} \qquad \textbf{(8-20)}$$

$$\left\{\left[2\boldsymbol{\Gamma}_e+\mathbf{I}\right]\frac{\partial\psi_e}{\partial\boldsymbol{\Gamma}_e}\right\}_{sym}-\mathbf{F}_v\left[(1-Q)\frac{\partial\psi_v}{\partial\boldsymbol{\Gamma}_v}-\frac{\partial Q}{\partial\boldsymbol{\Gamma}_v}\psi_v\right]\mathbf{F}_v{}^T=\mathbf{F}_v\frac{\partial\Phi}{\partial\dot{\mathbf{E}}_v}\mathbf{F}_v{}^T \qquad \textbf{(8-21)}$$

for the equation of viscoelastic and damage evolution which is exactly similar in the sense of the pure viscoelastic model,

$$\frac{1}{2}\left(\frac{\partial\Psi_e}{\partial\boldsymbol{\Gamma}_e}\mathbf{C}_e+\mathbf{C}_e\frac{\partial\Psi_e}{\partial\boldsymbol{\Gamma}_e}\right)-\mathbf{F}_v\left(\frac{\partial\Psi_v}{\partial\mathbf{E}_v}+\frac{\partial\Phi}{\partial\dot{\mathbf{E}}_v}\right)\mathbf{F}_v{}^T=\mathbf{0} \qquad \textbf{(8-22)}$$

and will be adopted accordingly and

$$\left\{\left[2\left(\mathbf{F}_v^{\,T}\boldsymbol{\Gamma}_e\mathbf{F}_v+\boldsymbol{\Gamma}_v\right)+\mathbf{I}\right]\mathbf{F}_p\mathbf{S}\mathbf{F}_p^{\,T}\right\}:\mathbf{L}_p\geq 0 \qquad \textbf{(8-23)}$$

for the plastic dissipation inequality; or equivalently the form

$$\left\{\mathbf{F}_v^{\,T}\mathbf{C}_e\frac{\partial\psi_e}{\partial\boldsymbol{\Gamma}_e}\mathbf{F}_v^{\,-T}\right\}:\mathbf{L}_p\geq 0 \qquad \textbf{(8-24)}$$

which holds for the proposed material model implicitly, with the definition of the Mandel Stress tensor as

$$\boldsymbol{\Sigma}=\mathbf{F}_v^{\,T}\mathbf{C}_e\frac{\partial\psi_e}{\partial\boldsymbol{\Gamma}_e}\mathbf{F}_v^{\,-T} \qquad \textbf{(8-25)}$$

9. MODELING PRE-STRESS IN ARTERIAL TISSUE

9.1. Introduction

It is known that the arteries are prestressed structures. An illustrative laboratory work is given in Figure12.8.

The prestress is discovered as the dissected artery demonstrates a reduction in length and an axial cut at a point throughout a segment of dissected artery yields a “lune” shaped stress-free wall. These can be modeled as an axial pre-stretch and pre-bending of the stress-free arterial wall structure to form a closed circular arterial tube segment.

9.2. Application to Constitutive Framework

From a kinematics point of view, the prestress can be thought as an elastic pre-deformation, under which the damage-coupled viscoelastic load-driven behavior of the artery is accounted for. Thus, the multiplicative decomposition can further be developed to include prestress effects:

$$\mathbf{F} = \mathbf{F}_m \mathbf{F}_0 \mathbf{F}_v \mathbf{F}_p \tag{9-1}$$

where

$$\mathbf{F} = \mathbf{F}_e \mathbf{F}_v \mathbf{F}_p \tag{9-2}$$

also reads. Thus, within the model, the elastic strain is assumed to have two components:

- The prestrain component that is due to developing substructure of the tissue and is constant
- The mechanical strain due to external loads over the prestrain.

The 1D graphical analog of the model finally reads as

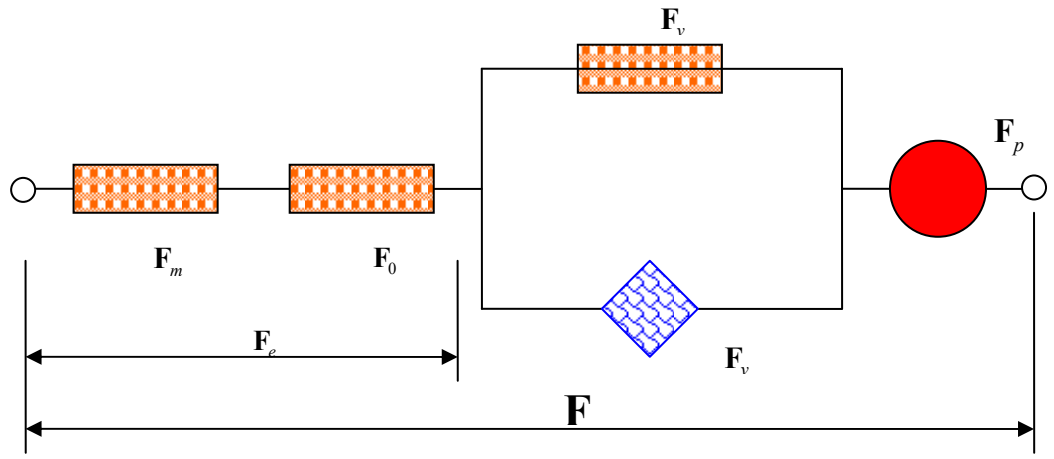

Red hatches indicate springs, the blue hatch is the viscous dissipation, and the red dot denotes plastic deformation element.

Figure 9.1 : The 1D Analogy of the Prestrained Viscoelastoplastic Model.

Here, the deformation tensor $\mathbf{F}_0$ is a measure of prestretch (and prestress relatively). Regarding what is stated as the assumptions of prestretch, the physical elements of the $\mathbf{F}_0$ deformation gradient tensor can be evaluated as

$$\mathbf{F}_0 = \begin{bmatrix} \dfrac{\partial R}{\partial R_0} & 0 & 0 \\ 0 & \dfrac{\pi}{\theta_0}\dfrac{R}{R_0} & 0 \\ 0 & 0 & \lambda_o \end{bmatrix} \tag{9-3}$$

where

$$R = R_0(R_0);\ \Theta = \frac{\pi}{\Theta_0};\ Z = \lambda_o Z_0 \tag{9-4}$$

are the coordinate transformations. Incompressibility is again assumed to hold, so that

$$\det[\mathbf{F}_0] = 1 \tag{9-5}$$

said to satisfy.

Regarding thermodynamics, and noticing that the time derivative of prestretch is zero

$$\dot{\mathbf{F}}_0 = 0 \tag{9-6}$$

the only effect of prestretch is on the stress values. With

Considering

$$\mathbf{S} : \dot{\mathbf{E}} - \dot{\psi} > 0 \tag{9-7}$$

and

$$\dot{\psi} = \frac{\partial \psi_e}{\partial \boldsymbol{\Gamma}_e} : \dot{\boldsymbol{\Gamma}}_e + \left[(1-Q) \frac{\partial \psi_v}{\partial \boldsymbol{\Gamma}_v} - \frac{\partial Q}{\partial \boldsymbol{\Gamma}_v} \psi_v \right] : \dot{\boldsymbol{\Gamma}}_v \tag{9-8}$$

Recalling the strain components of each deformation step relevant to our analysis as

$$\boldsymbol{\Gamma}_e = \frac{1}{2}\left(\mathbf{F}_e{}^T \mathbf{F}_e - \mathbf{I} \right) \tag{9-9}$$

$$\boldsymbol{\Gamma}_m = \frac{1}{2}\left(\mathbf{F}_m{}^T \mathbf{F}_m - \mathbf{I} \right) \tag{9-10}$$

$$\boldsymbol{\Gamma}_0 = \frac{1}{2}\left(\mathbf{F}_0{}^T \mathbf{F}_0 - \mathbf{I} \right) \tag{9-11}$$

where

$$\boldsymbol{\Gamma}_e = \frac{1}{2}\left((\mathbf{F}_m \mathbf{F}_0)^T (\mathbf{F}_m \mathbf{F}_0) - \mathbf{I} \right) \tag{9-12}$$

or, in another form

$$\boldsymbol{\Gamma}_e = \boldsymbol{\Gamma}_0 + \mathbf{F}_0{}^T \boldsymbol{\Gamma}_m \mathbf{F}_0 \tag{9-13}$$

holds.

The main question then degenerates into a form to decouple the total elastic response. From previous experience, it is clear that the decomposition of the elastic deformation content will only effect the terms related with $\frac{\partial \psi_e}{\partial \boldsymbol{\Gamma}_e}$.

The initiation of procedure can be given in the form of partial derivatives

$$\frac{\partial \psi_e}{\partial \boldsymbol{\Gamma}_e} : \dot{\boldsymbol{\Gamma}}_e = \frac{\partial \psi_e}{\partial \boldsymbol{\Gamma}_m} : \frac{\partial \boldsymbol{\Gamma}_m}{\partial \boldsymbol{\Gamma}_e} : \dot{\boldsymbol{\Gamma}}_e + \frac{\partial \psi_e}{\partial \boldsymbol{\Gamma}_0} : \frac{\partial \boldsymbol{\Gamma}_0}{\partial \boldsymbol{\Gamma}_e} : \dot{\boldsymbol{\Gamma}}_e \tag{9-14}$$

or in more detail

$$\frac{\partial \psi_e}{\partial \boldsymbol{\Gamma}_e} : \dot{\boldsymbol{\Gamma}}_e = \frac{\partial \psi_e}{\partial \boldsymbol{\Gamma}_m} : \frac{\partial \boldsymbol{\Gamma}_m}{\partial \boldsymbol{\Gamma}_e} : \dot{\boldsymbol{\Gamma}}_e + \frac{\partial \psi_e}{\partial \boldsymbol{\Gamma}_0} : \frac{\partial \boldsymbol{\Gamma}_0}{\partial \mathbf{F}_0} : \frac{\partial \mathbf{F}_0}{\partial \boldsymbol{\Gamma}_e} : \dot{\boldsymbol{\Gamma}}_e \tag{9-15}$$

The convective terms are $\frac{\partial \boldsymbol{\Gamma}_m}{\partial \boldsymbol{\Gamma}_e}$ and $\frac{\partial \boldsymbol{\Gamma}_0}{\partial \mathbf{F}_0} : \frac{\partial \mathbf{F}_0}{\partial \boldsymbol{\Gamma}_e}$. The treatment is as follows:

$$\frac{\partial \boldsymbol{\Gamma}_m}{\partial \boldsymbol{\Gamma}_e} = \frac{\partial \left(\mathbf{F}_0^{-T} \left(\boldsymbol{\Gamma}_e - \boldsymbol{\Gamma}_0 \right) \mathbf{F}_0^{-1} \right)_{ij}}{\partial \left(\boldsymbol{\Gamma}_e \right)_{ab}} = \left(\mathbf{F}_0^{-T} \right)_{ip} \left(\delta_{pa} \delta_{qb} \right) \left(\mathbf{F}_0^{-1} \right)_{qj} \tag{9-16}$$

Thus

$$\frac{\partial \psi_e}{\partial \boldsymbol{\Gamma}_m} : \frac{\partial \boldsymbol{\Gamma}_m}{\partial \boldsymbol{\Gamma}_e} : \dot{\boldsymbol{\Gamma}}_e = \left(\frac{\partial \psi_e}{\partial \boldsymbol{\Gamma}_m} \right)_{ij} \left(\mathbf{F}_0^{-T} \right)_{ip} \left(\delta_{pa} \delta_{qb} \right) \left(\mathbf{F}_0^{-1} \right)_{qj} \left(\dot{\boldsymbol{\Gamma}}_e \right)_{ab} = \left(\frac{\partial \psi_e}{\partial \boldsymbol{\Gamma}_m} \right)_{ij} \left(\mathbf{F}_0^{-T} \right)_{ia} \left(\mathbf{F}_0^{-1} \right)_{bj} \left(\dot{\boldsymbol{\Gamma}}_e \right)_{ab} \tag{9-17}$$

$$\frac{\partial \psi_e}{\partial \boldsymbol{\Gamma}_m} : \frac{\partial \boldsymbol{\Gamma}_m}{\partial \boldsymbol{\Gamma}_e} : \dot{\boldsymbol{\Gamma}}_e = \left(\mathbf{F}_0^{-1} \right)_{ai} \left(\frac{\partial \psi_e}{\partial \boldsymbol{\Gamma}_m} \right)_{ij} \left(\mathbf{F}_0^{-T} \right)_{jb} \left(\dot{\boldsymbol{\Gamma}}_e \right)_{ab} = \left(\mathbf{F}_0^{-1} \frac{\partial \psi_e}{\partial \boldsymbol{\Gamma}_m} \mathbf{F}_0^{-T} \right) : \dot{\boldsymbol{\Gamma}}_e \tag{9-18}$$

holds. The other term is $\frac{\partial \psi_e}{\partial \boldsymbol{\Gamma}_0} : \frac{\partial \boldsymbol{\Gamma}_0}{\partial \mathbf{F}_0} : \frac{\partial \mathbf{F}_0}{\partial \boldsymbol{\Gamma}_e} : \dot{\boldsymbol{\Gamma}}_e$ which can be denoted as a scalar

$$\frac{\partial \psi_e}{\partial \boldsymbol{\Gamma}_0} : \frac{\partial \boldsymbol{\Gamma}_0}{\partial \mathbf{F}_0} : \frac{\partial \mathbf{F}_0}{\partial \boldsymbol{\Gamma}_e} : \dot{\boldsymbol{\Gamma}}_e = \eta = \left(\frac{\partial \psi_e}{\partial \boldsymbol{\Gamma}_0} \right)_{ij} \frac{\partial \left(\boldsymbol{\Gamma}_0 \right)_{ij}}{\partial \left(\mathbf{F}_0 \right)_{mn}} \frac{\partial \left(\mathbf{F}_0 \right)_{mn}}{\partial \left(\boldsymbol{\Gamma}_e \right)_{ab}} \left(\dot{\boldsymbol{\Gamma}}_e \right)_{ab} \tag{9-19}$$

Thus, in index notation

$$\eta=\left(\frac{\partial\psi_e}{\partial\boldsymbol{\Gamma}_0}\right)_{ij}\frac{1}{2}\frac{\partial\left(\left(\mathbf{F}_0{}^T\right)_{ix}\left(\mathbf{F}_0\right)_{xj}-\delta_{ij}\right)}{\partial\left(\mathbf{F}_0\right)_{mn}}\frac{1}{\dfrac{\partial\left(\left(\mathbf{F}_0{}^T\right)_{ax}\left(\mathbf{F}_0\right)_{xb}-\delta_{ab}+\left(\mathbf{F}_0{}^T\right)_{ax}\left(\boldsymbol{\Gamma}_m\right)_{xy}\left(\mathbf{F}_0\right)_{yb}\right)}{\partial\left(\mathbf{F}_0\right)_{mn}}}\left(\dot{\boldsymbol{\Gamma}}_e\right)_{ab} \quad \textbf{(9-20)}$$

$$\eta=\frac{1}{2}\left(\frac{\partial\psi_e}{\partial\boldsymbol{\Gamma}_0}\right)_{ij}\frac{\left\{\left(\mathbf{F}_0{}^T\right)_{ix}\left(\delta_{mx}\delta_{nj}\right)+\left(\mathbf{F}_0\right)_{xj}\left(\delta_{mx}\delta_{ni}\right)\right\}}{\left(\mathbf{F}_0{}^T\right)_{ax}\left(\delta_{mx}\delta_{nb}\right)+\left(\mathbf{F}_0\right)_{xb}\left(\delta_{mx}\delta_{na}\right)+\left(\boldsymbol{\Gamma}_m\right)_{xy}\left\{\left(\mathbf{F}_0{}^T\right)_{ax}\left(\delta_{ym}\delta_{nb}\right)+\left(\mathbf{F}_0\right)_{xb}\left(\delta_{na}\delta_{mx}\right)\right\}}\left(\dot{\boldsymbol{\Gamma}}_e\right)_{ab} \quad \textbf{(9-21)}$$

$$\eta=\frac{1}{2}\left(\frac{\partial\psi_e}{\partial\boldsymbol{\Gamma}_0}\right)_{ij}\frac{\left\{\left(\mathbf{F}_0{}^T\right)_{im}\delta_{nj}+\left(\mathbf{F}_0\right)_{mj}\delta_{ni}\right\}}{\left(\mathbf{F}_0{}^T\right)_{am}\delta_{nb}+\left(\mathbf{F}_0\right)_{mb}\delta_{na}+2\left(\boldsymbol{\Gamma}_m\right)_{xm}\left(\mathbf{F}_0{}^T\right)_{ax}\delta_{nb}+2\left(\boldsymbol{\Gamma}_m\right)_{my}\left(\mathbf{F}_0\right)_{mb}\delta_{na}}\left(\dot{\boldsymbol{\Gamma}}_e\right)_{ab} \quad \textbf{(9-22)}$$

Getting rid of the denominator,

$$\left\{\delta_{na}\left(\left(\mathbf{F}_0\right)_{mb}+2\left(\boldsymbol{\Gamma}_m\right)_{my}\left(\mathbf{F}_0\right)_{mb}\right)+\delta_{nb}\left(2\left(\boldsymbol{\Gamma}_m\right)_{xm}\left(\mathbf{F}_0{}^T\right)_{ax}+\left(\mathbf{F}_0{}^T\right)_{am}\right)\right\}(\eta)=\left(\frac{\partial\psi_e}{\partial\boldsymbol{\Gamma}_0}\right)_{ij}\left\{\left(\mathbf{F}_0{}^T\right)_{im}\delta_{nj}+\left(\mathbf{F}_0\right)_{mj}\delta_{ni}\right\}\left(\dot{\boldsymbol{\Gamma}}_e\right)_{ab} \quad \textbf{(9-23)}$$

is obtained, after multiplication of both sides by δ_{na} which reads,

$$\left\{3\left(\left(\mathbf{F}_0\right)_{mb}+2\left(\boldsymbol{\Gamma}_m\right)_{my}\left(\mathbf{F}_0\right)_{mb}\right)+\left(2\left(\boldsymbol{\Gamma}_m\right)_{xm}\left(\mathbf{F}_0{}^T\right)_{bx}+\left(\mathbf{F}_0{}^T\right)_{bm}\right)\right\}(\eta)=\left(\frac{\partial\psi_e}{\partial\boldsymbol{\Gamma}_0}\right)_{ia}\left(\mathbf{F}_0{}^T\right)_{im}\left(\dot{\boldsymbol{\Gamma}}_e\right)_{ab}+\left(\frac{\partial\psi_e}{\partial\boldsymbol{\Gamma}_0}\right)_{aj}\left(\mathbf{F}_0\right)_{mj}\left(\dot{\boldsymbol{\Gamma}}_e\right)_{ab} \quad \textbf{(9-24)}$$

and more simplifies as follows:

$$\left\{3\left(\left(\mathbf{F}_0\right)_{mb}+2\left(\boldsymbol{\Gamma}_m\right)_{my}\left(\mathbf{F}_0\right)_{mb}\right)+\left(2\left(\boldsymbol{\Gamma}_m\right)_{xm}\left(\mathbf{F}_0{}^T\right)_{bx}+\left(\mathbf{F}_0{}^T\right)_{bm}\right)\right\}(\eta)=\left(\frac{\partial\psi_e}{\partial\boldsymbol{\Gamma}_0}\right)_{ia}\left(\mathbf{F}_0{}^T\right)_{im}\left(\dot{\boldsymbol{\Gamma}}_e\right)_{ab}+\left(\frac{\partial\psi_e}{\partial\boldsymbol{\Gamma}_0}\right)_{aj}\left(\mathbf{F}_0\right)_{mj}\left(\dot{\boldsymbol{\Gamma}}_e\right)_{ab} \quad \textbf{(9-25)}$$

$$\left\{4\left(\left(\mathbf{F}_0\right)_{mb}+2\left(\boldsymbol{\Gamma}_m\right)_{my}\left(\mathbf{F}_0\right)_{mb}\right)+\right\}(\eta)=\left(\mathbf{F}_0\right)_{mi}\left(\frac{\partial\psi_e}{\partial\boldsymbol{\Gamma}_0}\right)_{ia}\left(\dot{\boldsymbol{\Gamma}}_e\right)_{ab}+\left(\mathbf{F}_0\right)_{mj}\left(\frac{\partial\psi_e}{\partial\boldsymbol{\Gamma}_0}\right)_{ja}\left(\dot{\boldsymbol{\Gamma}}_e\right)_{ab}. \quad \textbf{(9-26)}$$

Returning to tensor form

$$\left\{4\left(\mathbf{I}+2\boldsymbol{\Gamma}_m\right)\mathbf{F}_0\right\}(\eta)=2\mathbf{F}_0\frac{\partial\psi_e}{\partial\boldsymbol{\Gamma}_0}\dot{\boldsymbol{\Gamma}}_e \quad \textbf{(9-27)}$$

and equivalently

$$\left\{\mathbf{C}_m\mathbf{F}_0\right\}\eta=\frac{1}{2}\mathbf{F}_0\frac{\partial\psi_e}{\partial\boldsymbol{\Gamma}_0}\dot{\boldsymbol{\Gamma}}_e \quad \textbf{(9-28)}$$

is accomplished. Forming $\{\mathbf{C}_m\mathbf{F}_0\}^{-1}$ and multiplying from left lets

$$\mathbf{I}\eta = \frac{1}{2}\mathbf{F}_0^{-1}\mathbf{C}_m^{-1}\mathbf{F}_0\frac{\partial\psi_e}{\partial\boldsymbol{\Gamma}_0}\dot{\boldsymbol{\Gamma}}_e \tag{9-29}$$

which can be "trace"d to yield

$$3\eta = \frac{1}{2}tr\left[\mathbf{F}_0^{-1}\mathbf{C}_m^{-1}\mathbf{F}_0\frac{\partial\psi_e}{\partial\boldsymbol{\Gamma}_0}\dot{\boldsymbol{\Gamma}}_e\right] \tag{9-30}$$

Consequently, the equivalent terms can be given as

$$\frac{\partial\psi_e}{\partial\boldsymbol{\Gamma}_0}:\frac{\partial\boldsymbol{\Gamma}_0}{\partial\mathbf{F}_0}:\frac{\partial\mathbf{F}_0}{\partial\boldsymbol{\Gamma}_e}:\dot{\boldsymbol{\Gamma}}_e = \frac{1}{6}\mathbf{F}_0^{-1}\mathbf{C}_m^{-1}\mathbf{F}_0\frac{\partial\psi_e}{\partial\boldsymbol{\Gamma}_0}:\dot{\boldsymbol{\Gamma}}_e \tag{9-31}$$

which, after summing up reads

$$\frac{\partial\psi_e}{\partial\boldsymbol{\Gamma}_e}:\dot{\boldsymbol{\Gamma}}_e = \left(\mathbf{F}_0^{-1}\frac{\partial\psi_e}{\partial\boldsymbol{\Gamma}_m}\mathbf{F}_0^{-T} + \frac{1}{6}\mathbf{F}_0^{-1}\mathbf{C}_m^{-1}\mathbf{F}_0\frac{\partial\psi_e}{\partial\boldsymbol{\Gamma}_0}\right):\dot{\boldsymbol{\Gamma}}_e \tag{9-32}$$

as the elastic rate of energy. Assuming an additive decomposition

$$\psi_e = \psi_0(\boldsymbol{\Gamma}_0) + \psi_m(\boldsymbol{\Gamma}_m) \tag{9-33}$$

a further reduction is possible which yields

$$\frac{\partial\psi_e}{\partial\boldsymbol{\Gamma}_e}:\dot{\boldsymbol{\Gamma}}_e = \left(\mathbf{F}_0^{-1}\frac{\partial\psi_m}{\partial\boldsymbol{\Gamma}_m}\mathbf{F}_0^{-T} + \frac{1}{6}\mathbf{F}_0^{-1}\mathbf{C}_m^{-1}\mathbf{F}_0\frac{\partial\psi_0}{\partial\boldsymbol{\Gamma}_0}\right):\dot{\boldsymbol{\Gamma}}_e \tag{9-34}$$

as the final form.

Letting $\mathbf{F}_0 = \mathbf{I}$ evidently recovers $\dfrac{\partial\psi}{\partial\boldsymbol{\Gamma}_0} = \mathbf{0}$, which lets $\mathbf{F}_m = \mathbf{F}_e$ and the original equations are recovered.

10. SUMMARY OF CONSIDERATIONS STATED

To sum up what has been stated by now, everything is in Table 10.1 – 10.3.

Table 10.1: The Equations of State

Constitutive Relations	$\Psi_e = C_1^e\left(I_1^e - 3\right) + \frac{C_2^e}{\alpha^e}\left[e^{\alpha^e\left(I_4^e - 1\right)^n} + e^{\alpha^e\left(I_6^e - 1\right)^n} - 2\right]$ $\Psi_v = C_1^v\left(I_1^v - 3\right) + \frac{C_2^v}{\alpha^v}\left[e^{\alpha^v\left(I_4^v - 1\right)^n} + e^{\alpha^v\left(I_6^v - 1\right)^n} - 2\right]$ $I_4 = \mathbf{M}_4^0 : \mathbf{C},\ I_6 = \mathbf{M}_6^0 : \mathbf{C}$
Dissipative Potential	(linear) $\Phi = \frac{1}{2}\eta_f\left(\dot{\gamma}_4{}^2 + \dot{\gamma}_6{}^2\right) + \frac{1}{2}\eta_{GS}\left[dev\left(\dot{\mathbf{E}}_v\right) : dev\left(\dot{\mathbf{E}}_v\right)\right]$ (exponential) $\Phi = \frac{1}{2}\frac{\eta_f}{\alpha_f}\left(e^{\alpha_f(\dot{\gamma}_4)^n} + e^{\alpha_f(\dot{\gamma}_6)^n} - 2\right) + \frac{1}{2}\eta_{GS}\left[dev\left(\dot{\mathbf{E}}_v\right) : dev\left(\dot{\mathbf{E}}_v\right)\right]$ $\dot{\gamma}_4 = \dot{\mathbf{E}}_v : \mathbf{D}_4^0,\ \dot{\gamma}_6 = \dot{\mathbf{E}}_v : \mathbf{D}_6^0$
Equation of Evolution for Damage-Coupled Viscoelasticity	$\left\{\left[2\boldsymbol{\Gamma}_e + \mathbf{I}\right]\frac{\partial \psi_e}{\partial \boldsymbol{\Gamma}_e}\right\}_{sym} - \mathbf{F}_v\left[\left(1 - Q\right)\frac{\partial \psi_v}{\partial \boldsymbol{\Gamma}_v} - \frac{\partial Q}{\partial \boldsymbol{\Gamma}_v}\psi_v\right]\mathbf{F}_v{}^T = \mathbf{F}_v\frac{\partial \Phi}{\partial \dot{\mathbf{E}}_v}\mathbf{F}_v{}^T$

Table 10.2: The Equations of Plasticity and Damage Evolution

Damage Accumulation Model	$Q = Q_\infty\left(1 - e^{-\frac{D}{\delta}}\right)$ $D(t) = \max\left\{\left(I_2^v - D_0\right), D\left(t^-\right)\right\};\ D(0) = 0;\ D_0 = 3$
Plastic Dissipation Inequality and the Mandel Stress Tensor	$\left\{\left[2\left(\mathbf{F}_v{}^T\boldsymbol{\Gamma}_e\mathbf{F}_v + \boldsymbol{\Gamma}_v\right) + \mathbf{I}\right]\mathbf{F}_p\mathbf{S}\mathbf{F}_p{}^T\right\}:\mathbf{L}_p \geq 0$ or $\left\{\mathbf{F}_v{}^T\left[\mathbf{C}_e\right]\frac{\partial\psi_e}{\partial\boldsymbol{\Gamma}_e}\mathbf{F}_v{}^{-T}\right\}:\mathbf{L}_p \geq 0$ Mandel Stress tensor: $\boldsymbol{\Sigma} = \mathbf{F}_v{}^T\mathbf{C}_e\frac{\partial\psi_e}{\partial\boldsymbol{\Gamma}_e}\mathbf{F}_v{}^{-T}$
Plastic Deformation Evolution Law	$\dot{\gamma}_\alpha = \dot{a}\ \mathrm{sgn}(\tau_\alpha)\left[\frac{\lVert\tau_\alpha\rVert}{g_\alpha}\right]^k,\ \gamma_\alpha = \int_0^t \dot{\gamma}_\alpha dt$ $\tau_\alpha = dev(\boldsymbol{\Sigma}):\left(\mathbf{n}_\alpha \otimes \mathbf{m}_\alpha\right)$ $g_\alpha = g_0 + \left(g_\infty - g_0\right)\tanh\left(\frac{h_0}{g_\infty - g_0}\gamma_\alpha\right)$ $\mathbf{L}_p = \sum_\alpha \dot{\gamma}_\alpha\left(\mathbf{n}_\alpha \otimes \mathbf{m}_\alpha\right)$
Prestress on Arterial Tissue	$\frac{\partial\psi_e}{\partial\boldsymbol{\Gamma}_e} = \mathbf{F}_0{}^{-1}\frac{\partial\psi_m}{\partial\boldsymbol{\Gamma}_m}\mathbf{F}_0{}^{-T} + \frac{1}{6}\mathbf{F}_0{}^{-1}\mathbf{C}_m{}^{-1}\mathbf{F}_0\frac{\partial\psi_0}{\partial\boldsymbol{\Gamma}_0}$ with $\boldsymbol{\Gamma}_e = \boldsymbol{\Gamma}_0 + \mathbf{F}_0{}^T\boldsymbol{\Gamma}_m\mathbf{F}_0$ (total elastic strain = prestrain + mechanical strain)

Table 10.3: Physical and Derived Quantities

Load/ Deformation Relations	$P_i = \int_a^b (\sigma_{\theta\theta} - \sigma_{rr}) \frac{1}{r} dr$ $N = \pi \left[\left(a^2 - R_T^{\,2} \right) P_i + \int_a^b (2\sigma_{zz} - \sigma_{\theta\theta} - \sigma_{rr}) r dr \right]$ $M_b = 2\pi \int_a^b \sigma_{z\theta} r^2 dr$
Incompressibility Considerations	$p(r) = (2\Gamma_{\rho\rho} + 1) \frac{\partial \psi_e}{\partial \Gamma_{\rho\rho}} + P_i - \int_a^r (\sigma_{\theta\theta} - \sigma_{rr}) \frac{1}{r} dr$

Thus the system can be solved for

- the material parameters running an optimization process
- for applied loads to obtain deformation states

for the system given above.

11. SOME SOLUTIONS TO PROPOSED MATERIAL MODEL

In this section, some (forward) solutions have been presented to the combined axisymmetric loading of a cylindrical uniform tube, using

- the material models that have been presented in the previous sections
- approximate representative material parameters
- predefined combinations of internal pressure, axial force and torsional moment
- different static and dynamic loading scenarios

to have an insight about how the model behaves (the tube deforms) under various assumptions and to validate if the behavior is compatible with expectations and solid mechanics.

11.1. Analysis without Plastic Deformations

11.1.1. Pure Elasticity

Table 11.1: Material Properties Used for Pure Elasticity Material Model Analysis in Section 11.1.1

Elastic ψ	C_1^e [kPa]	C_2^e [kPa]	α^e [-]		
	23.243	6.627	3.894		
Viscous ψ	C_1^v [kPa]	C_2^v [kPa]	α^v [-]		
	23.243	6.627	3.894		
Dissipation Φ	η_{GS} [kPa]	η_f [kPa]	α^f [-]		
	0.005	0.0	0.0		
Damage Q	Q_∞ [-]	δ [-]			
	0.0	0.0			
Plasticity	$\dot{a}$ [1/s]	g_0 [kPa]	g_∞ [kPa]	h_0 [kPa]	k [-]
	0.0	1400	4400	150	10

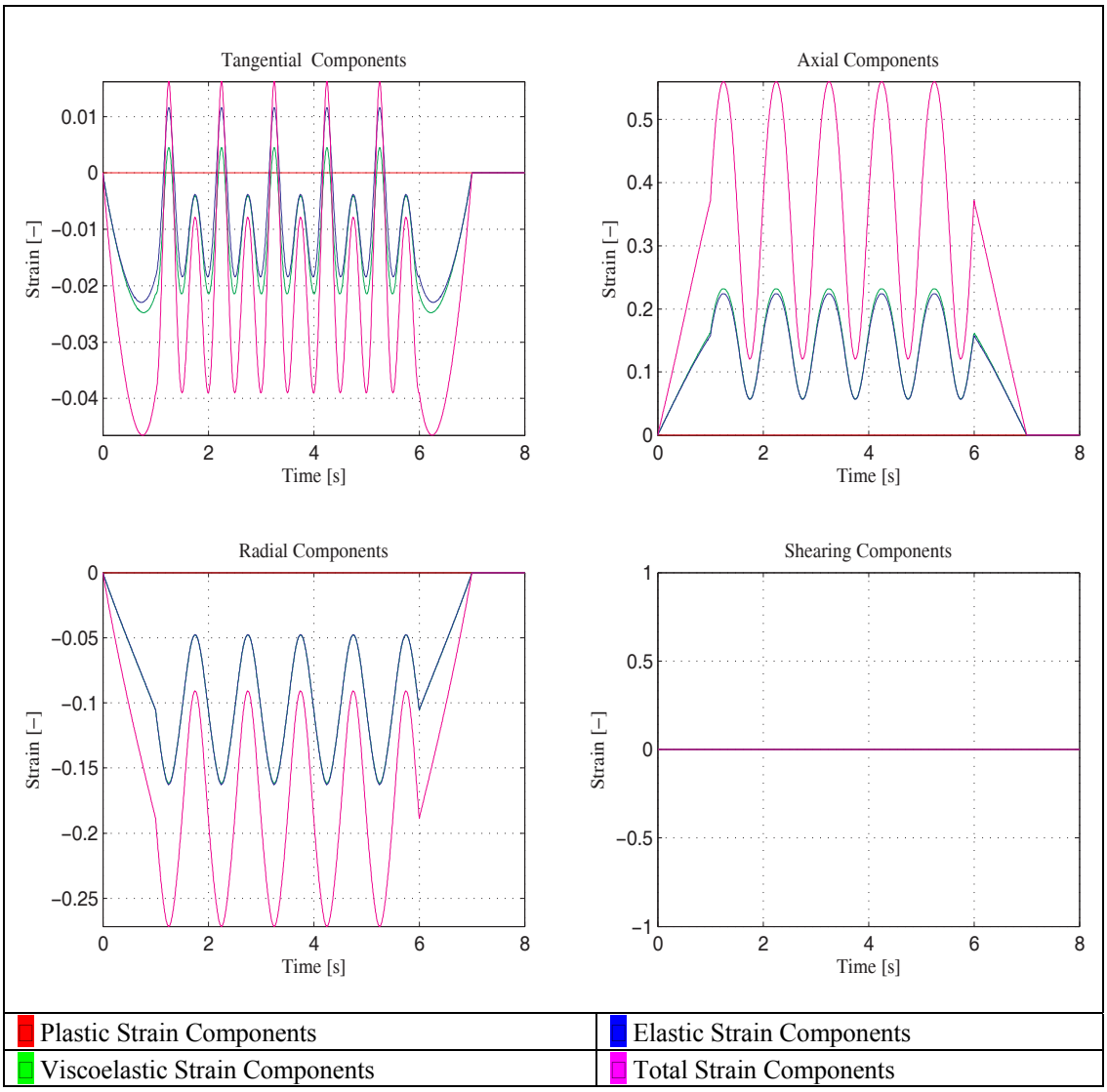

Figure 11.1 : Pure Elastic Strain vs. Time Graphs under Cyclic Loading at 1Hz

Initially, pure elastic loading has been considered. Under no torsional load, the pressure and the axial force has been made to fluctuate at 1 Hz. The figures 11.1-11.3 and A-1.1 to A-1.6 provide the loading protocols, the load-strain diagrams and the strains on the outer surface and variation of various quantities with time and within the wall thickness. The material properties for the analysis are provided in Table 11.1

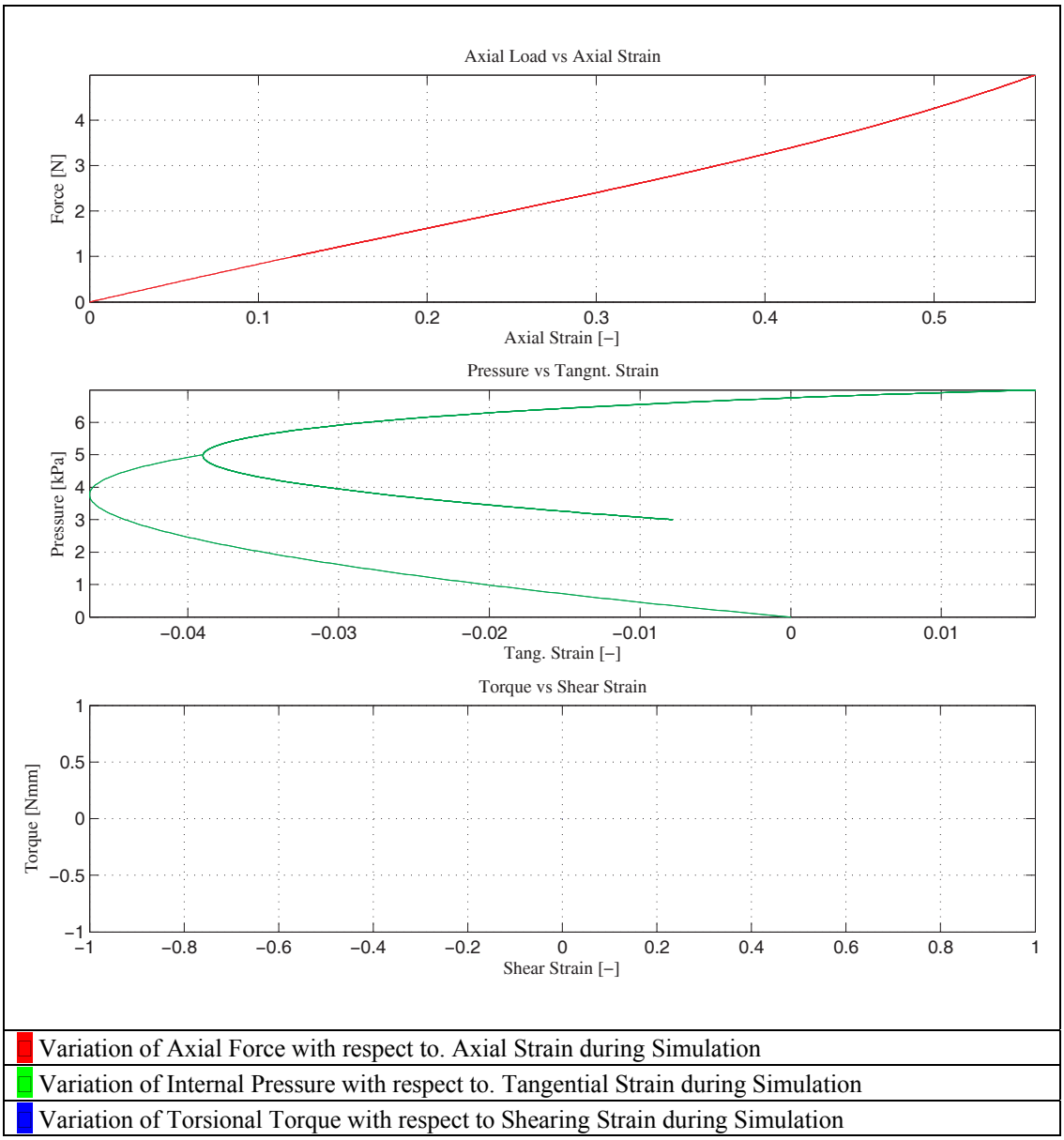

Figure 11.2 : Pure Elastic Strain vs. Load Graphs under Cyclic Loading at 1Hz

As expected from a thick-walled tube theory, and in parallel with the theoretical underpinnings that have been stated so far, the radial distribution of axial stress without the existence of shear is uniform, whereas tangential stress varies highly within the wall thickness; being highest in the inner surface. Also, it can be captured that the radial stress variation is in complete accordance with the theory, always zero on the outer surface and negative of the internal pressure at the inner surface. Thus, thin walled approximations to arterial modeling can be concluded to be regarded as over-simplifications to investigating issues that are related to quantities of "inner" type such as stress and plastic deformations.

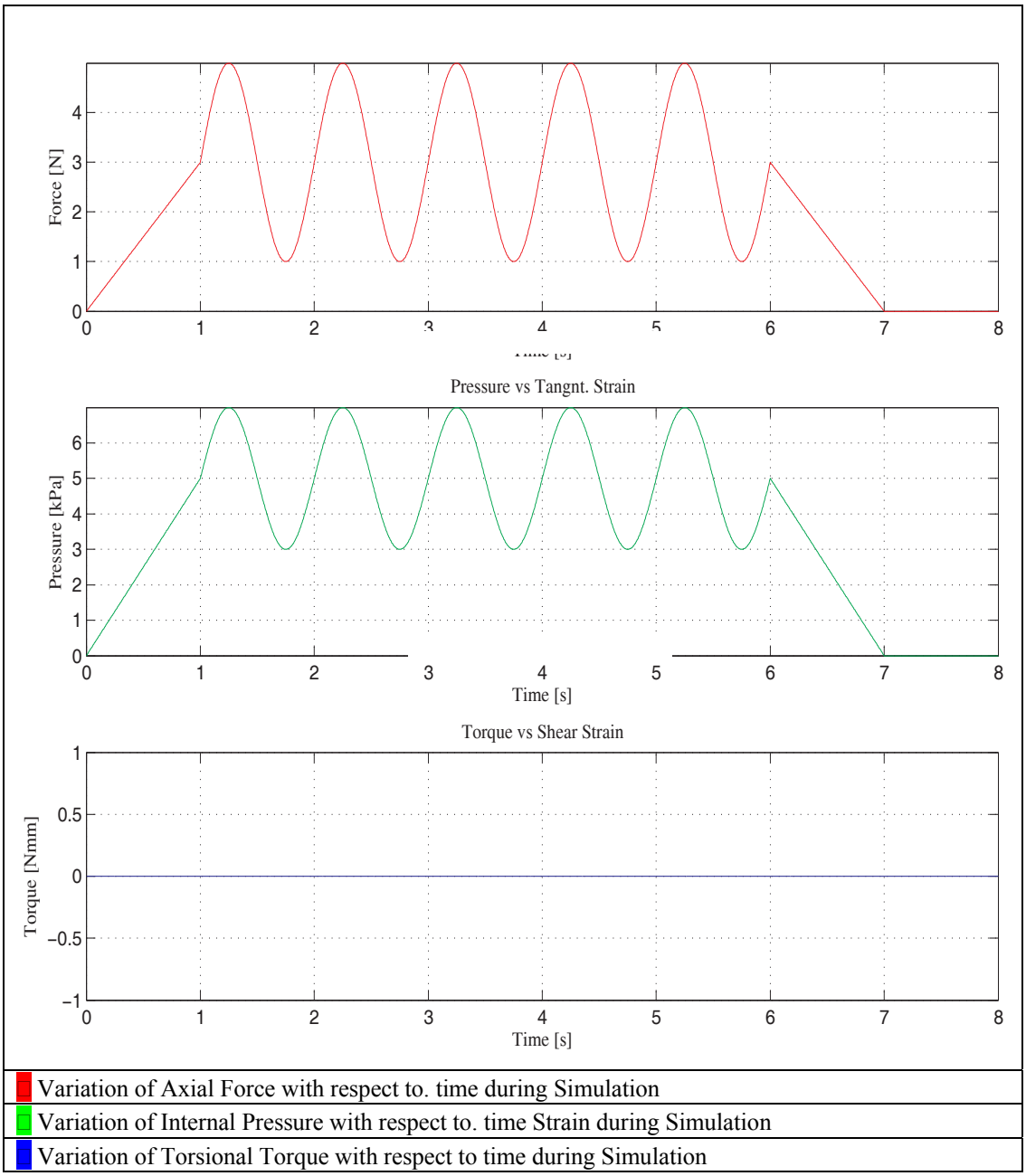

Figure 11.3 : Pure Elastic Load vs. Time Graphs under Cyclic Loading at 1Hz

11.1.2. Pure Elasticity with Softening

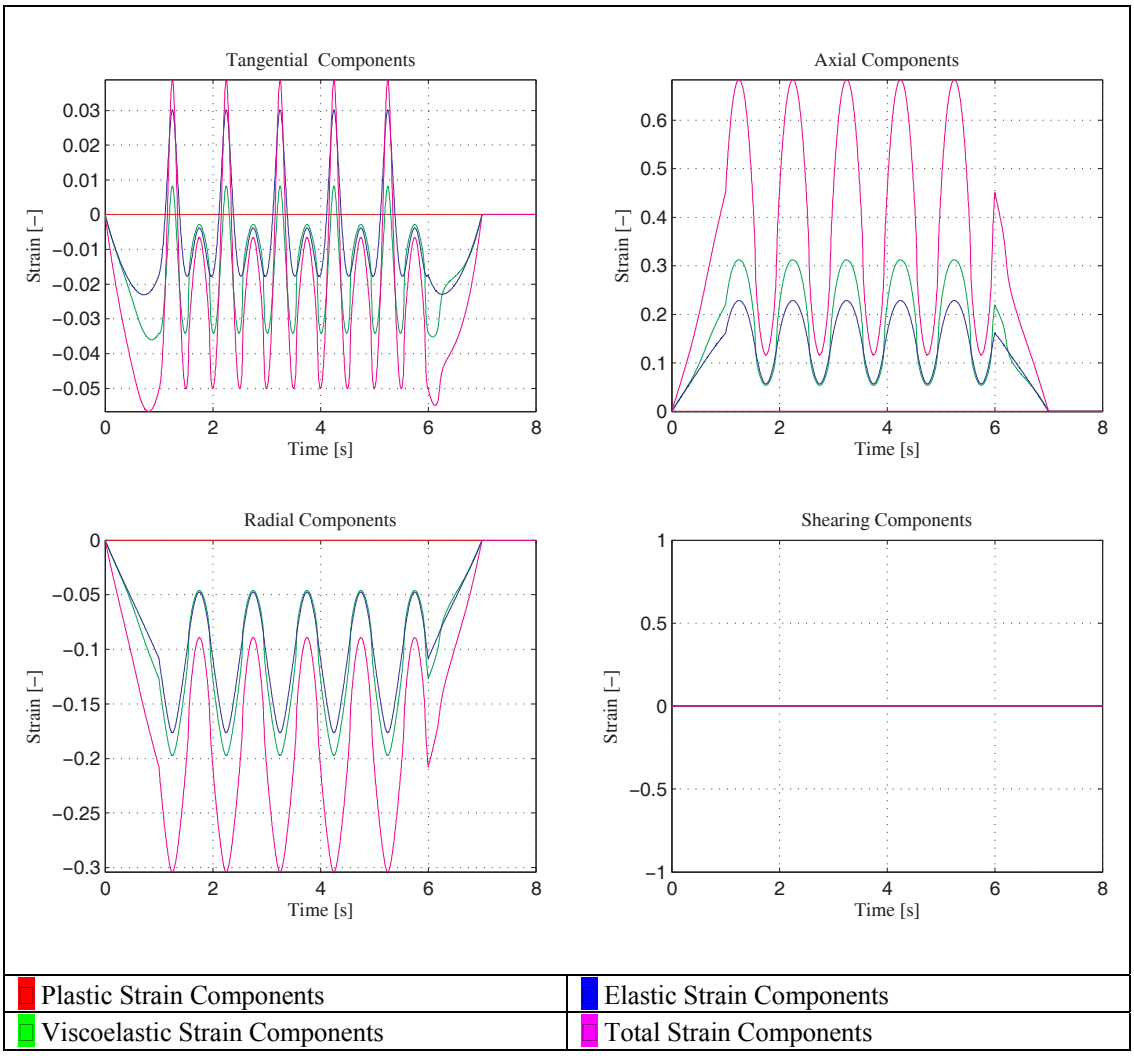

Figure 11.4 : Strain vs. Time Graphs under Cyclic Loading at 1Hz under Pure Elasticity with Softening Effects

Second model is exactly similar to the pure elasticity model, but there is the softening effect included. It is captured that the stress values record about 17% and 7% higer in the tangential and axial directions respectively. The load-deformation baths are also altered. No dissipation is observed, despite the fact that under biaxial loading conditions, the load-deformation paths exhibit a transient loop. Figures 11.4 – 11.6 and A-2.1 to A-1.6 represent the relevant quantities and their variations within the wall thickness and with time. The material properties for the analysis are provided in Table 11.2.

Table 11.2: Material Properties Used for Pure Elasticity with Softening Effect in Section 11.1.2

Elastic ψ	C_1^e [kPa]	C_2^e [kPa]	α^e [-]		
	23.243	6.627	3.894		
Viscous ψ	C_1^v [kPa]	C_2^v [kPa]	α^v [-]		
	23.243	6.627	3.894		
Dissipation Φ	η_{GS} [kPa]	η_f [kPa]	α^f [-]		
	0.005	0.0	0.0		
Damage Q	Q_∞ [-]	δ [-]			
	0.0	0.0			
Plasticity	$\dot{a}$ [1/s]	g_0 [kPa]	g_∞ [kPa]	h_0 [kPa]	k [-]
	0.0	1400	4400	150	10

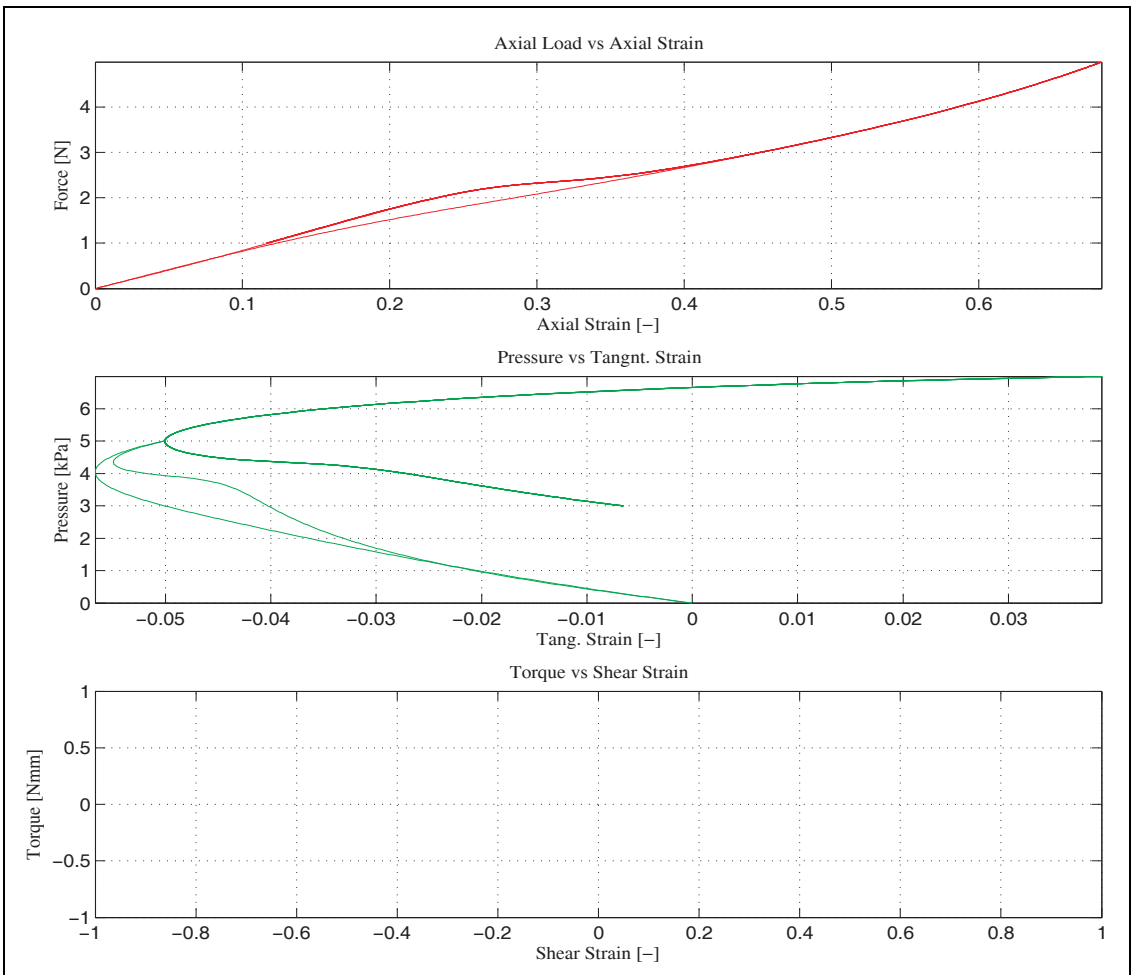

Variation of Axial Force with respect to. Axial Strain during Simulation

Variation of Internal Pressure with respect to. Tangential Strain during Simulation

Variation of Torsional Torque with respect to Shearing Strain during Simulation

Figure 11.5 : Strain vs. Load Graphs under Cyclic Loading at 1Hz under Pure Elasticity with Softening Effect

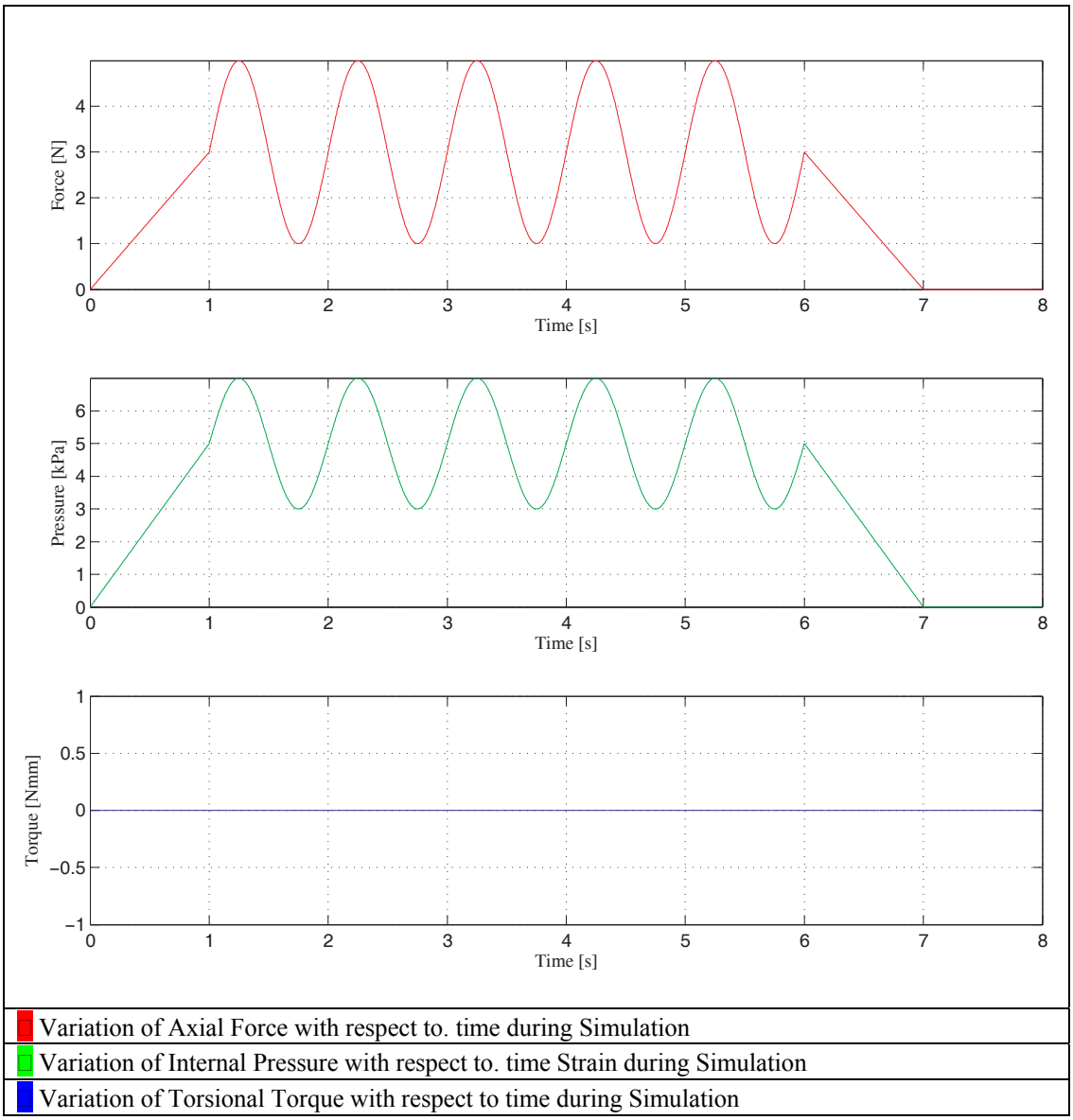

Variation of Axial Force with respect to. time during Simulation

Variation of Internal Pressure with respect to. time Strain during Simulation

Variation of Torsional Torque with respect to time during Simulation

Figure 11.6 : Load vs. Time Graphs under Cyclic Loading at 1Hz under Pure Elasticity with Softening Effect

11.1.3. Isotropic Viscoelasticity

The investigation of effects of occurrence dissipation has been achieved with this model. It has been checked whether the expected lag and load-strain curves are achieved, which are well-known for materials with dissipative characteristics. No softening has been considered. The dissipation has been assumed to rise due to rate-dependency effects only due to the isotropic content of the material (modeled) (i.e., due to dissipative effects within the base material).

Table 11.3: Material Properties Used for Isotropic Viscoelasticity Model Analysis in Section 11.1.3

Elastic ψ	C_1^e [kPa]	C_2^e [kPa]	α^e [-]		
	23.243	6.627	3.894		
Viscous ψ	C_1^v [kPa]	C_2^v [kPa]	α^v [-]		
	23.243	6.627	3.894		
Dissipation Φ	η_{GS} [kPa]	η_f [kPa]	α^f [-]		
	10.005	0.0	0.0		
Damage Q	Q_∞ [-]	δ [-]			
	0.0	0.0			
Plasticity	$\dot{a}$ [1/s]	g_0 [kPa]	g_∞ [kPa]	h_0 [kPa]	k [-]
	0.0	1400	4400	150	10

It is of considerable importance to denote that the stress distribution is again follows a thick-walled approach especially in the tangential direction; and the viscous effects have the impact over axial stress values. The tangential stress values, in contrary, seem to decrease. Figures 11.7 – 11.9 and A-3.1 to A-3.6 represent the relevant quantities and their variations within the wall thickness and with time. The material properties for the analysis are provided in Table 11.3.

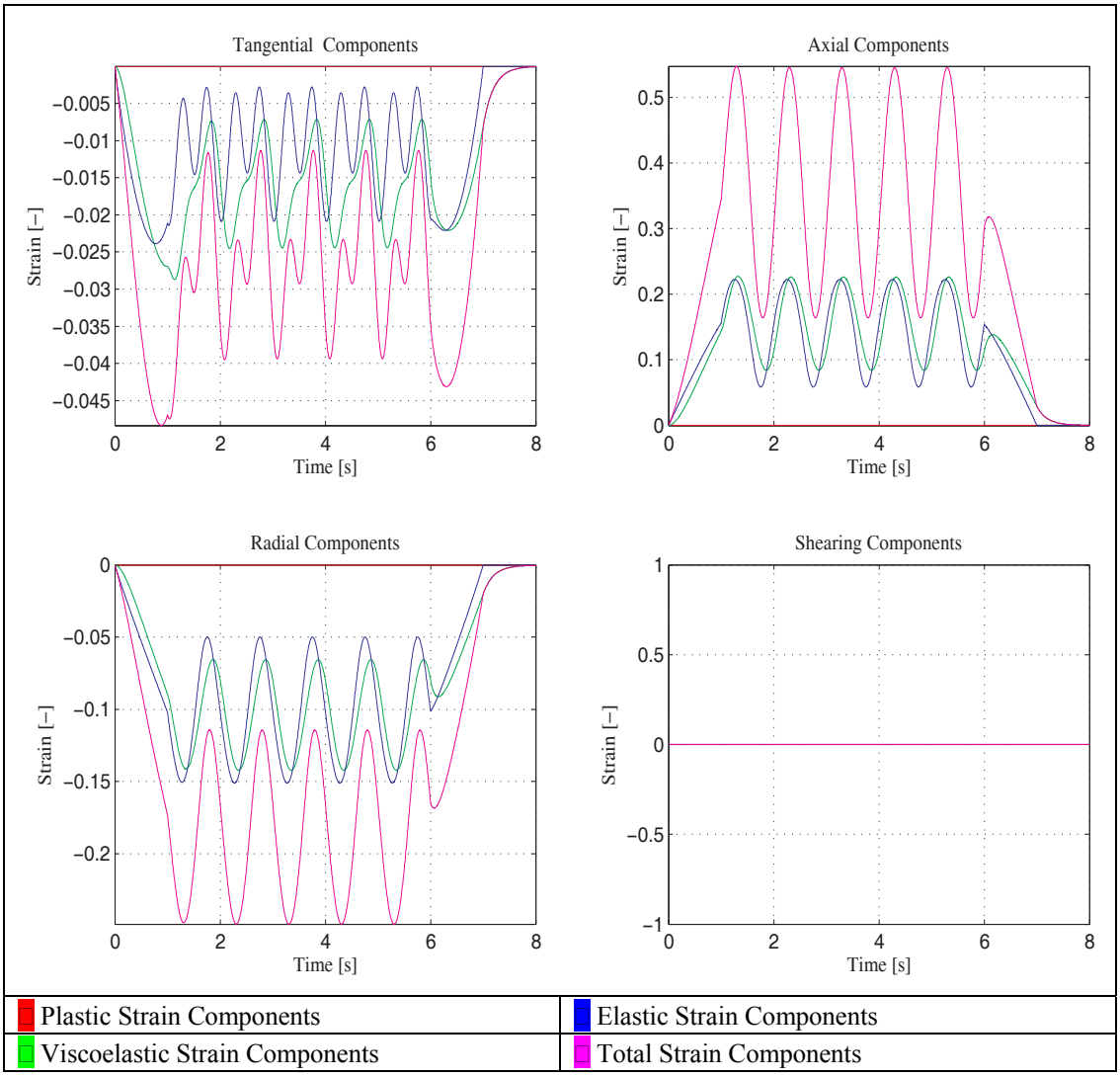

Figure 11.7 : Strain vs. Time Graphs under Cyclic Loading at 1Hz under Isotropic Viscoelasticity

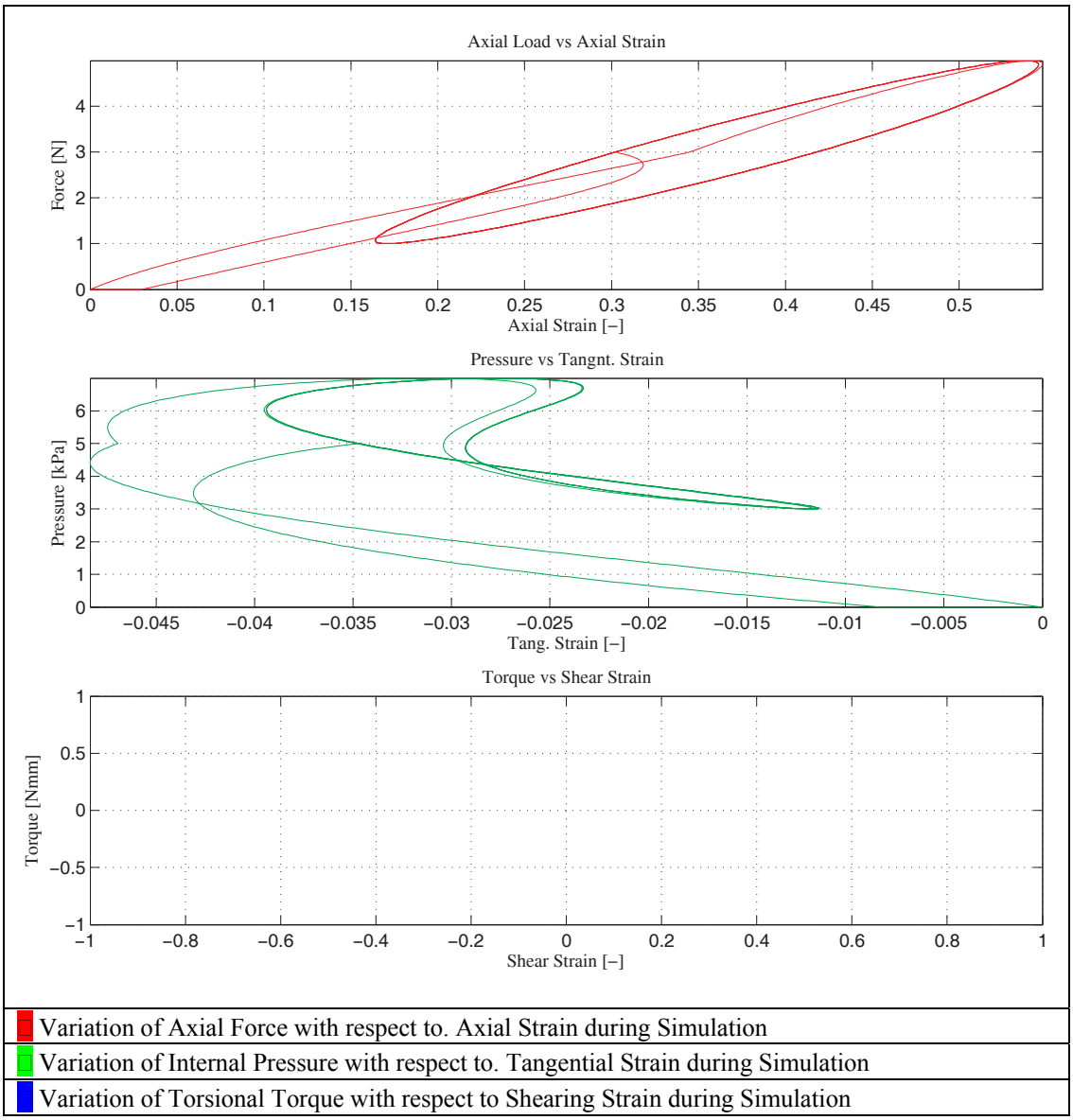

Variation of Axial Force with respect to. Axial Strain during Simulation
Variation of Internal Pressure with respect to. Tangential Strain during Simulation
Variation of Torsional Torque with respect to Shearing Strain during Simulation

Figure 11.8 : Strain vs. Load Graphs under Cyclic Loading at 1Hz under Isotropic Viscoelasticity

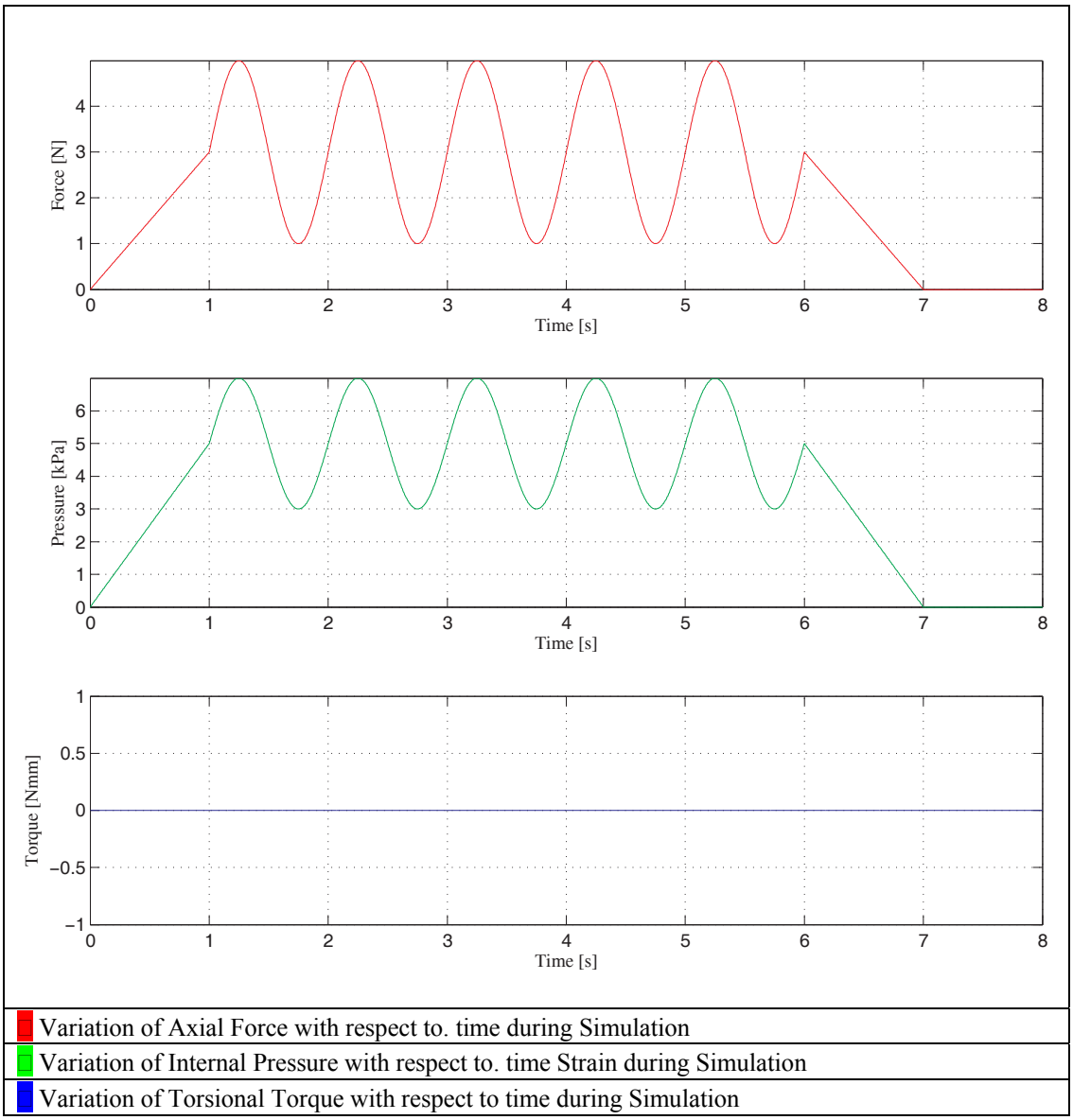

Variation of Axial Force with respect to. time during Simulation

Variation of Internal Pressure with respect to. time Strain during Simulation

Variation of Torsional Torque with respect to time during Simulation

Figure 11.9 : Load vs. Time Graphs under Cyclic Loading at 1Hz under Isotropic Viscoelasticity

11.1.4. Nonlinear Viscoelasticity

Contrary to the isotropic dissipation model, a low-effect anisotropic dissipation model has been implemented. It has been seen that the fiber-direction dissipative effects contribute to the behavior of the model in a compatible way with the isotropic dissipation model.

The material properties for the analysis are provided in Table 11.4.

Table 11.4: Material Properties Used for Nonlinear Viscoelasticity Analysis in Section 11.1.4

Elastic ψ	C_1^e [kPa]	C_2^e [kPa]	α^e [-]		
	23.243	6.627	3.894		
Viscous ψ	C_1^v [kPa]	C_2^v [kPa]	α^v [-]		
	23.243	6.627	3.894		
Dissipation Φ	η_{GS} [kPa]	η_f [kPa]	α^f [-]		
	0.005	3.0	0.09		
Damage Q	Q_∞ [-]	δ [-]			
	0.0	0.0			
Plasticity	$\dot{a}$ [1/s]	g_0 [kPa]	g_∞ [kPa]	h_0 [kPa]	k [-]
	0.0	1400	4400	150	10

Notice the slight difference in pressure-tangentail strain curve. Aslo, the material behavior, as expected, exhibits a steady loop for the load-deformation curves, indicating the dissipative behavior.

Figures 11.10 – 11.12 and A-4.1 to A-4.6 demonstrate the characteristics of behavior of the model proposed with non-linear viscoelastic effects.

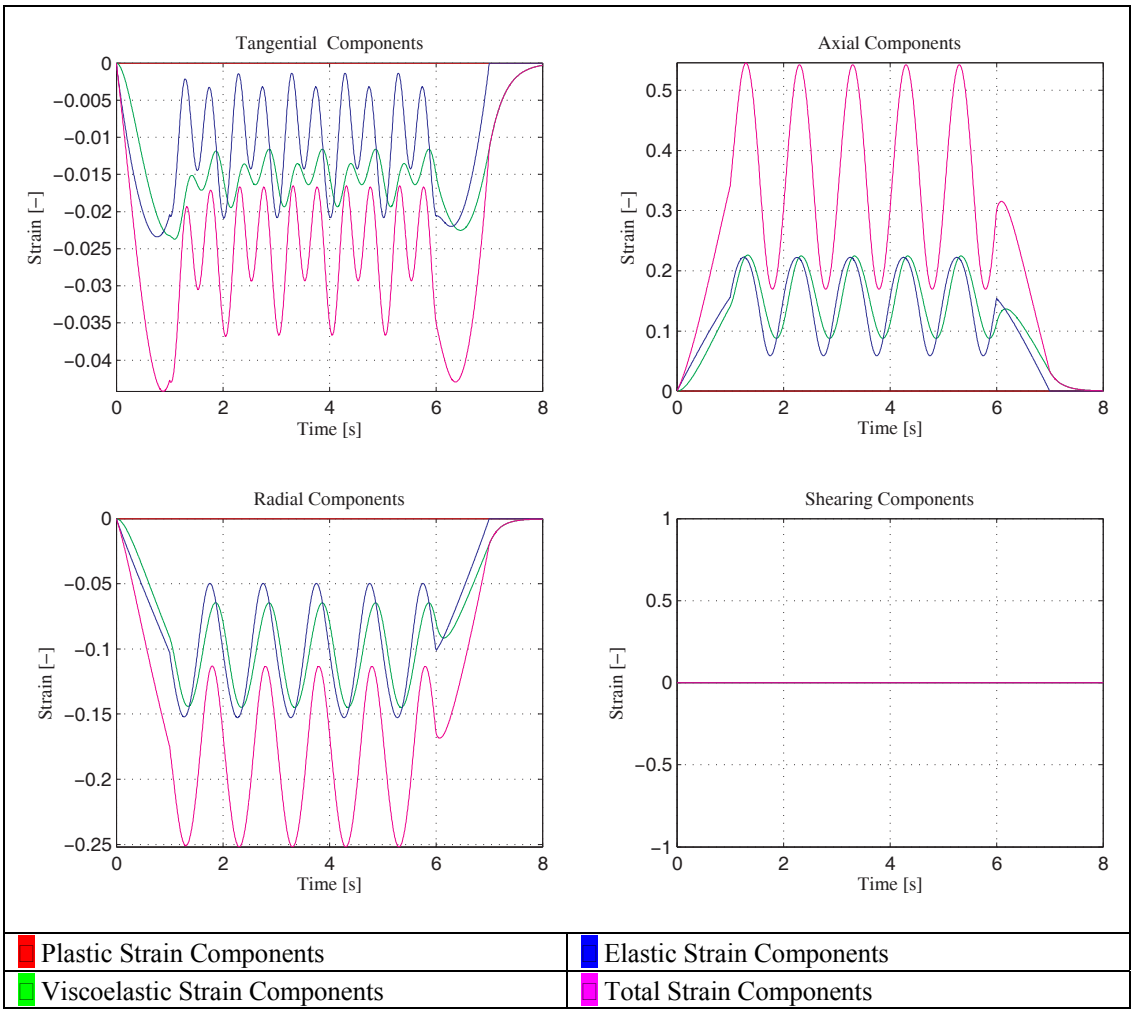

Figure 11.10 :–Strain vs. Time Graphs under Cyclic Loading at 1Hz using NonLinear Viscoelasticity Model

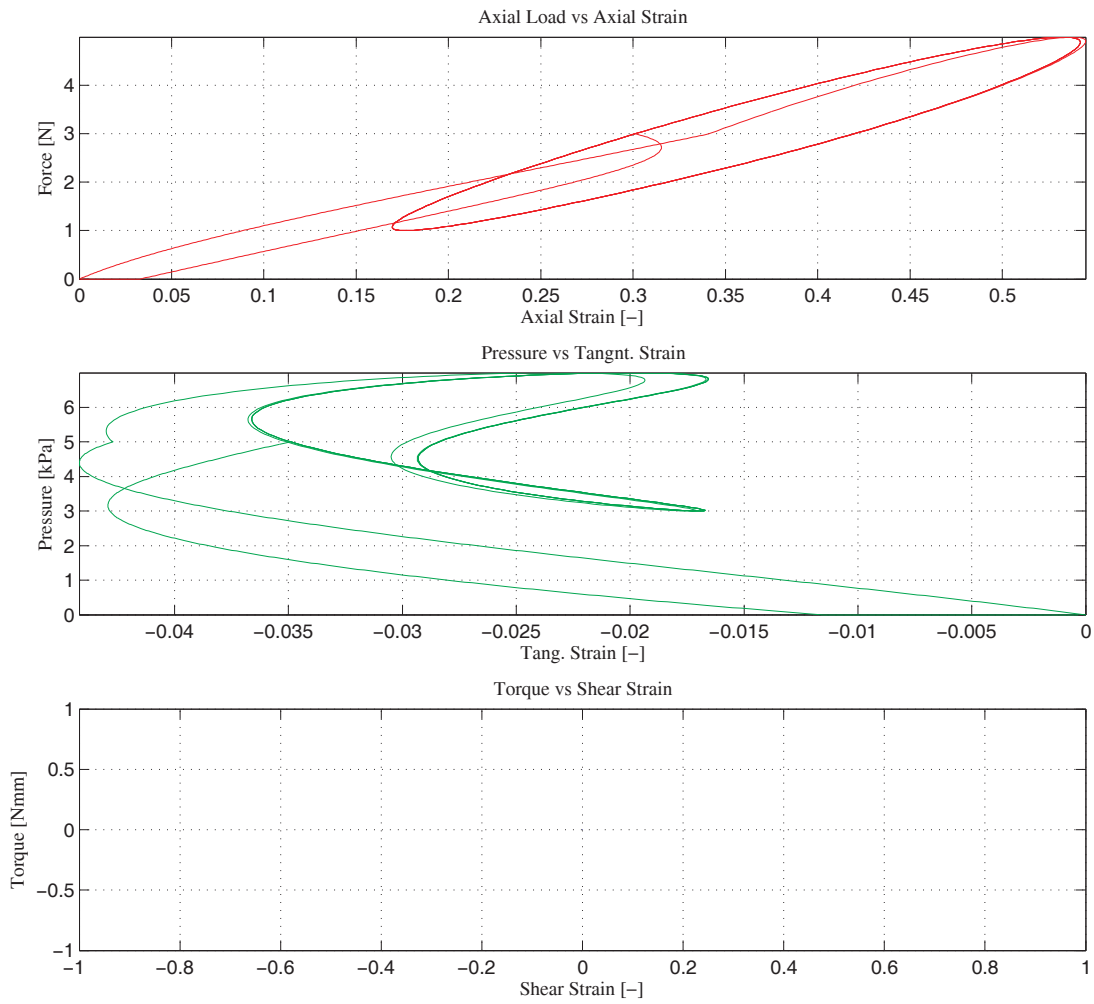

Variation of Axial Force with respect to. Axial Strain during Simulation
Variation of Internal Pressure with respect to. Tangential Strain during Simulation
Variation of Torsional Torque with respect to Shearing Strain during Simulation

Figure 11.11 :–Strain vs. Load Graphs under Cyclic Loading at 1Hz using NonLinear Viscoelasticity Model

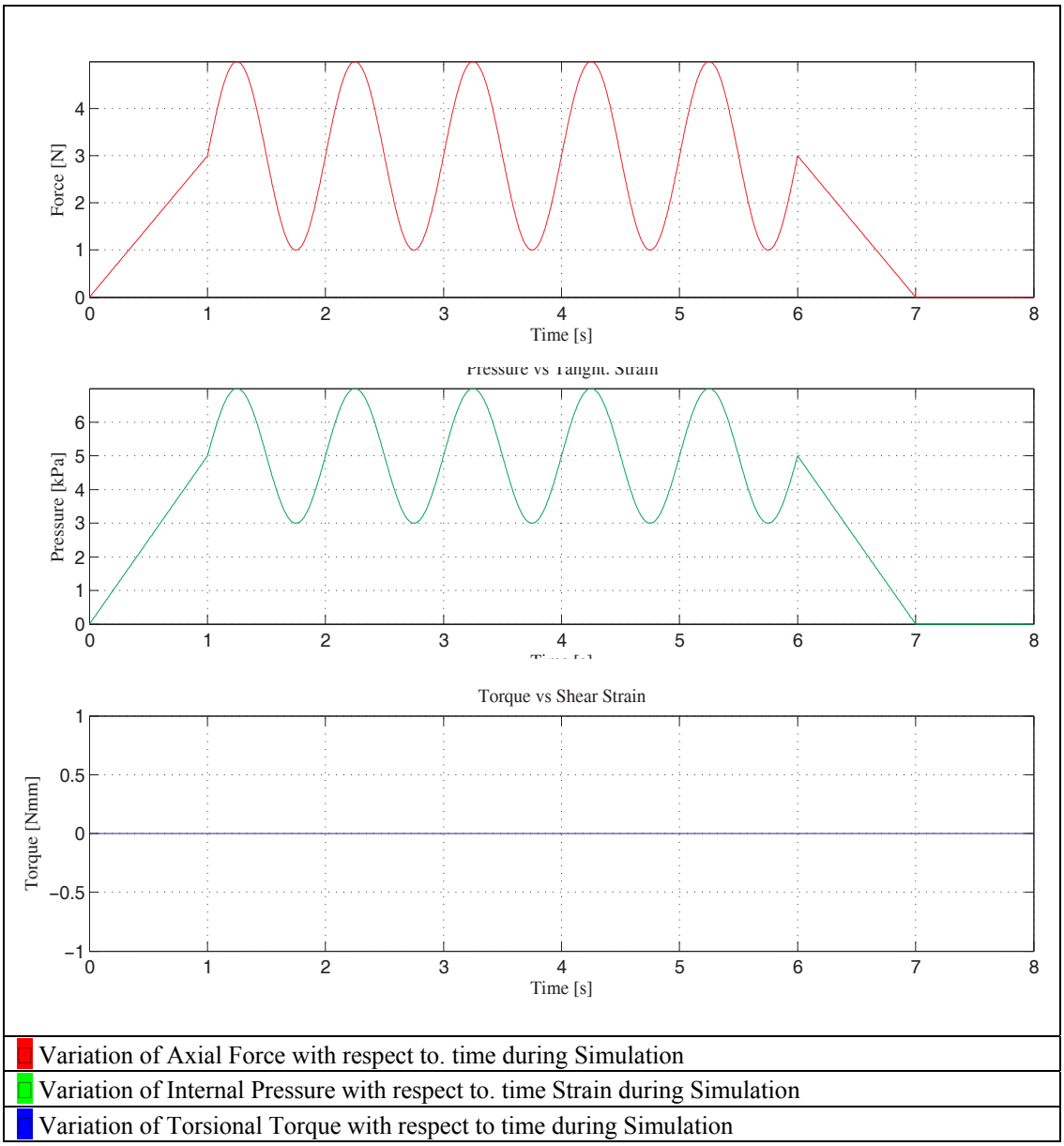

Variation of Axial Force with respect to. time during Simulation

Variation of Internal Pressure with respect to. time Strain during Simulation

Variation of Torsional Torque with respect to time during Simulation

Figure 11.12 : Load vs. Time Graphs under Cyclic Loading at 1Hz using NonLinear Viscoelasticity Model

11.1.5. Isotropic Viscoelasticity with Softening

The investigation of dissipation and its consequences on damage evolution has been achieved with this model.

It has been checked whether the expected lag and load-strain curves are achieved, which are well-known for materials with dissipative characteristics. The dissipation has been assumed to rise due to rate-dependency effects only due to the isotropic content of the material (modeled).

The material properties for the analysis are provided in Table 11.5.

Table 11.5: Material Properties Used for Pure Isotropic Viscoelasticity Analysis with Softening Effect in Section 11.1.5

Elastic ψ	C_1^e [kPa]	C_2^e [kPa]	α^e [-]		
	23.243	6.627	3.894		
Viscous ψ	C_1^v [kPa]	C_2^v [kPa]	α^v [-]		
	23.243	6.627	3.894		
Dissipation Φ	η_{GS} [kPa]	η_f [kPa]	α^f [-]		
	10.005	0.0	0.0		
Damage Q	Q_∞ [-]	δ [-]			
	0.70	75.0			
Plasticity	$\dot{a}$ [1/s]	g_0 [kPa]	g_∞ [kPa]	h_0 [kPa]	k [-]
	0.0	1400	4400	150	10

The model has been seen to capture both models' characteristics represented in Sections 11.1.2 and 11.1.3. It is worth to indicate the transient loops due to softening of the material and the steady loops due to dissipative effects in all load-deformation curves. Also, the creep of the material at zero load is captured at the end of the loading cycle, thus every loop in all load-deformation curves are closed.

Figures 11.13 – 11.15 and A-5.1 to A-5.6 demonstrate the characteristics of behavior of the model proposed with non-linear viscoelastic effects.

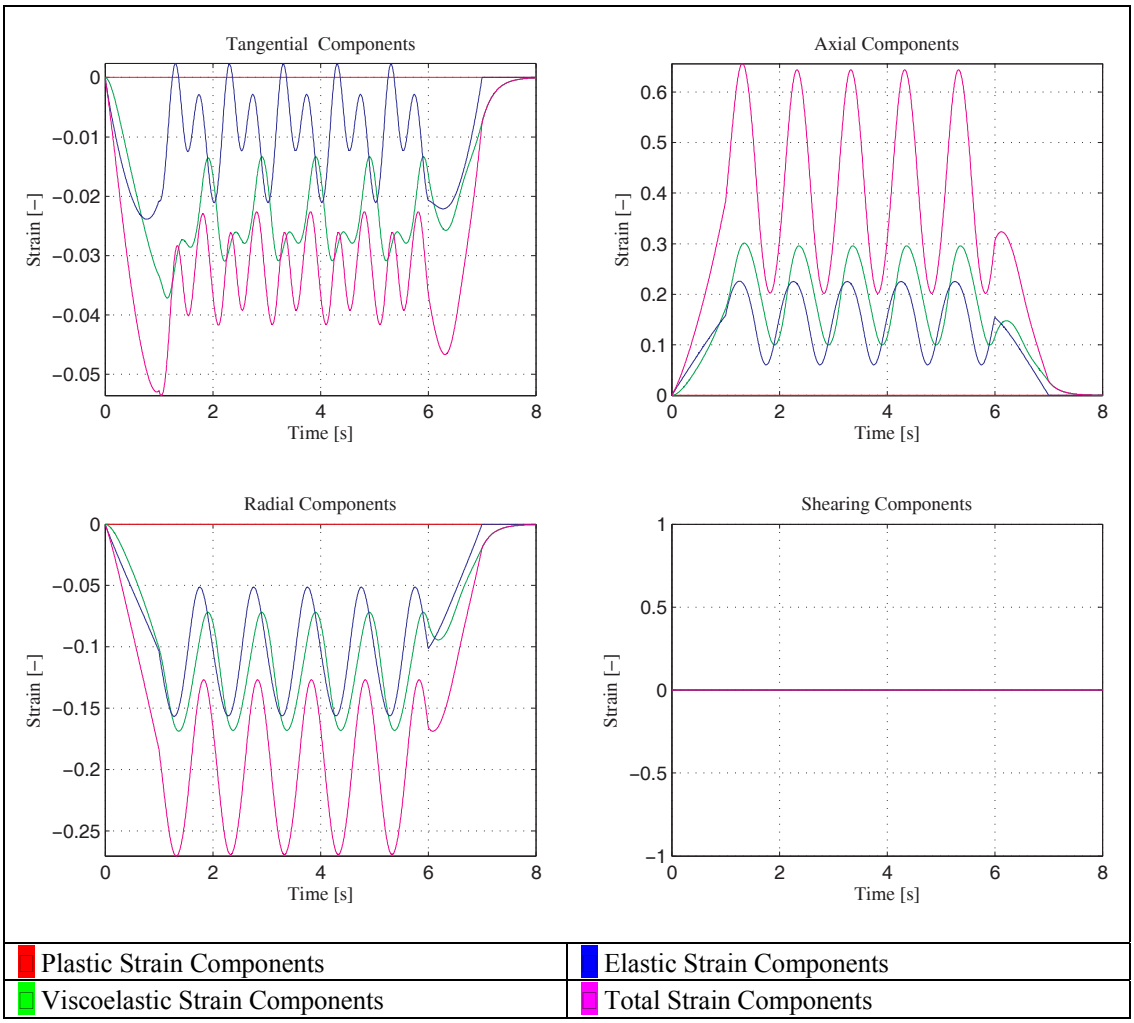

Figure 11.13 : Strain vs. Time Graphs under Cyclic Loading at 1Hz using Isotropic Viscoelasticity Model with Softening Effects

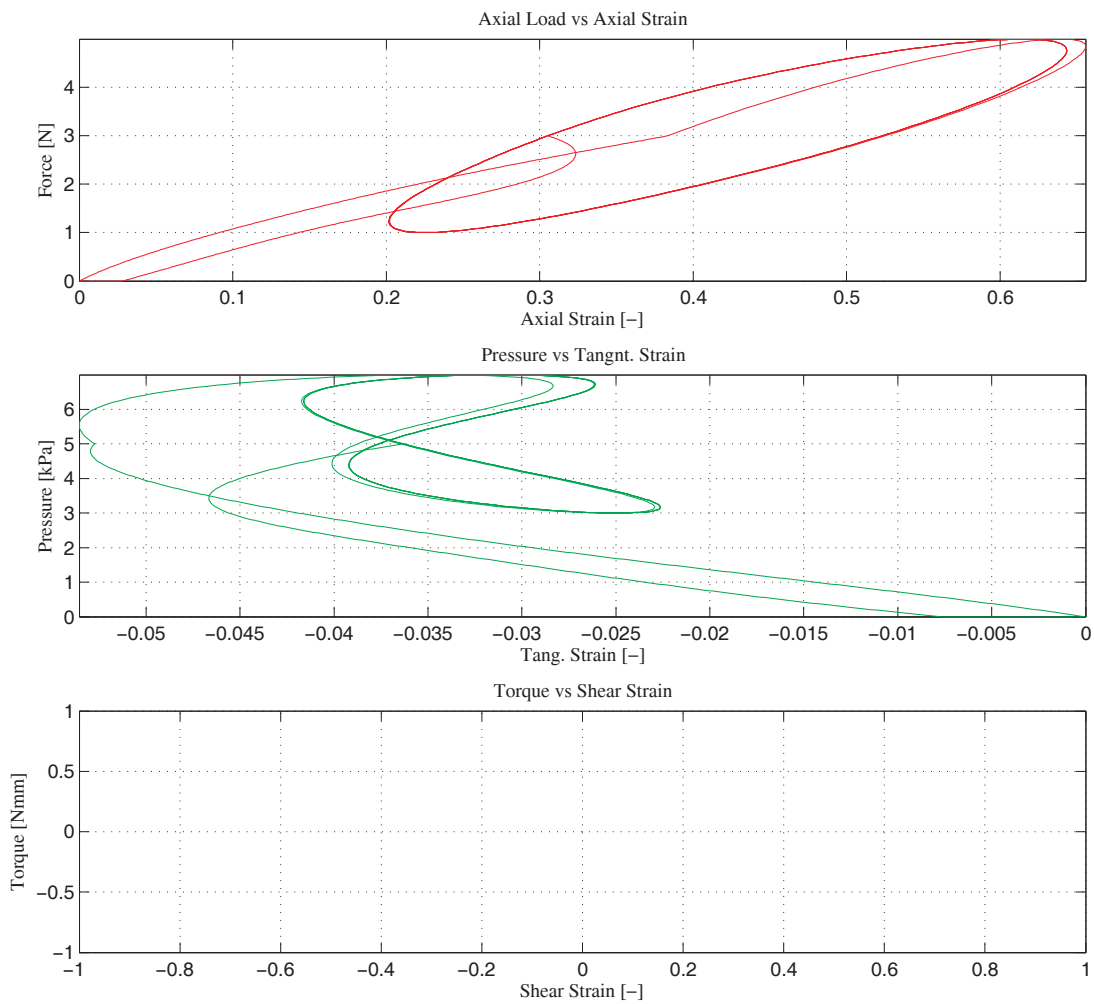

Variation of Axial Force with respect to. Axial Strain during Simulation
Variation of Internal Pressure with respect to. Tangential Strain during Simulation
Variation of Torsional Torque with respect to Shearing Strain during Simulation

Figure 11.14 : Strain vs. Load Graphs under Cyclic Loading at 1Hz using Isotropic Viscoelasticity Model with Softening Effects

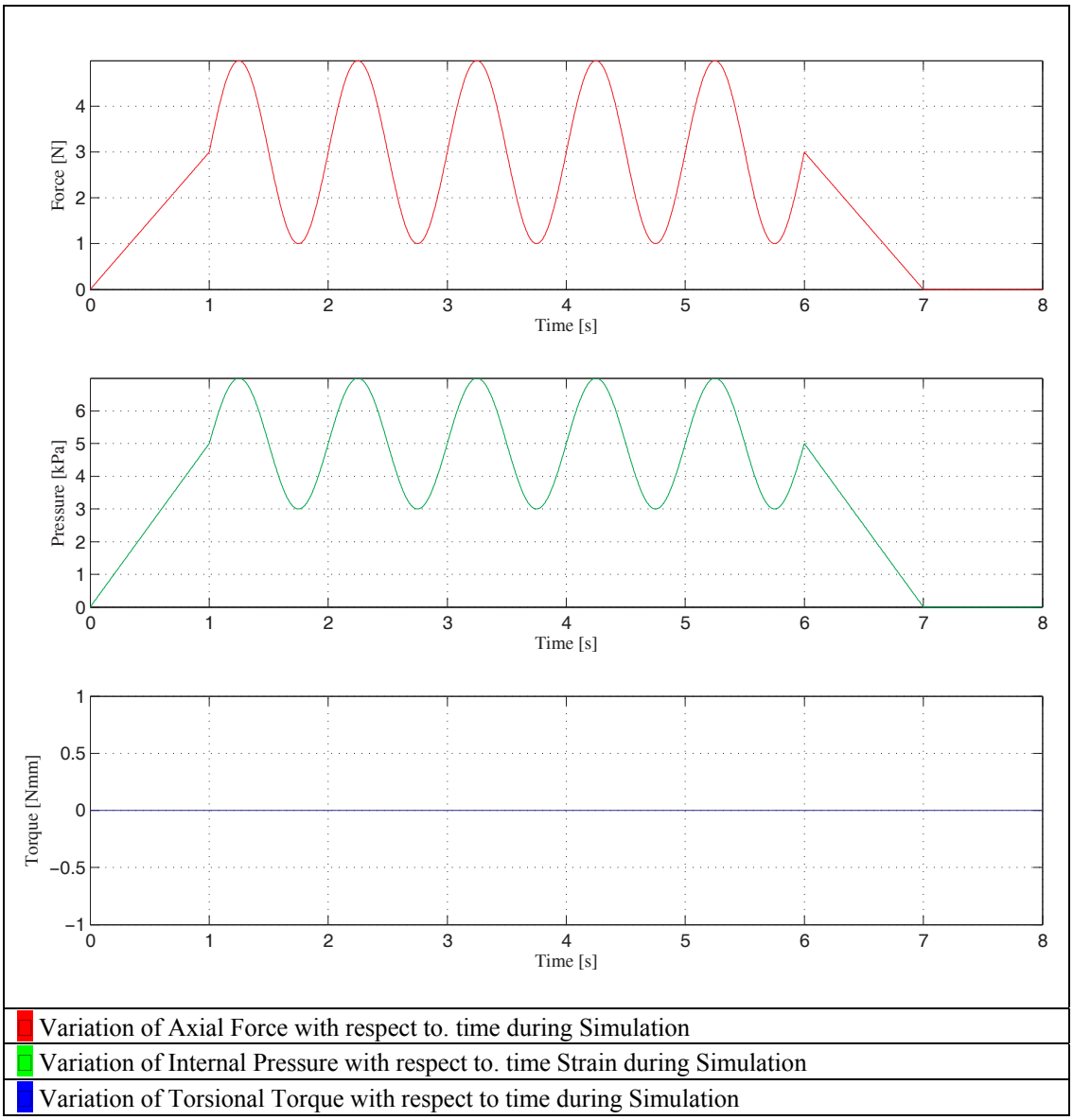

Figure 11.15 : Load vs. Time Graphs under Cyclic Loading at 1Hz using Isotropic Viscoelasticity Model with Softening Effects

11.1.6. Isotropic Viscoelasticity with Softening and Static Torsion.

Effect of shearing on material behavior has been investigated. Damping and softening has been considered. The figures below provide the loading protocols, the load-strain diagrams and the strains on the outer surface and variation of various quantities with time and within the wall thickness.

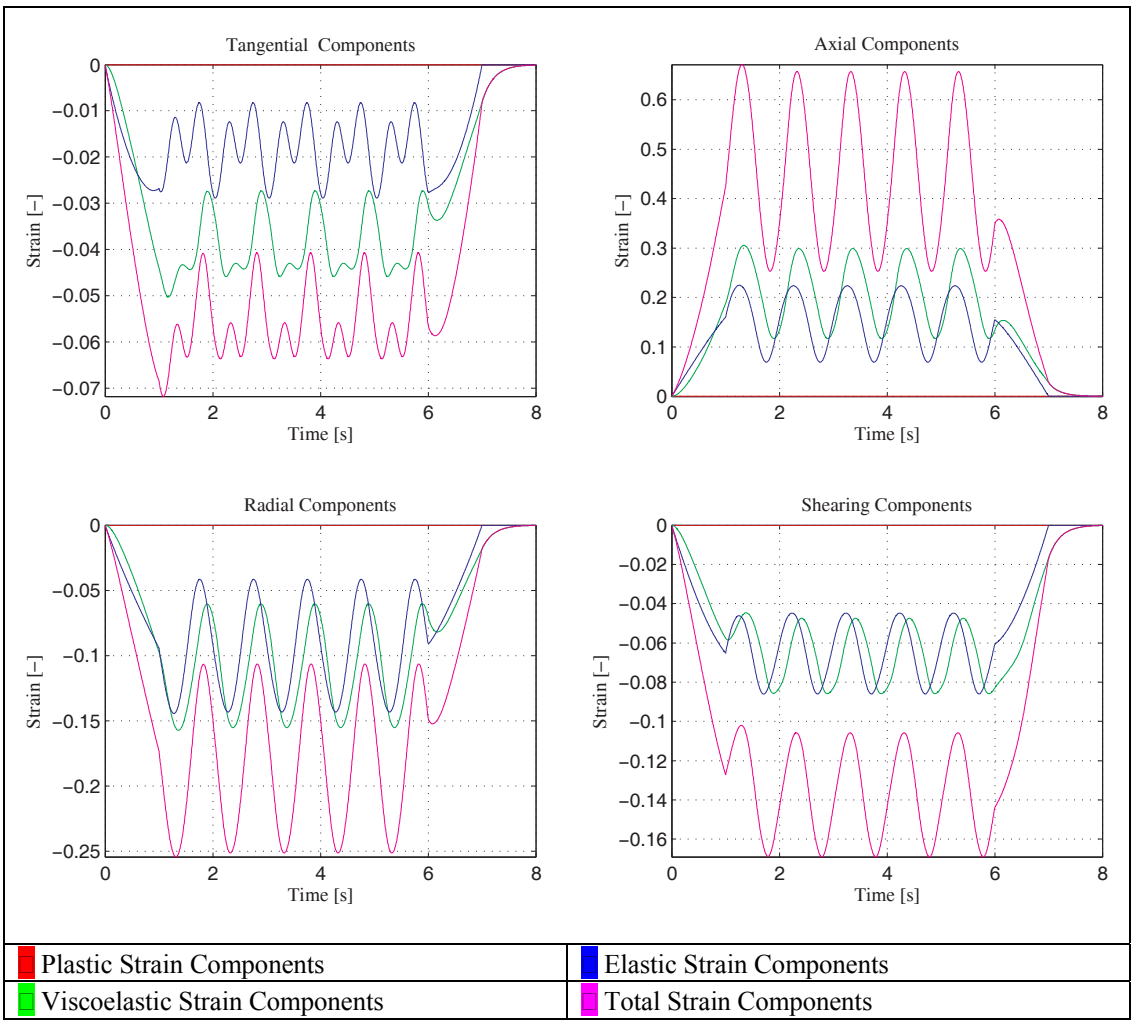

Figure 11.16 : Strain vs. Time Graphs under Cyclic Loading at 1Hz over Static Torsion using Isotropic Viscoelasticity Model with Softening Effects

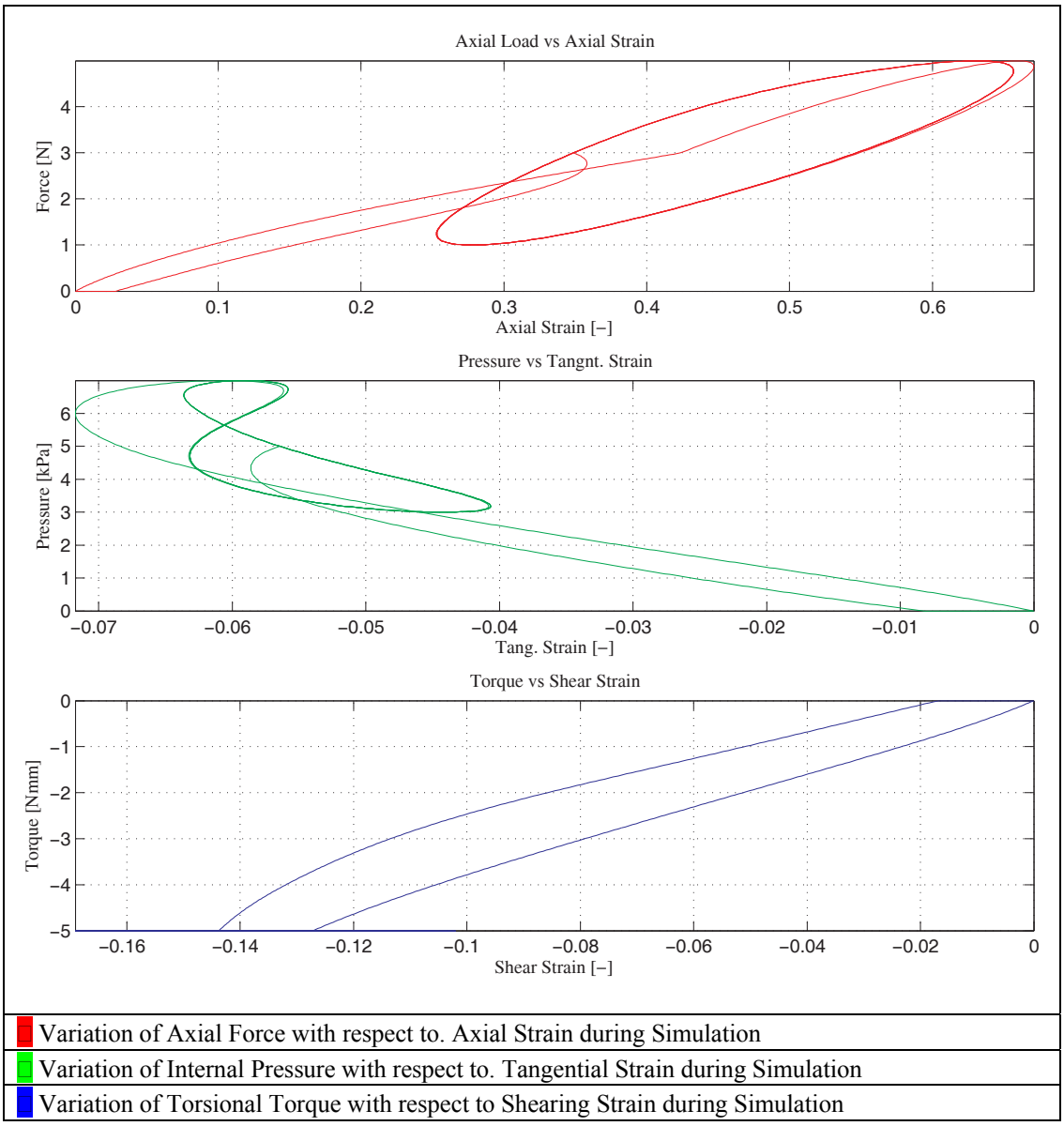

Variation of Axial Force with respect to. Axial Strain during Simulation
Variation of Internal Pressure with respect to. Tangential Strain during Simulation
Variation of Torsional Torque with respect to Shearing Strain during Simulation

Figure 11.17 : Strain vs. Load Graphs under Cyclic Loading at 1Hz over Static Torsion using Isotropic Viscoelasticity Model with Softening Effects

The material properties for the analysis are provided in Table 11.6.

Table 11.6: Material Properties Used for Pure Isotropic Viscoelasticity Analysis with Softening Effect in Section 11.1.6

Elastic ψ	C_1^e [kPa]	C_2^e [kPa]	α^e [-]		
	23.243	6.627	3.894		
Viscous ψ	C_1^v [kPa]	C_2^v [kPa]	α^v [-]		
	23.243	6.627	3.894		
Dissipation Φ	η_{GS} [kPa]	η_f [kPa]	α^f [-]		
	10.005	0.0	0.0		
Damage Q	Q_∞ [-]	δ [-]			
	0.70	75.0			
Plasticity	$\dot{a}$ [1/s]	g_0 [kPa]	g_∞ [kPa]	h_0 [kPa]	k [-]
	0.0	1400	4400	150	10

For fiber reinforced materials, it is known that when the plane of symmetry does not hold for loading conditions (such as a pressurized tube under torsion) the fiber stretches no more stay symmetrical. Adding a static torsion to the previous task represented in Section 11.1.5 is aimed at capturing the outcomes of disturbing this symmetry. The most critical outcomes that have been observed are can be stated to be the radial distribution of stress and strain in the longitudinal direction. Additionally, due to the presence of softening effects, the loading and unloading curves, besides the dissipative loops, differ greatly for the torsion-shear strain curve.

Figures 11.16-11.18 and A-6.1 to A-6.8 point out graphically the relevant issues about unsymmetrical loading.

Also, it is worth to mention that, though the torsional moment is kept constant, the shear strains fluctuate with variations in other external loads.

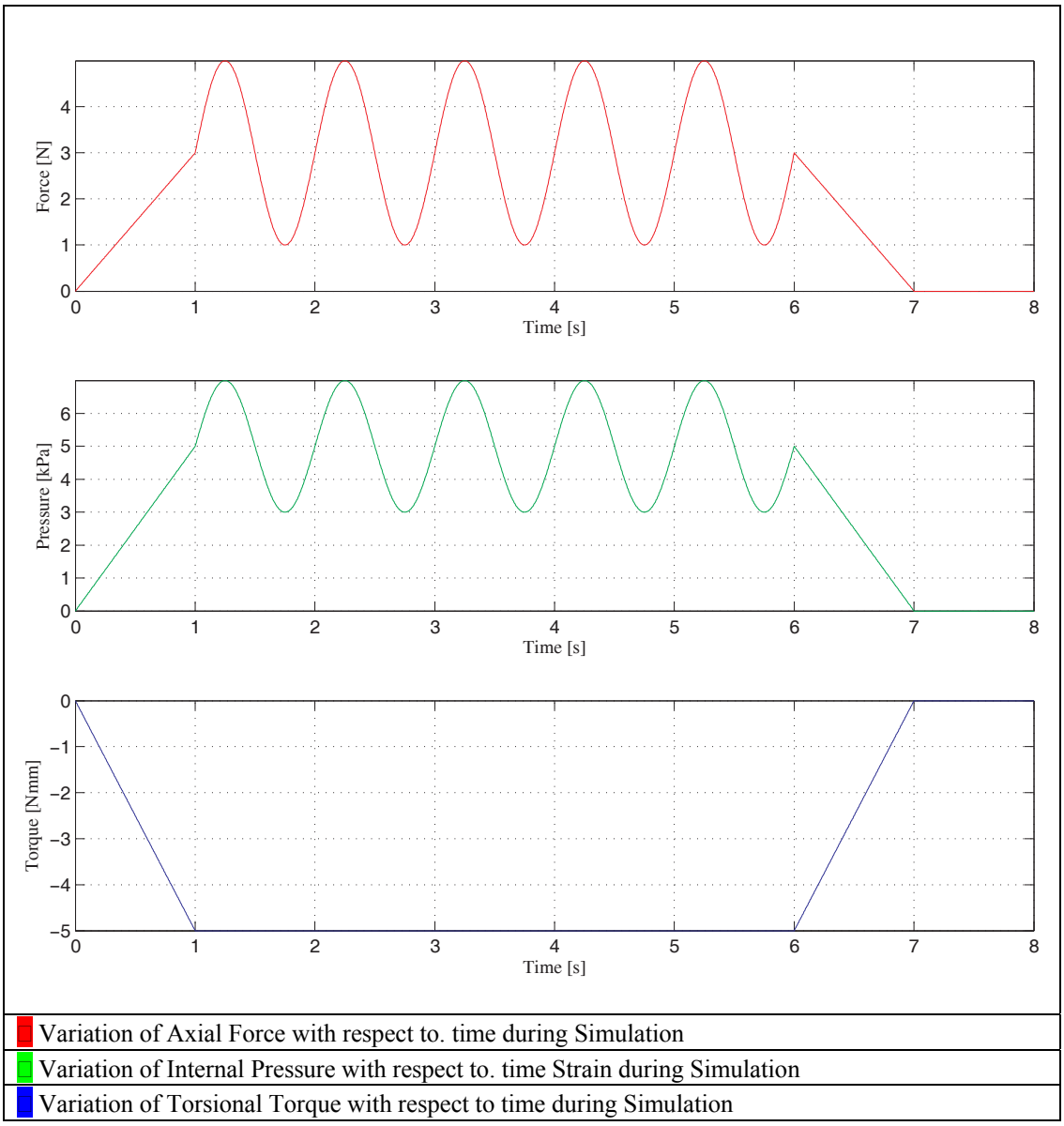

Figure 11.18 : Load vs. Time Graphs under Cyclic Loading at 1Hz over Static Torsion using Isotropic Viscoelasticity Model with Softening Effects

11.1.7. Isotropic Viscoelasticity with Softening and Dynamic Torsion over Static Pressure and Axial Force

Effect of dynamic shearing has been investigated. Damping and softening has been considered. The figures 11.19 to 11.21 and A-7.1 to A-7.8 provide the loading protocols, the load-strain diagrams and the strains on the outer surface and variation of various quantities with time and within the wall thickness.

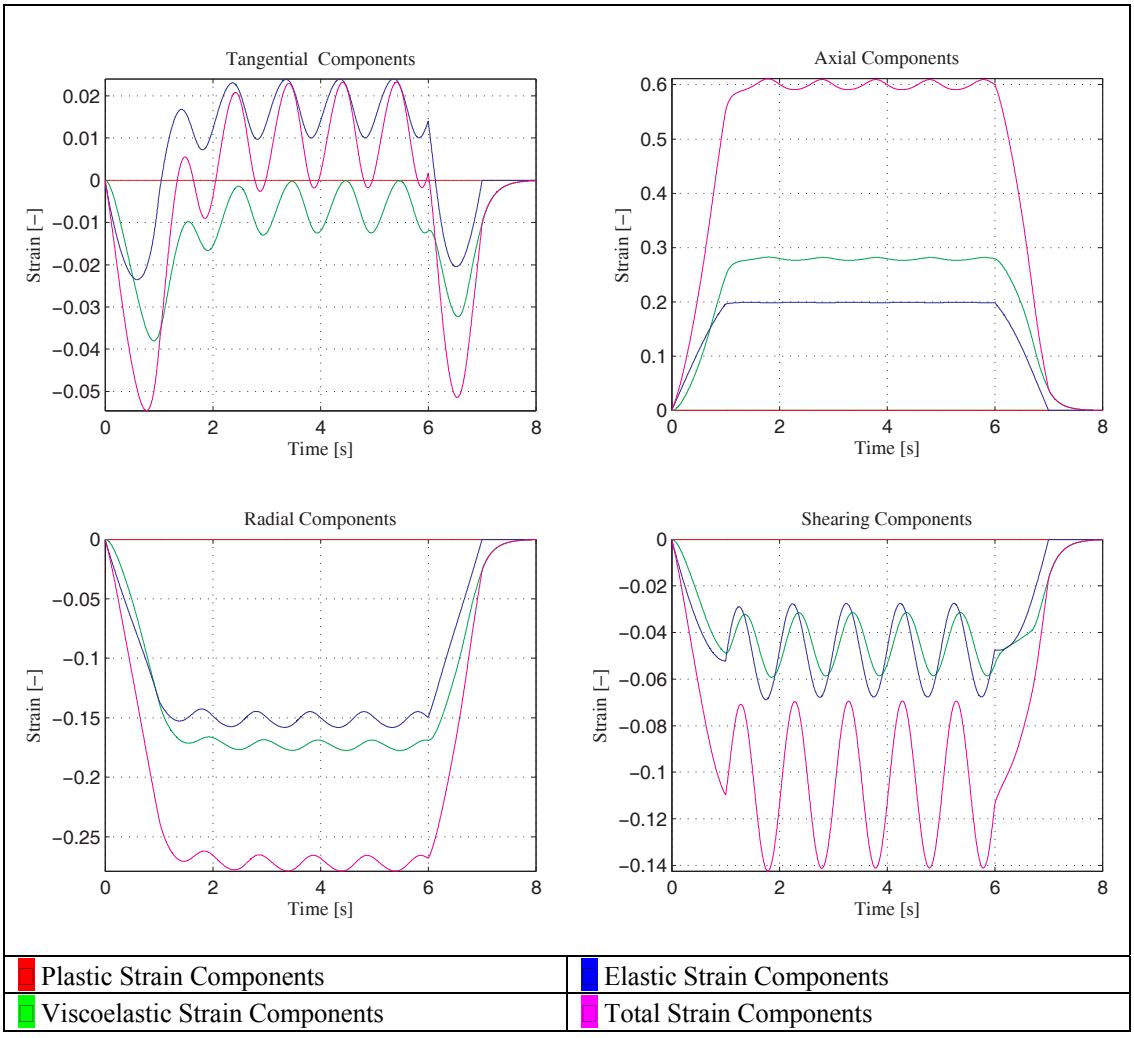

Figure 11.19 : Strain vs. Time Graphs under Cyclic Loading at 1Hz with Torsion using Isotropic Viscoelasticity Model with Softening Effects"

The material properties for the analysis are provided in Table 11.7.

Table 11.7: Material Properties Used for Pure Isotropic Viscoelasticity Analysis with Softening Effect in Section 11.1.7

Elastic ψ	C_1^e [kPa]	C_2^e [kPa]	α^e [-]		
	23.243	6.627	3.894		
Viscous ψ	C_1^v [kPa]	C_2^v [kPa]	α^v [-]		
	23.243	6.627	3.894		
Dissipation Φ	η_{GS} [kPa]	η_f [kPa]	α^f [-]		
	10.005	0.0	0.0		
Damage Q	Q_∞ [-]	δ [-]			
	0.70	75.0			
Plasticity	$\dot{a}$ [1/s]	g_0 [kPa]	g_∞ [kPa]	h_0 [kPa]	k [-]
	0.0	1400	4400	150	10

In this analysis, different from Section 11.1.6, the internal pressure and the axial force has been kep constant at some fixed level, and dynamic torsional moment has been applied over the tube model.

The interesting outcomes have been recorded as the fluctuations in the axial and tangential (thus, respectively radial) strains during dynamic torsional loading, despite the other quantities have been kept fixed. These are related to properties with the non-linear couplings and coupling effects due to structural properties of fiber-reinforced composites.

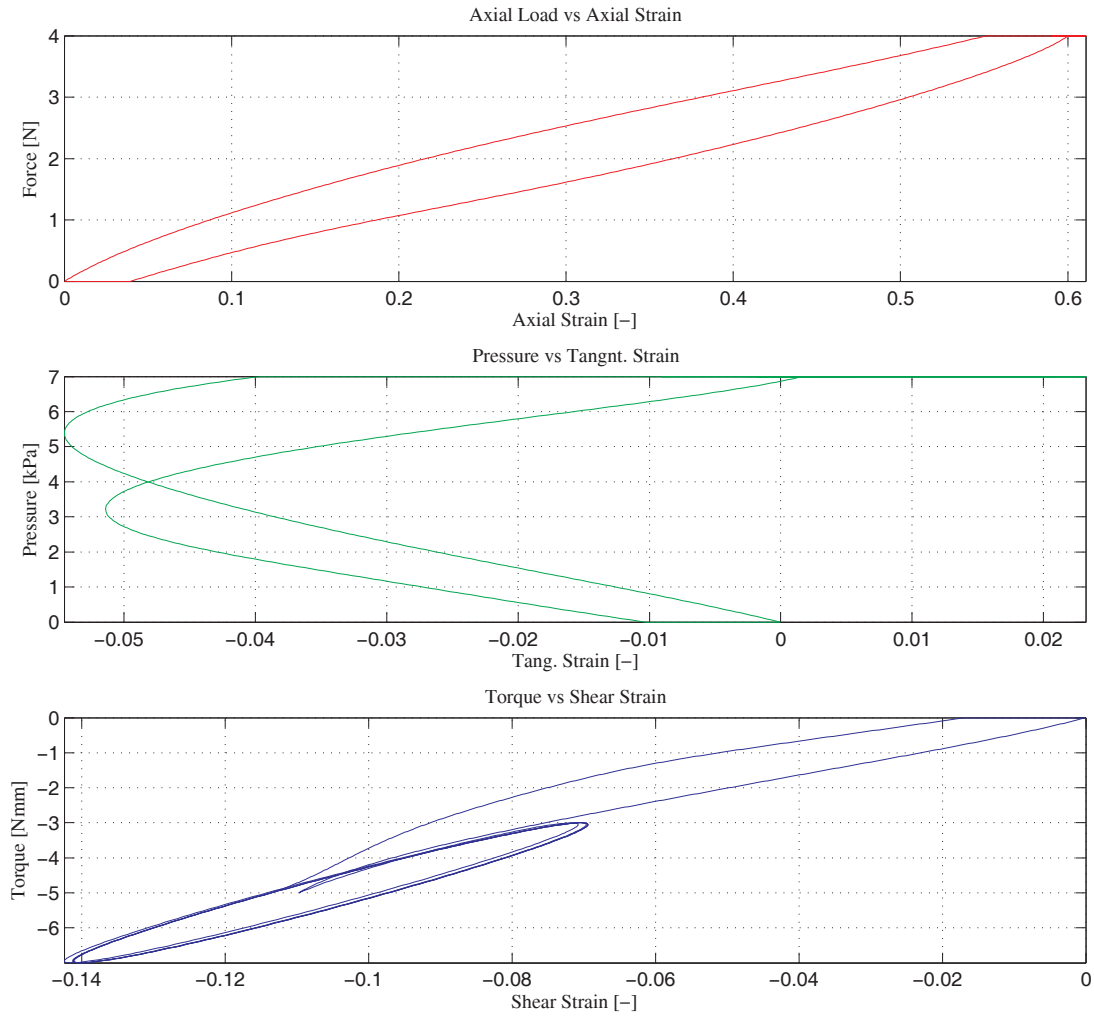

Variation of Axial Force with respect to. Axial Strain during Simulation
Variation of Internal Pressure with respect to. Tangential Strain during Simulation
Variation of Torsional Torque with respect to Shearing Strain during Simulation

Figure 11.20 : Strain vs. Load Graphs under Cyclic Loading at 1Hz with Torsion using Isotropic Viscoelasticity Model with Softening Effects

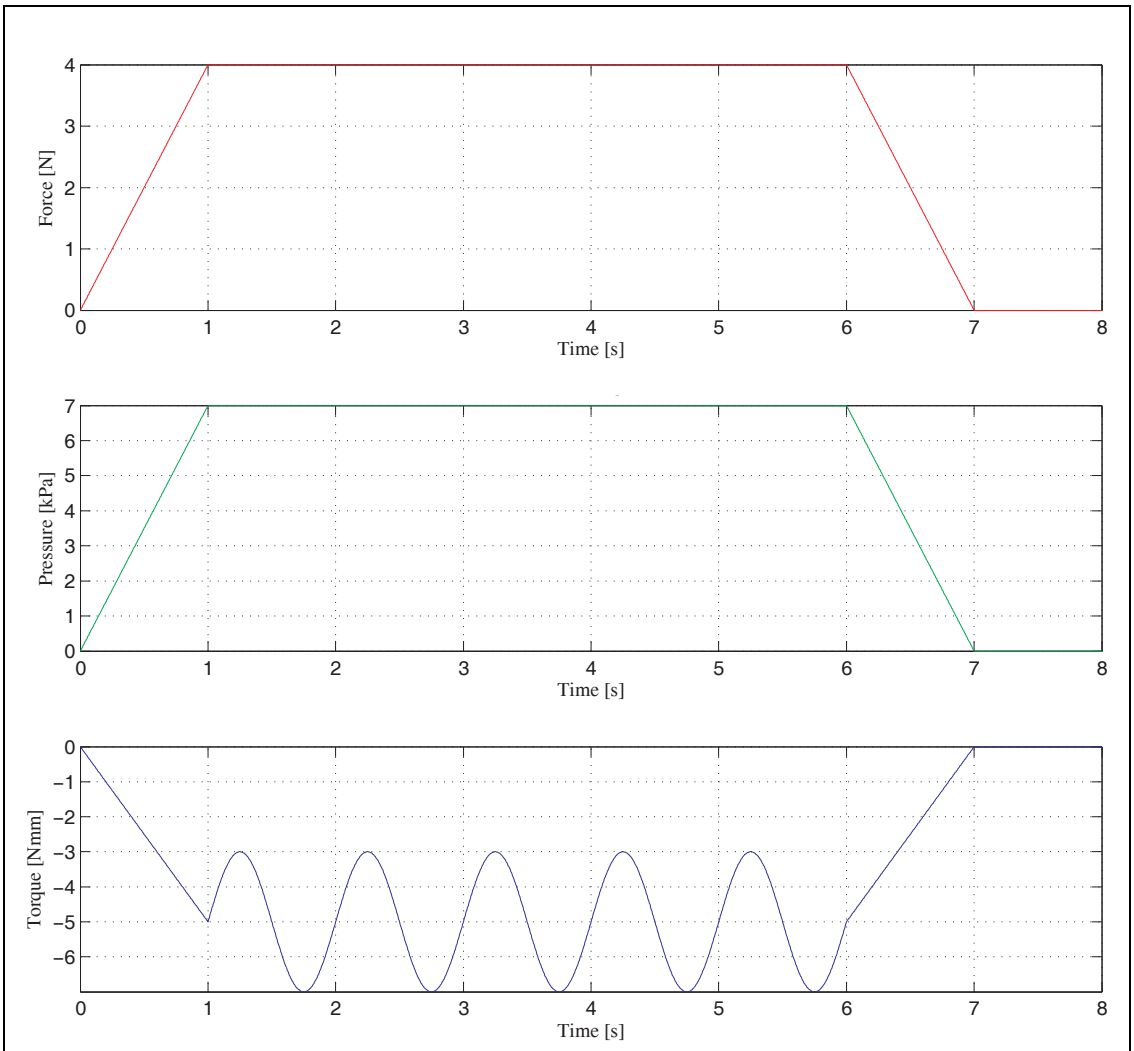

Figure 11.21 : Load vs. Time Graphs under Cyclic Loading at 1Hz with Torsion using Isotropic Viscoelasticity Model with Softening Effects

11.1.8. Isotropic Viscoelasticity with Softening and Under Dynamic Inflation and Torsion with Static Axial Load

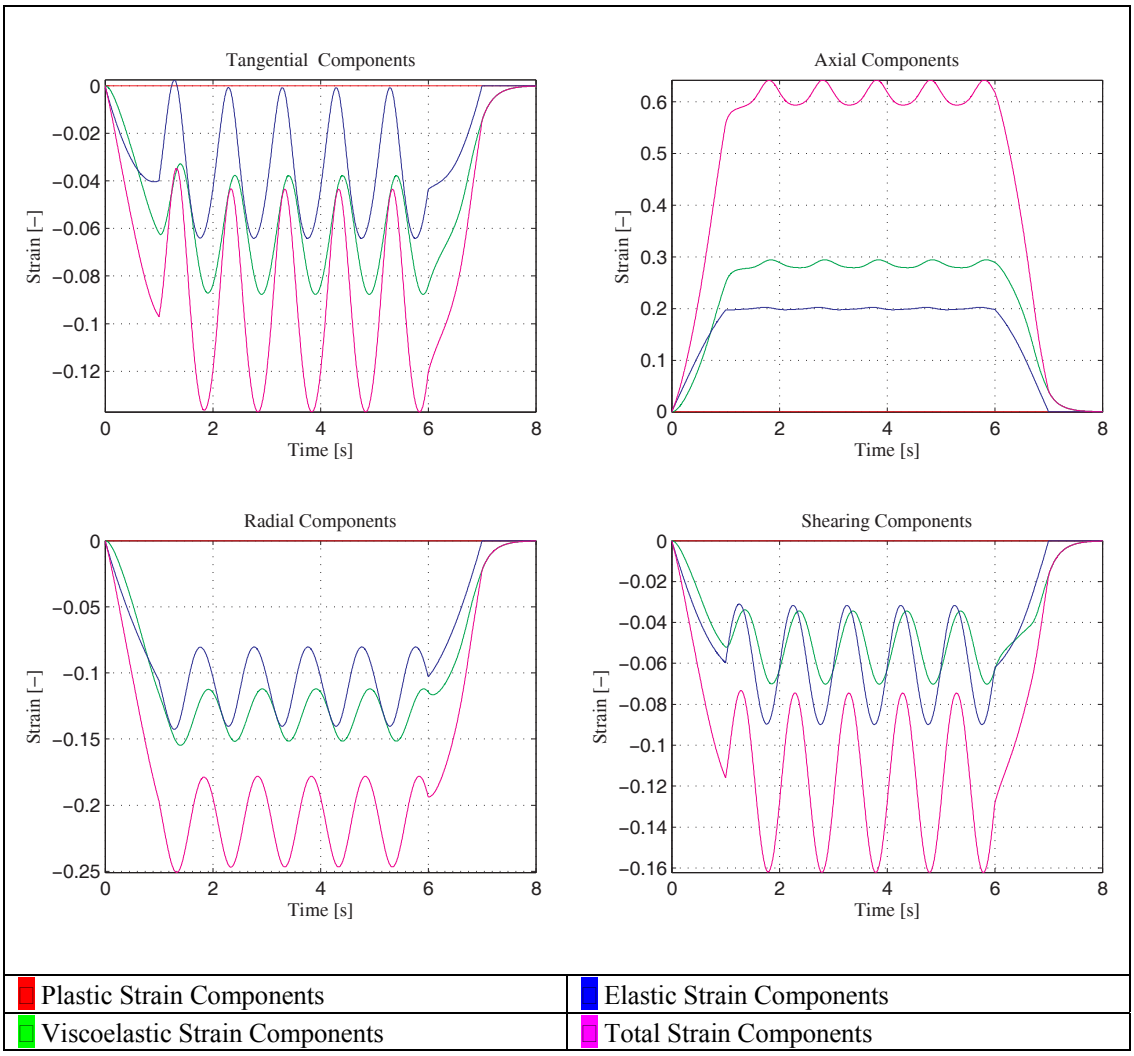

Figure 11.22 : Strain vs. Time Graphs under Cyclic Loading at 1Hz with Torsion using Isotropic Viscoelasticity Model with Softening Effects

Coupled dynamic loading protocol has been applied to see cross-effects among dynamic components. Damping and softening has been considered. The figures 11.22 – 11.25 and A-8.1 to A-8.8 provide the loading protocols, the load-strain diagrams and the strains on the outer surface and variation of various quantities with time and within the wall thickness.

The material properties for the analysis are provided in Table 11.8.

Table 11.8: Material Properties Used for Pure Isotropic Viscoelasticity Analysis with Softening Effect in Section 11.1.8

Elastic ψ	C_1^e [kPa]	C_2^e [kPa]	α^e [-]		
	23.243	6.627	3.894		
Viscous ψ	C_1^v [kPa]	C_2^v [kPa]	α^v [-]		
	23.243	6.627	3.894		
Dissipation Φ	η_{GS} [kPa]	η_f [kPa]	α^f [-]		
	10.005	0.0	0.0		
Damage Q	Q_∞ [-]	δ [-]			
	0.70	75.0			
Plasticity	$\dot{a}$ [1/s]	g_0 [kPa]	g_∞ [kPa]	h_0 [kPa]	k [-]
	0.0	1400	4400	150	10

In this exercise, the coupling between dynamic inflation and shearing has been investigated.

The phase lags are observed as usual and the dissipative loops in load-deformation curves exist. The radial variation of quantities are again observed.

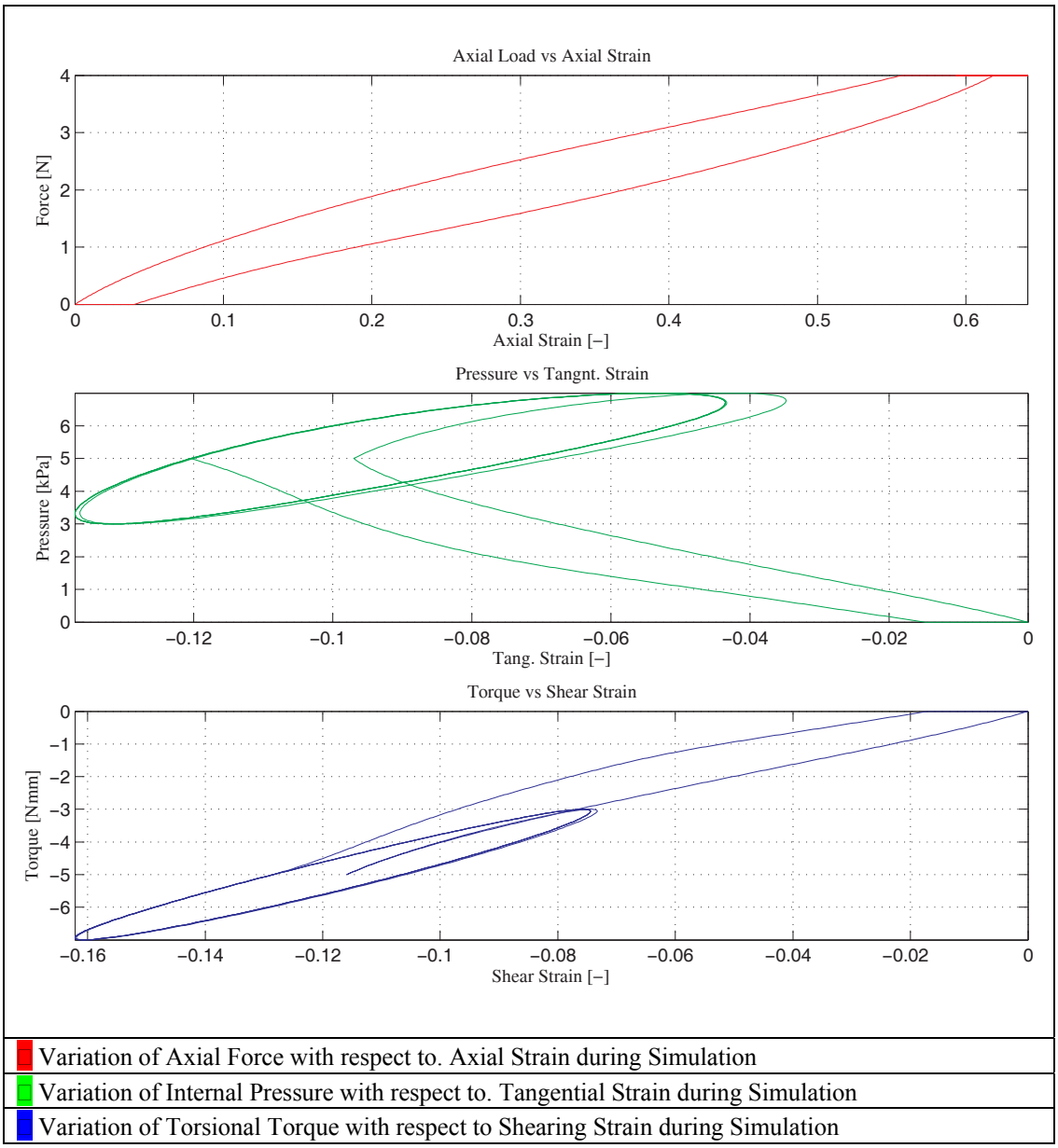

Variation of Axial Force with respect to. Axial Strain during Simulation
Variation of Internal Pressure with respect to. Tangential Strain during Simulation
Variation of Torsional Torque with respect to Shearing Strain during Simulation

Figure 11.23 : Strain vs. Load Graphs under Cyclic Loading at 1Hz with Torsion using Isotropic Viscoelasticity Model with Softening Effects

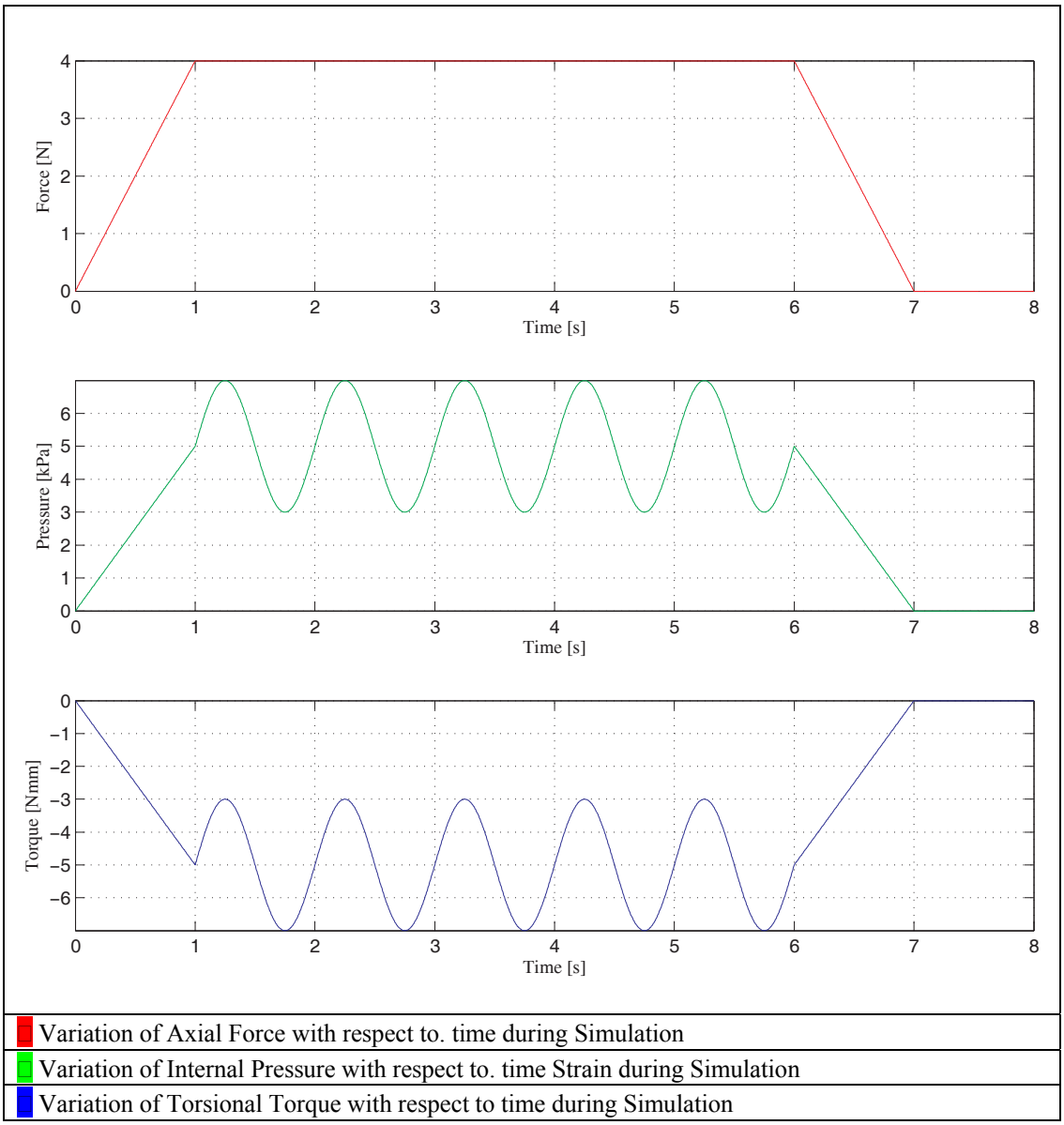

Figure 11.24 : Load vs. Time Graphs under Cyclic Loading at 1Hz with Torsion using Isotropic Viscoelasticity Model with Softening Effects

11.2. Analysis Incorporating Plastic Deformations

Having investigated in Section 11.1 the elastic material behavior due to the constitutive and kinematics assumptions that have been laid within thescope of this study, it can be concluded that the (visco) elastic part of the model behaves as expected by both the solid mechanics' view and the specific aims of the study.

To investigate how the material responds when plasticity is added to the constitutive behavior, the following analysis have been conducted, whose details are provided in Sections 11.2.1 and 11.2.2.

11.2.1. Elastoplasticity

Table 11.9: Material Properties Used for Elastoplasticity Material Model Analysis in Section 11.2.1

Elastic ψ	C_1^e [kPa]	C_2^e [kPa]	α^e [-]		
	23.243	6.627	3.894		
Viscous ψ	C_1^v [kPa]	C_2^v [kPa]	α^v [-]		
	23.243	6.627	3.894		
Dissipation Φ	η_{GS} [kPa]	η_f [kPa]	α^f [-]		
	0.005	0.0	0.0		
Damage Q	Q_∞ [-]	δ [-]			
	0.0	0.0			
Plasticity	$\dot{a}$ [1/s]	g_0 [kPa]	g_∞ [kPa]	h_0 [kPa]	k [-]
	0.83	14	44	150	10

Within the elastoplasticity concept, it has been assumed that no dissipation and/or softening is considered. But in the contrary, plastic dissipation (irreversible deformations) are enabled after some threshold level that is within the applied stress ranges, so that permanent deformations are observed at the end of the loading/unloading cycle.

The material properties for the analysis are provided in Table 11.9.

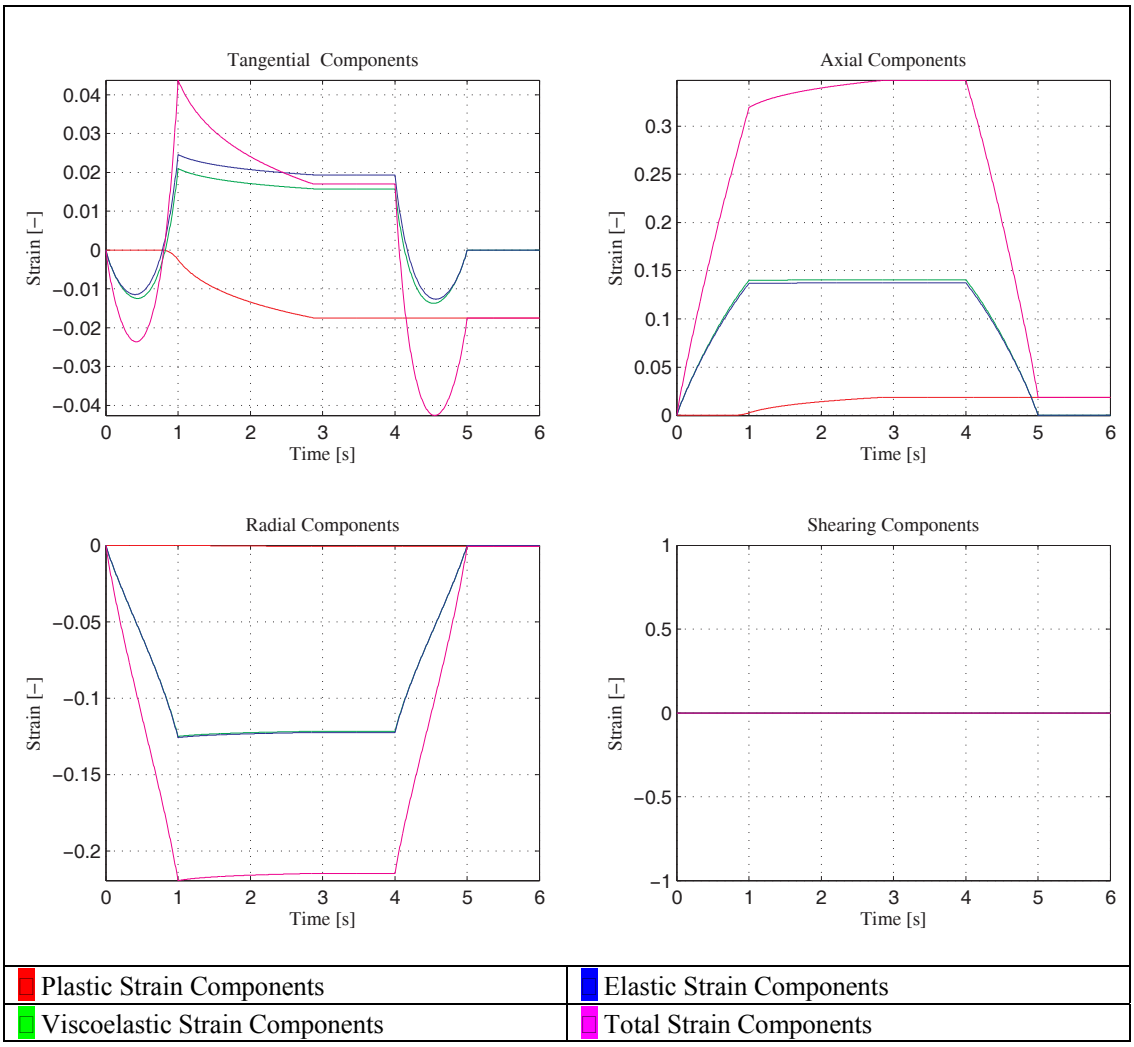

Figure 11.25 : Strain Components During an Elastoplastic Analysis of Axisymetric Tube as to details provided Section 11.2.1

The hardening model proposed, with the provided material parameters are observed to work as desired, based on the findings from the results that tough the material deformation enables stress values to go up with plastic deformations, as the cross-secitonal values change in favor of increasing stress, the plastic flow stops at a point and no more plastic deformation takes place. This issue is easily recovered in especially Figure 11.79, and through all the Figures 11.25 – 11.27 and A-9.1 to A-9.9.

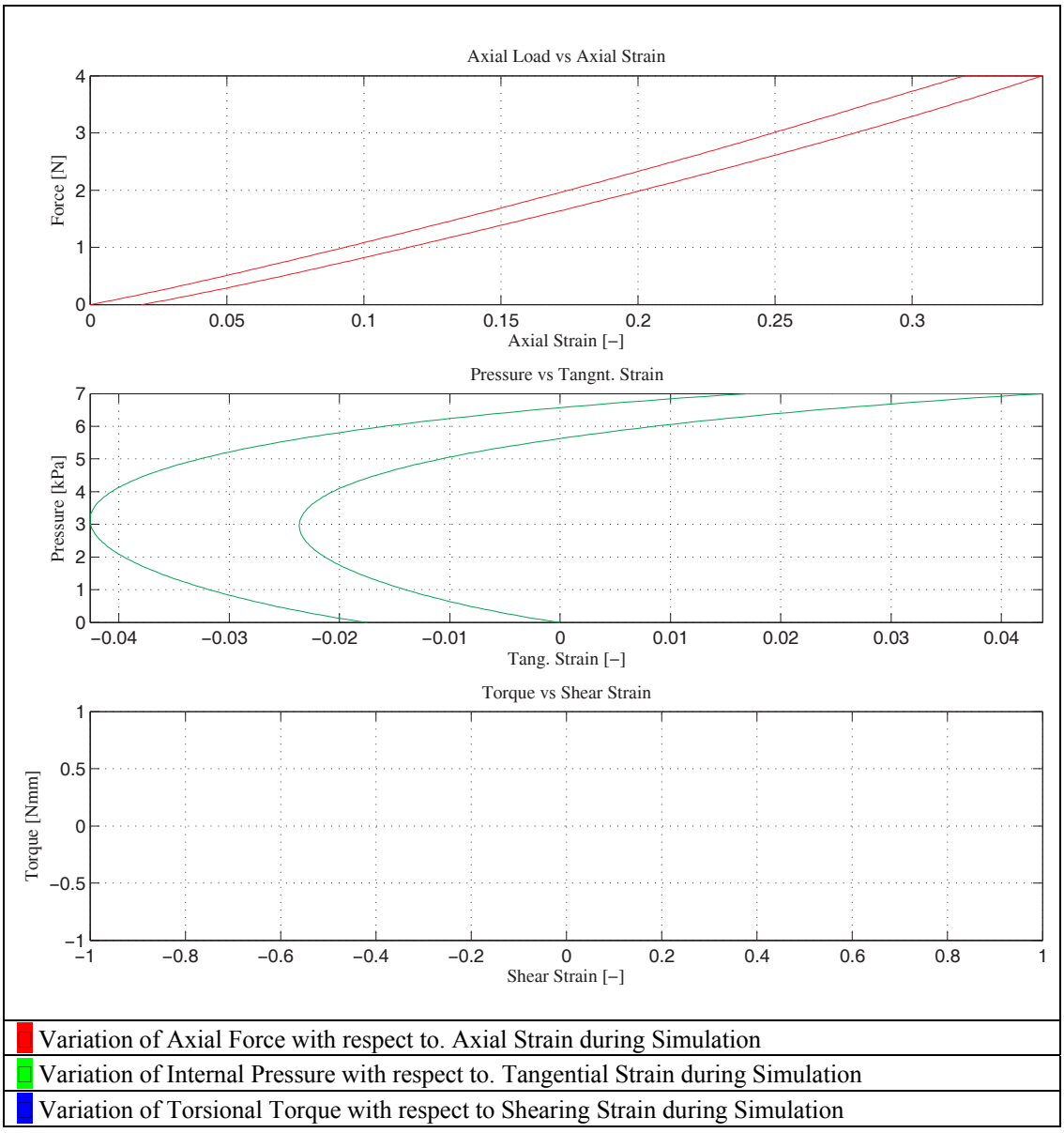

Variation of Axial Force with respect to. Axial Strain during Simulation
Variation of Internal Pressure with respect to. Tangential Strain during Simulation
Variation of Torsional Torque with respect to Shearing Strain during Simulation

Figure 11.26 : Load-Deformation Curves During an Elastoplastic Analysis of Axisymetric Tube as to details provided Section 11.2.1

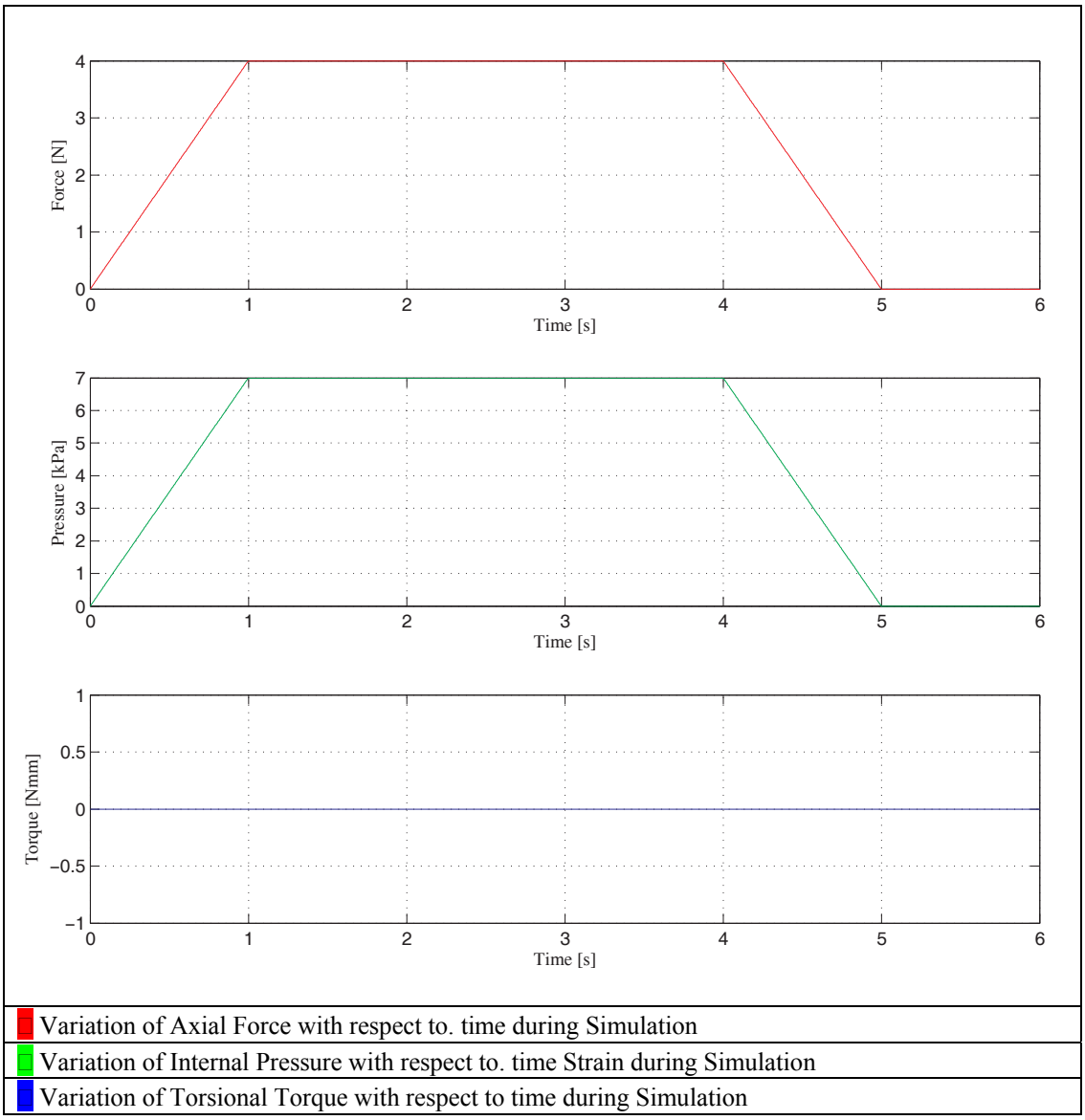

Figure 11.27 : Load-Deformation Curves During an Elastoplastic Analysis of Axisymetric Tube as to details provided Section 11.2.1

11.2.2. Viscoelastoplasticity with Isotropic Damping

The results provided in this section have been acquired form a completely similar scenario that has been presented in Section 11.1.2, but the only difference is said to be the existence of some damping on the material model. Some changes have taken place with respect to the induced effects, which are mostly delay related.

The material properties for the analysis are provided in Table 11.10 , and the relevant outcomes of the analysis are provided in Figures 11.28 – 11.30 and A-10.1 to A-10.9.

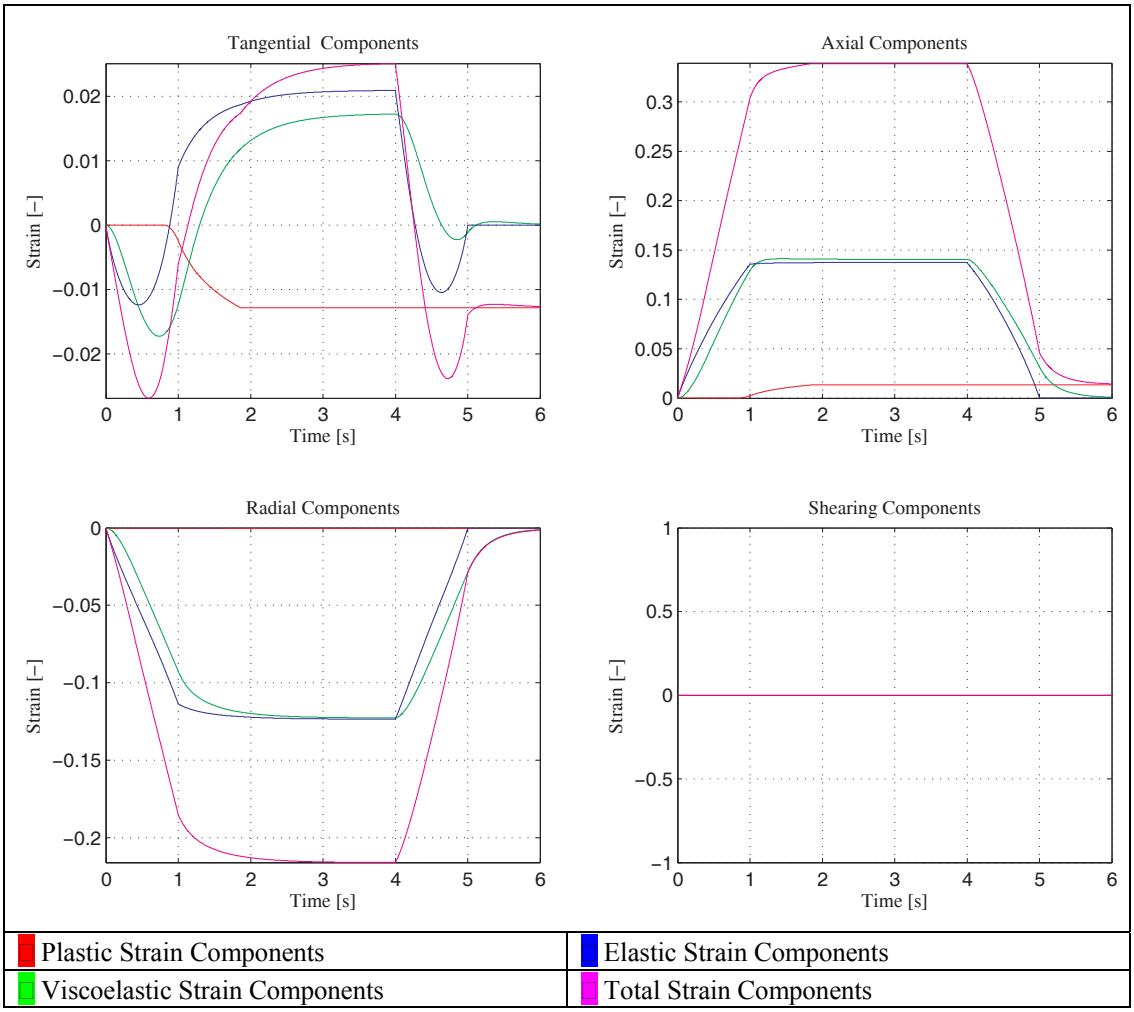

Figure 11.28 : Strain Components During a Viscoelastoplastic Analysis of Axisymetric Tube as to details provided Section 11.2.2

Table 11.10: Material Properties Used for Isotropic Viscoelasticity and Anisotropic Plasticity Analysis

Elastic ψ	C_1^e [kPa]	C_2^e [kPa]	α^e [-]		
	23.243	6.627	3.894		
Viscous ψ	C_1^v [kPa]	C_2^v [kPa]	α^v [-]		
	23.243	6.627	3.894		
Dissipation Φ	η_{GS} [kPa]	η_f [kPa]	α^f [-]		
	15.005	0.0	0.0		
Damage Q	Q_∞ [-]	δ [-]			
	0.0	0.0			
Plasticity	$\dot{a}$ [1/s]	g_0 [kPa]	g_∞ [kPa]	h_0 [kPa]	k [-]
	0.83	14	44	150	10

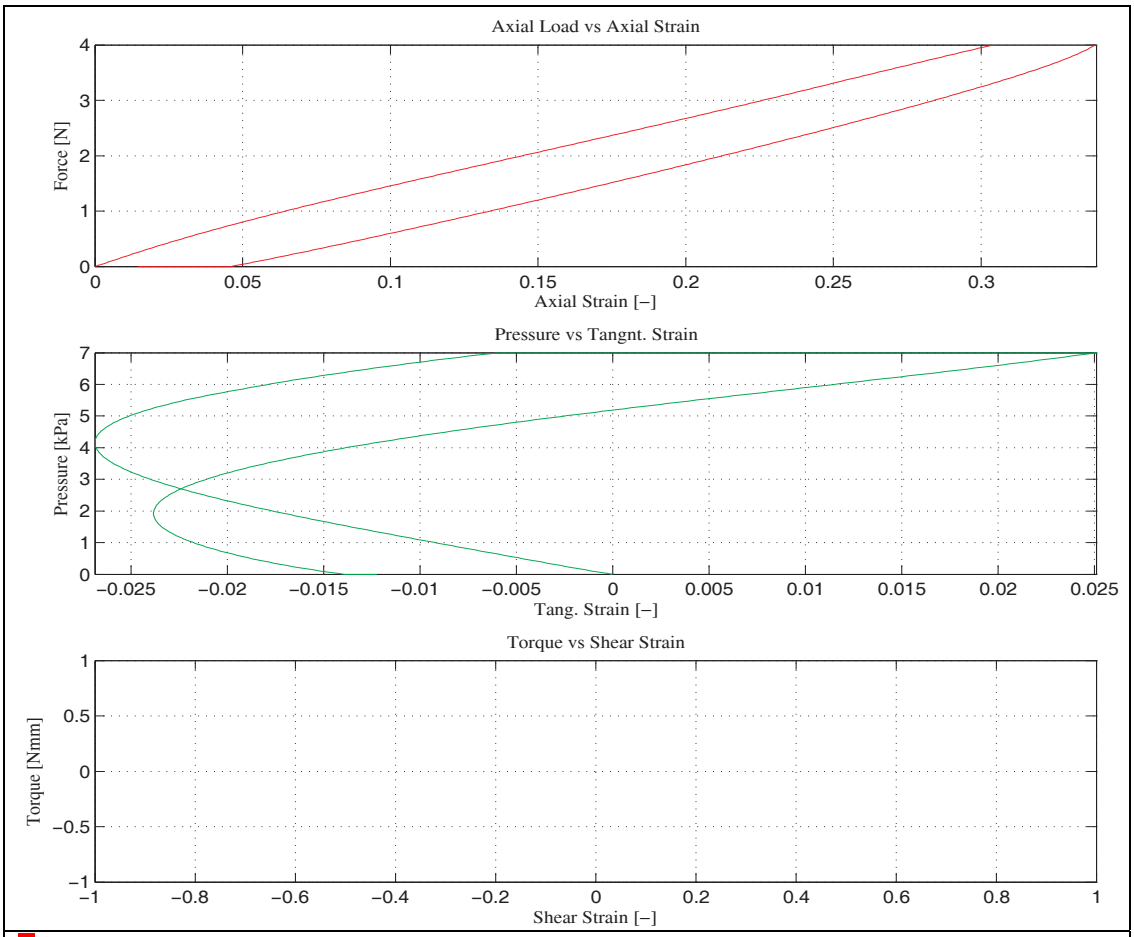

Variation of Axial Force with respect to. Axial Strain during Simulation

Variation of Internal Pressure with respect to. Tangential Strain during Simulation

Variation of Torsional Torque with respect to Shearing Strain during Simulation

Figure 11.29 : Load-Deformation Curves During anViscoelastoplastic Analysis of Axisymetric Tube as to details provided Section 11.2.2

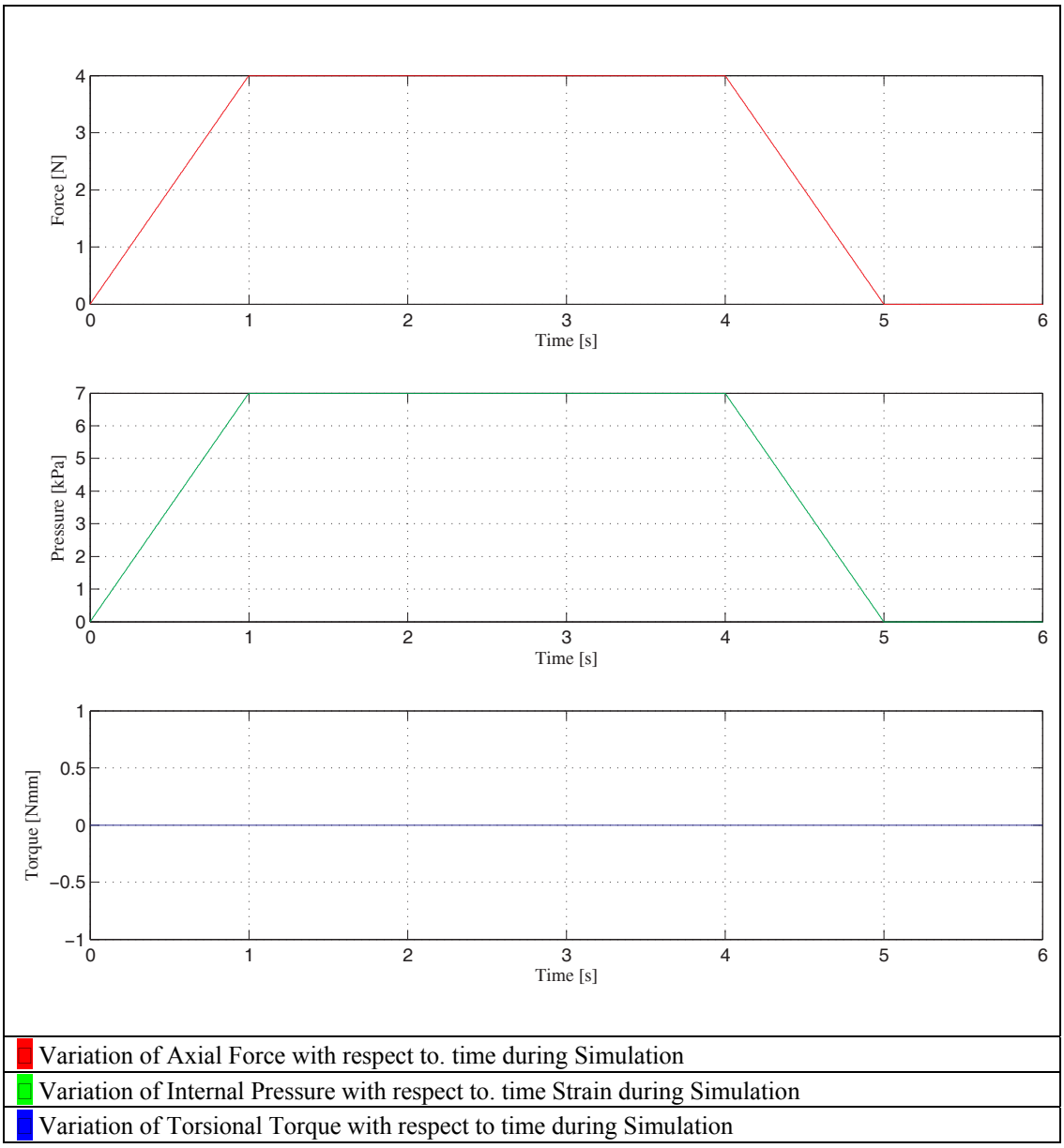

Figure 11.30 : Load-Deformation Curves During anViscoelastoplastic Analysis of Axisymetric Tube as to details provided Section 11.2.2

12. EXPERIMENTAL METHOD FOR PARAMETER ESTIMATION

Any material model is useful when there is some (easy) way for determining its material parameters.

12.1. The Experimental Setup

The experiments for material parameter estimation have been carried out in the Laboratory of Strength of Materials and Biomechanics, Faculty of Mechanical Engineering, Istanbul Technical University. The facilities used and details on the experiments are provided below.

Figure 12.1 : Laboratory of Strength of Materials and Biomechanics, Istanbul Technical University, Faculty of Mechanical Engineering

12.1.1. Layout of the Setup and Measurement Principles

The aim of the current work is to apply the arterial specimens independently controlled Axial/Torsional loads along with internal pressure and displacements in static or dynamic environments and record the deformation values due to these loads. For some experiments, it is also possible to run the system displacement controlled, but not strain controlled.

The following equipment have ben used throughout the experimental studies:

- The mainframe MTS 858 Mini Bionix II Axial / Torsional System, with 3-channel input and controller loops.
- 50N/2Nm Axial/Torsional Loadcell (Novatech, Type F310UFR0H0 Serial No: 37669)
- 1-bar differential Pressure Transducer (HBM Model PD1, $\Delta p = 1$ bar, Serial No: 7909)
- Positive Displacement Water Pump (FLUID-E-TECH Type MGP80 Serial No: 0385
- Synchronous Servomotor with analogue Control (Sew-Eurodrive Controller Model MDX61B) to enable dynamic pressure application and control
- HAAKE (Berlin) WaterBath System
- Quasi-Static Image Capturing Cameras (ATV DOLPHIN Type DCD2.0 Serial No: 00372751 and 00405555)
- High-Speed Image Capturing Cameras (Photron Fastcam 1024PCI Serial No: 145506109 and 145506110)
- Optical Strain Calculation System (VIC3D2006 Software, LIMESS GmBH)
- BOEWE Illumination Kit and Additional High-Performance Illumination of approximately 2000W total illumination power

The connectors and the mounting system has been designed neatly in full symmetry where available to enable exact symmetrical mounting of the arterial specimen, and prohibit any interference among different quantities applied. The experimental system has been set up as sketched in Figure 12.2 and photographs are provided in Figures12.3 and 12.4.

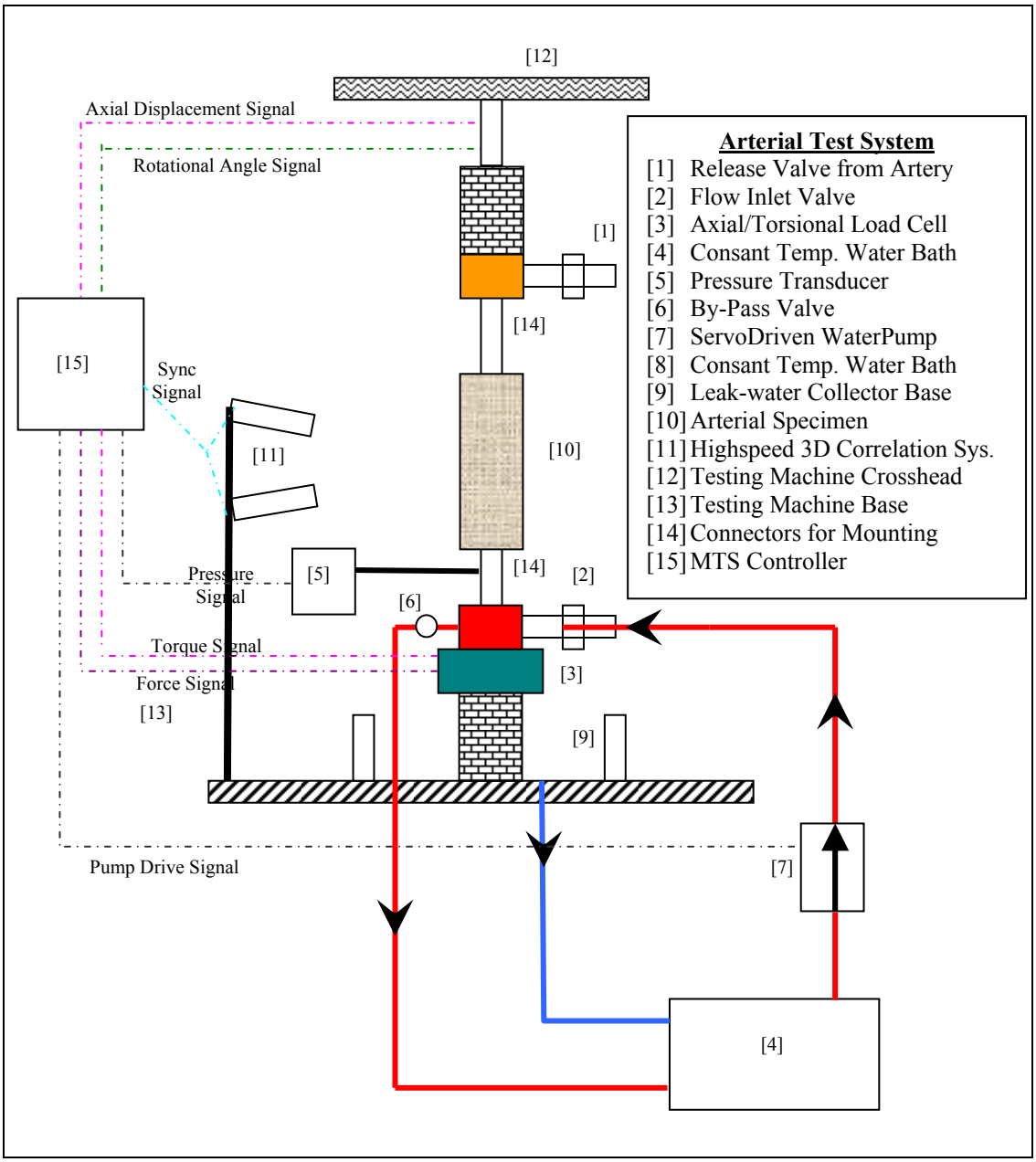

Figure 12.2 : Layout of the Experimental Setup

Throughout the experiments and numerical data evaluation :

- Due to gravitational effects, the vertical variation of the pressure within the arterial specimen has been neglected. A sample height of approximetly 50 mm and water density of 1 gr/cm^3, results in less than 5 mbar pressure difference. At a minimum of 5 kPa internal pressure, the pressure is difference is less than 10% from top to bottom.

- The inertial effects of arterial wall during dynamic deformations have been neglected.
- The inertial effects of water contained in the artery during dynamical deformation have been neglected.
- Dissipation due to viscous effects of contained water has been neglected.
- Specimen behavior measured around a point is assumed to be homogeneous

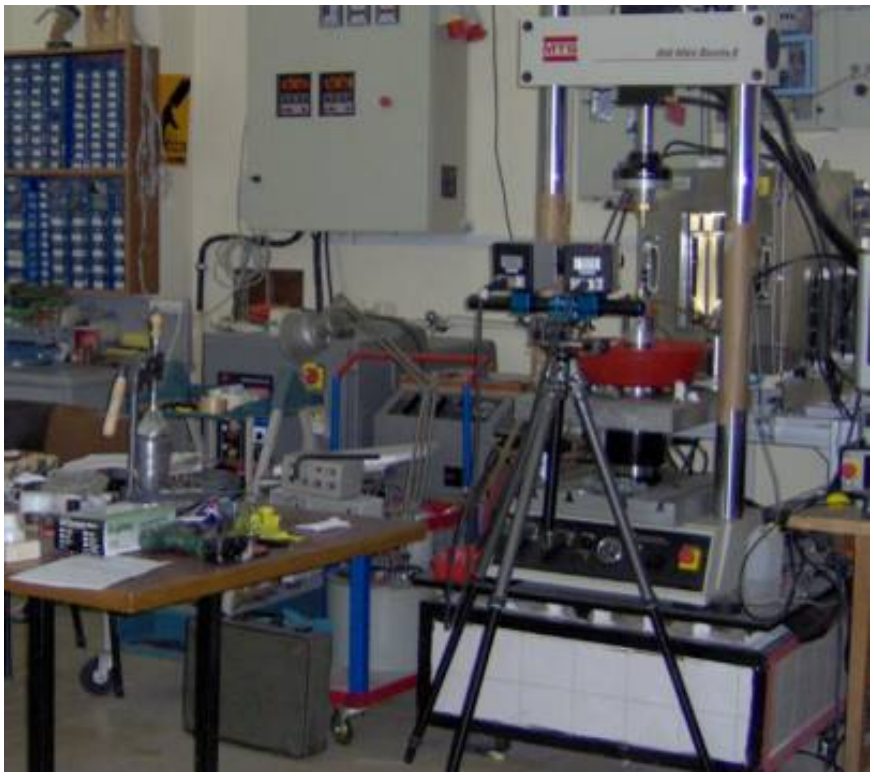

Figure 12.3 : View of Testing System During Set-up with the High Speed Cameras

12.1.2. Specimen Preperation

In the experimental procedure, pulmonary arteries harvested from lambs have been used. The lamb were 12 months old on average. The vast availability of sheep pulmonary arteries have been the factor for choosing this specimen. The “raw” form of the arteries while being harvested from the slaughterhouse is given in Figure 12.5.

Figure 12.4 : View of Testing System with Illumination and Artery Mounted

Figure 12.5 : Harvesting of Pulmonary Arteries by author.

The arteries then are treated by a plastic surgeon, and resulted in specimens as shown in Figure 12.6. In this step, the outer tissues other than the arterial wall, which are mainly fat, muscles and protective membranes, have been removed neatly. The most important part of this stage has been looping of the secondary branches that diverge from the main tube. Standart surgical ropes have been used during looping, to ensure the tightness. This enabled the application of internal pressure to the vessel with water. Being fixed to the connectors and then to the testing system, as in Figure 12.7, the specimens have been treated with contrast powder for optical strain measurements.

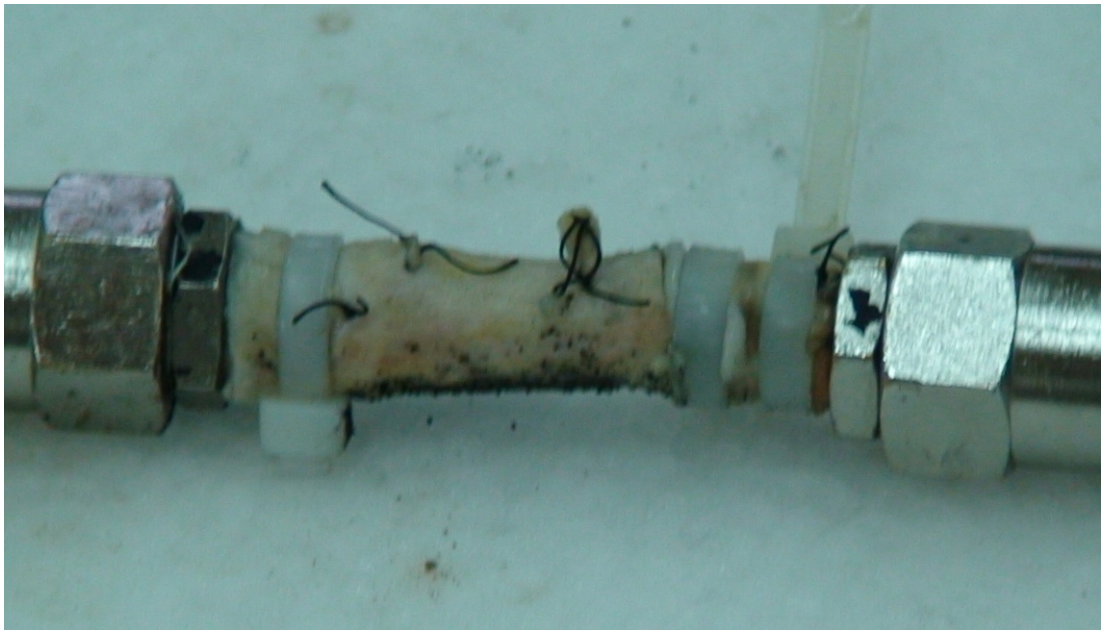

Figure 12.6: The secondary branches on the lamb pulmonary artery that have been closed with the aid of Plastic Surgeon Burcak ERDINC, M.D.

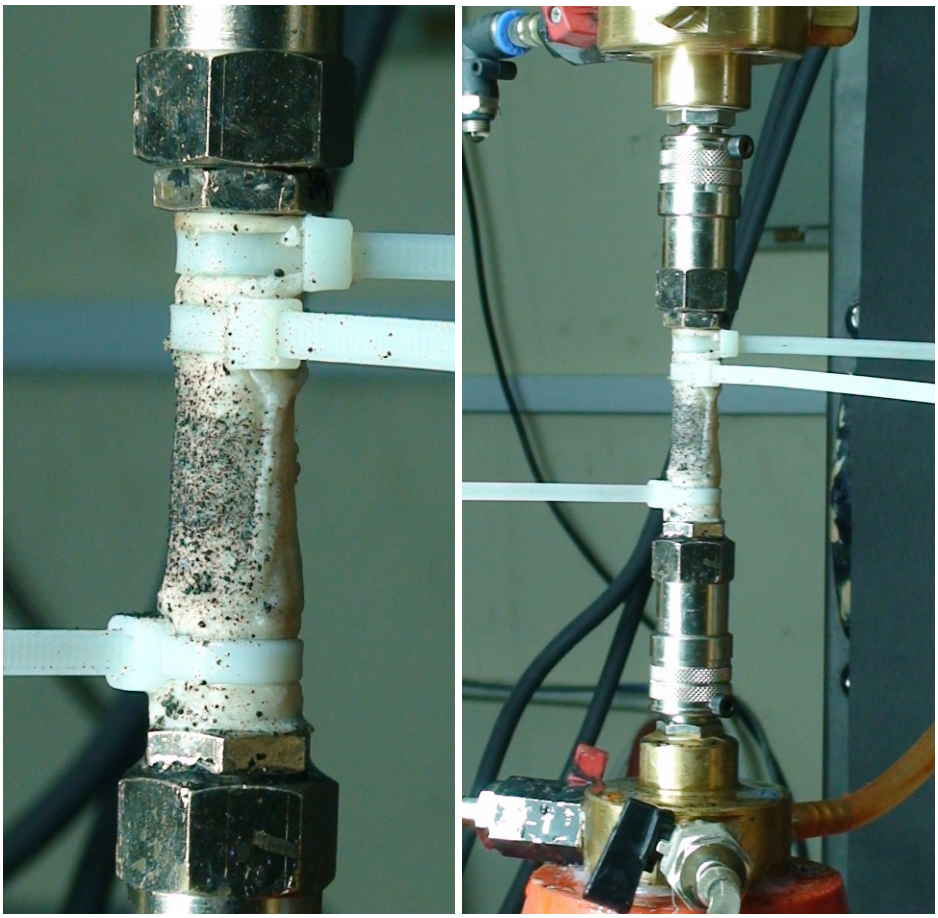

Figure 12.7 : The Speckled Artery Connected to the Testing System.

Figure 12.8 : A demonstration of PreStress in Arterial Tissue.

12.1.3. Experimental Loading Protocols for Specimens

Within the theoretical model and the testing system, the following parameters are available for controlling

- Axial Force
- Internal Pressure
- Torsional Moment
- Axial Displacement of Crosshead
- Torsional Rotation of Crosshead

These quantities can either be fixed constant or time-varied. For a viscoelastic material,

- Creep / relaxation behaviour
- Response to Harmonic excitation

are important loading protocols for determination of characteristics.

An illustrative sequence of pictures from real tests are provided in Figure 12.9 to Figure 12.12, with the strains overlayed on deformation.

The loading protocol is a complex axial/ torsional loading which has been presented in Section 12.3.4

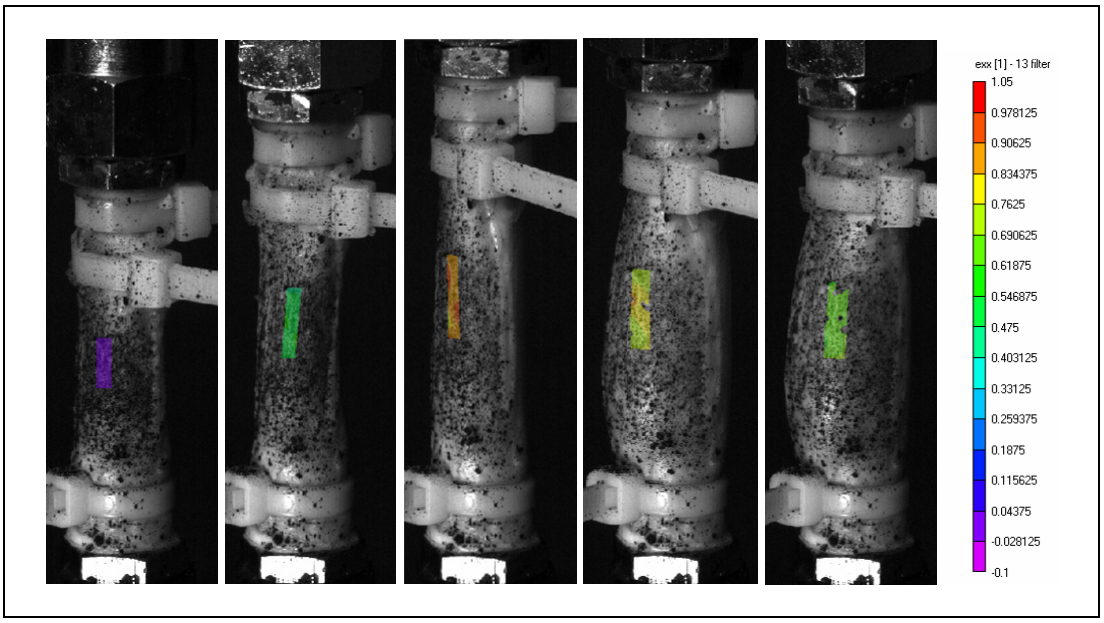

Figure 12.9 : Sample pictures from a loading protocol and respective Axial Lagrangian Strain values superposed over deformed arterial specimen

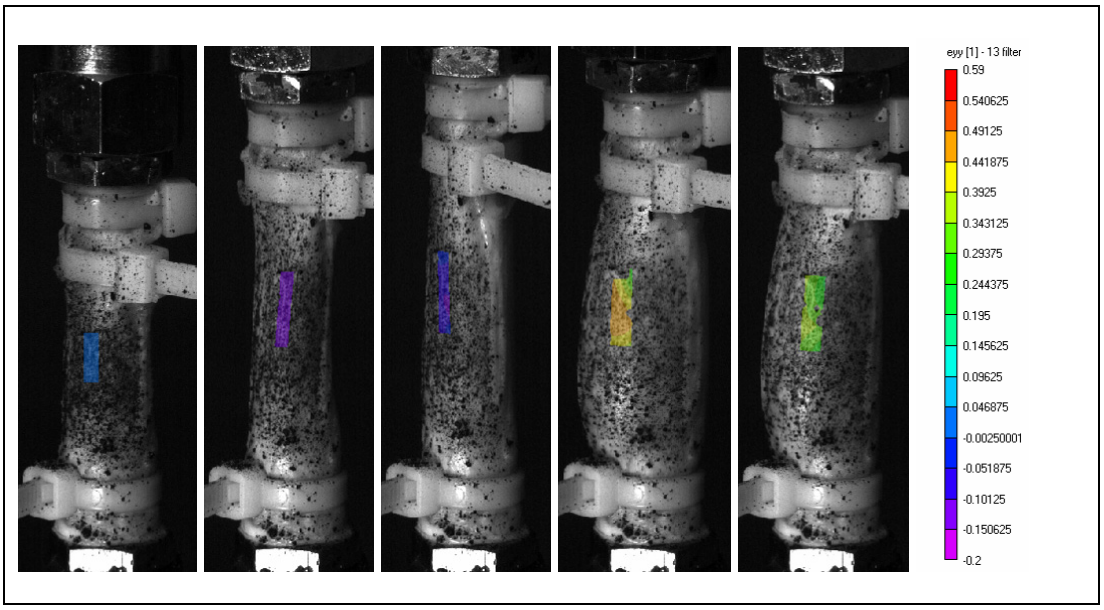

Figure 12.10 : Sample pictures from the loading protocol same in Figure 12.9 and respective Tangential Lagrangian Strain values superposed onto.

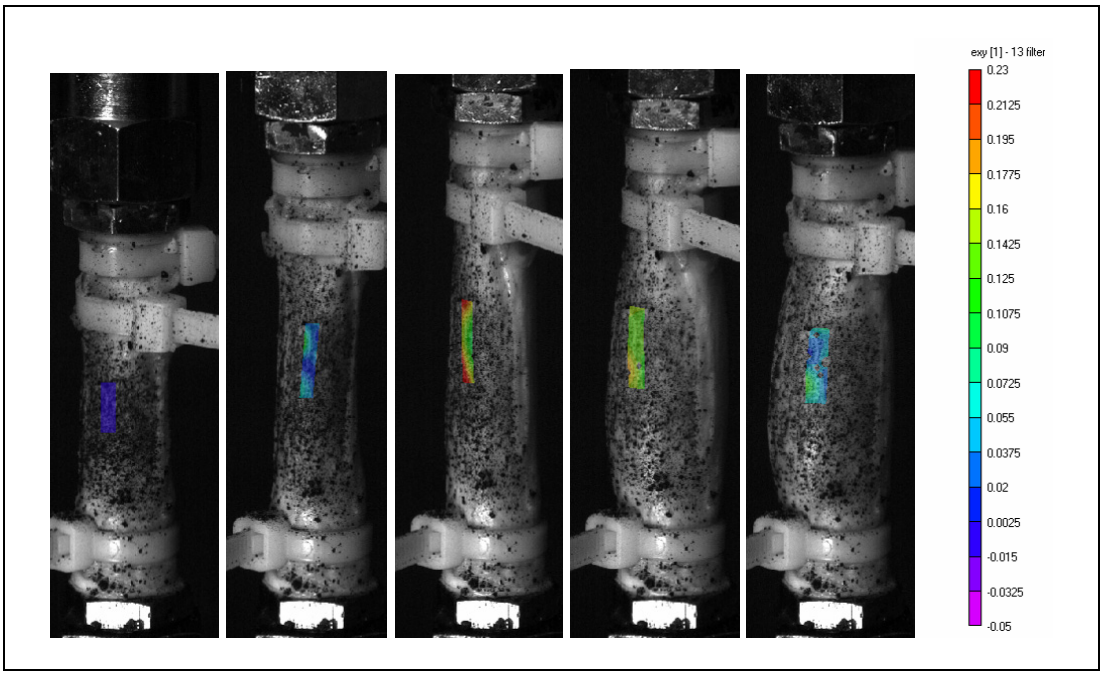

Figure 12.11 : Sample pictures from the loading protocol same in Figure 12.9 and respective Shearing Lagrangian Strain values superposed onto.

12.2. Numerical Data Evaluation

To run the data evaluation process, scalar equations of state are required to solve the differential equations of tensorial variables.

The thing to notice is that, all the deformation measurements are carried on on the *outer surface* of the specimen mounted to the testing machine. However, the theory for a thick walled tube suggests integration of variables that vary with the radial coordinate. Thus, a relation should be established that propagates the "outer" deformation throughout the wall thickness.

Using the definition

$$F_e(2,2)(r,\rho)=\frac{r}{\rho} \qquad \textbf{(12-1)}$$

For the outer surface, this reads

$$F_e(2,2)(r=b,\rho=\beta)=\frac{b}{\beta} \qquad \textbf{(12-2)}$$

The incompressibility condition

$$b^2 - r^2 = \frac{1}{\lambda_e}\left(\beta^2 - \rho^2\right) \tag{12-3}$$

furnishes and the tangential stretch becomes

$$\frac{r}{\rho} = \frac{r}{\left[\lambda_e\left(r^2 - b^2\right) + \beta^2\right]^{1/2}} \tag{12-4}$$

that depends only on r. Non dimensional forms can be obtained with

$$\frac{r}{\rho} = \frac{b\dfrac{r}{b}}{\beta\left[\lambda_e\left(\dfrac{r^2}{b^2\dfrac{\beta^2}{b^2}} - \dfrac{b^2}{\beta^2}\right) + 1\right]^{1/2}} \tag{12-5}$$

and simplifying it reads

$$\frac{r}{\rho} = \frac{b}{\beta}\frac{\dfrac{r}{b}}{\left[\lambda_e\dfrac{b^2}{\beta^2}\left(\dfrac{r^2}{b^2} - 1\right) + 1\right]^{1/2}}$$

If one lets

$$\frac{b}{\beta} = K \tag{12-6}$$

and

$$\frac{r}{b} = y \tag{12-7}$$

$$\frac{r}{\rho} = K\frac{y}{\left[\lambda_e K^2\left(y^2 - 1\right) + 1\right]^{1/2}} \tag{12-8}$$

Further more, since the deformation is two-fold (i.e., there is the intermediate configuration), one needs the same procedure for also the viscoelastic intermediate deformation

$$F_v(2,2)(\rho,R)=\frac{\rho}{R} \tag{12-9}$$

$$F_v(2,2)(\rho=\beta,R=B)=\frac{\beta}{B} \tag{12-10}$$

The incompressibility in this stage reads and furnishes

$$\frac{\rho}{R}=\frac{\left[\lambda_e\left(r^2-b^2\right)+\beta^2\right]^{1/2}}{\left[\lambda_e\lambda_v\left(r^2-b^2\right)+B^2\right]^{1/2}} \tag{12-11}$$

$$\frac{\rho}{R}=\frac{b\left[\lambda_e\left(\frac{r^2}{b^2}-1\right)+\frac{\beta^2}{b^2}\right]^{1/2}}{b\left[\lambda_e\lambda_v\left(\frac{r^2}{b^2}-1\right)+\frac{B^2}{b^2}\right]^{1/2}} \tag{12-12}$$

$$\frac{\rho}{R}=\frac{\left[\lambda_e\left(y^2-1\right)+\frac{1}{K^2}\right]^{1/2}}{\left[\lambda_e\lambda_v\left(y^2-1\right)+\frac{B^2}{b^2}\right]^{1/2}} \tag{12-13}$$

with the change of variables again $\frac{b}{\beta}=K$ and $\frac{r}{b}=y$ again

Similar procedures can also be carried out for shearing components:

$$F_v(2,3)=\rho\varphi_v=b\frac{\rho}{b} \tag{12-14}$$

$$\rho\varphi_v=b\left[\lambda_e\left(\frac{r^2}{b^2}-1\right)+\frac{\beta^2}{b^2}\right]^{1/2}\varphi_v \tag{12-15}$$

$$\rho\varphi_v = K\left[\lambda_e\left(y^2-1\right)+\frac{1}{K^2}\right]^{1/2}\beta\varphi_v \qquad \textbf{(12-16)}$$

The $\beta\varphi$ values are measured directly.

It is easy to notice the high level of nonlinearity involved in these equations. But besides, there is the important fact that, if one knows the deformation and its discrimination among the two presumed stages of deformation, the variation of deformation along the wall thickness can be calculated, with the aid of incompressibility. Thus, the evolution equation needs only be solved at one point throughout the wall thickness. Readily, this point is chosen to be the outer surface, where the measured quantities for deformation are exactly known.

12.2.1. Algorithm

Any parameter estimation algorithm has a form of minimizing the error residual. What is employed here is somewhat the same thing, with additional cases that enable the specific model run. A simple flowchart of the parameter estimation algorithm is given in Figure 12.12.

Unfortunately, no experiment in a single run can let the identification of material parameters in a non-linear model. For a model to be valid for a very extended rage of loading and deformation conditions, many combinations of stress-strain states should be traced with experiments. The simplest case of isotropic Mooney-Rivlin rubber is a well known example to this phenomenon, where, if biaxial tests are not conducted, the estimated material parameters may exhibit instable or over-stiff behaviour.

Regarding the stated issue, an algorithm has been derived that would include many different loading protocols applied on the *same* specimen, to find a set of coefficients for one specimen with as many points in strain energy space as possible.

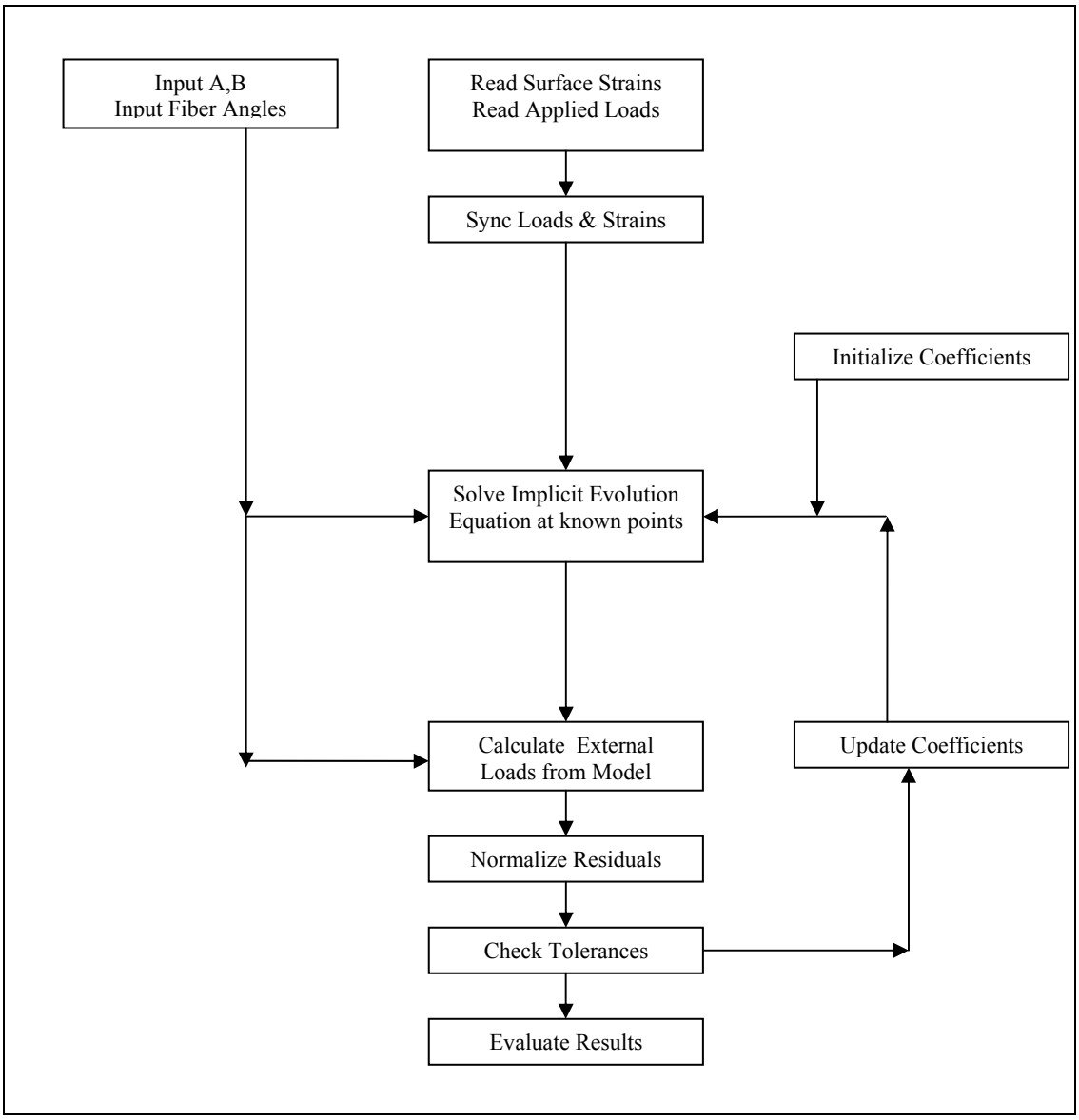

Figure 12.12 : Simple layout of algorithm

The main problem in the proposed model is the multiplicative decomposition of total deformation. One should find how the deformation of either part has taken place. This needs the solution of a differential equation (nonlinear, first order in time) "as time goes by".

For experimental data, however, this is not possible due to the fact that digital sampling is *discrete*. Thus, the problem is formulated based on the deformation history, and the evolution of internal state variables are tracked, with

$$\mathbf{F}_v(t=0)=\mathbf{I} \qquad \textbf{(12-17)}$$

as the initial condition. Since the nonlinear differential equation of evolution can only be evaluated at discrete time points, the problem has been formulated as a solution of series of implicit equations for rate which is simply of the form

$$f\left(\left(\mathbf{F}_v\right)_i, \frac{\left(\mathbf{E}_v\right)_i - \left(\mathbf{E}_v\right)_{i-1}}{\Delta t}\right) = g\left(\left(\mathbf{F}_v\right)_i, \left(\mathbf{F}_e\right)_i\right) \qquad \textbf{(12-18)}$$

with the material parameters *unknown*.

The parameters input to the parameter estimation software are

- The fiber angles for the two families of fibers
- The initial radius and thickness values
- The sample rates of the data files for (a)strains (b)loads

The software

- synchronizes the data in both files
- makes any unit conversion if necessary
- form strain and deformation gradient tensors

automatically, and then starts the parameter estimation algorithm.

The load estimation layout is two-fold:

1. Solve the evolution equation and find the distribution of $\mathbf{F} = \mathbf{F}_e\mathbf{F}_v$

    a. Set $\mathbf{F}_v{}^j = \mathbf{F}_v{}^{j-1}$ as initial condition

    b. Solve $\mathbf{F}_e{}^j = \mathbf{F}^j\left(\mathbf{F}_v{}^{-1}\right)^j$

    c. Calculate $\dot{\mathbf{F}}_v{}^j = \dfrac{\mathbf{F}_v{}^j - \mathbf{F}_v{}^{j-1}}{\Delta t^j}$ and $\dot{\mathbf{E}}_v{}^j = \dfrac{1}{2}\left(\dot{\mathbf{F}}_v{}^T\mathbf{F}_v + \mathbf{F}_v{}^T\dot{\mathbf{F}}_v\right)^j$ (Implicit)

d. Calculate $\frac{1}{2}\left(\frac{\partial \Psi_e}{\partial \boldsymbol{\Gamma}_e}\mathbf{C}_e + \mathbf{C}_e\frac{\partial \Psi_e}{\partial \boldsymbol{\Gamma}_e}\right) - \mathbf{F}_v\left(\frac{\partial(1-Q)\Psi_v}{\partial \mathbf{E}_v} + \frac{\partial \Phi}{\partial \dot{\mathbf{E}}_v}\right)\mathbf{F}_v^{\,T} = \mathbf{e}$

e. Due to kinematics of deformation, the only independent terms are $e(2,2)$, $e(2,3)$ and $e(3,3)$, that turns the system into 3 equations in 3 unknowns, that are namely ρ, φ and Λ.

f. Iterate until $e(2,2)$, $e(2,3)$ and $e(3,3)$ are zero (less than tol.; i.e. 10^{-6}).

2. Calculate external load values using

   a. Stresses at a radial cross-section of the wall using

      i. the theoretical stress/strain relations

      ii. radial distribution of strains

   b. External applied loads with formulas via integrating as to formulae in Sections 5.3.4 to 5.3.6.

As the "theoretical" and "experimental" loads are known, than the residuals can be calculated as

$$r^j = \left(\begin{bmatrix} w_p{}^2 & w_N{}^2 & w_M{}^2 \end{bmatrix} \begin{bmatrix} \left(p_i{}^{teo} - p_i{}^{\exp}\right)^2 \\ \left(N^{teo} - N^{\exp}\right)^2 \\ \left(M_b{}^{teo} - M_b{}^{\exp}\right)^2 \end{bmatrix} \right)^j \qquad \textbf{(12-19)}$$

for each experimental data point. The $\mathbf{w}$ vector is the weights vector that homogenizes the orders of errors among different variables. In this study, they are adjusted so that they convert each difference to its Cauchy Stress Component - Von-Mises Equivalent:

$$\mathbf{w} = \left[\left(0.97\frac{b_2 + a_2}{(b_2 - a_2)}\right) \quad \left(\frac{1}{\pi\left(b_2{}^2 - a_2{}^2\right)}\right) \quad \left(1.73\frac{b_2}{\pi\left(b_2{}^4 - a_2{}^4\right)}\right) \right] \qquad \textbf{(12-20)}$$

Notice that b_2 and a_2 are the *deformed* outer and inner radii respectively, and vary with the deformation. The sum-of-square of residuals for a test is then again normalized to number of points in a test so that a test with many points does not "over-stiffen" the system.

A detailed layout of the whole scheme is provided in Figure 12.13. The whole algorithm is employed in MATLAB software with using standard built-in optimization routines that use the Levenberg-Marquart algorithm.

To ensure material stability (since L/M routines in MATLAB does not allow bound constraints) the material coefficients are normalized to "squares" of varying coefficients that lie in the range -1 to 1.

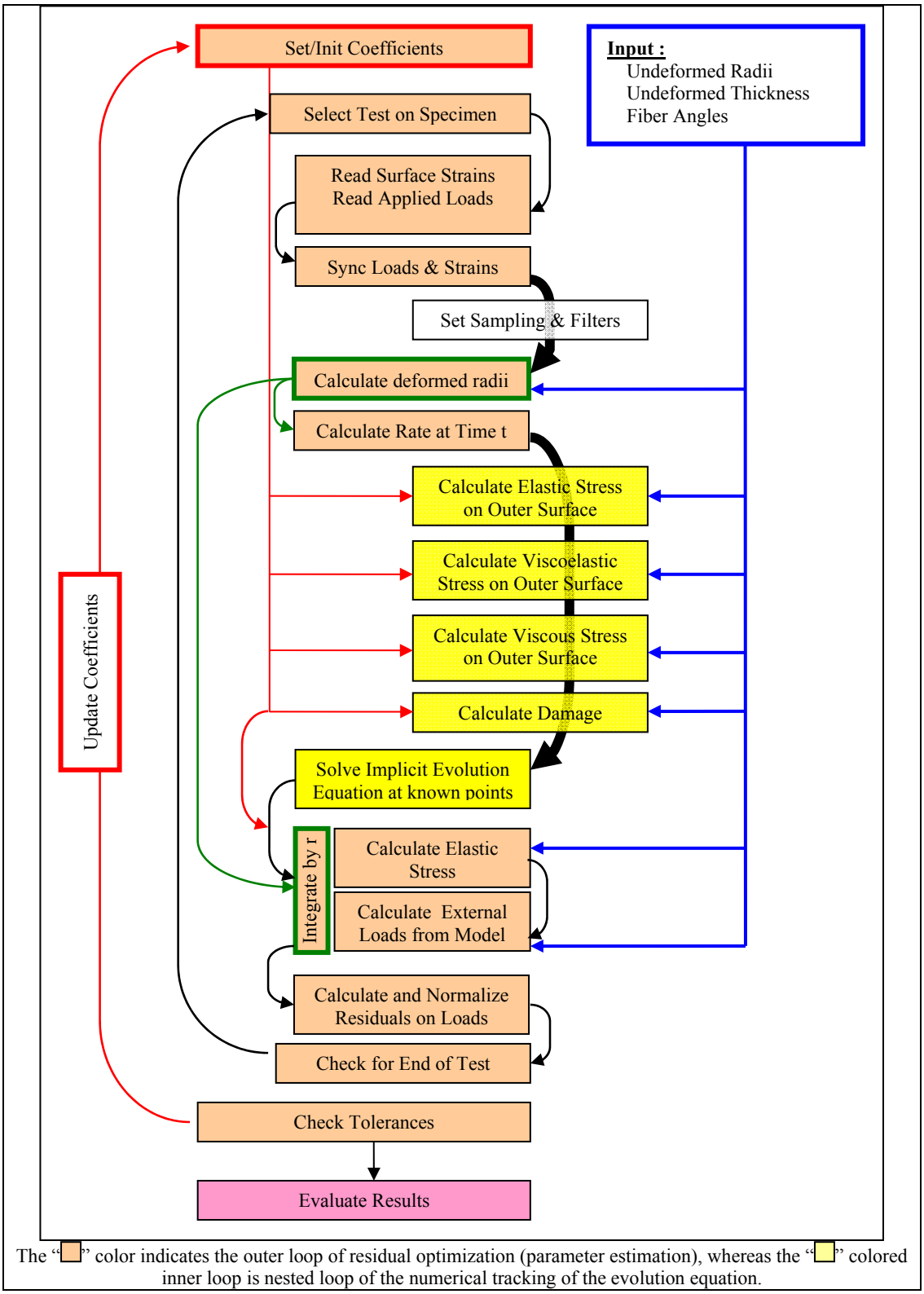

Figure 12.13 : The flowchart of parameter estimation algorithm

12.3. Experimental Loading Protocols for Elastic Parameter Estimation

12.3.1. Summary of Tests Performed

Since the arterial tissue exhibits multi-dimensional behavior, it is a necessity that in the strain energy space, the experimental data should sweep as much points as possible. Thus, unlike isotropic engineering materials such as steel, brass, uniaxial tension tests are not capable of being complete in terms of defining the material's behavior within any loading protocol. In nonlinear mechanics, multi dimensional tests have to be carried on (even for rubber, which is a (mostly) material of isotropy) to capture multi-dimensional stress/deformation behavior. Moreover, our material of interest is

a) continuous fiber-reinforced composite

b) tubular in shape

c) "thick-walled" in the sense that at the beginning the diameter to thickness ratio is lower than 10%.

Regarding these issues, a series of tests have been performed on the prepared specimens of sheep pulmonary arteries. The sample loading protocols that have been considered for parameter estimation are discussed in the next titles. It has to be mentioned that, since the artery is very weak with respect to torsional loading, especially at low loading ranges, the torsion control has been set to be angular displacement, whereas, the axial and pressure controls are used in "load-control" settings. The tuning of the MTS testing machine for best performance with the large deforming tissue has been performed before the real tests have been carried out.

12.3.2. In-Phase Static Extension and Inflation for Elastic Parameter Estimation

The initial procedure that has been carried on considered on determining elastic properties of the arterial wall. No prestress has been assumed to exist. Extension up to 10N and pressurizing up t0 15 kPa has been applied, and the loads were in phase. The iteration convergence is presented in Figures 12.14 – 12.16.

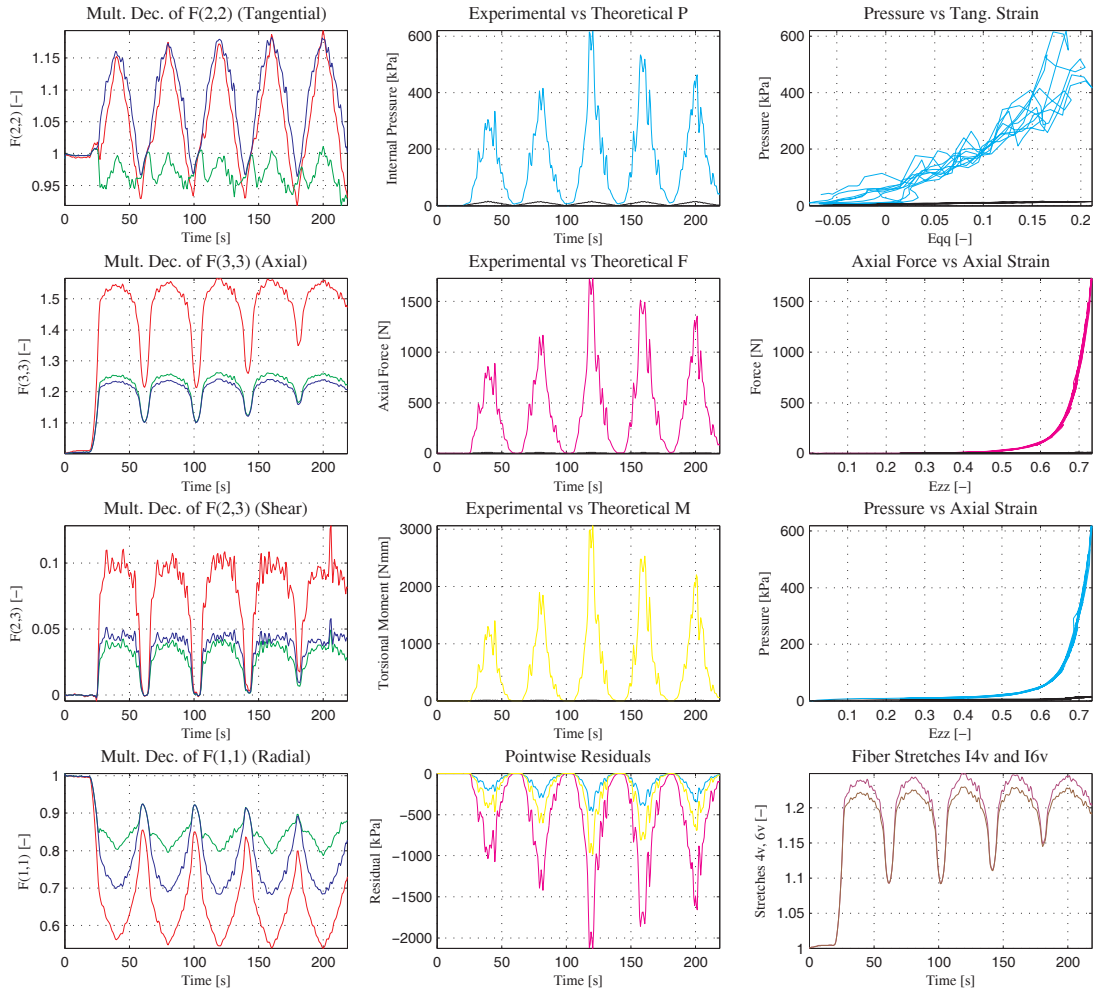

Iteration Plots for 72deg–Whole–Statik–S07 Scenario S07 at Coefficients:
C1e= 60.295 C2e= 15.543 Alphae= 26.138
EtaGS= 0.000 Etaf= 0.000 Alphaf= 0.000
Qinf= 0.000 Delta= 0.000

Experimental Deformation Gradient Component (Ft)	Axial Force Calculated using Theory	Experimentally Determined Values of Corresponding Data in the Plot
Deformation Gradient Component of Intermediate Config. (Fv)	Internal Pressue Calculated using Theory	Stretch of Fiber Family 4 to reach intermediate configuration (of I4v)
Deformation Gradient Component of Pure Elastic Configuration (Fe)	Torsional Moment Calculated using Theory	Stretch of Fiber Family 6 to reach intermediate configuration (of I6v)

Figure 12.14 : Demonstration of Deformation Gradient Components, Comparison of Experimental and Theoretical Data at Initial Iteration as to 12.3.2

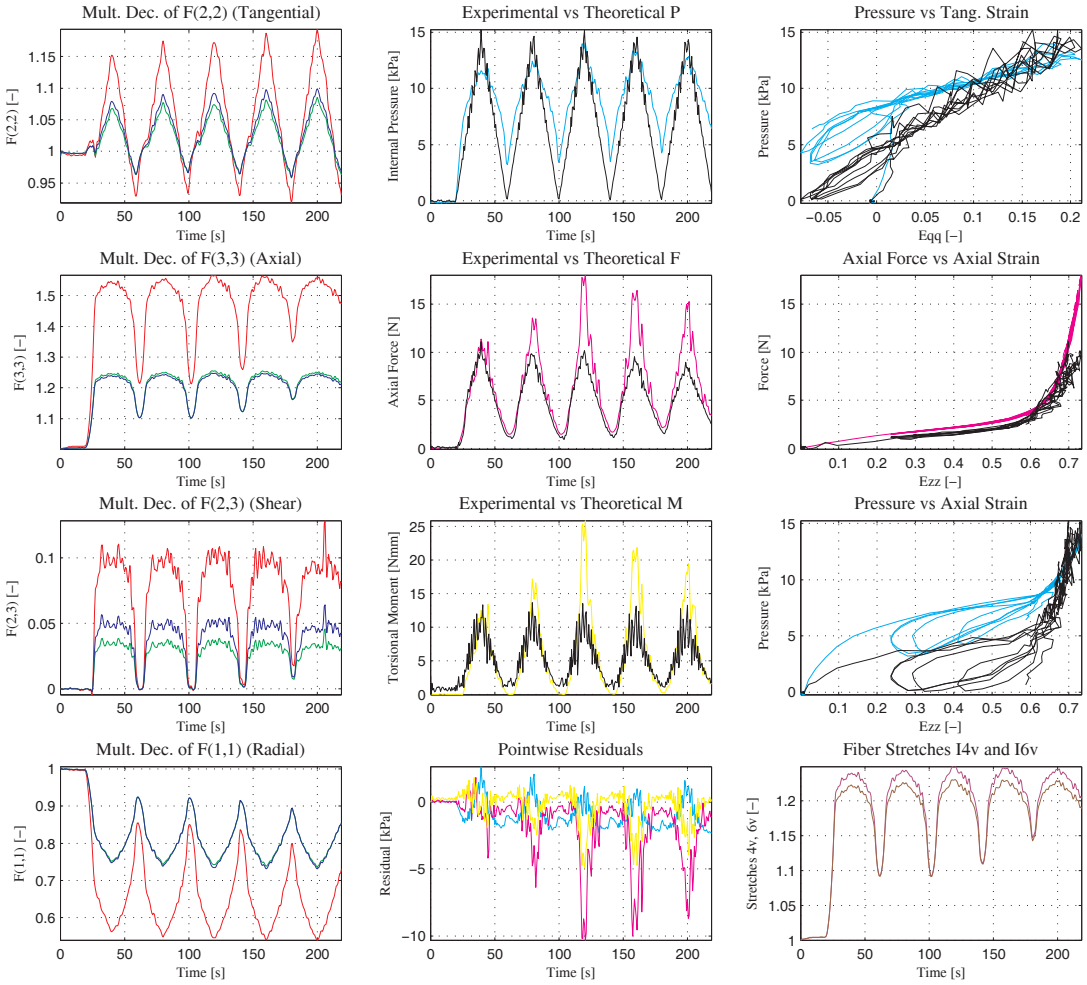

Iteration Plots for 72deg–Whole–Statik–S07 Scenario S07 at Coefficients:
C1e= 41.528 C2e= 0.247 Alphae= 24.475
EtaGS= 0.000 Etaf= 0.000 Alphaf= 0.000
Qinf= 0.000 Delta= 0.000

Experimental Deformation Gradient Component (Ft)	Axial Force Calculated using Theory	Experimentally Determined Values of Corresponding Data in the Plot
Deformation Gradient Component of Intermediate Config. (Fv)	Internal Pressue Calculated using Theory	Stretch of Fiber Family 4 to reach intermediate configuration (of I4v)
Deformation Gradient Component of Pure Elastic Configuration (Fe)	Torsional Moment Calculated using Theory	Stretch of Fiber Family 6 to reach intermediate configuration (of I6v)

Figure 12.15 : Demonstration of Deformation Gradient Components, Comparison of Experimental and Theoretical Data at an Intermediate Iteration as to 12.3.2

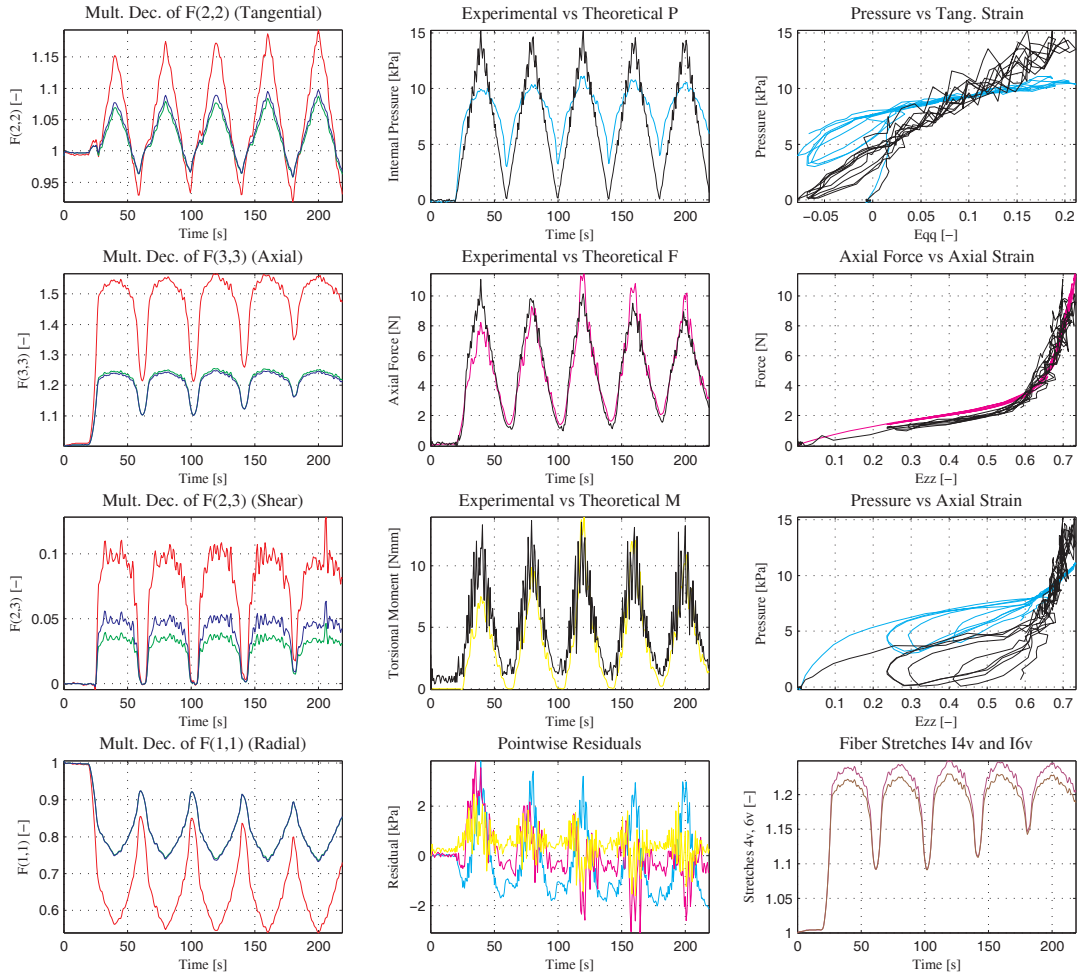

Iteration Plots for 72deg–Whole–Statik–S07 Scenario S07 at Coefficients:
C1e= 38.838 C2e= 0.304 Alphae= 21.074
EtaGS= 0.000 Etaf= 0.000 Alphaf= 0.000
Qinf= 0.000 Delta= 0.000

Experimental Deformation Gradient Component (Ft)	Axial Force Calculated using Theory	Experimentally Determined Values of Corresponding Data in the Plot
Deformation Gradient Component of Intermediate Config. (Fv)	Internal Pressue Calculated using Theory	Stretch of Fiber Family 4 to reach intermediate configuration (of I4v)
Deformation Gradient Component of Pure Elastic Configuration (Fe)	Torsional Moment Calculated using Theory	Stretch of Fiber Family 6 to reach intermediate configuration (of I6v)

Figure 12.16 : Demonstration of Deformation Gradient Components, Comparison of Experimental and Theoretical Data at Convergence Iteration as to 12.3.2

12.3.3. In-Phase Extension, Torsion Inflation for Elastic Parameter Estimation

This time, effect via disturbing the fiber-orientation symmetry has been. considered on determining elastic properties of the arterial wall. No prestress has been assumed to exist. Extension up to 10N, angular displacement of the tube by 20 degrees and pressurizing up to15 kPa has been applied, and the loads were in phase. The iteration convergence is presented in Figures 12.17-12.19.

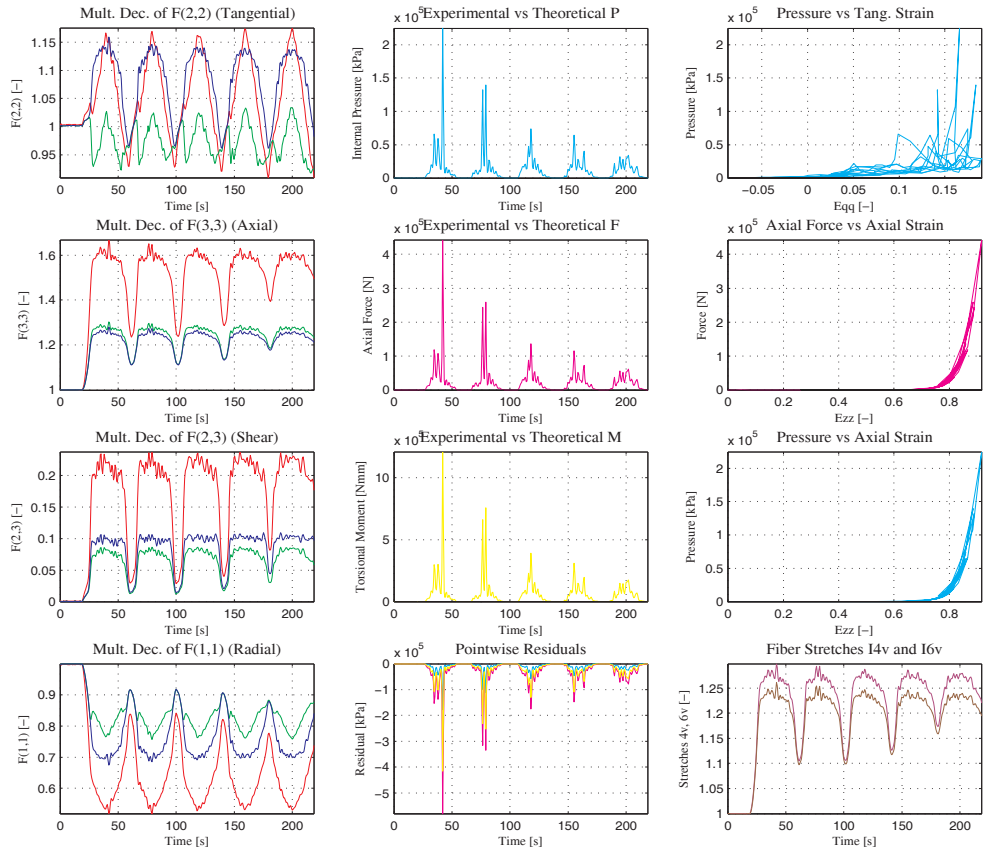

Iteration Plots for 72deg–Whole–Statik–S10 Scenario S10 at Coefficients:
C1e=527.081 C2e= 55.024 Alphae= 26.168
EtaGS= 0.000 Etaf= 0.000 Alphaf= 0.000
Qinf= 0.000 Delta= 0.000

Experimental Deformation Gradient Component (Ft)	Axial Force Calculated using Theory	Experimentally Determined Values of Corresponding Data in the Plot
Deformation Gradient Component of Intermediate Config. (Fv)	Internal Pressue Calculated using Theory	Stretch of Fiber Family 4 to reach intermediate configuration (of I4v)
Deformation Gradient Component of Pure Elastic Configuration (Fe)	Torsional Moment Calculated using Theory	Stretch of Fiber Family 6 to reach intermediate configuration (of I6v)

Figure 12.17 : Demonstration of Deformation Gradient Components, Comparison of Experimental and Theoretical Data at Initial Iteration as to 12.3.3

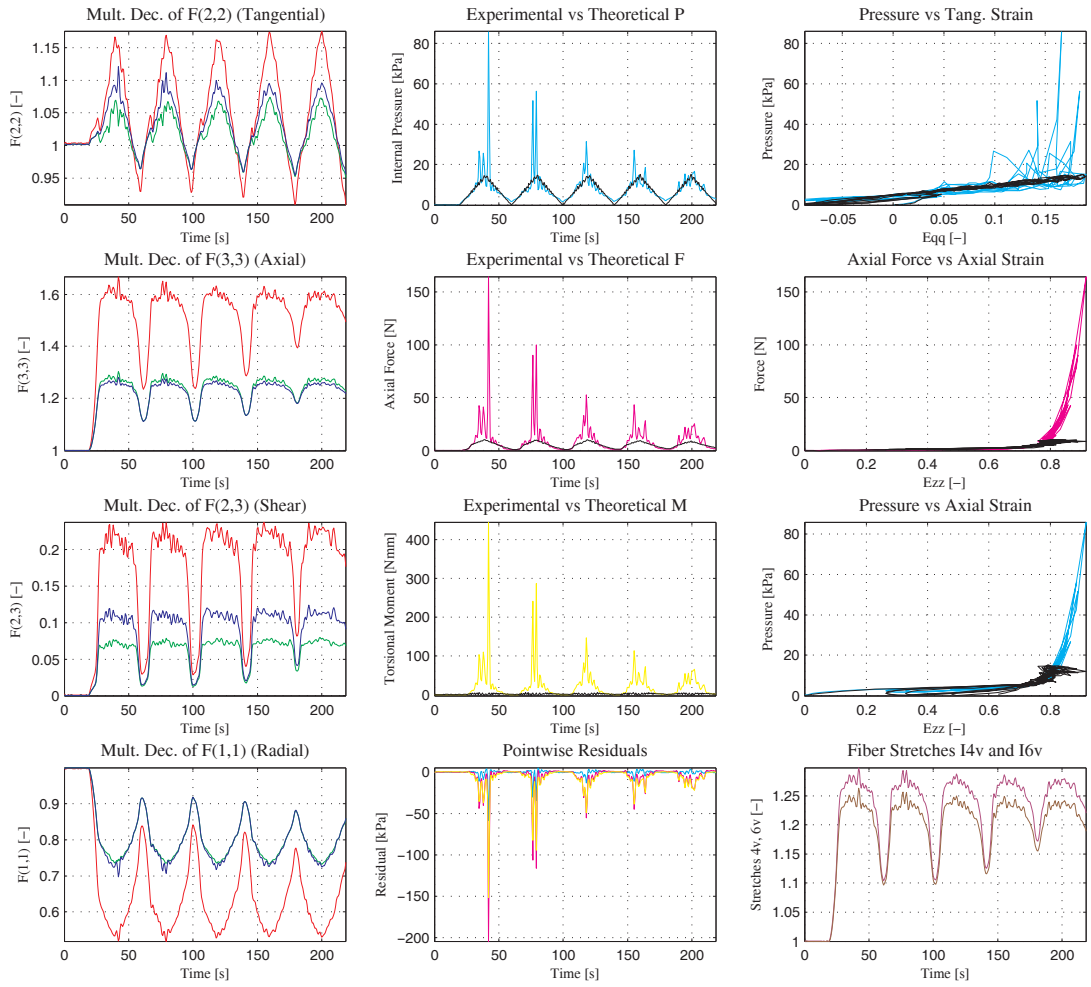

Iteration Plots for 72deg–Whole–Statik–S10 Scenario S10 at Coefficients:
C1e= 19.739 C2e= 0.028 Alphae= 25.875
EtaGS= 0.000 Etaf= 0.000 Alphaf= 0.000
Qinf= 0.000 Delta= 0.000

Experimental Deformation Gradient Component (Ft)	Axial Force Calculated using Theory	Experimentally Determined Values of Corresponding Data in the Plot
Deformation Gradient Component of Intermediate Config. (Fv)	Internal Pressue Calculated using Theory	Stretch of Fiber Family 4 to reach intermediate configuration (of I4v)
Deformation Gradient Component of Pure Elastic Configuration (Fe)	Torsional Moment Calculated using Theory	Stretch of Fiber Family 6 to reach intermediate configuration (of I6v)

Figure 12.18 : Demonstration of Deformation Gradient Components, Comparison of Experimental and Theoretical Data at an Intermediate Iteration as to 12.3.3

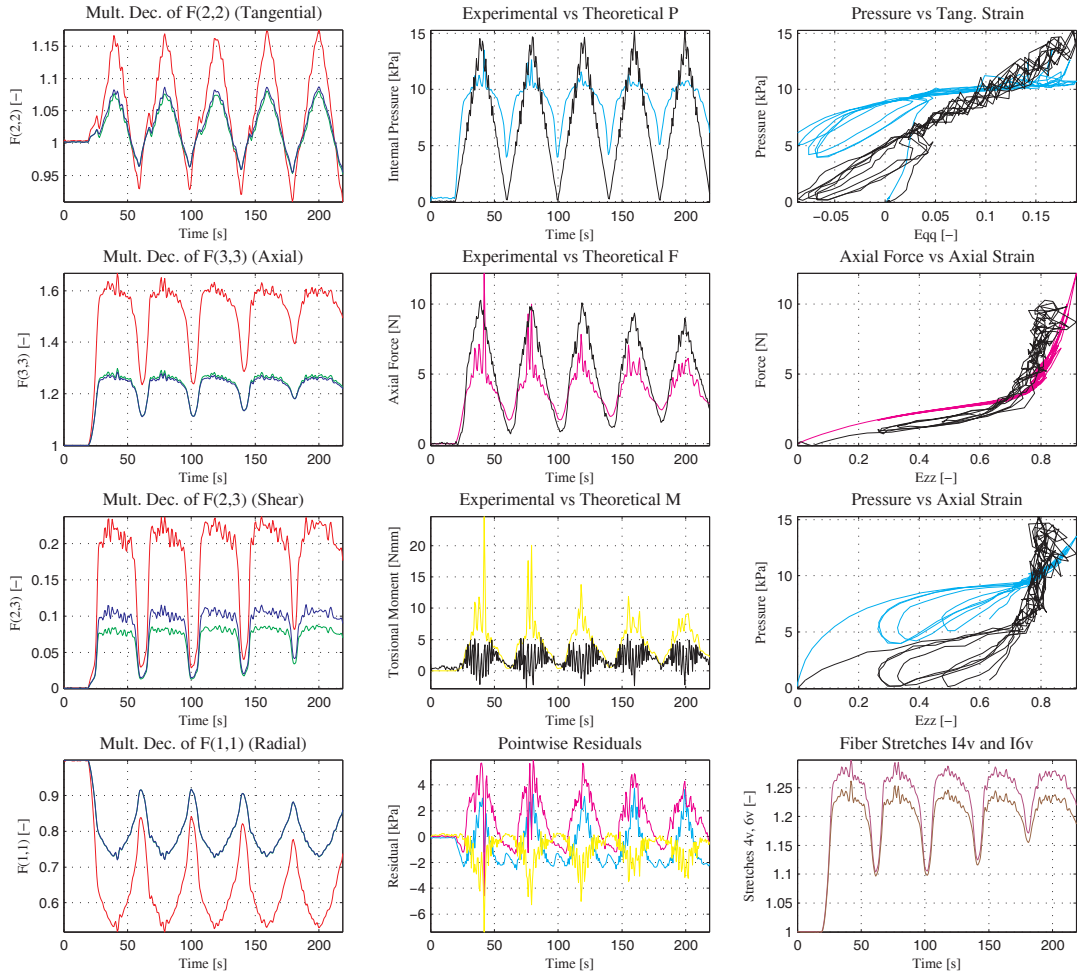

Iteration Plots for 72deg–Whole–Statik–S10 Scenario S10 at Coefficients:
C1e= 44.674 C2e= 0.027 Alphae= 18.743
EtaGS= 0.000 Etaf= 0.000 Alphaf= 0.000
Qinf= 0.000 Delta= 0.000

Experimental Deformation Gradient Component (Ft)	Axial Force Calculated using Theory	Experimentally Determined Values of Corresponding Data in the Plot
Deformation Gradient Component of Intermediate Config. (Fv)	Internal Pressue Calculated using Theory	Stretch of Fiber Family 4 to reach intermediate configuration (of I4v)
Deformation Gradient Component of Pure Elastic Configuration (Fe)	Torsional Moment Calculated using Theory	Stretch of Fiber Family 6 to reach intermediate configuration (of I6v)

Figure 12.19 : Demonstration of Deformation Gradient Components, Comparison of Experimental and Theoretical Data at Convergence Iteration as to 12.3.3

12.3.4. Out-of-Phase Static Extension, Inflation and Torsion for Elastic Parameter Estimation

To see how the material behaves under combination of different load application scenarios, a test has been carried on considered on determining elastic properties of the arterial wall with loads varying with a phase. No prestress has been assumed to exist. Extension up to 10N (Master signal – No Phase), angular displacement varying between -10 and +30 degrees (with a delay of 45 degrees in a load-unload cycle of approximately 40 seconds as 360 degrees) and pressurizing up to 15 kPa (with a delay of 135 degrees in a load-unload cycle of approximately 40 seconds) has been applied, and the loads were in phase. The iteration convergence is presented in Figures 12.20 – 12.22.

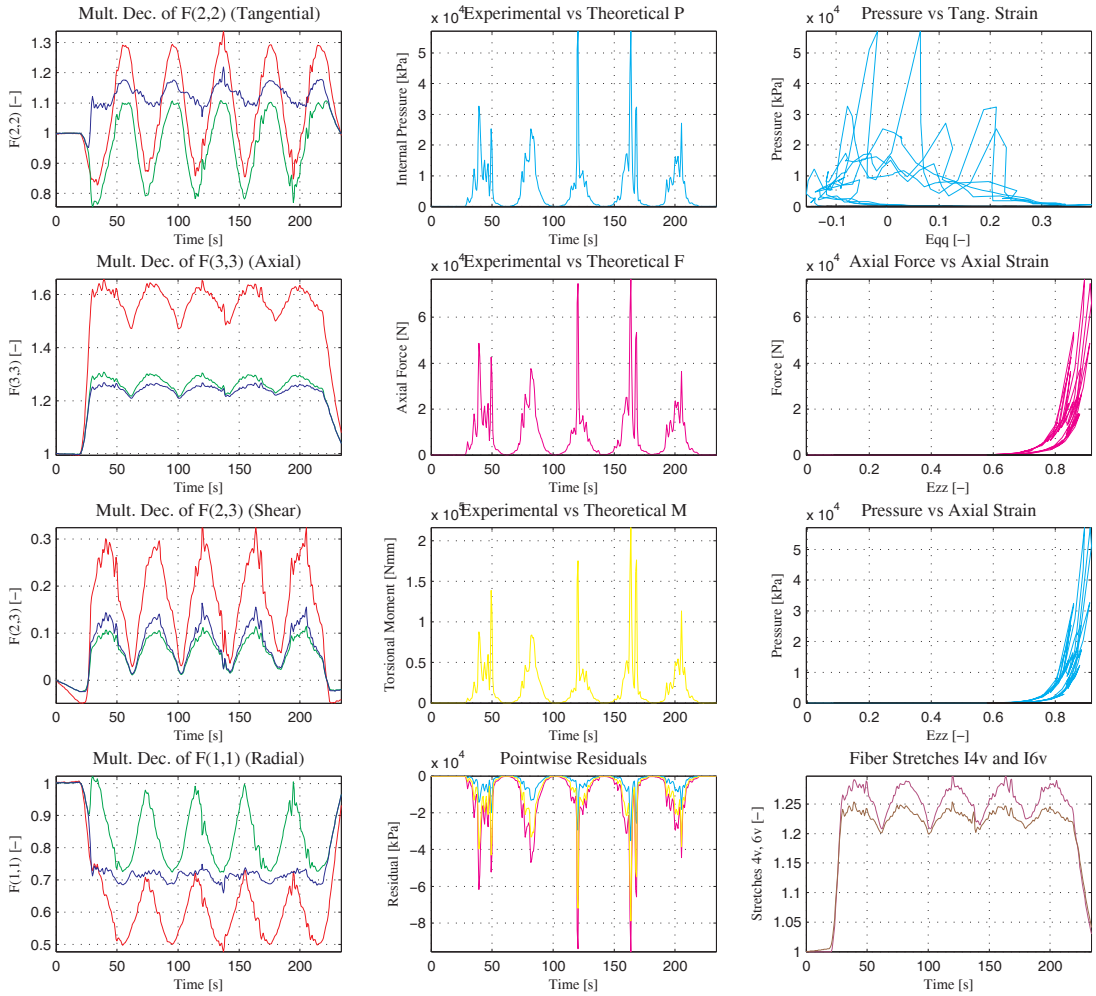

Iteration Plots for 72deg–Whole–Statik–S14 Scenario S14 at Coefficients:
C1e= 60.295 C2e= 15.543 Alphae= 26.138
EtaGS= 0.000 Etaf= 0.000 Alphaf= 0.000
Qinf= 0.000 Delta= 0.000

Experimental Deformation Gradient Component (Ft)	Axial Force Calculated using Theory	Experimentally Determined Values of Corresponding Data in the Plot
Deformation Gradient Component of Intermediate Config. (Fv)	Internal Pressue Calculated using Theory	Stretch of Fiber Family 4 to reach intermediate configuration (of I4v)
Deformation Gradient Component of Pure Elastic Configuration (Fe)	Torsional Moment Calculated using Theory	Stretch of Fiber Family 6 to reach intermediate configuration (of I6v)

Figure 12.20 : Demonstration of Deformation Gradient Components, Comparison of Experimental and Theoretical Data at Initial Iteration as to 12.3.4

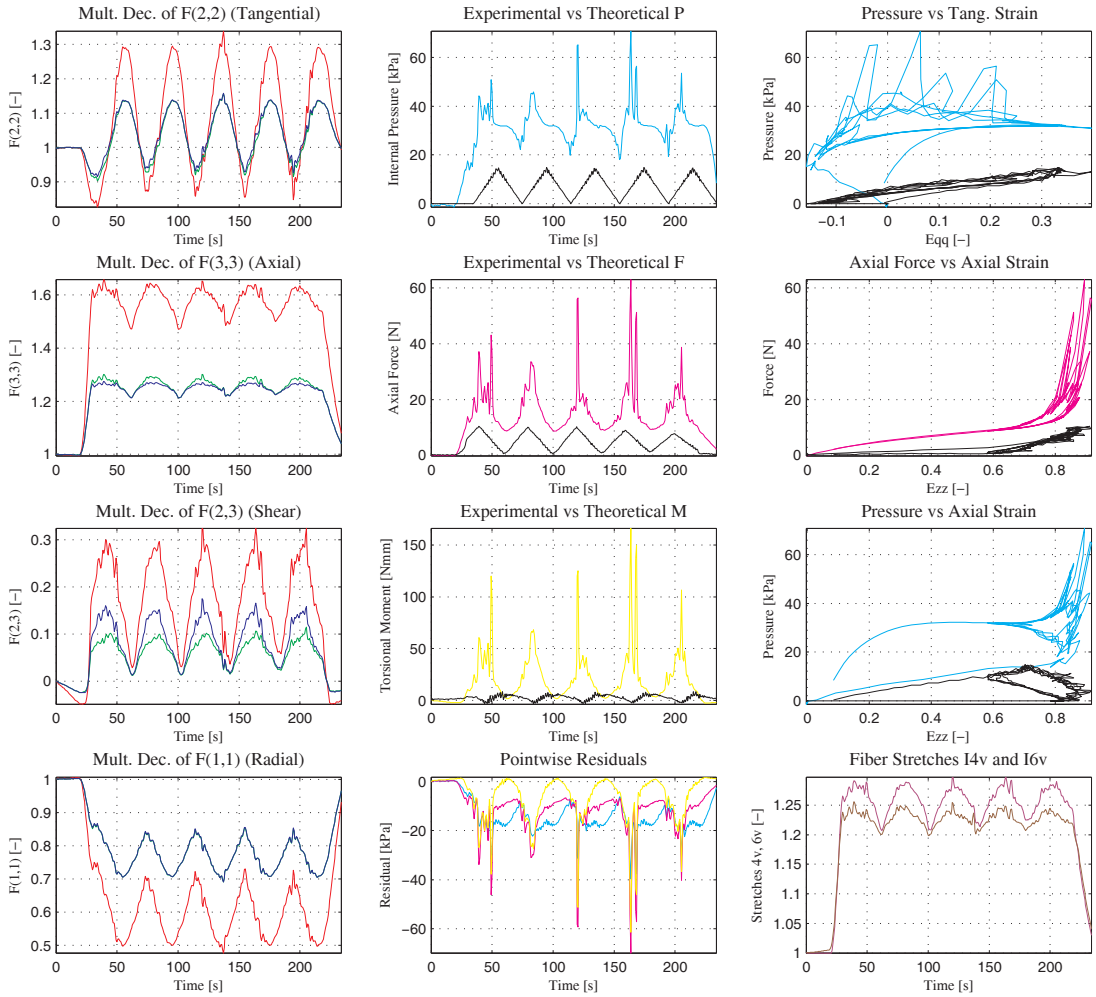

Iteration Plots for 72deg–Whole–Statik–S14 Scenario S14 at Coefficients:
C1e=145.418 C2e= 0.025 Alphae= 24.579
EtaGS= 0.000 Etaf= 0.000 Alphaf= 0.000
Qinf= 0.000 Delta= 0.000

Experimental Deformation Gradient Component (Ft)	Axial Force Calculated using Theory	Experimentally Determined Values of Corresponding Data in the Plot
Deformation Gradient Component of Intermediate Config. (Fv)	Internal Pressue Calculated using Theory	Stretch of Fiber Family 4 to reach intermediate configuration (of I4v)
Deformation Gradient Component of Pure Elastic Configuration (Fe)	Torsional Moment Calculated using Theory	Stretch of Fiber Family 6 to reach intermediate configuration (of I6v)

Figure 12.21 : Demonstration of Deformation Gradient Components, Comparison of Experimental and Theoretical Data at an Intermediate Iteration as to 12.3.4

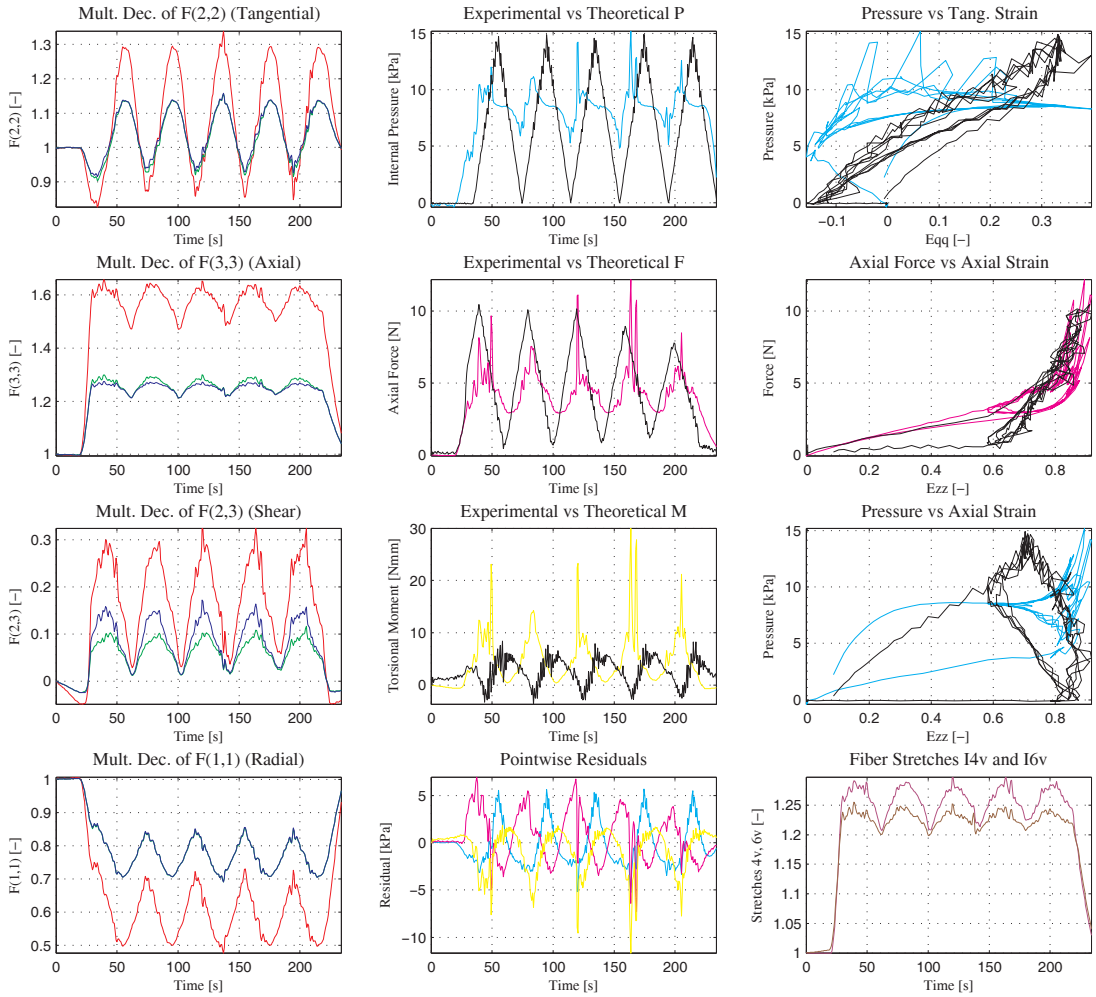

Iteration Plots for 72deg–Whole–Statik–S14 Scenario S14 at Coefficients:
C1e= 38.814 C2e= 0.020 Alphae= 20.654
EtaGS= 0.000 Etaf= 0.000 Alphaf= 0.000
Qinf= 0.000 Delta= 0.000

Experimental Deformation Gradient Component (Ft)	Axial Force Calculated using Theory	Experimentally Determined Values of Corresponding Data in the Plot
Deformation Gradient Component of Intermediate Config. (Fv)	Internal Pressue Calculated using Theory	Stretch of Fiber Family 4 to reach intermediate configuration (of I4v)
Deformation Gradient Component of Pure Elastic Configuration (Fe)	Torsional Moment Calculated using Theory	Stretch of Fiber Family 6 to reach intermediate configuration (of I6v)

Figure 12.22 : Demonstration of Deformation Gradient Components, Comparison of Experimental and Theoretical Data at Convergence Iteration as to 12.3.4

12.3.5. Out-of-Phase Static Extension, Inflation and Torsion for Elastic Parameter Estimation

To see how the material behaves under combination of different load application scenarios, a test has been carried on considered on determining elastic properties of the arterial wall with loads varying with a phase.

No prestress has been assumed to exist. Extension up to 17N (with a delay of 45 degrees in a load-unload cycle of approximately 40 seconds as 360 degrees), angular displacement varying between -20 and +40 degrees (Master signal – No Phase) and pressurizing up to 22 kPa (with a delay of 135 degrees in a load-unload cycle of approximately 40 seconds) has been applied, and the loads were in phase.

The iteration convergence is presented in Figures 12.23 – 12.25.

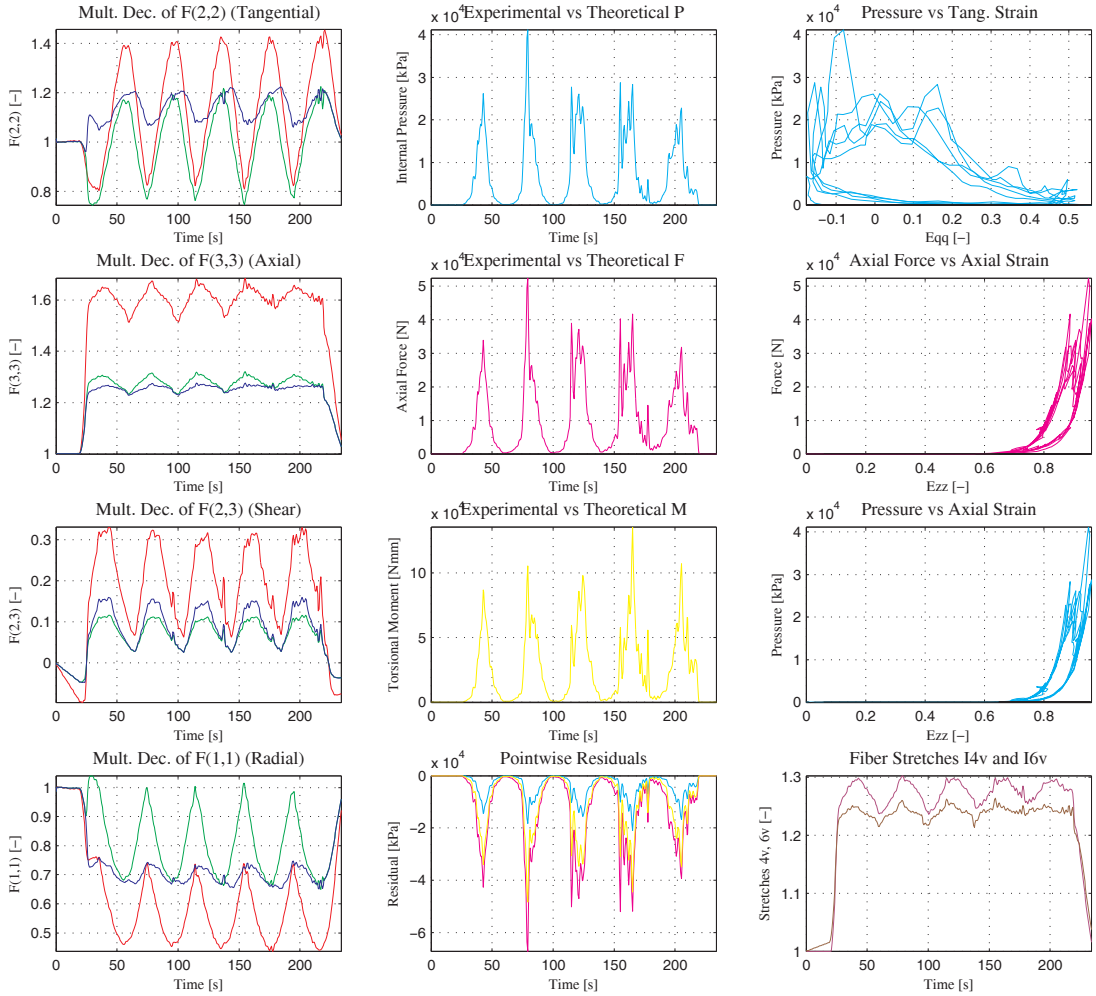

Iteration Plots for 72deg–Whole–Statik–S16 Scenario S16 at Coefficients:
C1e= 17.396 C2e= 6.456 Alphae= 26.138
EtaGS= 0.000 Etaf= 0.000 Alphaf= 0.000
Qinf= 0.000 Delta= 0.000

Experimental Deformation Gradient Component (Ft)	Axial Force Calculated using Theory	Experimentally Determined Values of Corresponding Data in the Plot
Deformation Gradient Component of Intermediate Config. (Fv)	Internal Pressue Calculated using Theory	Stretch of Fiber Family 4 to reach intermediate configuration (of I4v)
Deformation Gradient Component of Pure Elastic Configuration (Fe)	Torsional Moment Calculated using Theory	Stretch of Fiber Family 6 to reach intermediate configuration (of I6v)

Figure 12.23 : Demonstration of Deformation Gradient Components, Comparison of Experimental and Theoretical Data at Initial Iteration as to 12.3.5

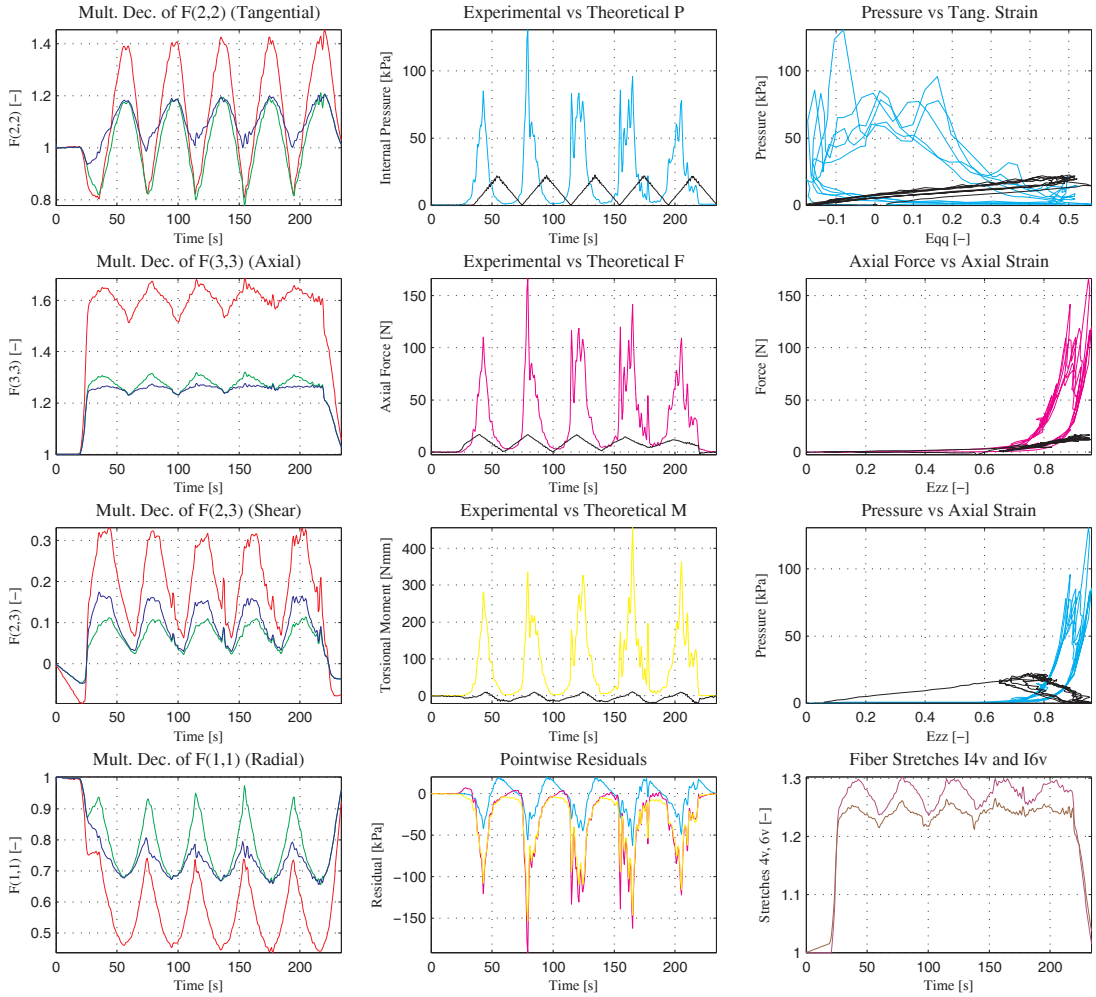

Iteration Plots for 72deg–Whole–Statik–S16 Scenario S16 at Coefficients:
C1e= 3.019 C2e= 0.028 Alphae= 25.585
EtaGS= 0.000 Etaf= 0.000 Alphaf= 0.000
Qinf= 0.000 Delta= 0.000

Experimental Deformation Gradient Component (Ft)	Axial Force Calculated using Theory	Experimentally Determined Values of Corresponding Data in the Plot
Deformation Gradient Component of Intermediate Config. (Fv)	Internal Pressue Calculated using Theory	Stretch of Fiber Family 4 to reach intermediate configuration (of I4v)
Deformation Gradient Component of Pure Elastic Configuration (Fe)	Torsional Moment Calculated using Theory	Stretch of Fiber Family 6 to reach intermediate configuration (of I6v)

Figure 12.24 : Demonstration of Deformation Gradient Components, Comparison of Experimental and Theoretical Data at an Intermediate Iteration as to 12.3.5

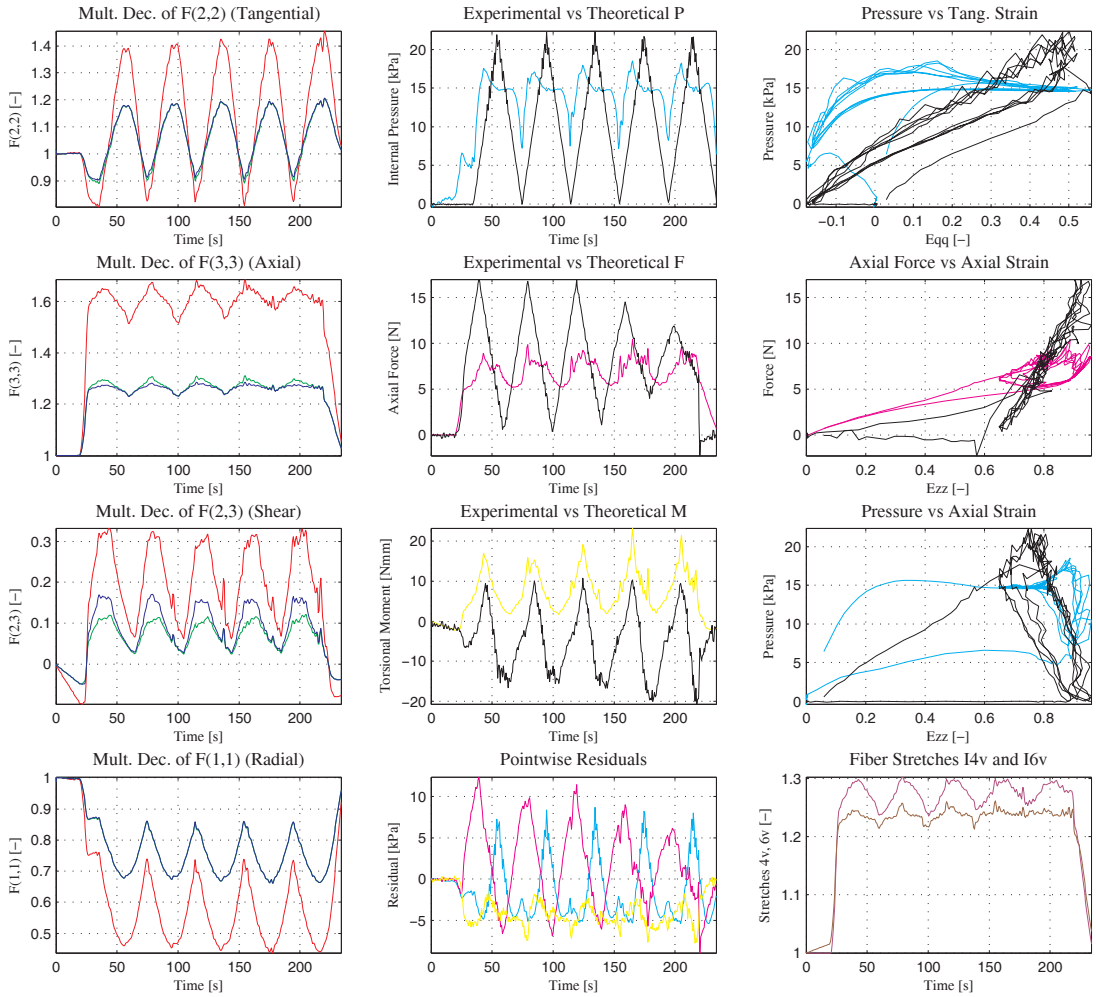

Iteration Plots for 72deg–Whole–Statik–S16 Scenario S16 at Coefficients:
C1e= 69.526 C2e= 0.008 Alphae= 20.772
EtaGS= 0.000 Etaf= 0.000 Alphaf= 0.000
Qinf= 0.000 Delta= 0.000

Experimental Deformation Gradient Component (Ft)	Axial Force Calculated using Theory	Experimentally Determined Values of Corresponding Data in the Plot
Deformation Gradient Component of Intermediate Config. (Fv)	Internal Pressue Calculated using Theory	Stretch of Fiber Family 4 to reach intermediate configuration (of I4v)
Deformation Gradient Component of Pure Elastic Configuration (Fe)	Torsional Moment Calculated using Theory	Stretch of Fiber Family 6 to reach intermediate configuration (of I6v)

Figure 12.25 : Demonstration of Deformation Gradient Components, Comparison of Experimental and Theoretical Data at Convergence Iteration as to 12.3.5

12.3.6. Summary

The summary of material parameters obtained by conducting elastic parameter estimation algorithm is presented in Table 12.1

Table 12.1: Material Properties Obtained for Pure Elastic Model

Loading Conditions	C_1^e **[kPa]**	C_2^e **[kPa]**	α^e **[-]**
12.3.2	38.838	0.304	21.074
12.3.3	44.674	0.027	18.743
12.3.4	38.814	0.020	20.654
12.3.5	69.520	0.008	20.772

It has been observed that, the proposed material model, under the kinematic assumptions aforementioned, fails to prove well if the loads in various axices are out of phase (i.e., they are independently applied) under the assumption of pure elastic deformations.

It is of interest that, though the discrepancy between the test data and the analytical values exist, one should mention about the correlation between the material parameters. Several conclusions can be gathered, knowing that these tests have been performed sequentially on one specimen of artery for demonstrative purposes.

- As more test are conducted on the artery, the material tends to get more "homogeneous".

- As more tests are conducted, fiber contribution decreases.

Enhancements should be made to the testing system to capture the changes with the time. One idea should be running all the test procedures without stopping the tests in between different tasks so that up to failure, the whole data should be based on the initial "strain" values measured. Though it sounds logical, this approach is not useful

with the proposed material model, since for correct parameter estimation over different loading conditions, various tasks should be performed separately, each starting form a “stress-free” and “undamaged” configuration, for the evolution equation(s) to respond appropriately.

12.4. Experimental Loading Protocols for Viscoelastic Parameter Estimation

Similar to analysis that has been described in section 12.3, dynamical tests performed on arterial structures have been fed into the parameter estimation algorithm for determining the dissipative material parameters.

The elastic parameters used for the viscoelastic parameter estimation are given in Table 12.2. These parameters are obtained from the same specimen on which the viscoelastic parameter estimation is conducted, using the pure elastic assumption as in section 12.3,

Table 12.2: Material Properties Obtained for Pure Elastic Model

Loading Conditions	C_1^e **[kPa]**	C_2^e **[kPa]**	α^e **[-]**
12.4.1	22.823	5.415	7.821
12.4.2	18.571	14.278	4.744
12.4.3	30.673	0.933	18.559

Table 12.3: Material Properties Obtained for Viscoelastic Model

Loading Conditions	η_{GS} **[kPa]**	η_f **[kPa]**	α_f **[-]**
12.4.1	0.012	9.869	7.821
12.4.2	27.772	0.012	0.066
12.4.3	26.163	0.378	0.066

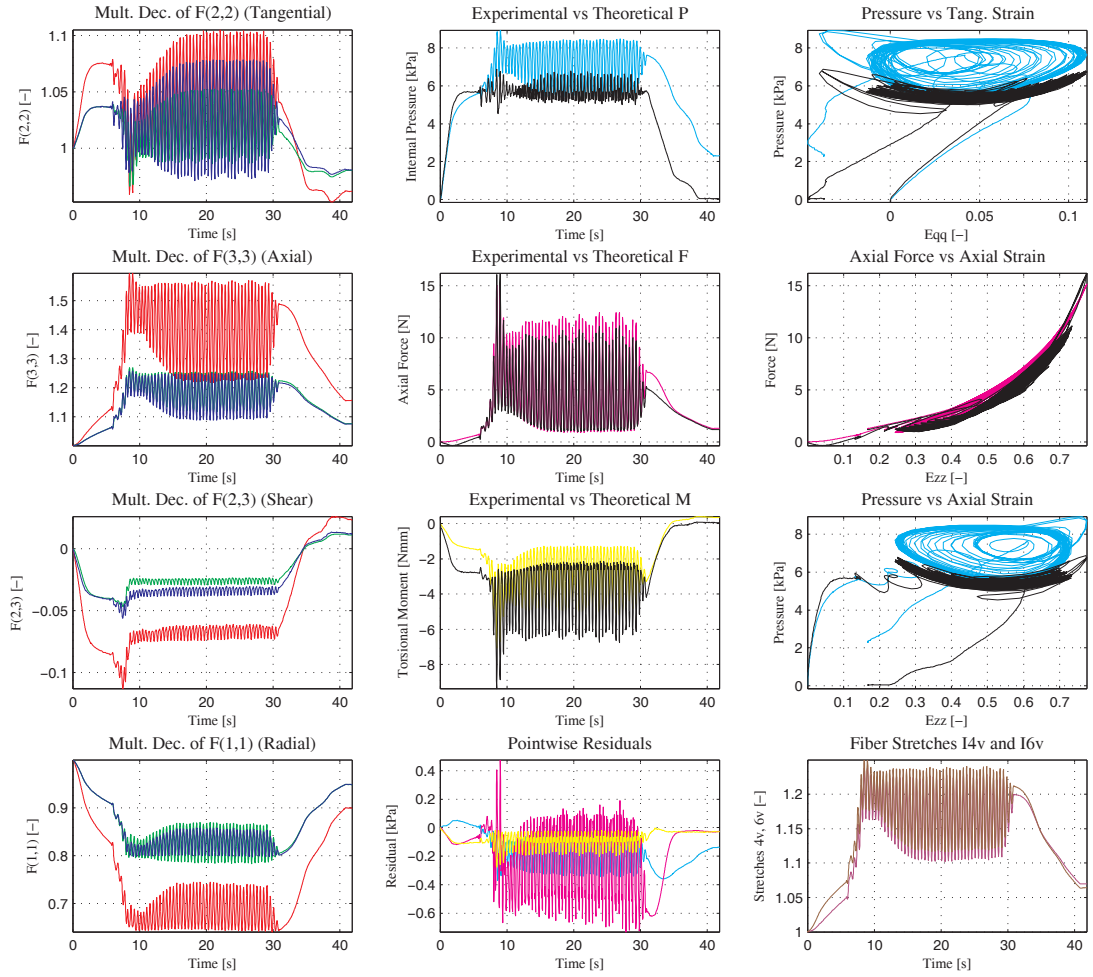

Iteration Plots for Task 5 – k23 Scenario k23 at Coefficients:
C1e= 22.823 C2e= 5.415 Alphae= 7.821
EtaGS= 0.012 Etaf= 9.869 Alphaf= 0.000
Qinf= 0.000 Delta= 0.000

Experimental Deformation Gradient Component (Ft)	Axial Force Calculated using Theory	Experimentally Determined Values of Corresponding Data in the Plot
Deformation Gradient Component of Intermediate Config. (Fv)	Internal Pressue Calculated using Theory	Stretch of Fiber Family 4 to reach intermediate configuration (of I4v)
Deformation Gradient Component of Pure Elastic Configuration (Fe)	Torsional Moment Calculated using Theory	Stretch of Fiber Family 6 to reach intermediate configuration (of I6v)

Figure 12.26 : Demonstration of Deformation Gradient Components, Comparison of Experimental and Theoretical Data at Convergence Iteration for as to 12.4.1

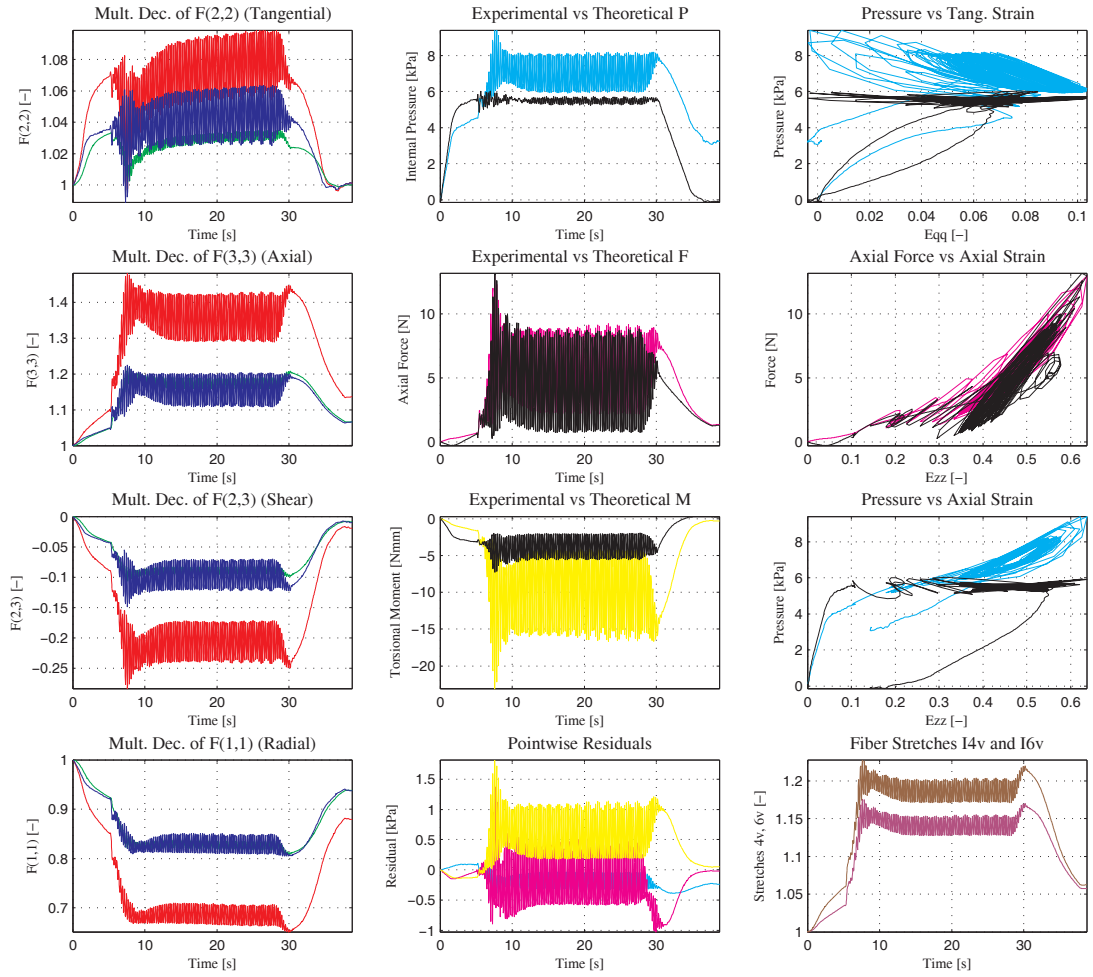

Iteration Plots for Task 5 – k24 Scenario k24 at Coefficients:
C1e= 18.571 C2e= 14.278 Alphae= 4.744
EtaGS= 27.772 Etaf= 0.012 Alphaf= 0.066
Qinf= 0.000 Delta= 0.000

Experimental Deformation Gradient Component (Ft)	Axial Force Calculated using Theory	Experimentally Determined Values of Corresponding Data in the Plot
Deformation Gradient Component of Intermediate Config. (Fv)	Internal Pressue Calculated using Theory	Stretch of Fiber Family 4 to reach intermediate configuration (of I4v)
Deformation Gradient Component of Pure Elastic Configuration (Fe)	Torsional Moment Calculated using Theory	Stretch of Fiber Family 6 to reach intermediate configuration (of I6v)

Figure 12.27 : Demonstration of Deformation Gradient Components, Comparison of Experimental and Theoretical Data at Convergence Iteration as to 12.4.2

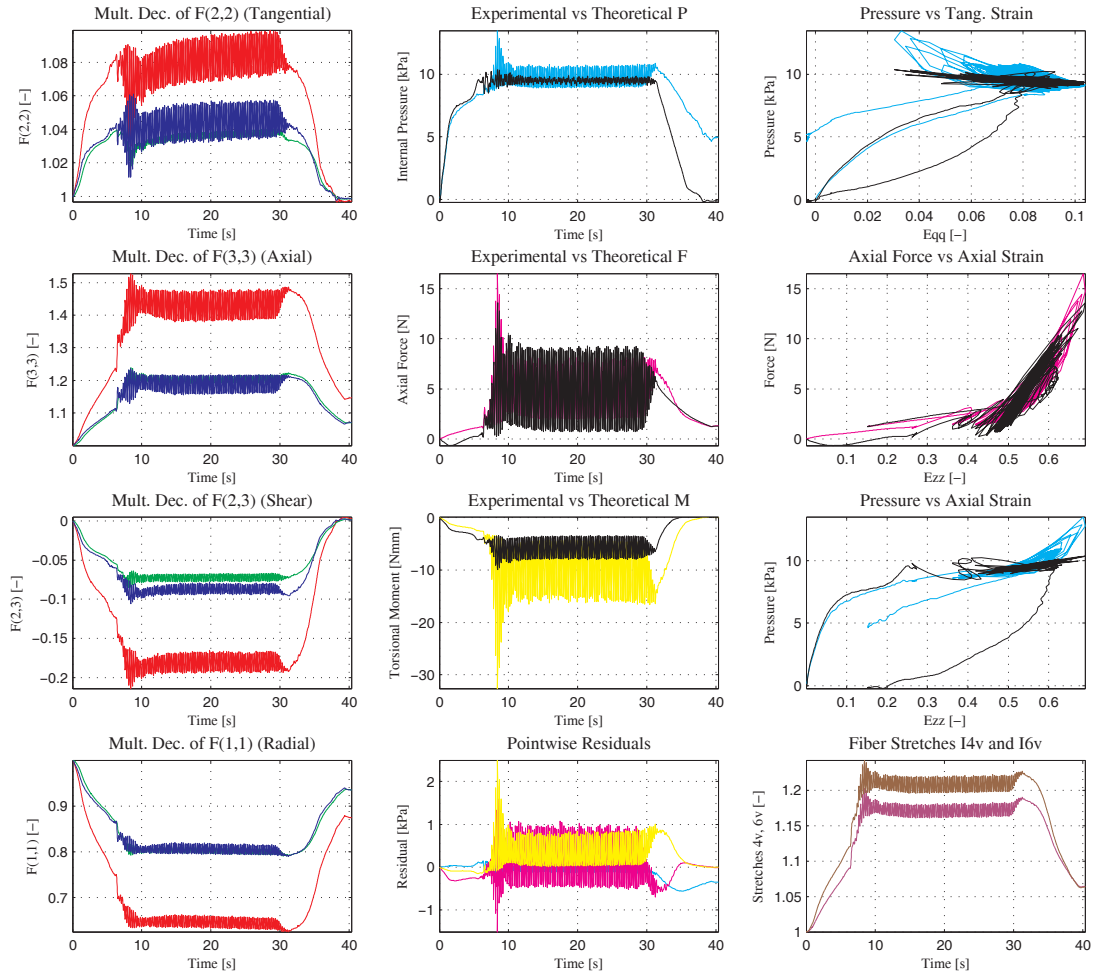

Iteration Plots for Task 5 – k25 Scenario k25 at Coefficients:
C1e= 30.673 C2e= 0.933 Alphae= 18.559
EtaGS= 26.164 Etaf= 0.378 Alphaf= 0.066
Qinf= 0.000 Delta= 0.000

Experimental Deformation Gradient Component (Ft)	Axial Force Calculated using Theory	Experimentally Determined Values of Corresponding Data in the Plot
Deformation Gradient Component of Intermediate Config. (Fv)	Internal Pressue Calculated using Theory	Stretch of Fiber Family 4 to reach intermediate configuration (of I4v)
Deformation Gradient Component of Pure Elastic Configuration (Fe)	Torsional Moment Calculated using Theory	Stretch of Fiber Family 6 to reach intermediate configuration (of I6v)

Figure 12.28 : Demonstration of Deformation Gradient Components, Comparison of Experimental and Theoretical Data at Convergence Iteration as to 12.4.3

12.5. Parameter Estimation Regarding Plastic Deformations and Damage Evolution

It has been demonstrated in the previous titles that, both the model proposed and the algorithms developed so far work well in the context they have been postulated. There is a modular structure that enables separation of different contributions to material behavior and enables investigation of different parameters together or separately.

It has been shown that, with "roughly estimated" parameters it is possible to run an analysis and get plastic deformations due to excessive loadings due to some criteria. Examples have been provided in Section 11.2, where plastic deformations and relevant stress analysis are discussed in detail. Though it is straightforward within the given context to run a test that will raise permanent deformations on arterial tissue, and obtain the material parameters to material model (or a part of it, as defined thereafter under different assumptions) given in Sections 7-10, it has been of no practical application within the study program of this study, and the test have not succeeded as expected. The faults that have been observed are:

- **Roughness of the Available Materials:** Due to its vast availability, pulmonary arteries harvested from fresh limb of approximately 12 months have been used during tests. These arteries unfortunately had geometric irregularities (see figure 12.6) that did not enable a homogeneous deformation up to limit points of material's available constitutive range. Thus, it has been impossible to get fully controlled axisymmetric plastic deformations.

- **Connections to testing system:** The arterial specimens have been connected to the testing system as demonstrated in Figure 12.7, where plastic strips have been applied over the tissue to tighten and enable non-slipping and watertight structure for inflation, torsion and extension tests. However, this system at the limit of plastic deformations cause an "irregularity" for the plastic flow to begin where, the "analytical assumptions" do not hold, and at the areas of interest, successful plasticity cannot be obtained.

Future work can concentrate on running tests on plasticity with more “enhanced” specimens to meet the requirements of the testing for plasticity. Cartoid arteries from lamb, pig or human, if possible, where minimal or no branching is observed would be the best specimens to run tests on additionally, to overcome “end-effects”, a new installation system that would enable “zero stress” around the connector regions at the overloading conditions of arterial specimens should be designed.

12.6. Comments on Parameter Estimation

It has been demonstrated that a sequence of well-designed experiments should be conducted for efficient parameter estimation to models of non-linear materials.

It has been shown that tests on even a single specimen might have different responses to same loading conditions, as the material becomes pre-conditioned as more tasks are applied upon.

It can be concluded that, to be comparable, each repeated test should also be in the same “time space” to be comparable among specimens.

Various loading protocols should be applied, and the response of material model to in-phase and out-of-phase multiaxial loading conditions should be investigated.

It has been noticed that, the proposed material model does not cope well with the real world data when the loading applied is due to sources that are not in phase. It can be stated that this is a known limitation of the proposed model. Additional degrees of freedom can be added to the constitutive model applied to capture such behavior, such as enabling “compressibility”. From an engineering point of view, the model can be regarded as “capable” of modeling the arterial tissue in the sense that in the body, all the external loads are generated due to the “heartbeat”, and all are in phase.

13. CONCLUSIONS

A new material model that incorporates

- the nonlinear deformation characteristics,
- continuous fiber-reinforced material properties,
- dissipative characteristics,
- damage softening
- plastic deformation capabilities,

has been derived using standard arguments of continuum mechanics and thermodynamics. A novel test setup has been established for parameter estimation to nonlinear behaving materials, in terms of both deformation and constitutive behavior. Lamb pulmonary arteries, that have been fresh-grabbed from slaughterhouse has been used for experimental studies, and all the tests have been carried at 37 degree Celsius. The prescribed-kinematics analytical model of a thick-walled mono-layered tube has been applied to the specific case, and analytical expressions have been derived for calculating

- Internal Pressure
- Axial Force
- Torsional Moment

using (surface) strain data from real test specimens.

The test data and the analytical expressions have been embedded in an optimization algorithm, where different aspects of the material behavior have been investigated. Tests have also been conducted to check the validity of the provided material model, with presumable characteristics.

Within the study, it has been captured that in the literature, little experimental data are provided for material parameter fitting to arterial tissues. This has triggered the fact that within the context of study,

- A novel testing system for nonlinear tubes is to be set-up
- A modular material model should be developed
- A modular parameter estimation algorithm should be developed
- A theoretical investigation of nonlinear dissipative behavior of large deforming materials with (stress-free) intermediate configuration

should be carried on.

It has been concluded that, the current model may fail in predicting response under out-of-phase loading. Parameter estimations under such circumstances have not proven to be successful. Enhancements to incorporate other effects that would yield in more accurate results are necessary, if the loading conditions are not like single-phase “heart-beat”. The most probable option to represent in the model would be the existence of “compressibility”.

Experiments on plastic deformations could not be conducted due to problems with the specimens and reasons due to connecting the specimens to the testing system discussed in detail in the experimental studies section. This is left as an open subject, though the model is capable of incorporating such effects into account very easily. Also, not to make things more complex, the effects of prestress, especially in the tangential direction has not been considered, and left open, though the framework of incorporating prestress and mechanical stress is presented on the theoretical basis.

It has been seen that, from clinical and engineering points of view, the current model is clear enough to compete with the realistic modeling of viscoelastoplastic behavior of arterial tissues for in-phase loading conditions as in real life. This model, and everything that has been developed within the scope of this study is easily applicable to engineering materials, where nonlinear effects are of great importance, since no kinematical and constitutive simplification has been made other than

- assuming the material be incompressible
- assuming that the intermediate configurations are spin-free

Future studies are encouraged to incorporate

- extension of remodeling triggered by stress and strain driven parameters,
- experimental setups to cope with problems at “high-level” loading conditions
- compressibility of material,
- though hard to achieve good results; multi-layered analytical models,
- extension of fiber constituents in the radial direction,
- investigation of delaminating between media and adventitia.

where a lot stay exists yet to get discovered.

REFERENCES

[1] **J. A. G. Rhodin**, 1980. Architecture of the vessel wall. In H. V. Sparks Jr. D. F. Bohr, A. D. Somlyo and S. R. Geiger, editors, Handbook of Physiology, the cardiovascular system, volume2, pages 1-31. American Physiology society, Bethesda, Mryland.

[2] **J. Staubesand**, 1959. Anatomic der Blutgefabe, I. Funktionelle Morhologie der Arterien, Venen und arterio-venösen anastomesen. In M. Ratschow, editor, Anilogy, chapter 2, pages 23-82. Thieme, Stutgart.

[3] **G.A. Holzapfel**, **T.C. Gasser**, **R.W. Ogden**, 2000. A new constitutive framework for arterial wall mechanics and a comparative study of material models, Institute for Structural Analysis, Computational Biomechanics Graz University of Technology, Schiesstattgasse 14B, A-8010 Graz, Austria

[4] **G.A. Holzapfel**, **T.C. Gasser**, **R.W. Ogden**, 2000. A new constitutive framework for arterial wall mechanics and a comparative study of material models, *Journal of Elasticity* **61**, 1-48

[5] **M.L. Raghavan**, Lecture Notes on Cardiovascular Bio-solid Mechanics, Department of Biomedical Engineering University of Iowa.

[6] **G.A. Holzapfel**, 2000. Biomechanics of Soft Tissue, Institute for Structural Analysis, Graz University of Technology.

[7] **H. Bader**, 1967. Dependence of wall stress in the human thoracic aorta on age and pressure. Circ. Res., 20:354-361.

[8] **T. E. Carew**, **R. N. Vaishnav**, and **D. J. Patel**, 1968. Compressibility of the arterial wall. Circ.Res., 23:61-68.

[9] **R. H. Cox**, 1983. Comparison of arterial wall mechanics using ring and cylindrical segments, *Am. J. Phy*., 244:H298-H303.

[10] **R.F.Fuchs**, 1900. Zur Physiologie und Wachstumsmechanik des BlutgefaBsystems. Archiv fur die .qe.S'um.te Phy.S'iologie, 28.

[11] **B. M. Learoyd** and **M. G. Taylor**, 1966. Alteration.., with age in the viscoelastic properties of human arterial walls, Circ. Res., 18:278-292.

[12] **R. N. Vaishnav** and **J. Vossoughi**, 2003. Estimation of residual strains in aortic segments, In Biomedical Engineering II: Recent Developments, C. W. Hall (Ed.), New York.

[13] **J. Xie**, **J. Zhou**, and **Y. C. Fung**, 1995. Bending of blood vessel wall: Stress-strain laws of the intima-media and adventitia layers, *J. Biomech. Engr*., 117:136-145.

[14] **J. D. Humphrey**, 1995. Mechanics of arterial wall: Review and directions, Critical Reviews in Biomed. Engr., 23:1-162.

[15] **C. S. Roy**, 1980-1982. The elastic properties of the arterial wall, *The Journal of Physiology*, 3:125-159.

[16] **Y. C. Fung**, **K. Fronek**, and **P. Patitucci**, 1979. Pseudoelasticity of arteries and the choice of its mathematical expression, Am. J. Physiol., 237:H62Q-H631.

[17] **G. A. Holzapfel**, **C. A. J. Schulze-Bauer**, and **M. Stadler**, 2000. Mechanics of angioplasty: Wall, balloon and stent. In Mechanics in Biology, J. Casey and G. Bao (Eds), New York, AMDVol. 242/BED- Vol. 46, The American Society of Mechanical Engineers. 141-156.

[18] **D. J. Patel** and **D. L. Fry**, 1969. The elastic symmetry of arterial segments in dogs. Circ. Res., 24:1-8.

[19] **H. S. Oktay**, **T. Kang**, **J. D. Humphrey**, and **G. G. Bishop**, 1991. Changes in the mechanical behavior of arteries following balloon angioplasty, In 1991 ASME Advances in Bioengineering, New York.

[20] **T. C. Gaser**, **C. A. J. Schulze-Bauer**, **E. Pernkopf**, **M. Stadler**, and **G. A. Holzapfel,** 2000. Rate-independent elastoplastic constitutive modeling of biological soft tissues: Part II. Percutaneous transluminal angioplasty.

[21] **J. Bonet , R. D. Wood**, 1997. Nonlinear Continuum Mechanics for Finite Element Analysis. Cambridge University Press.

[22] **J. D. Humphrey**, 2001. Cardiovascular Solid Mechanics, Springer-Verlag, New York, Inc.

[23] **G. A. Holzapfel**, 2000. Nonlinear Solid Mechanics; A continuum Approach for Engineering.

[24] **B. Brodersen**, 2004. Ogden Type Materials in Nonlinear Continuum Mechanics, Study work, Braunschweig.

[25] **A. Rachev** and **K. Hayashi**, 1999. Theoretical study of the effects of vascular smooth muscle contraction on strain and stress distributions in arteries, Ann. Biomed. Eng., **27**, 459-468.

[26] **B. R. Simon**, **M. V. Kaufmann**, **M. A. McAfee** and **A. L. Baldwin**, 1998. Porohyperelastic finite element analysis of large arteries using ABAQUS, *J. Biomech. Eng*., **120**, 296-298.

[27] **A. Tözeren**, 1984. elastic properties of arteries and their influence on the cardiovascular system, *J. Biomech*., **106**, 182-185.

[28] **F. L. Wuyts**, **V. J. Vanhuyse**, **G. J. Langewouters**, **W. F. Decraemer**, **E. R. Raman and S. Buyle**, 1995. Elastic properties of human aortas in relation to age and atherosclerosis: A structural model, Phys. Med. Biol., **40**, 1577-1597.

[29] **W. W. Von Maltzahn**, **D. Besdo and W. Wiemer**, 1981. Elastic properties of arteries: A nonlinear two layer cylindrical model, *J. Biomech*., 14, 389-397.

[30] **H. Demiray**, 1991. A layered cylindrical shell model for an aorta, *Int. J. Engr. Sci.,* **29**, 47-54.

[31] **A. Rachev**, 1997. Theoretical study of the effects of stress-dependent remodeling on arterial geometry under hypertensive conditions, *J. Biomech*., **30**, 819-827.

[32] **R. N. Vaishnav, J. T. Young and d. J. Patel**, 1973. Distribution of Stresses and of Strain-Energy Density through the Wall Thickness. *Circ. Res.* **32,** 577-583.

[33] **G. A. Holzapfel, and H. W. Weizsäcker**, 1998. Biomechanical behavior of the arterial wall and its numerical characterization. *Computers in Biology and Medicine* **28**, 377-392.

[34] **C.J. Chuong and Y.C. Fung**, 1984. Compressibility and constitutive equation of arterial wall in radial compression experiments. *J. Biomech*. **17**, 35-40.

[35] **V.A. Lubarda**, 2001. Elastoplasticity Theory, CRC.

[36] **E. H. Lee**, 1969. Elastic-plastic deformation at finite strains, *J. Applie. Mech.* **36**, 1–6.

[37] **J. P. Boehler**, 1987. Introduction to the Invariant Formulation of Anisotropic Constitutive Equations. In "*Applications of Tensor Functions in Solid*

Mechanics, CISM Course No. 292", J.P. Boehler (ed.), Springer-Verlag.

[38] **N. Huber and C. Tsakmakis**, 2000. Finite deformation viscoelasticity laws *Mechanics of Materials* **32**, 1-18

[39] **Larry A. Taber**, 2004. Nonlinear theory of elasticity : applications in biomechanics River Edge, NJ : World Scientific

[40] **T.C. Gasser, G.A. Holzapfel**, 2002. A rate-independent elastoplastic constitutive model for (biological) fiber-reinforced composites at finite strains: Continuum basis, algorithmic formulation and finite element implementation. *Computational Biomechanics* **29**, 340-360.

[41] **V. A. Lubarda**, 1999. Duality in constitutive formulation of Finite-strain elastoplasticity based on F=FeFp and F=FpFe decompositions. *International Journal of Plasticity* **15**, 1277-1290

[42] http://web.earthsci.unimelb.edu.au/wilson/ice1/criticalrss.html (2007)

[43] **F.J. Harewood, P.E. McHugh**, 2006. Investigation of finite element mesh independence in rate dependent materials. *Computational Materials Science* **37**, 442–453.

[44] **L. Laiarinandrasanaa, R. Piquesa, A. Robisson**, 2003. Visco-hyperelastic model with internal state variable coupled with discontinuous damage concept under total Lagrangian formulation. *International Journal of Plasticity* **19**, 977–1000.

ADDENDUM-A:STRESS AND STRAIN DISTRIBUTION IN VESSEL WALL

A-1. Pure Elastic Material Model (due to Section 11.1.1)

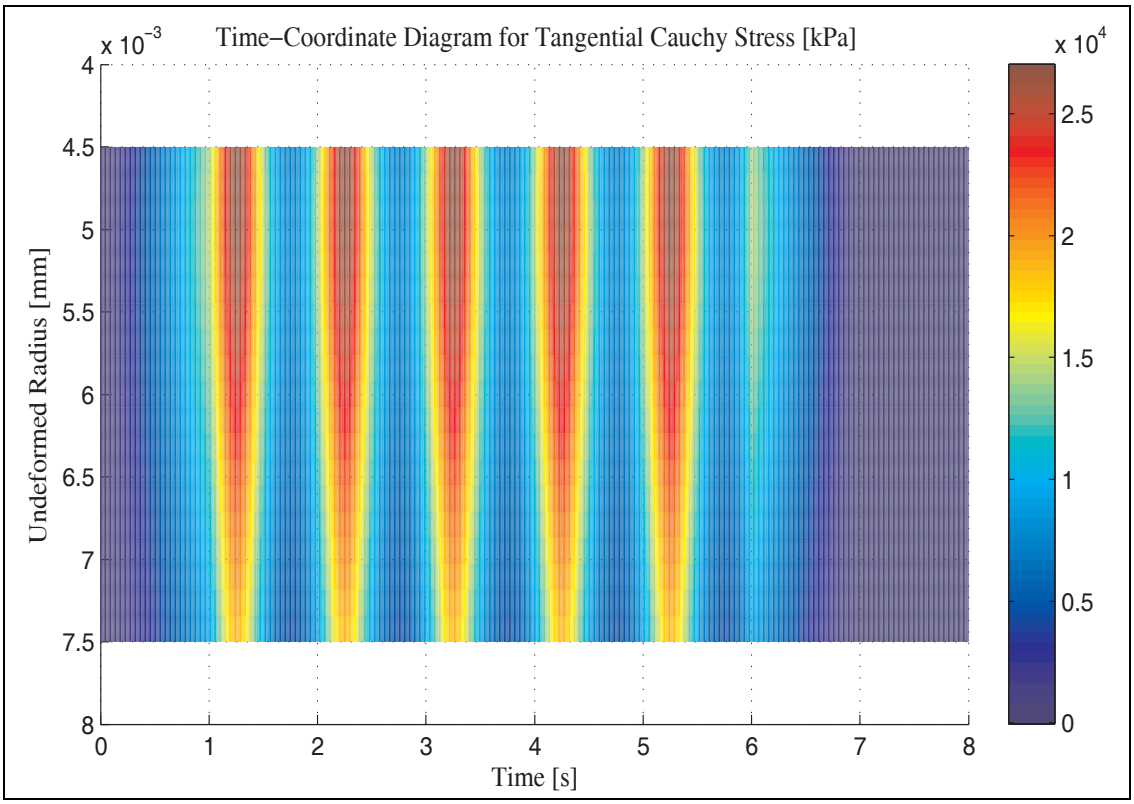

Figure A-1.1: Variation of Tangential Stress with Time and within Wall Thickness under Cyclic Loading at 1Hz

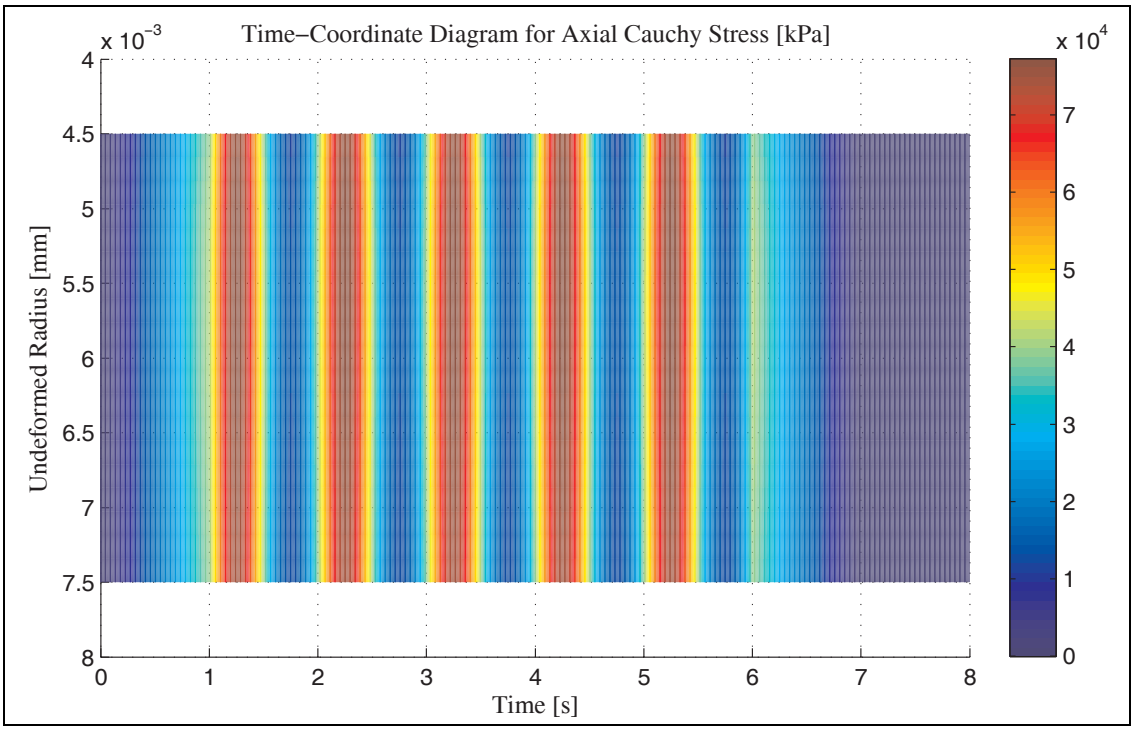

Figure A-1.2: Variation of Axial Stress with Time and within Wall Thickness under Cyclic Loading at 1Hz

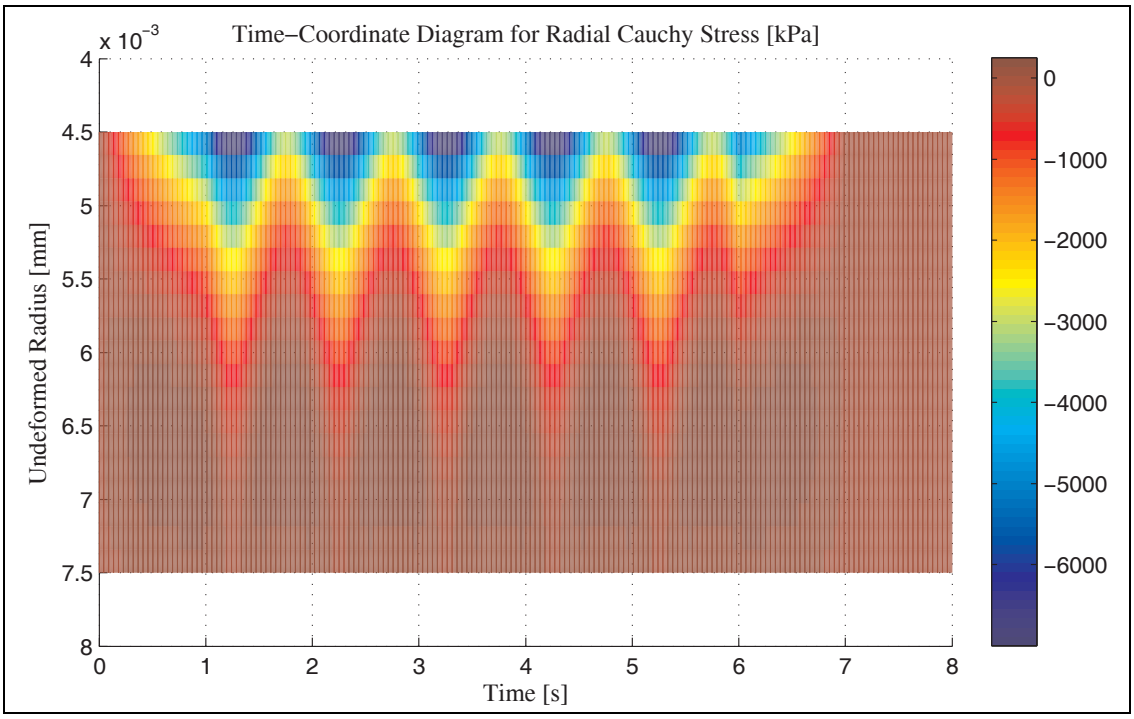

Figure A-1.3: Variation of Radial Stress with Time and within Wall Thickness under Cyclic Loading at 1Hz

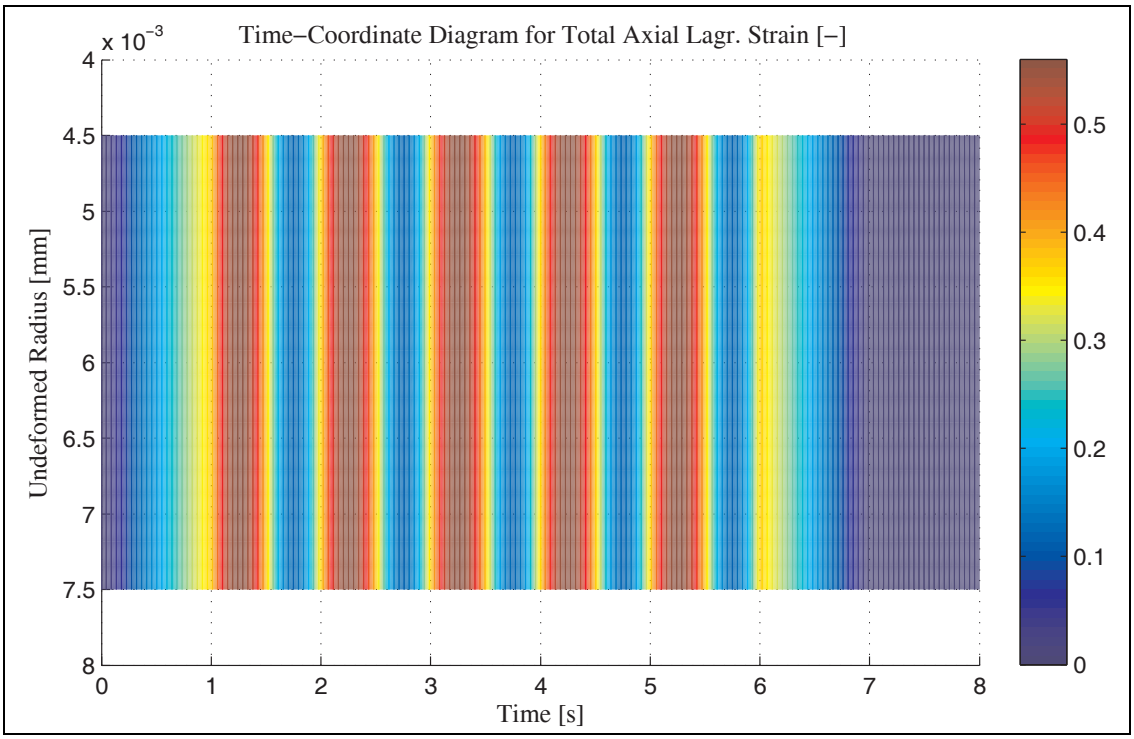

Figure A-1.4: Variation of Axial Total Strain with Time and within Wall Thickness under Cyclic Loading at 1Hz

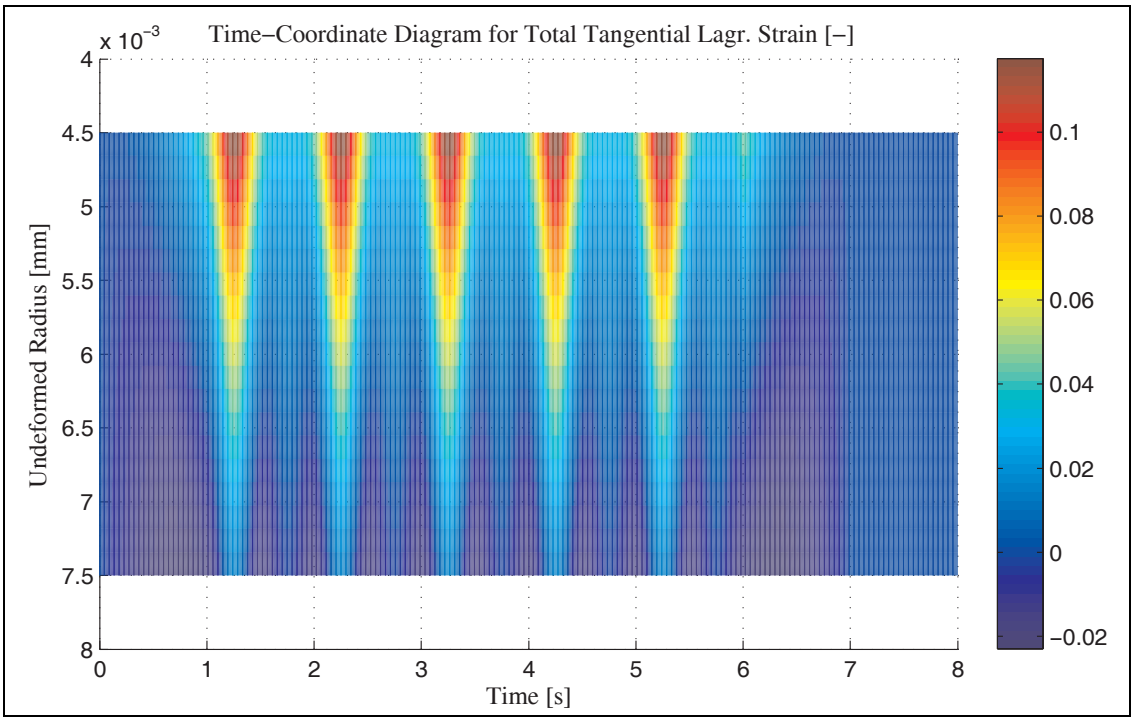

Figure A-1.5: Variation of Tangential Total Strain with Time and within Wall Thickness under Cyclic Loading at 1Hz

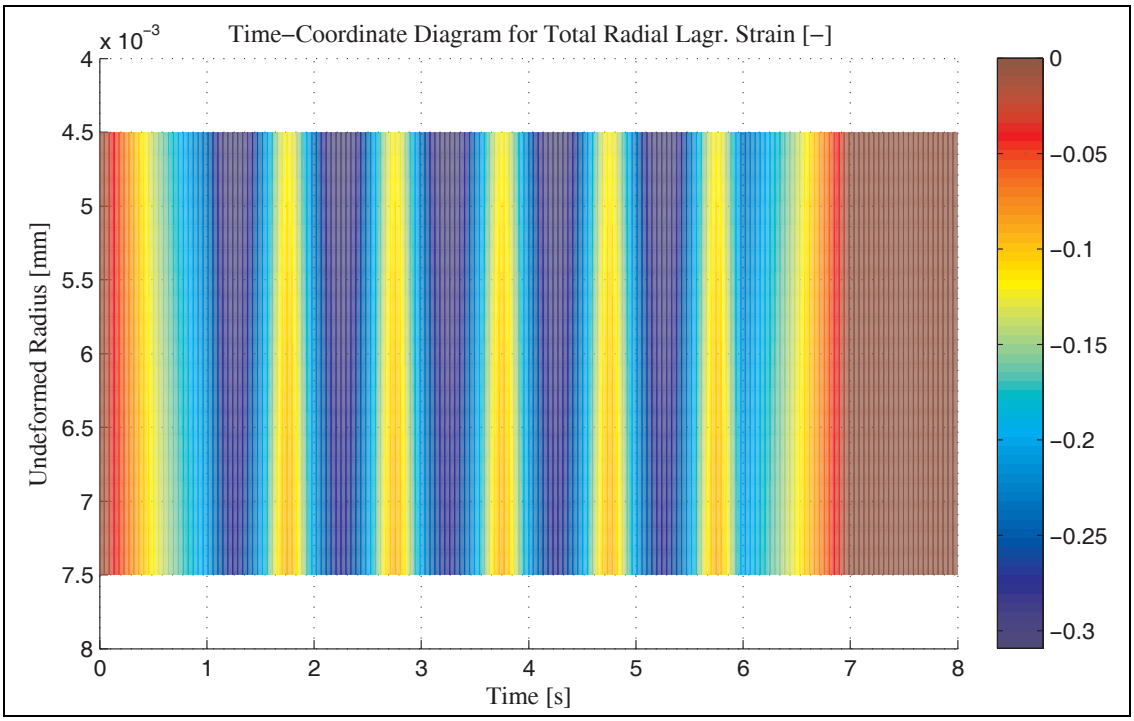

Figure A-1.6: Variation of Radial Total Strain with Time and within Wall Thickness under Cyclic Loading at 1Hz

A-2. Pure Elastic Material Model with Softening (due to Section 11.1.2)

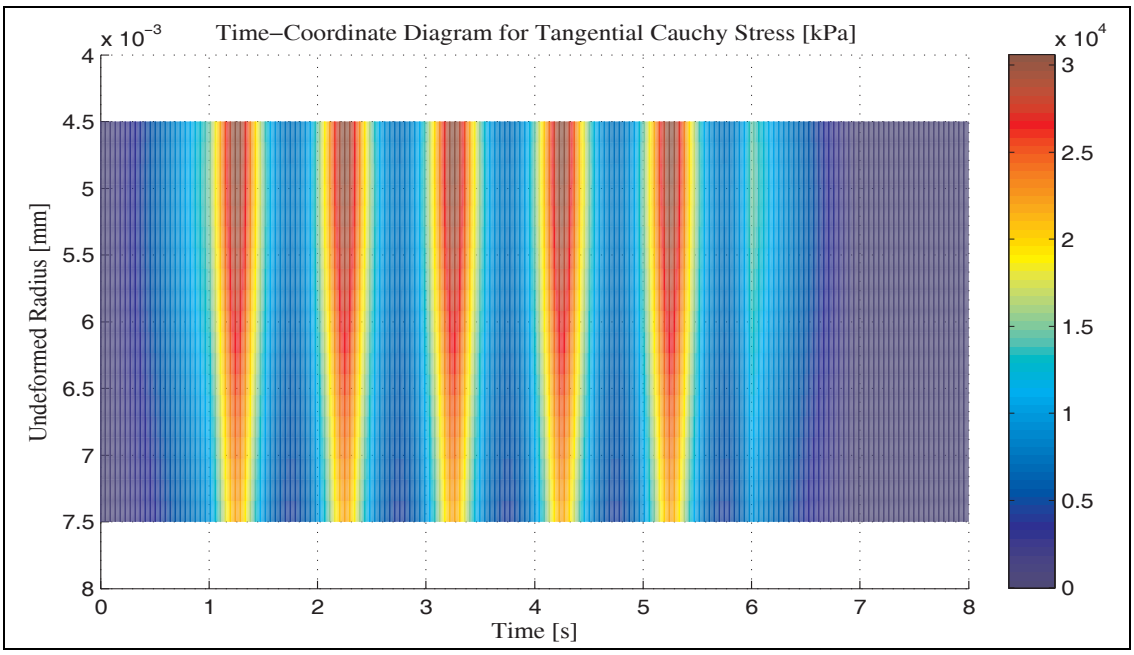

Figure A-2.1: Variation of Tangential Stress with Time and within Wall Thickness under Pure Elasticity with Softening Effect

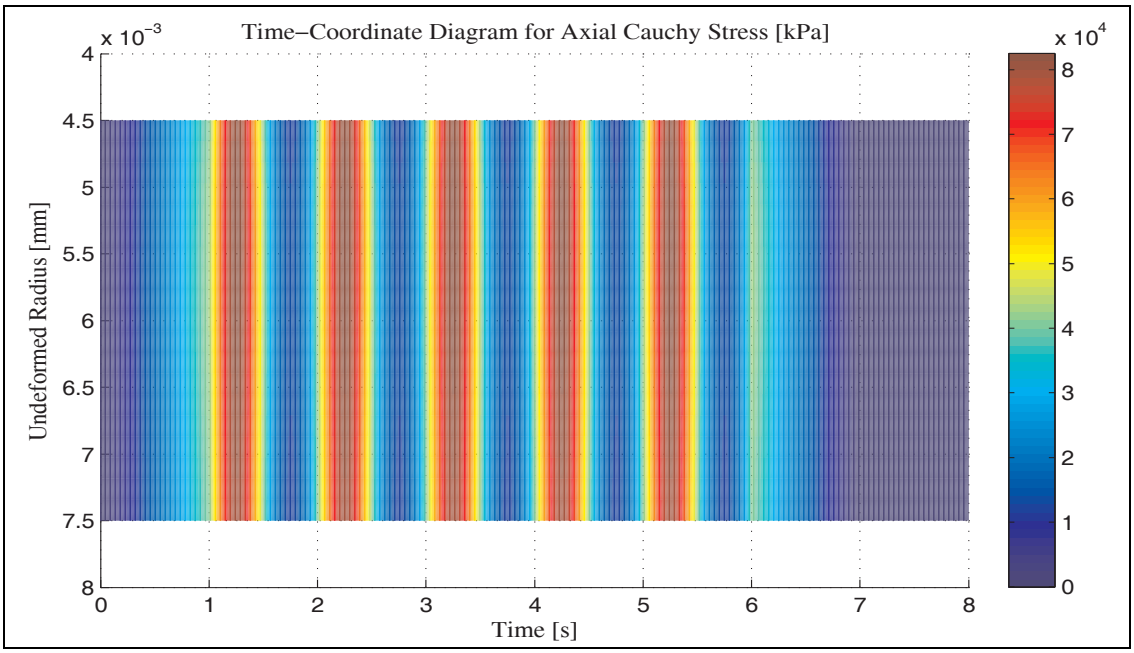

Figure A-2.2: Variation of Axial Stress with Time and within Wall Thickness under Pure Elasticity with Softening Effect

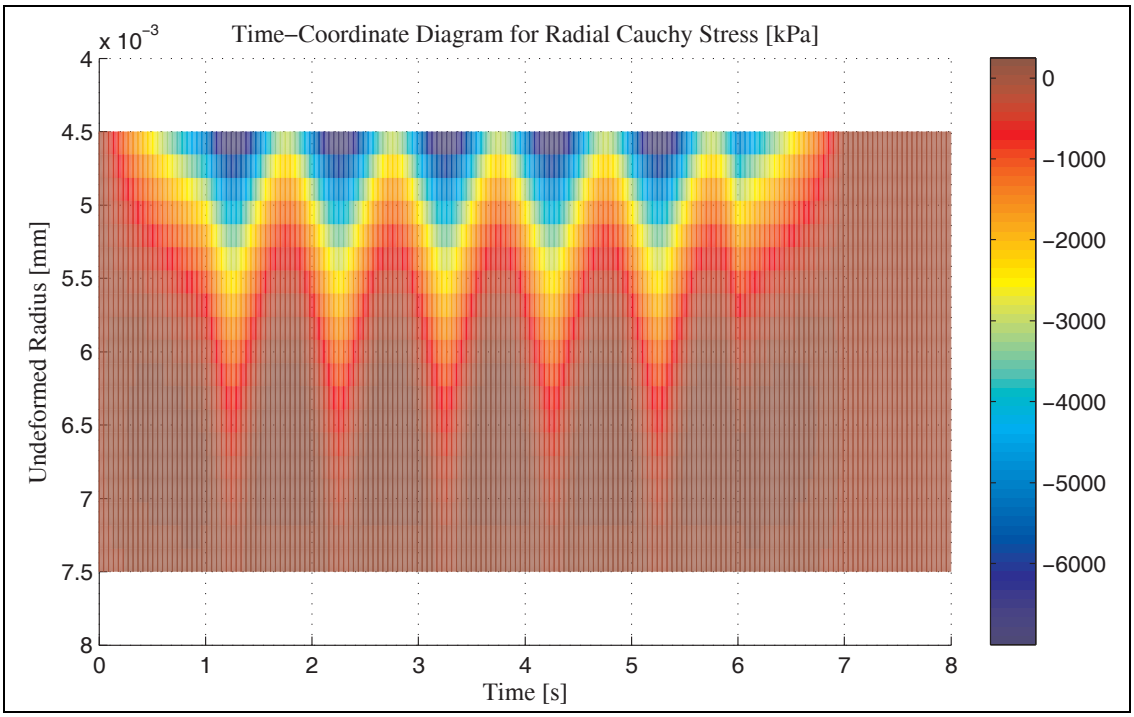

Figure A-2.3: Variation of Radial Stress with Time and within Wall Thickness under Pure Elasticity with Softening Effect

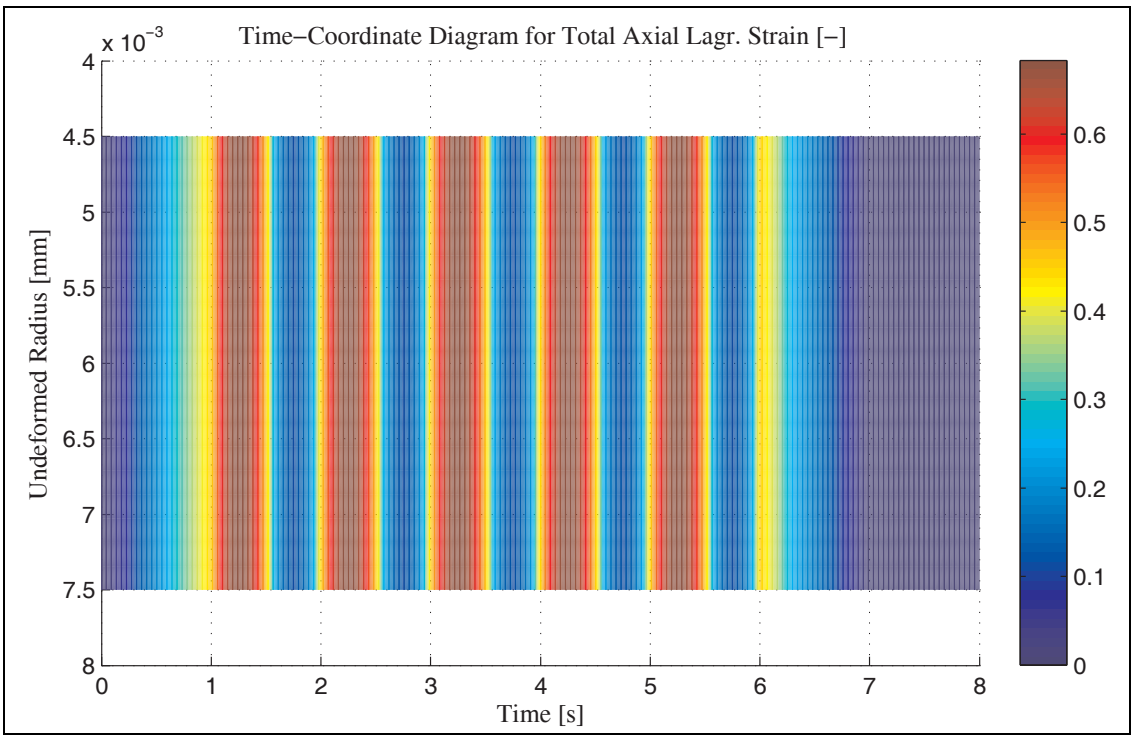

Figure A-2.4: Variation of Axial Total Strain with Time and within Wall Thickness under Pure Elasticity with Softening Effect

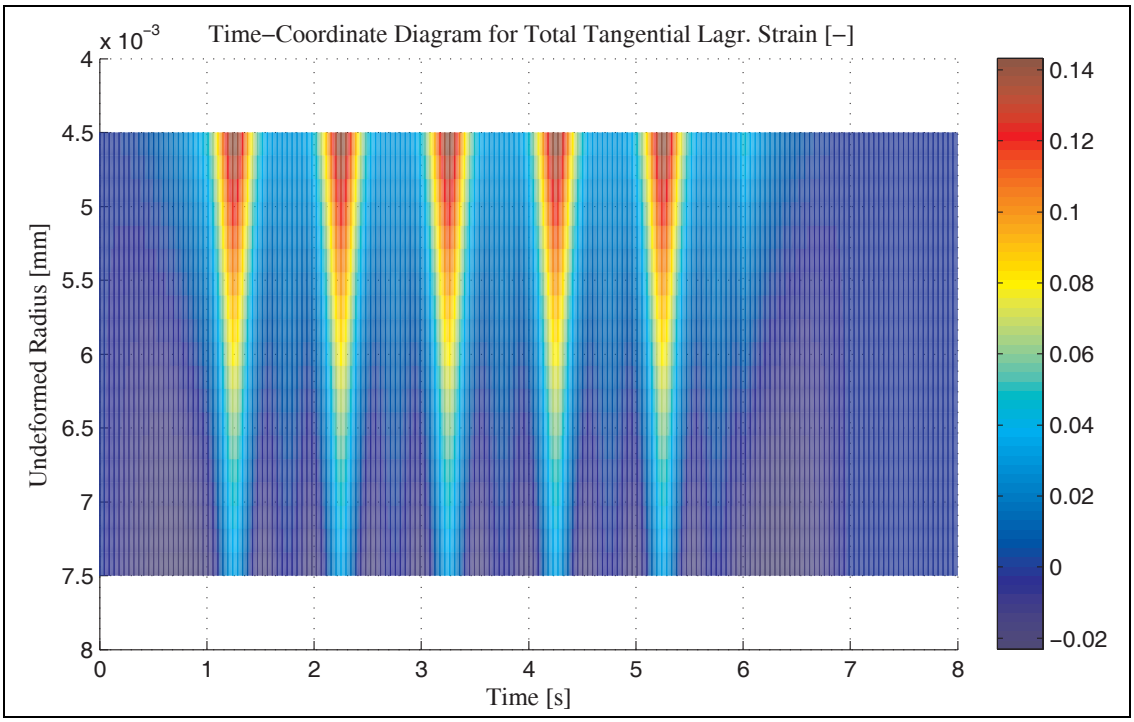

Figure A-2.5: Variation of Tangential Total Strain with Time and within Wall Thickness under Pure Elasticity with Softening Effect

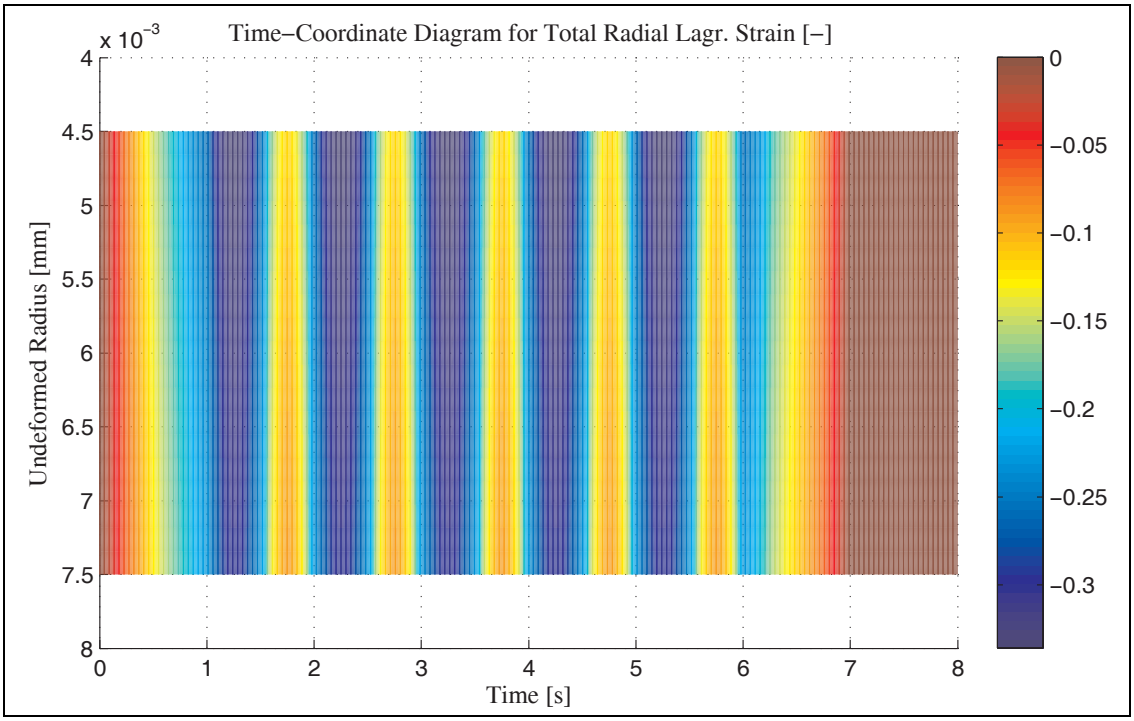

Figure A-2.6: Variation of Radial Total Strain with Time and within Wall Thickness under Pure Elasticity with Softening Effect

A-3. Isotropic Viscoelasticity Model (due to Section 11.1.3)

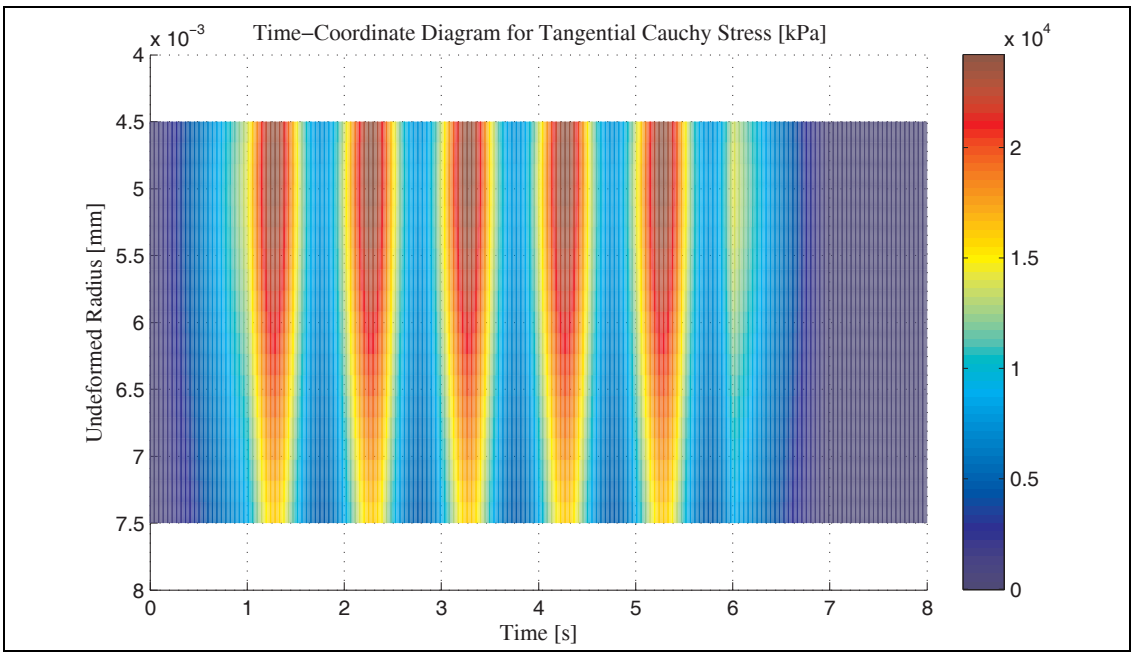

Figure A-3.1: Variation of Tangential Stress with Time and within Wall Thickness under Isotropic Viscoelasticity

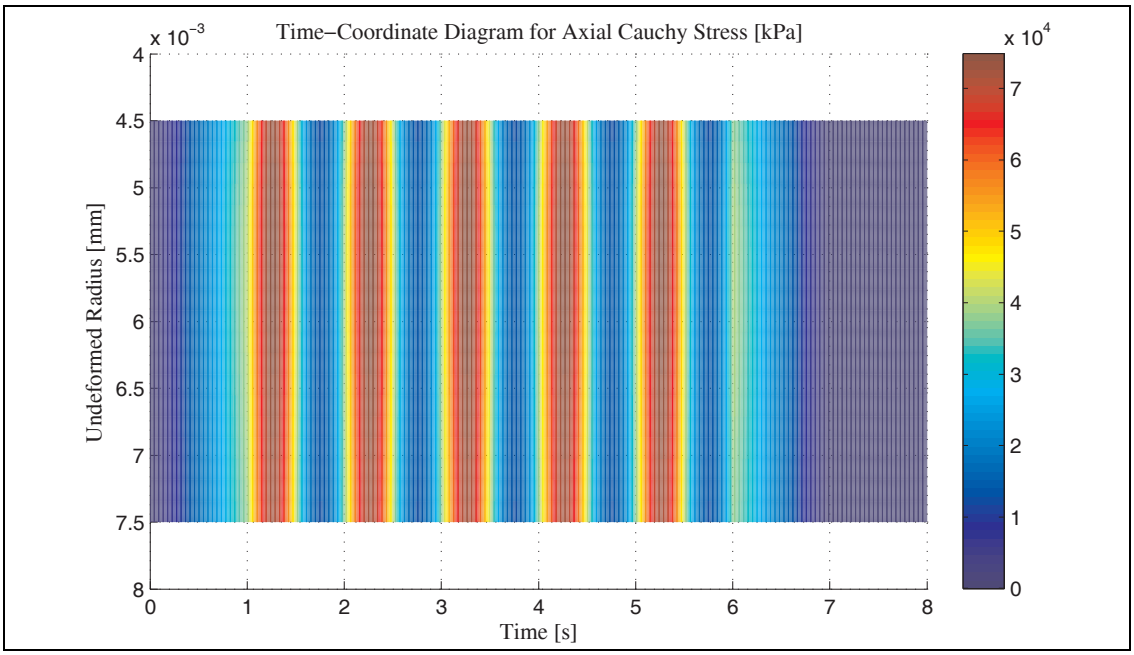

Figure A-3.2: Variation of Axial Stress with Time and within Wall Thickness under Isotropic Viscoelasticity

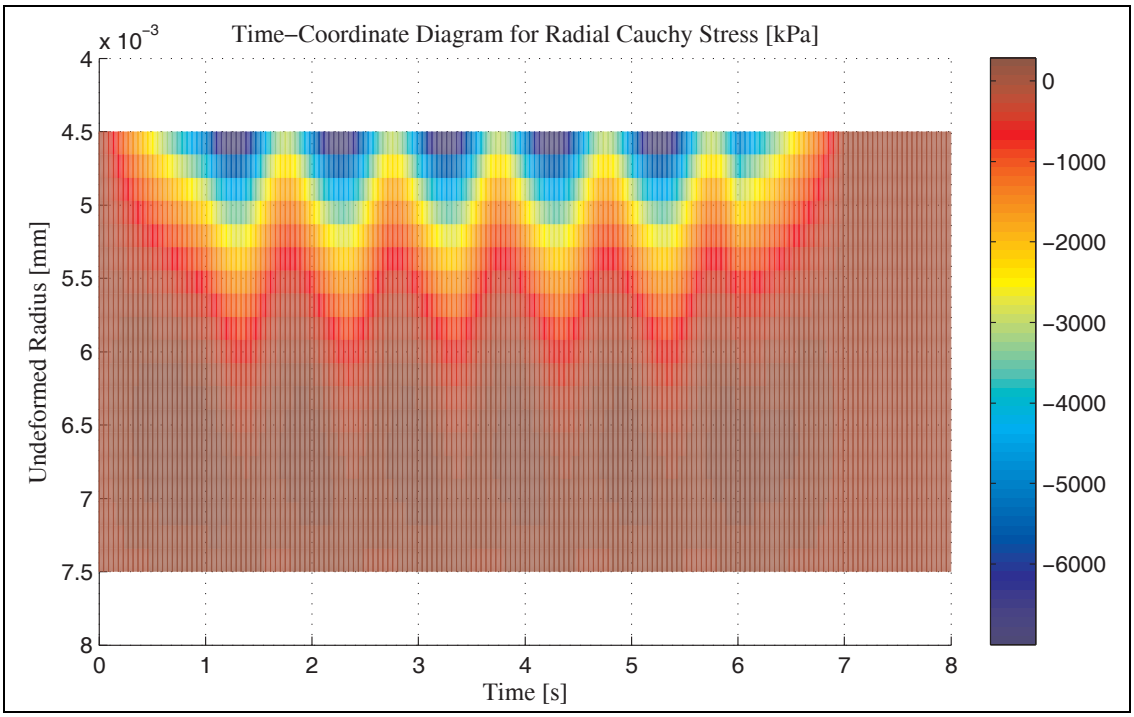

Figure A-3.3: Variation of Radial Stress with Time and within Wall Thickness under Isotropic Viscoelasticity

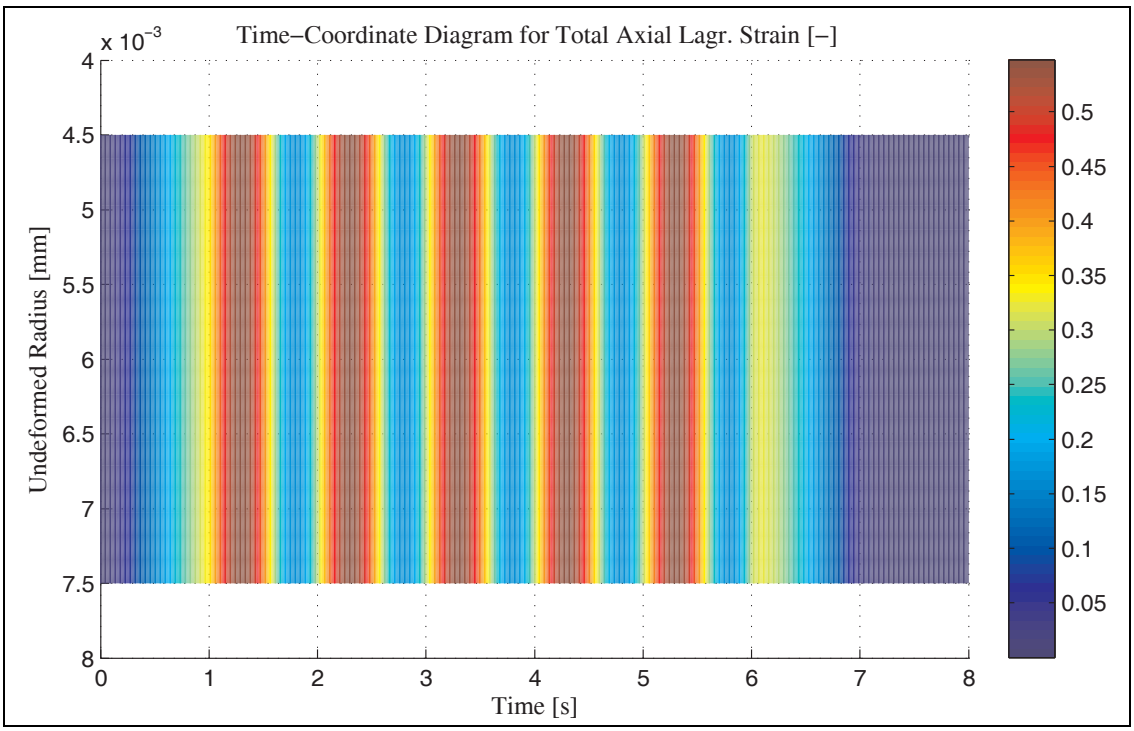

Figure A-3.4: Variation of Axial Total Strain with Time and within Wall Thickness under Isotropic Viscoelasticity

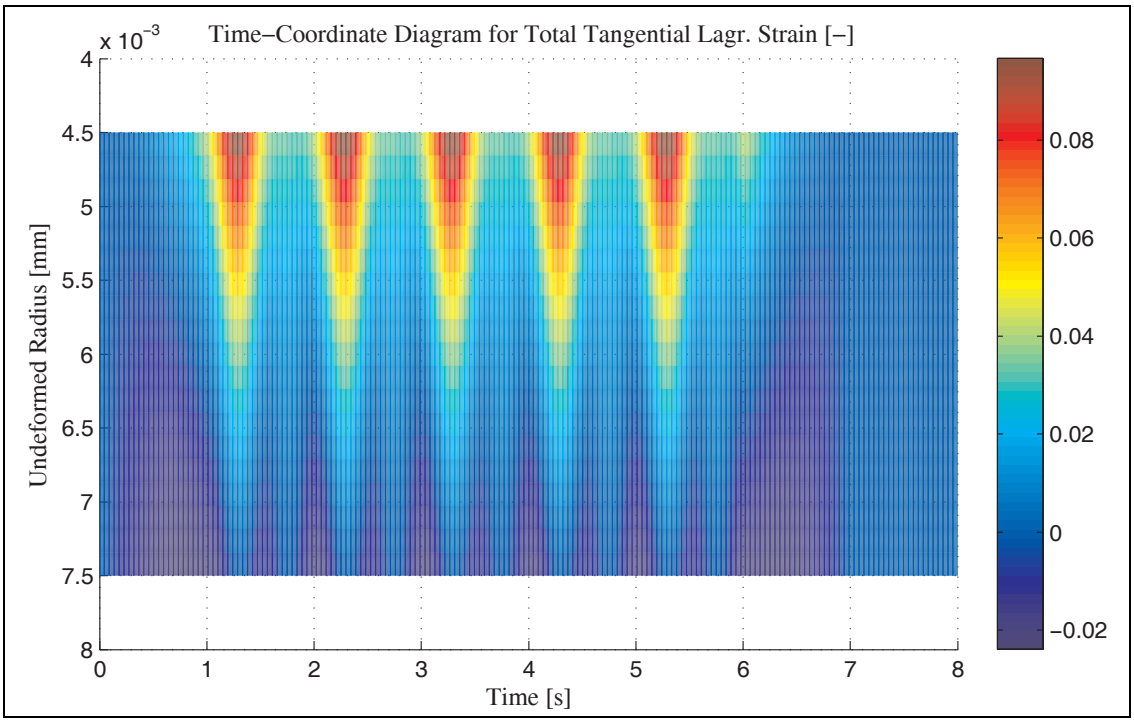

Figure A-3.5: Variation of Tangential Total Strain with Time and within Wall Thickness under Isotropic Viscoelasticity

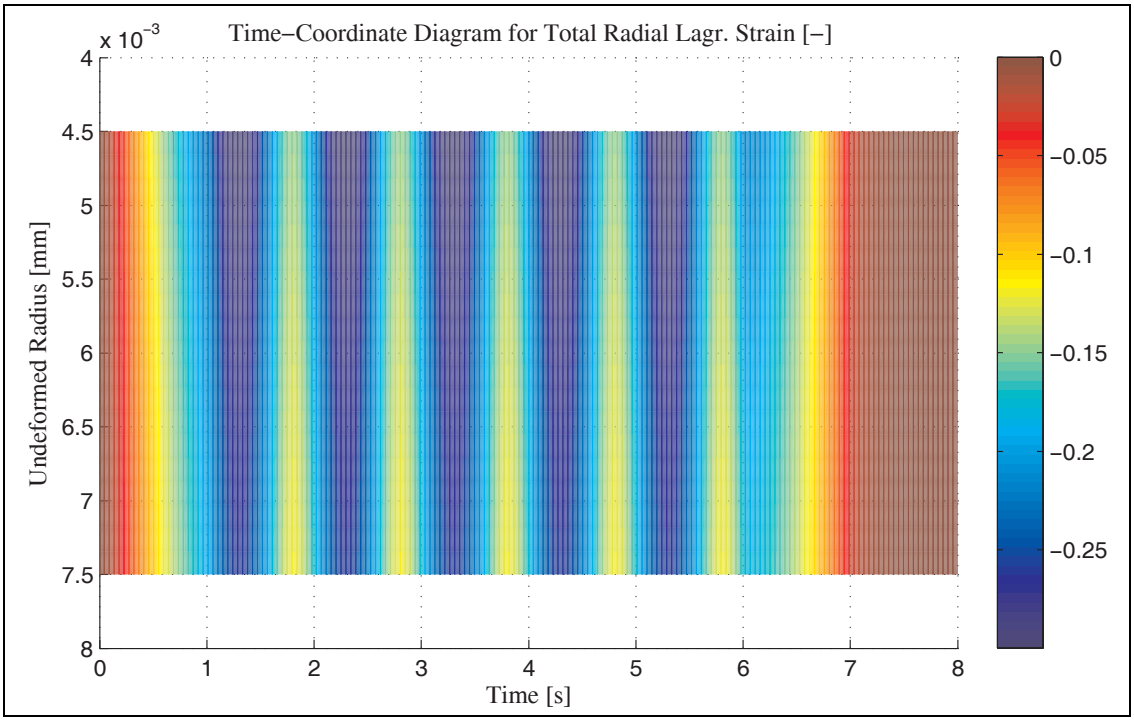

Figure A-3.6: Variation of Radial Total Strain with Time and within Wall Thickness under Isotropic Viscoelasticity

A-4. Nonlinear Viscoelasticity Model (due to Section 11.1.4)

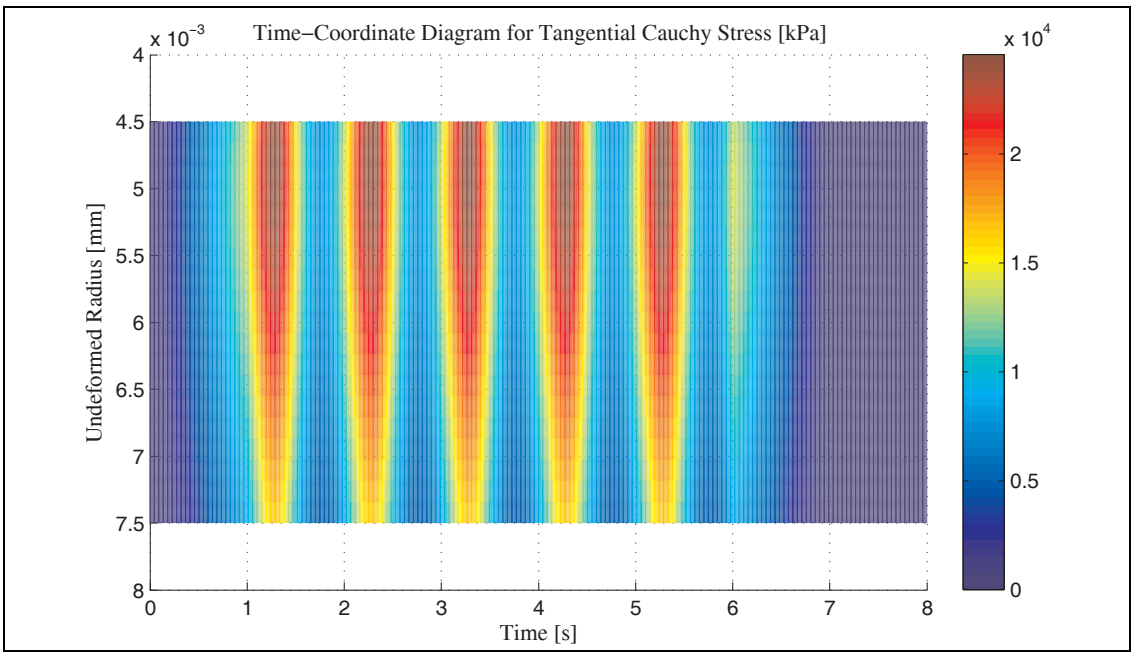

Figure A-4.1: Variation of Tangential Stress with Time and within Wall Thickness under Cyclic Loading at 1Hz using NonLinear Viscoelasticity Model

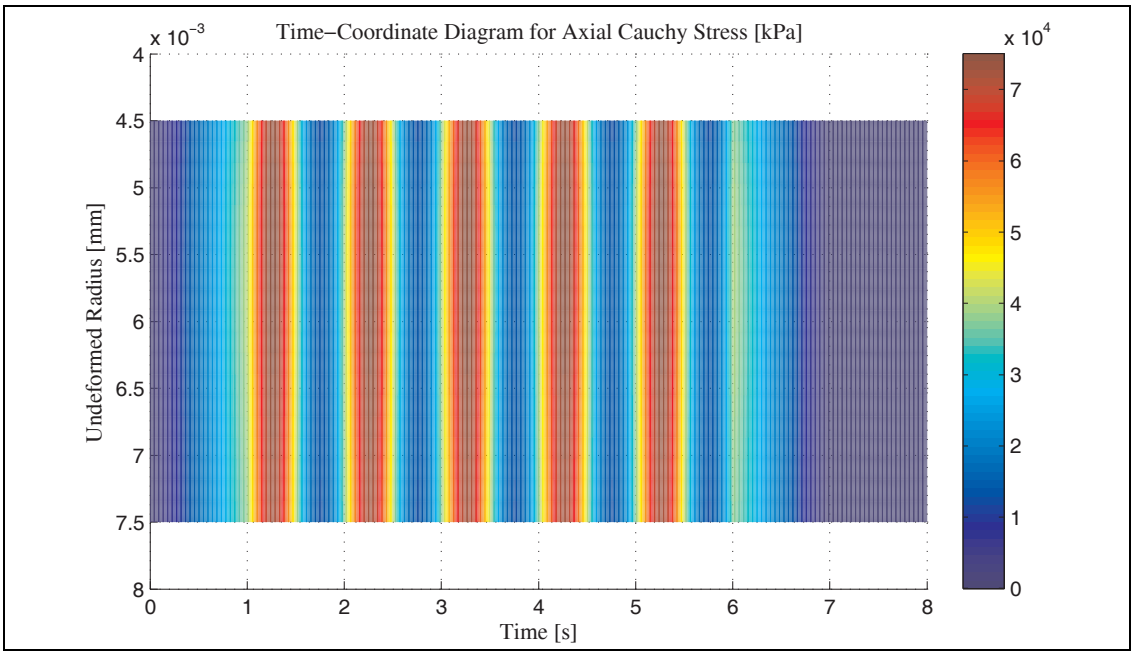

Figure A-4.2: Variation of Axial Stress with Time and within Wall Thickness under Cyclic Loading at 1Hz using NonLinear Viscoelasticity Model

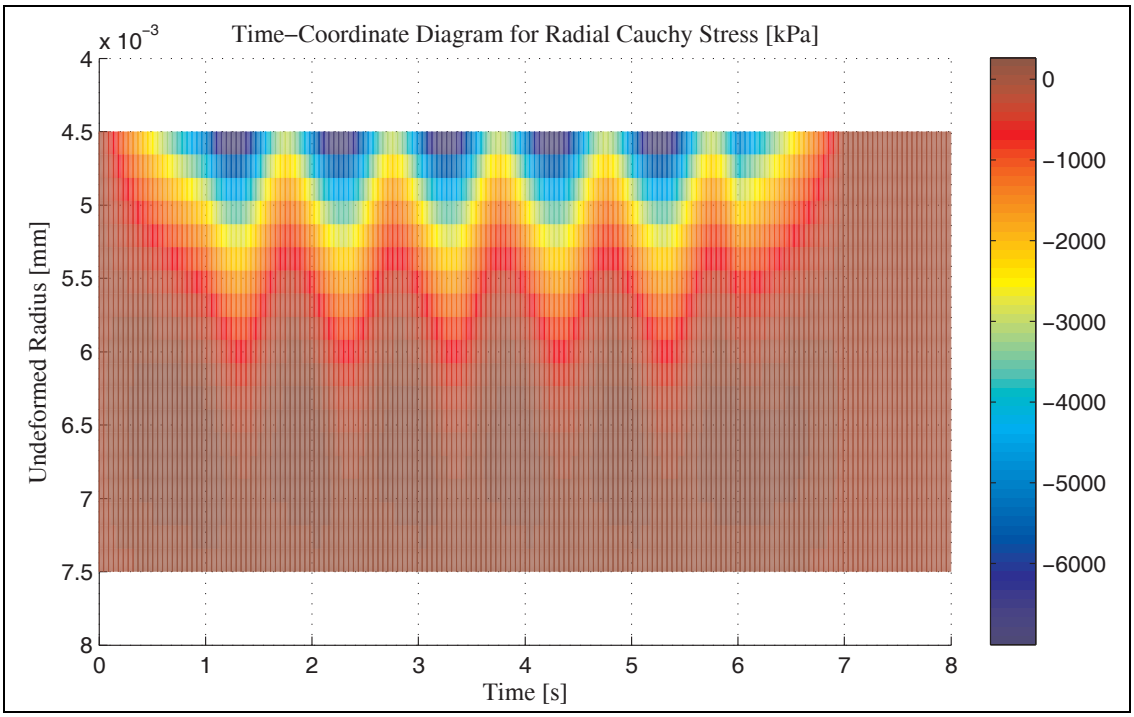

Figure A-4.3: Variation of Radial Stress with Time and within Wall Thickness under Cyclic Loading at 1Hz using NonLinear Viscoelasticity Model

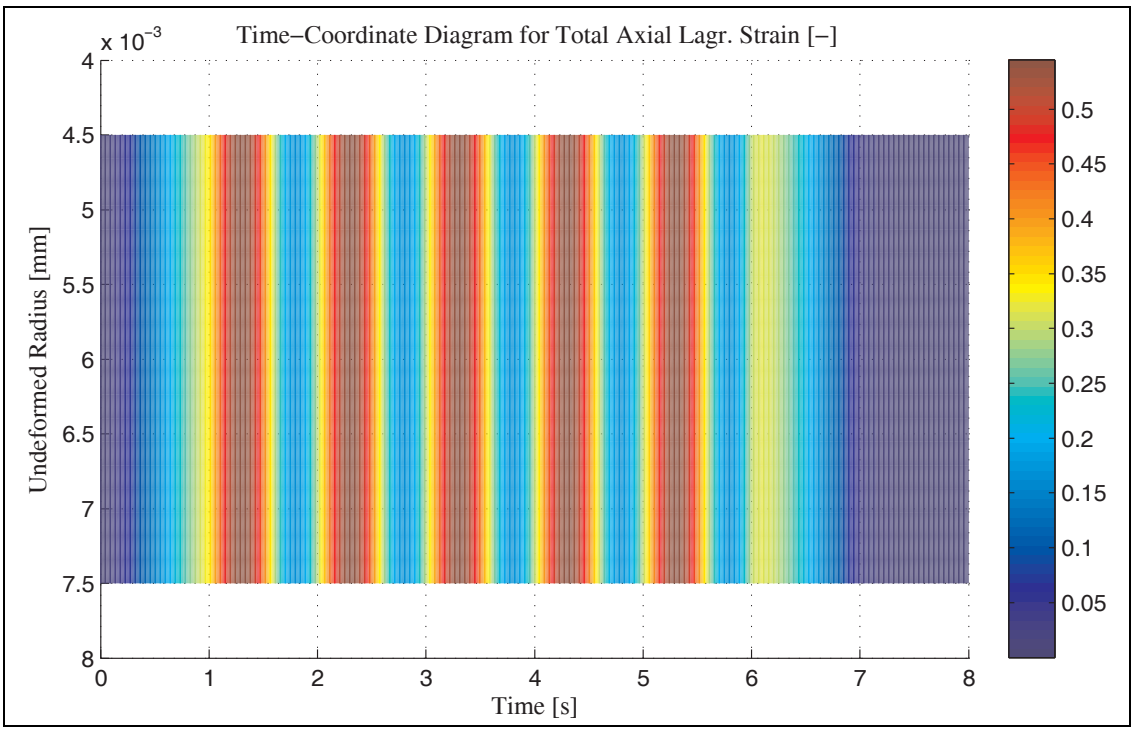

Figure A-4.4: Variation of Axial Total Strain with Time and within Wall Thickness under Cyclic Loading at 1Hz using NonLinear Viscoelasticity Model

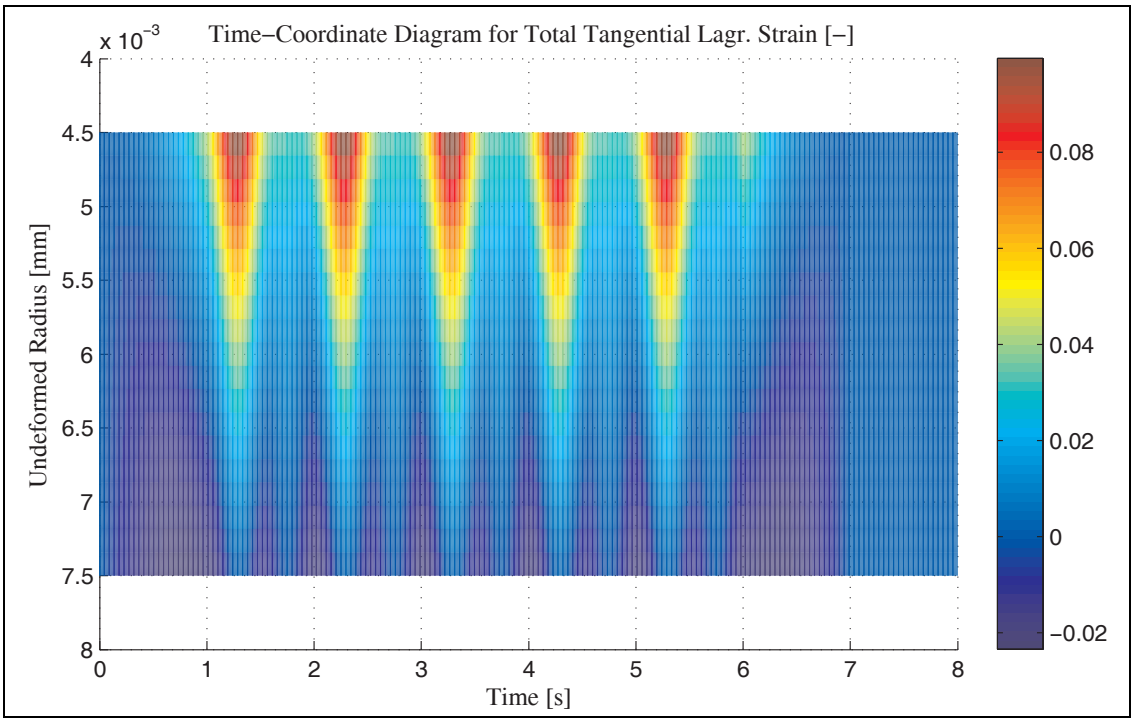

Figure A-4.5: Variation of Tangential Total Strain with Time and within Wall Thickness under Cyclic Loading at 1Hz using NonLinear Viscoelasticity Model

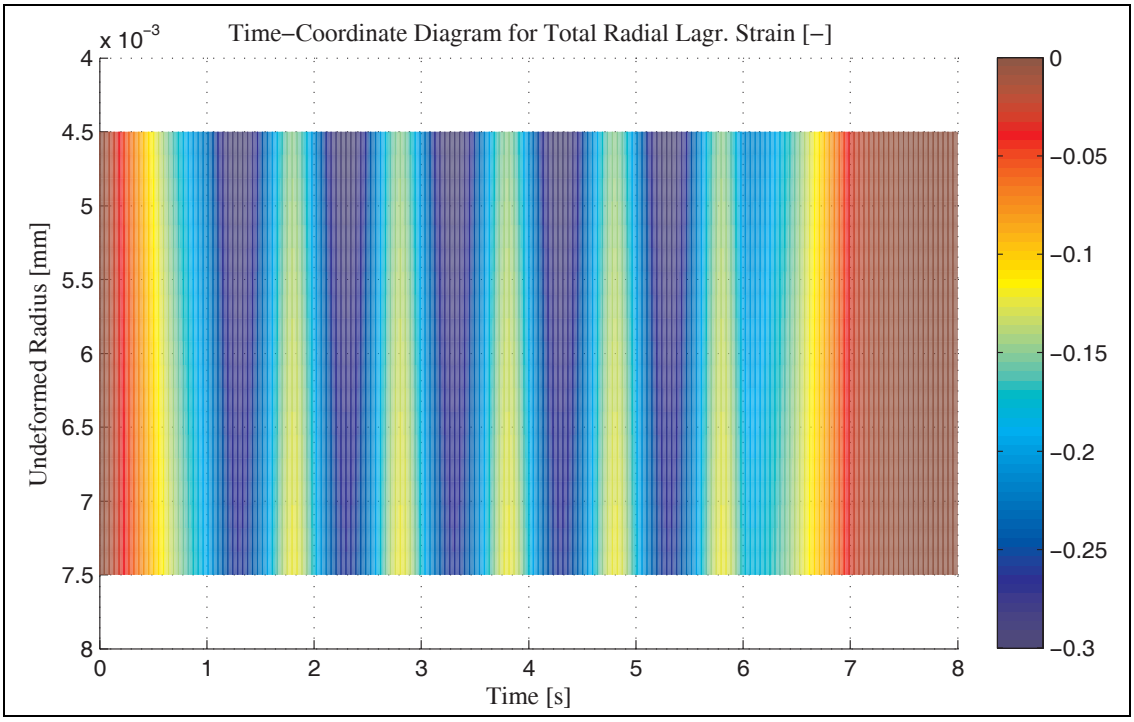

Figure A-4.6: Variation of Radial Total Strain with Time and within Wall Thickness under Cyclic Loading at 1Hz using NonLinear Viscoelasticity Model

A-5. Isotropic Viscoelasticity Model with Softening (due to Section 11.1.5)

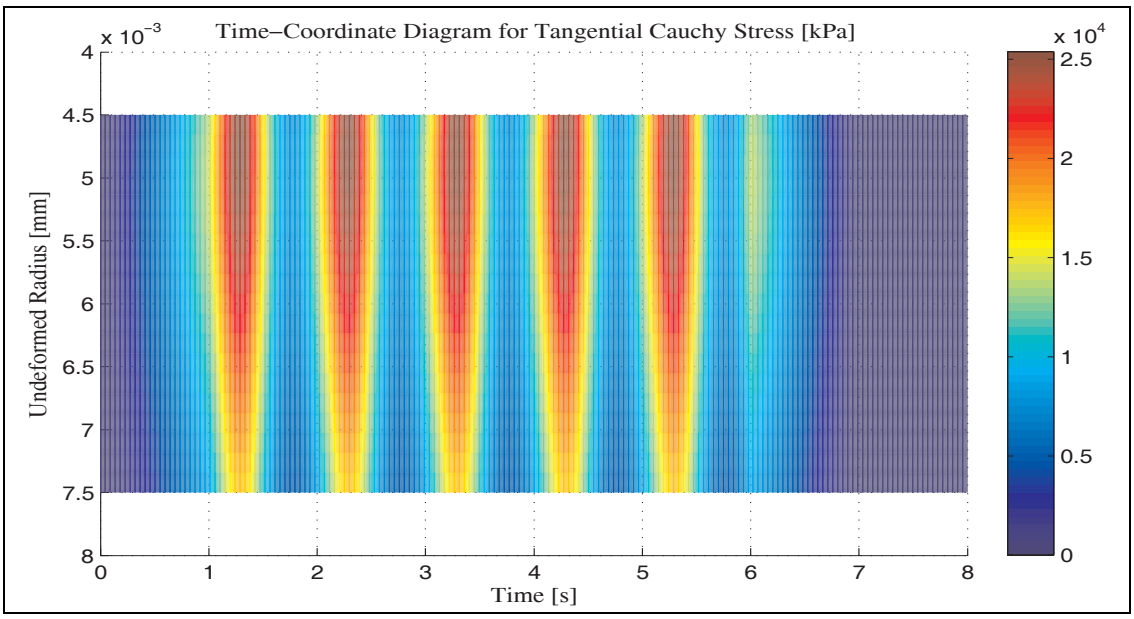

Figure A-5.1: Variation of Tangential Stress with Time and within Wall Thickness under Cyclic Loading at 1Hz using Isotropic Viscoelasticity Model and Softening

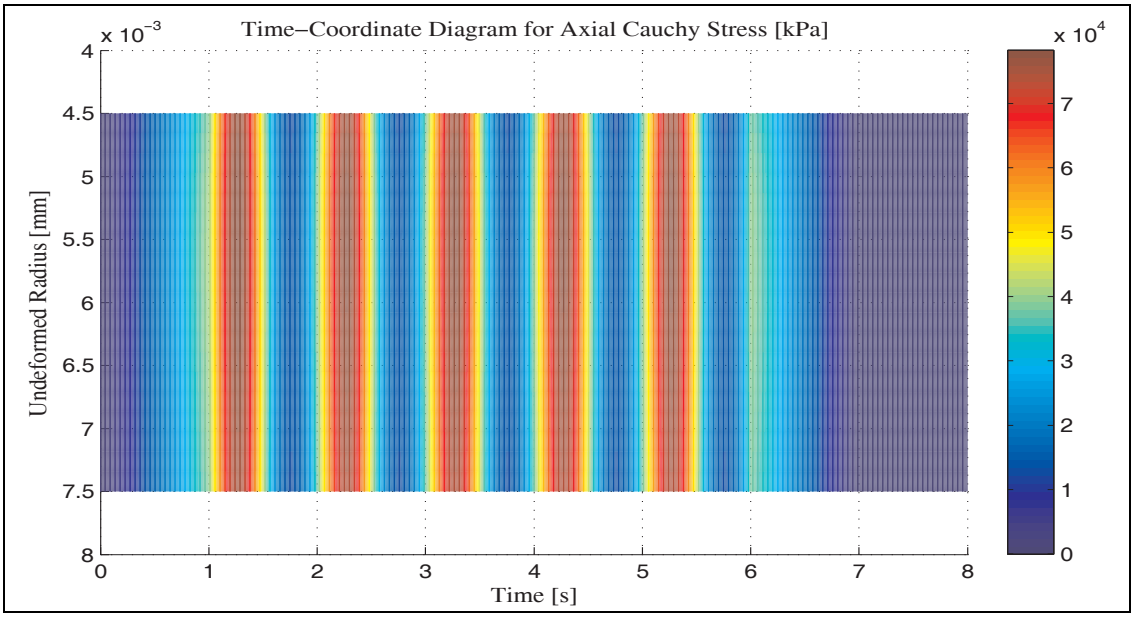

Figure A-5.2: Variation of Axial Stress with Time and within Wall Thickness under Cyclic Loading at 1Hz using Isotropic Viscoelasticity Model and Softening"

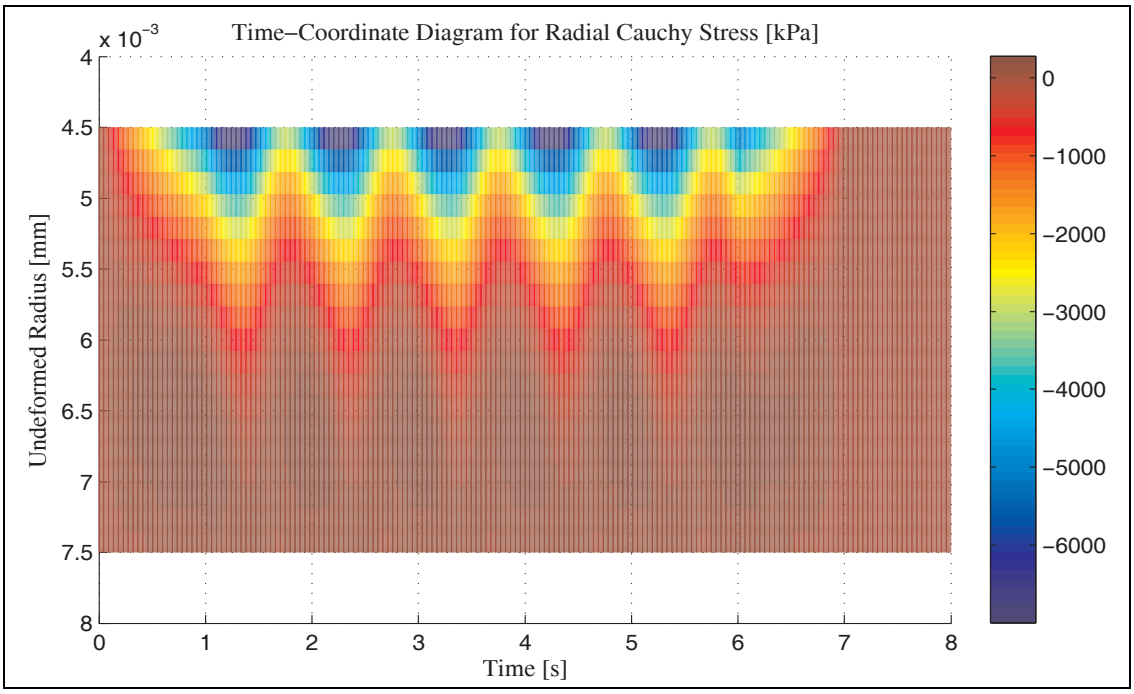

Figure A-5.3: Variation of Radial Stress with Time and within Wall Thickness under Cyclic Loading at 1Hz using Isotropic Viscoelasticity Model and Softening

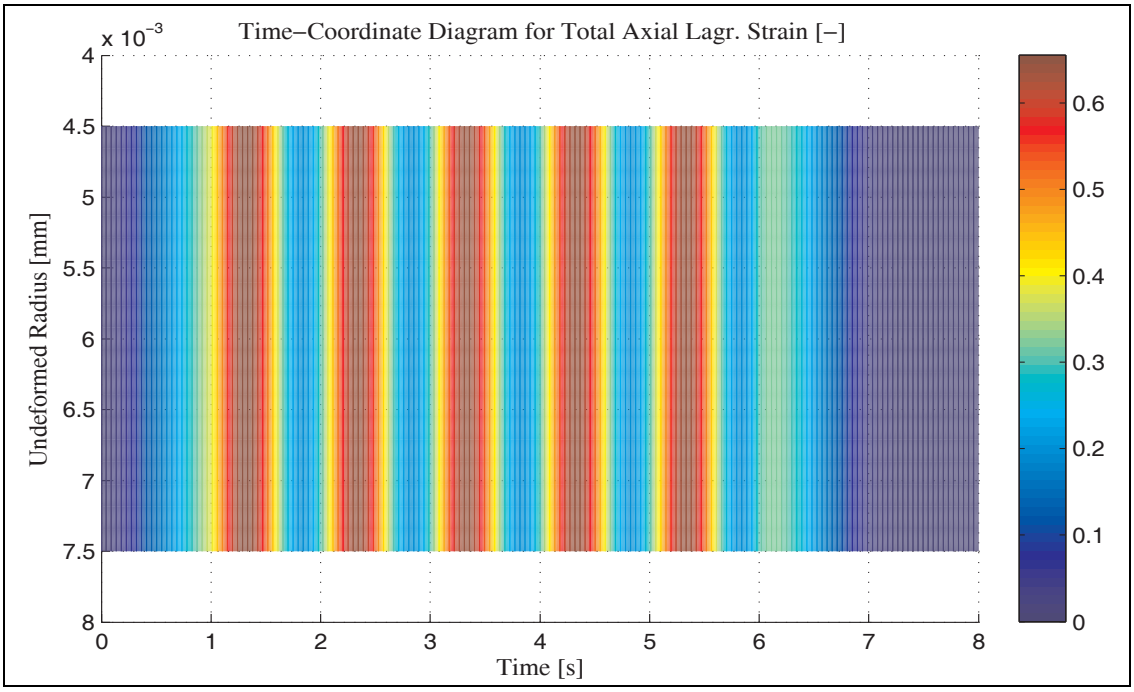

Figure A-5.4: Variation of Axial Total Strain with Time and within Wall Thickness under Cyclic Loading at 1Hz using Isotropic Viscoelasticity Model and Softening

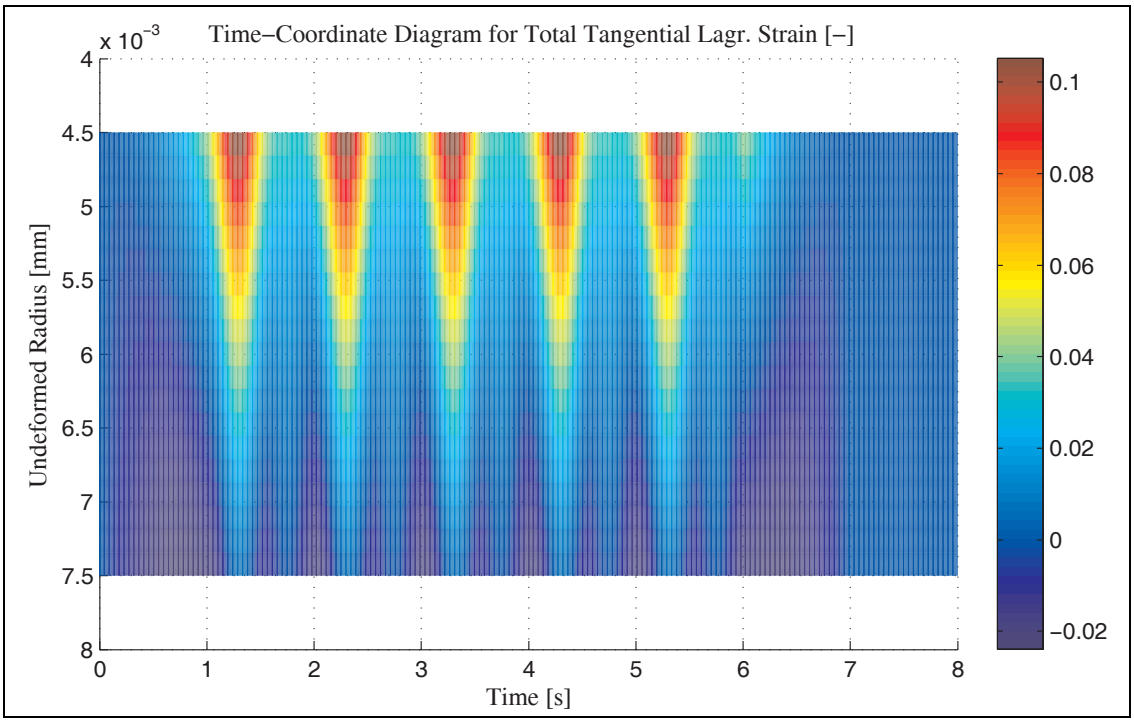

Figure A-5.5: Variation of Tangnt. Total Strain with Time and within Wall Thickness under Cyclic Loading at 1Hz using Isotropic Viscoelasticity Model and Softening

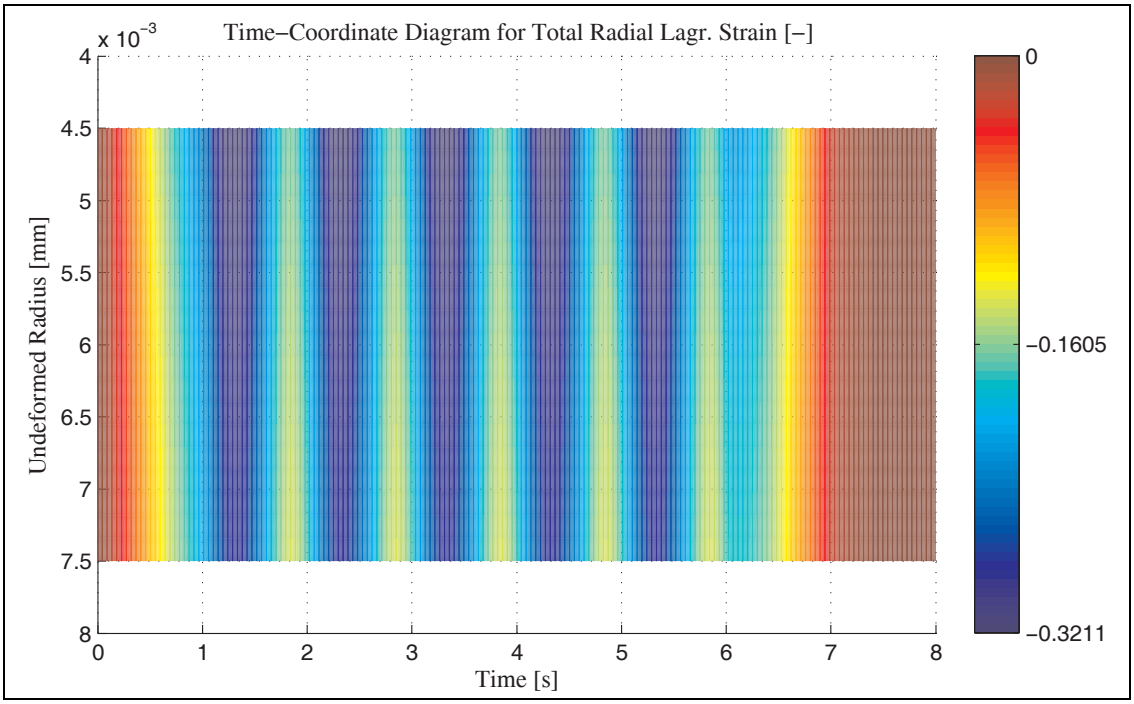

Figure A-5.6: Variation of Radial Total Strain with Time and within Wall Thickness under Cyclic Loading at 1Hz using Isotropic Viscoelasticity Model and Softening

A-6. Isotropic Viscoelasticity Model with Softening and Static Torsion (due to Section 11.1.6)

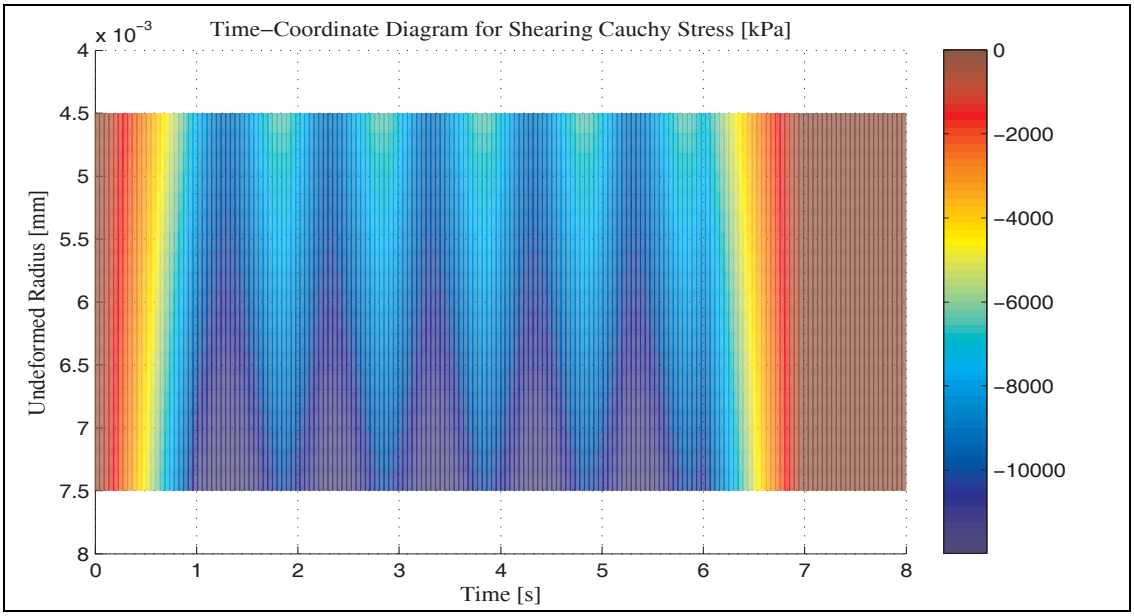

Figure A-6.1: Variation of Shear Stress with Time and within Wall Thickness under Cyclic Loading at 1Hz over Static Torsion using Isotropic Viscoelasticity Model with Softening Effects"

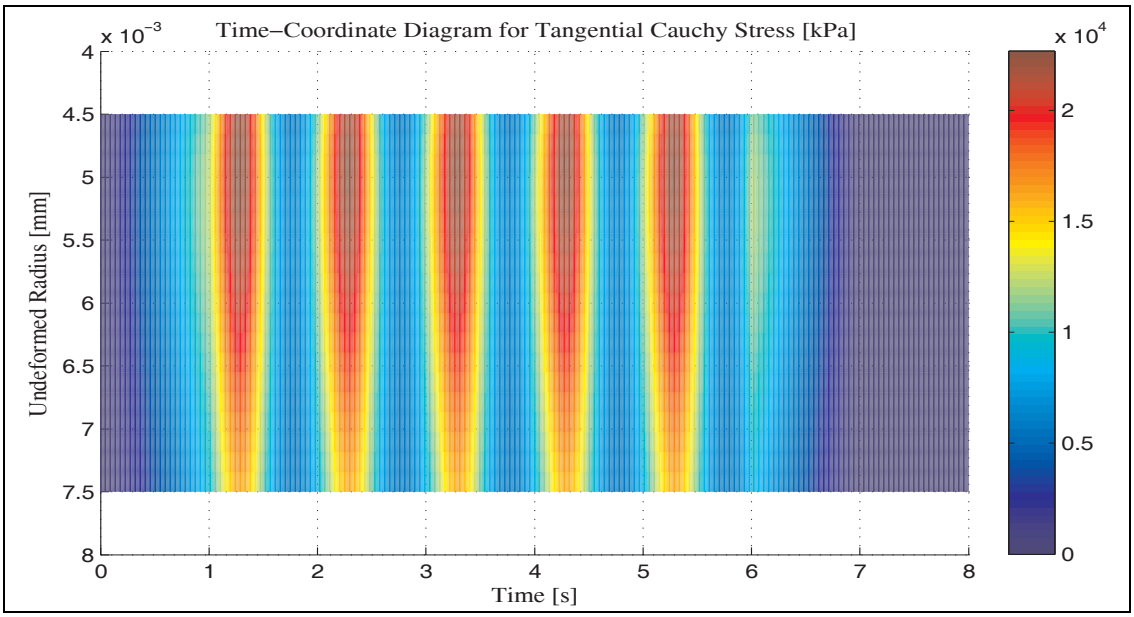

Figure A-6.2: Variation of Tangential Stress with Time and within Wall Thickness under Cyclic Loading at 1Hz over Static Torsion using Isotropic Viscoelasticity Model with Softening Effects

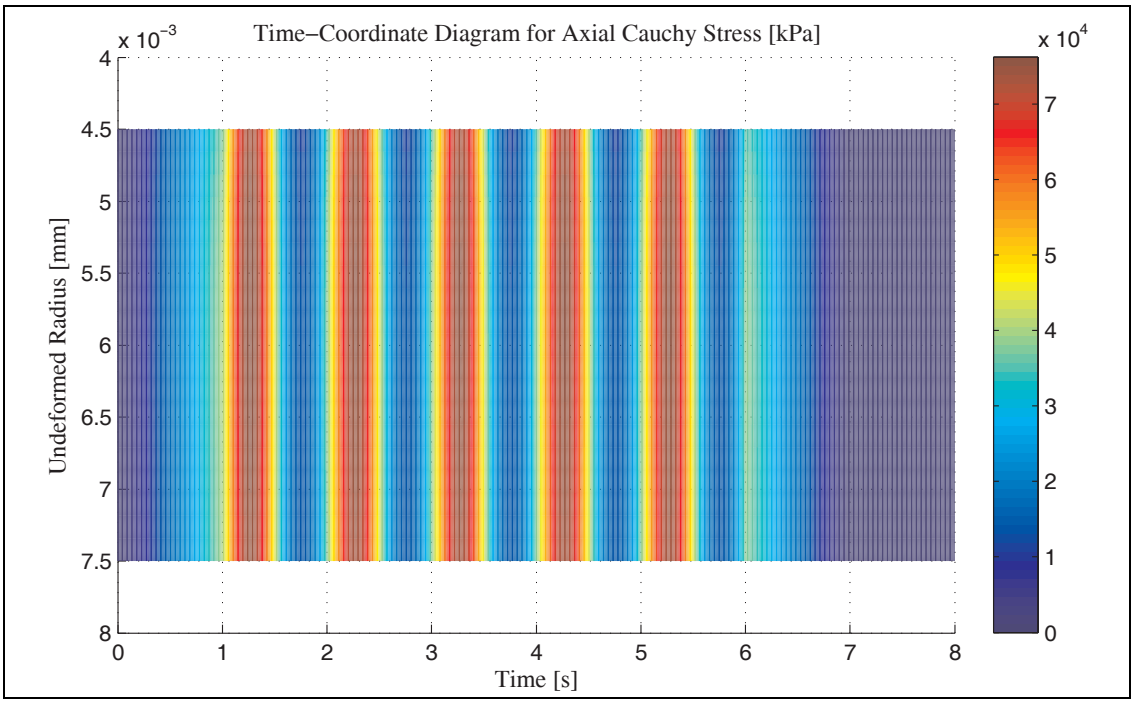

Figure A-6.3: Variation of Axial Stress with Time and within Wall Thickness under Cyclic Loading at 1Hz over Static Torsion using Isotropic Viscoelasticity Model with Softening Effects

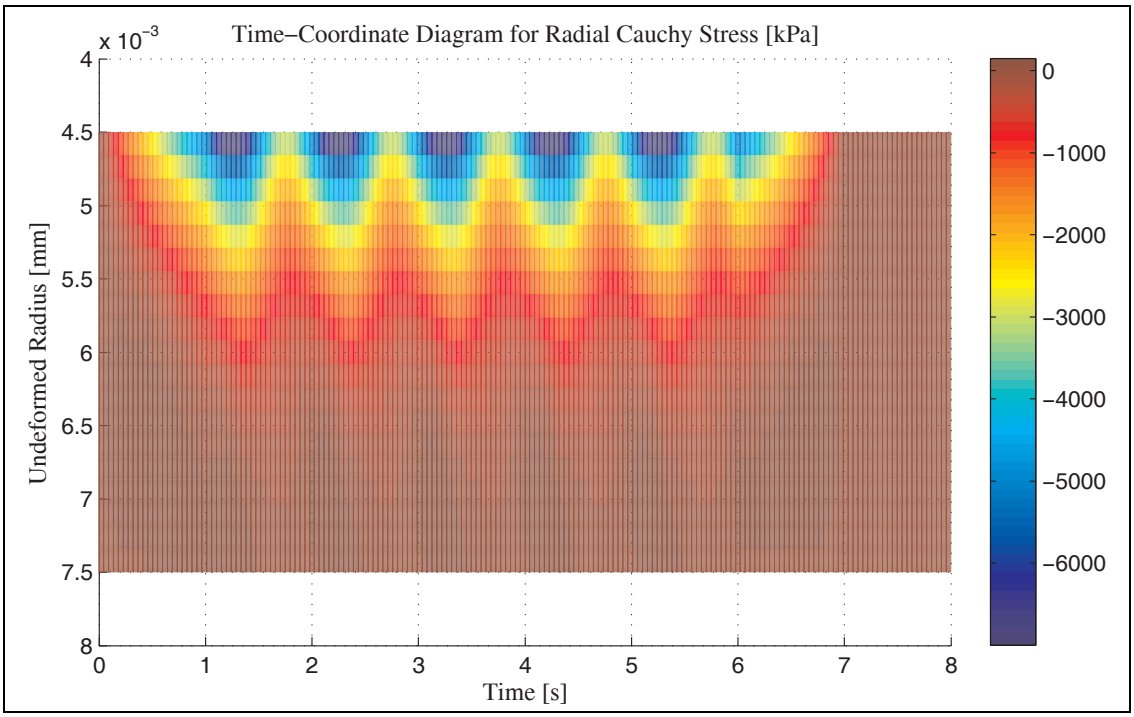

Figure A-6.4: Variation of Radial Stress with Time and within Wall Thickness under Cyclic Loading at 1Hz over Static Torsion using Isotropic Viscoelasticity Model with Softening Effects

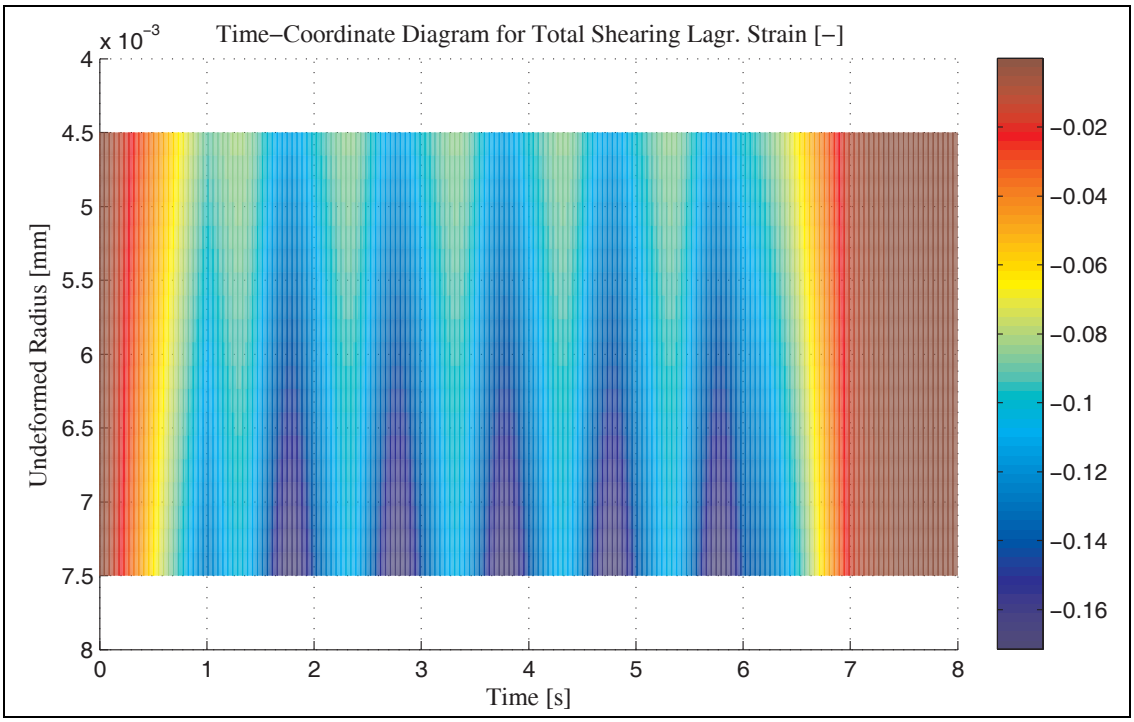

Figure A-6.5: Variation of Total Shear Strain with Time and within Wall Thickness under Cyclic Loading at 1Hz over Static Torsion using Isotropic Viscoelasticity Model with Softening Effects

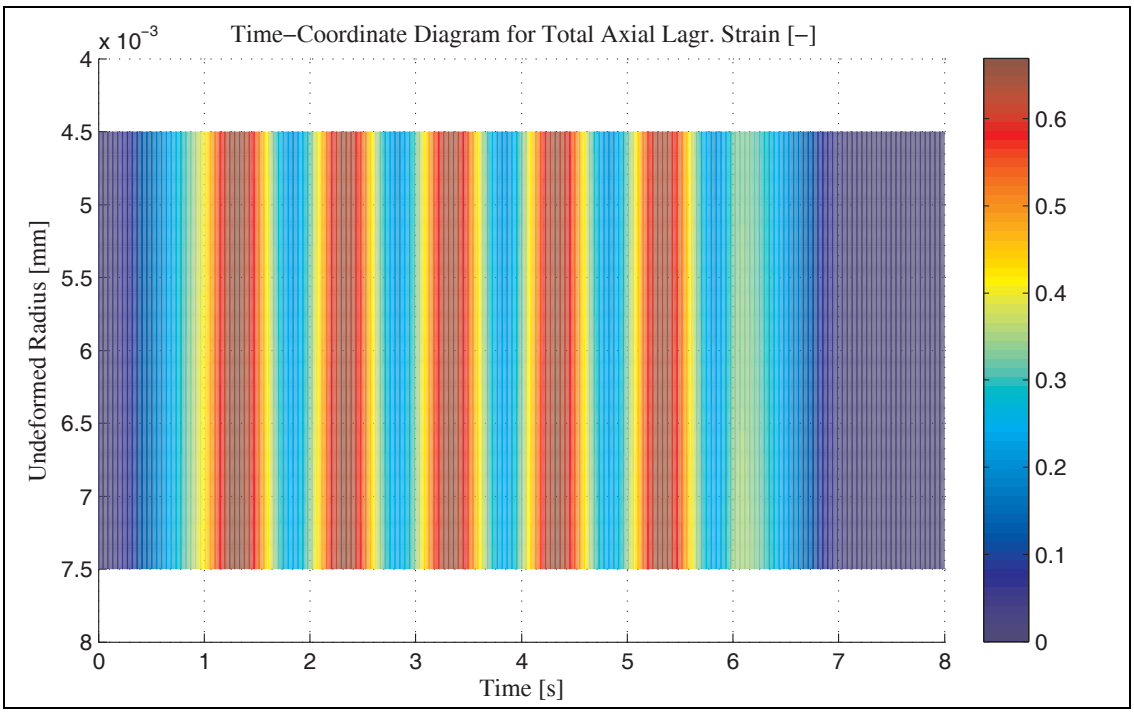

Figure A-6.6: Variation of Axial Total Strain with Time and within Wall Thickness under Cyclic Loading at 1Hz over Static Torsion using Isotropic Viscoelasticity Model with Softening Effects

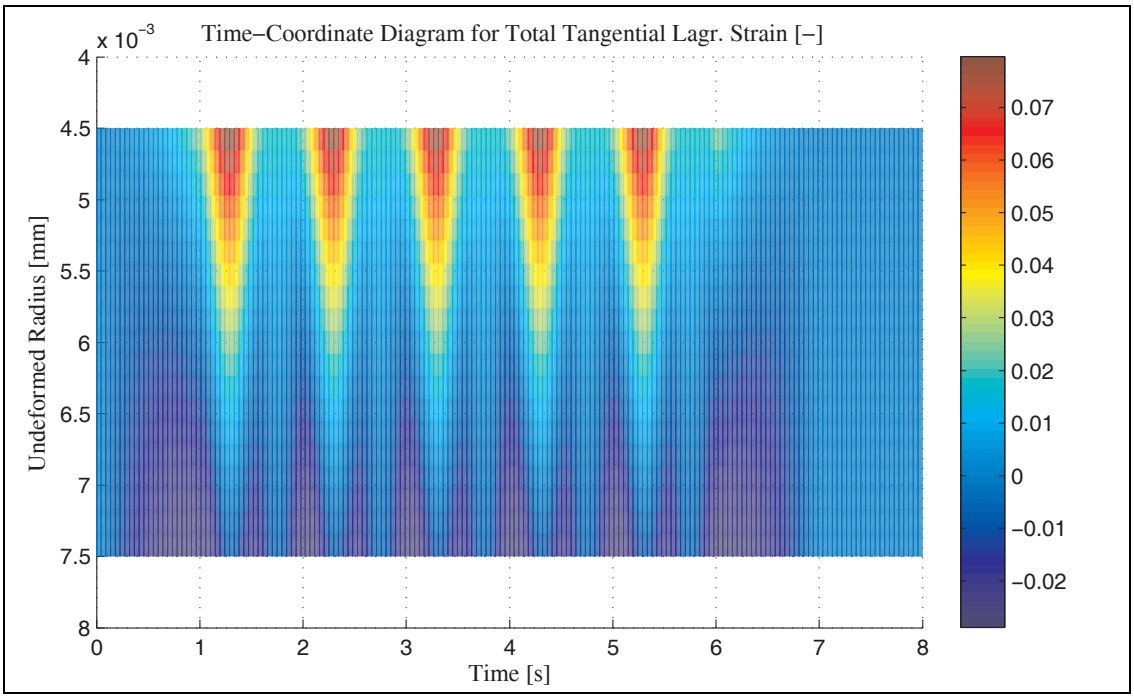

Figure A-6.7: Variation of Tangential Total Strain with Time and within Wall Thickness under Cyclic Loading at 1Hz over Static Torsion using Isotropic Viscoelasticity Model with Softening Effects

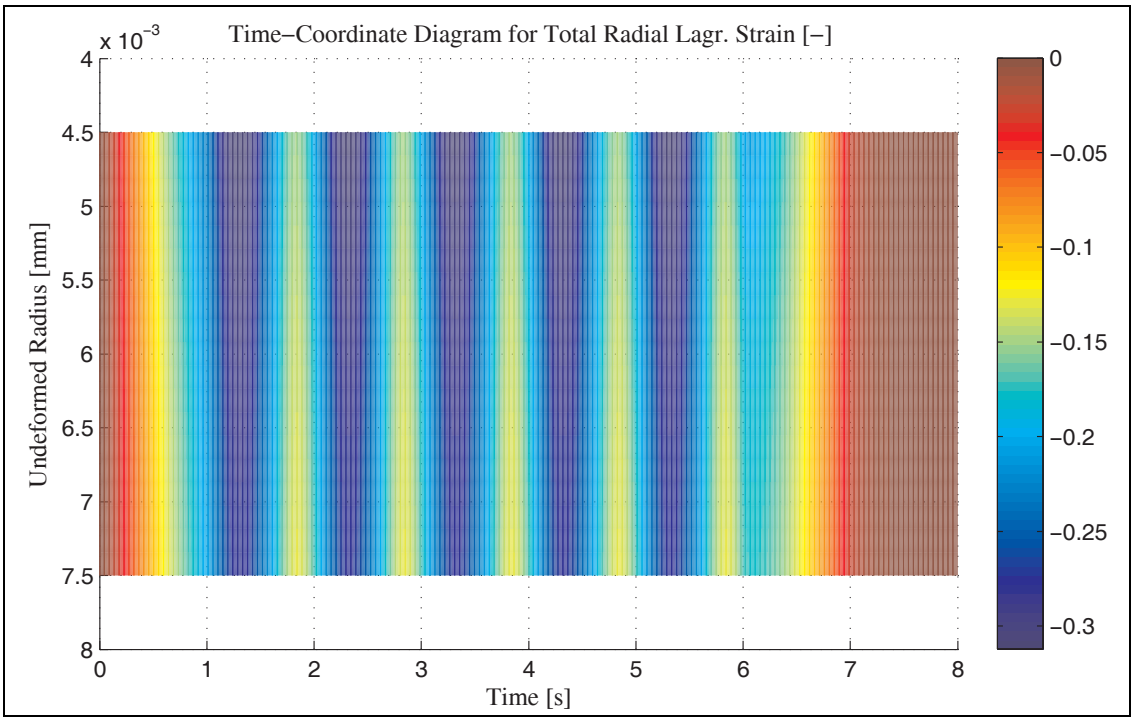

Figure A-6.8: Variation of Radial Total Strain with Time and within Wall Thickness under Cyclic Loading at 1Hz over Static Torsion using Isotropic Viscoelasticity Model with Softening Effects

A-7. Isotropic Viscoelasticity Model with Softening and Dynamic Torsion over Static Pressure and Axial Force (due to Section 11.1.7)

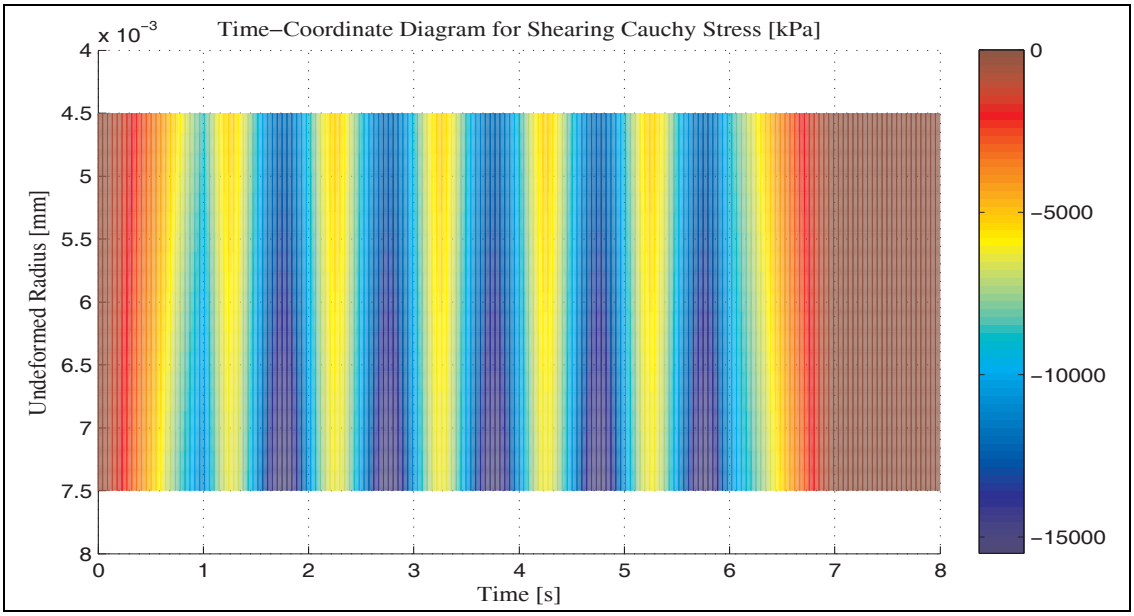

Figure A-7.1: Variation of Shear Stress with Time and within Wall Thickness under Cyclic Loading at 1Hz with Torsion using Isotropic Viscoelasticity Model with Softening Effects

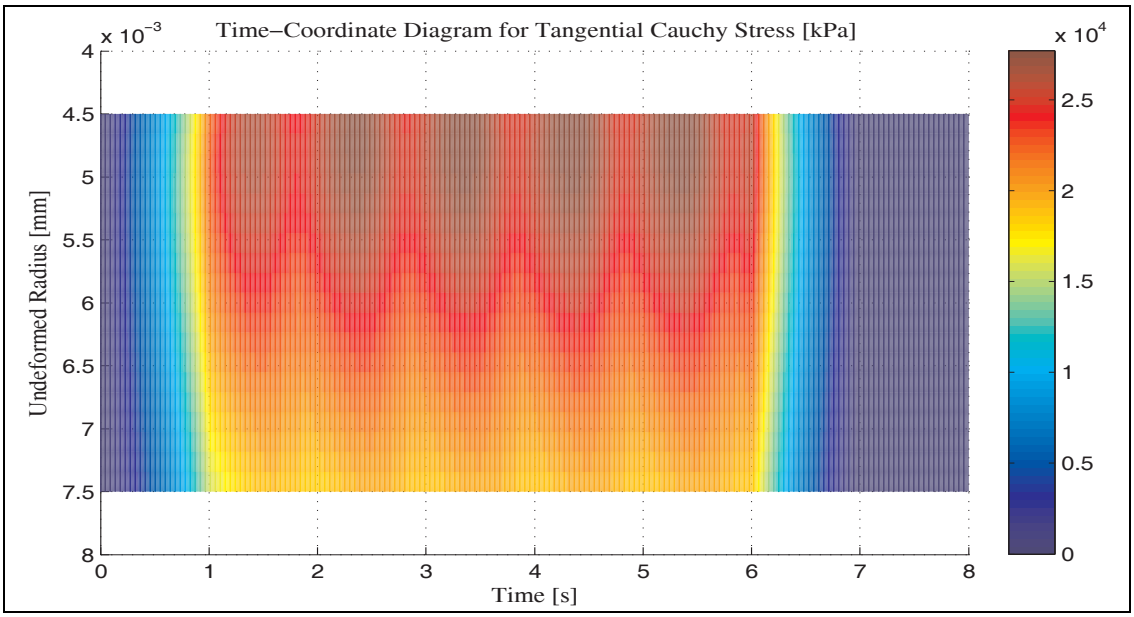

Figure A-7.2: Variation of Tangential Stress with Time and within Wall Thickness under Cyclic Loading at 1Hz with Torsion using Isotropic Viscoelasticity Model with Softening Effects

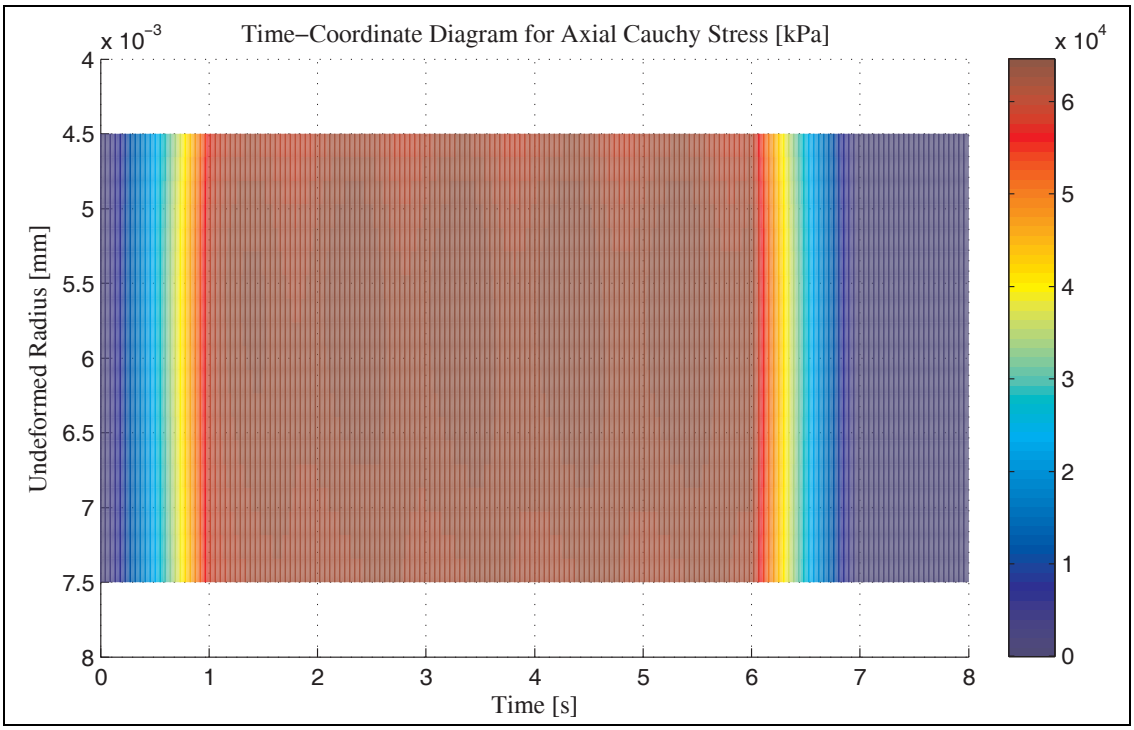

Figure A-7.3: Variation of Axial Stress with Time and within Wall Thickness a under Cyclic Loading at 1Hz with Torsion using Isotropic Viscoelasticity Model with Softening Effects

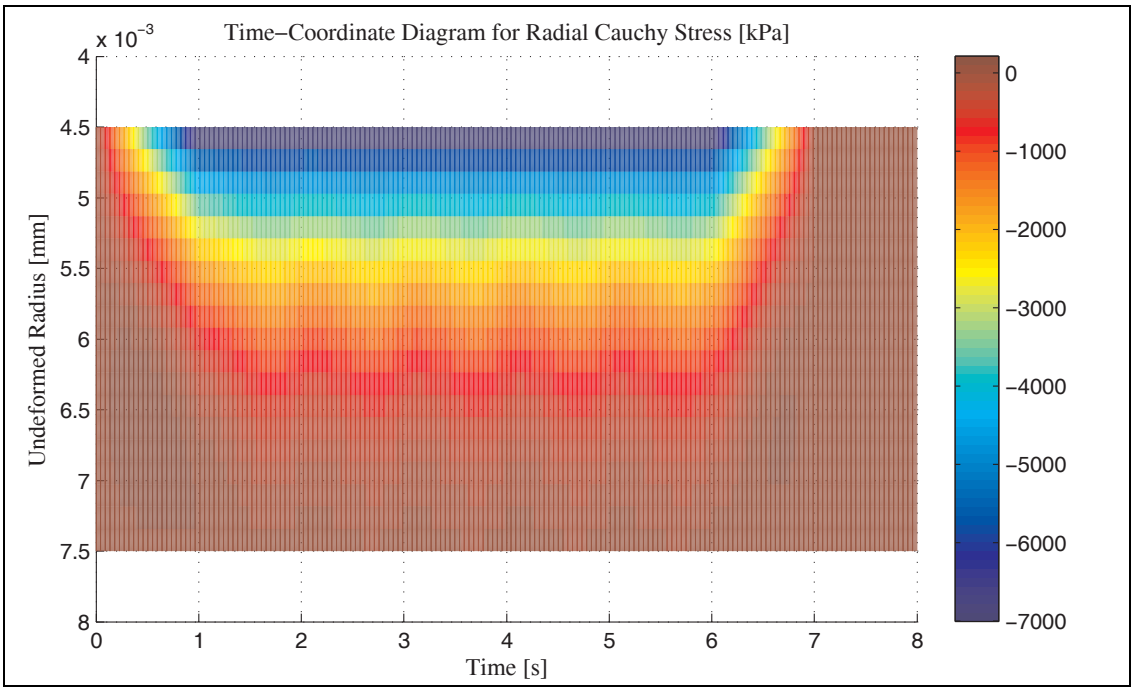

Figure A-7.4: Variation of Radial Stress with Time and within Wall Thickness under Cyclic Loading at 1Hz with Torsion using Isotropic Viscoelasticity Model with Softening Effects

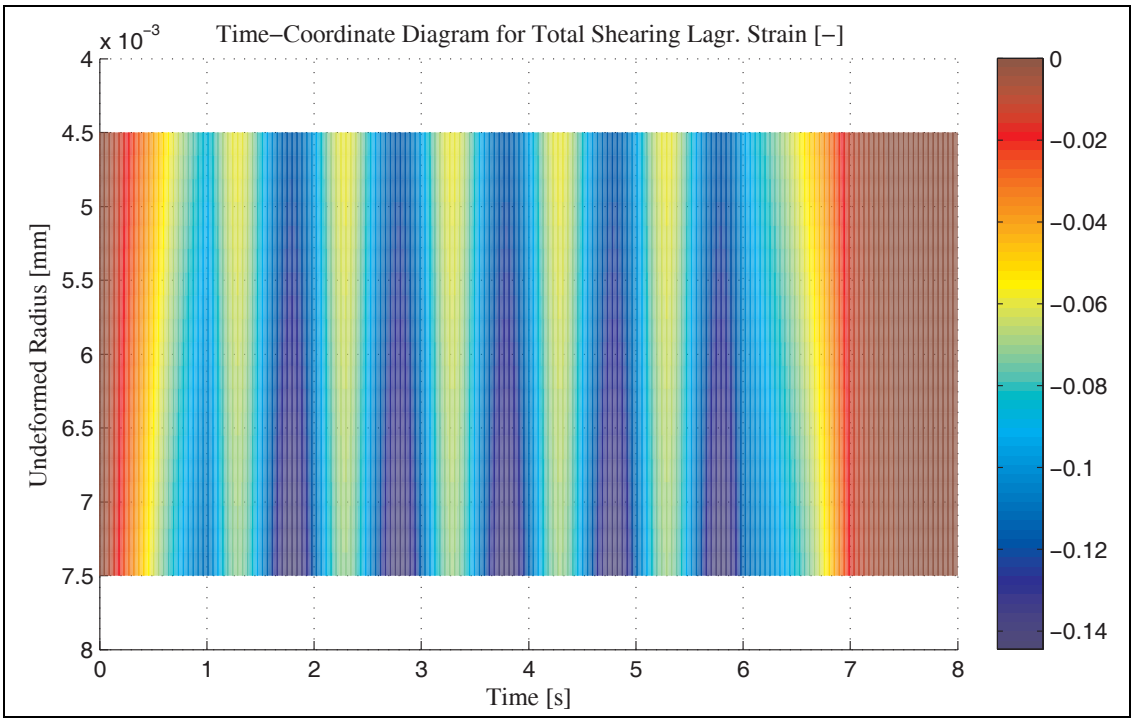

Figure A-7.5: Variation of Total Shear Strain with Time and within Wall Thickness under Cyclic Loading at 1Hz with Torsion using Isotropic Viscoelasticity Model with Softening Effects

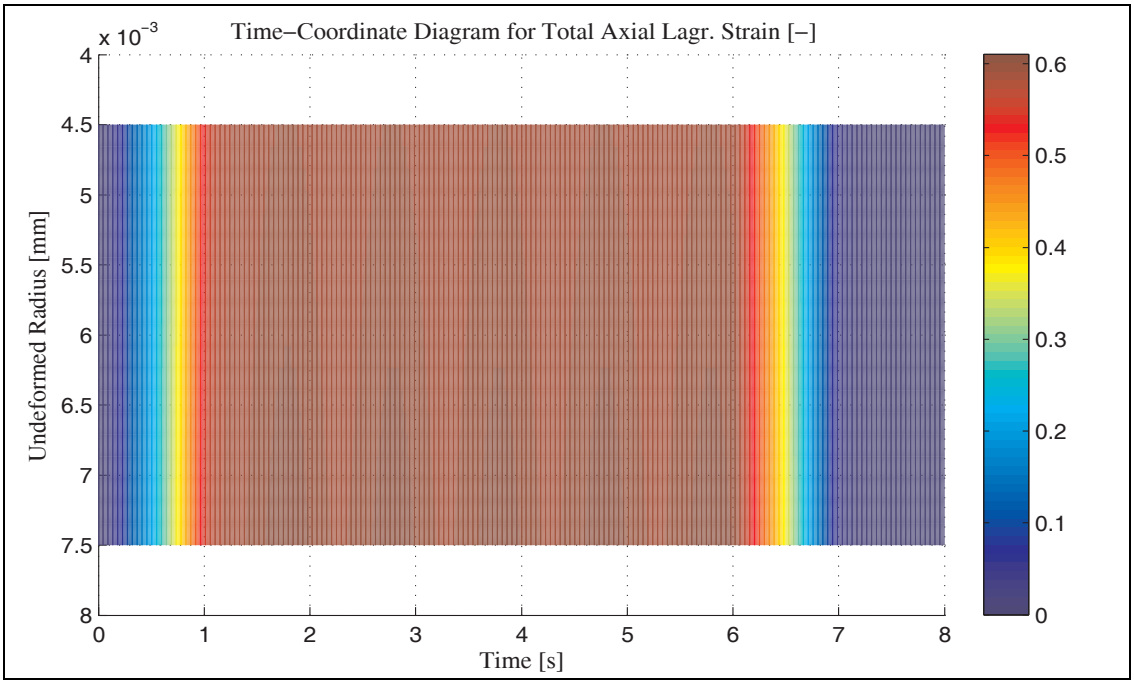

Figure A-7.6: Variation of Axial Total Strain with Time and within Wall Thickness under Cyclic Loading at 1Hz with Torsion using Isotropic Viscoelasticity Model with Softening Effects

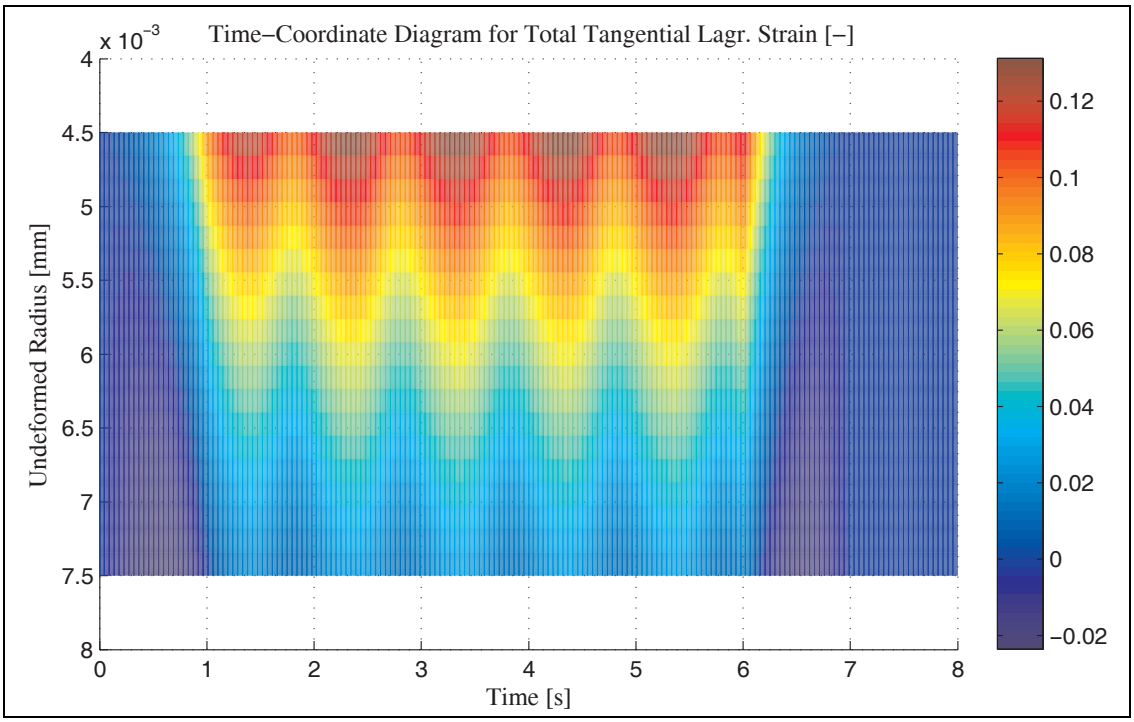

Figure A-7.7: Variation of Tangential Total Strain with Time and within Wall Thickness under Cyclic Loading at 1Hz with Torsion using Isotropic Viscoelasticity Model with Softening Effects

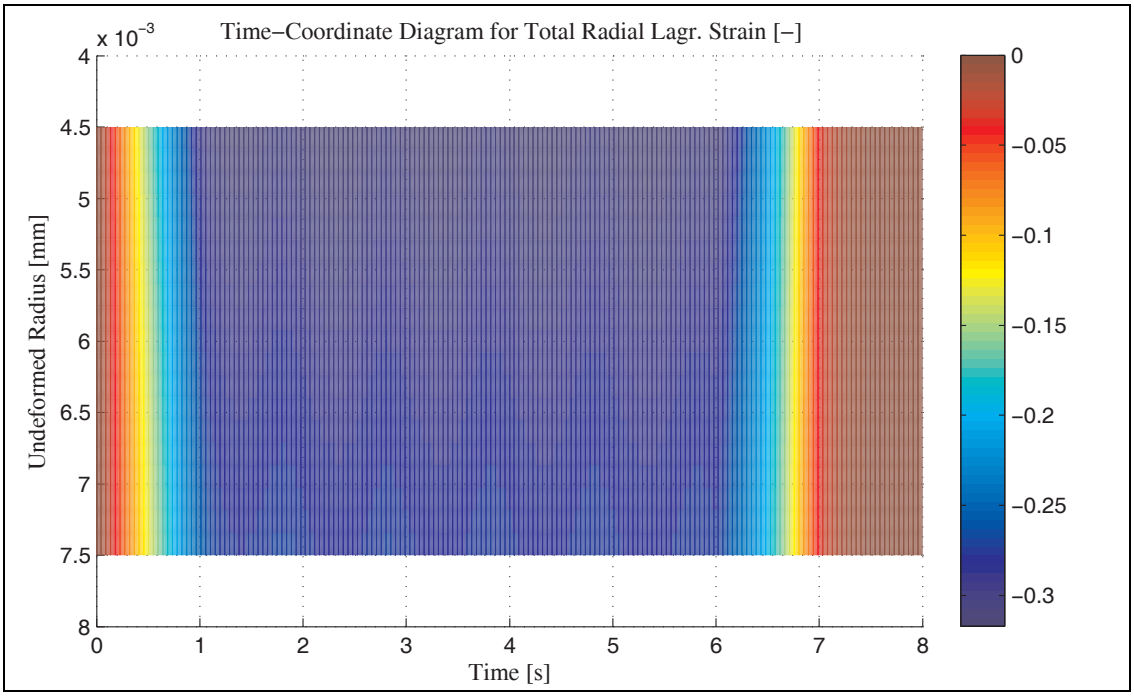

Figure A-7.8: Variation of Radial Total Strain with Time and within Wall Thickness under Cyclic Loading at 1Hz with Torsion using Isotropic Viscoelasticity Model with Softening Effects"

A-8. Isotropic Viscoelasticity Model with Softening and Under Dynamic Inflation and Torsion with Static Axial Load (due to Section 11.1.8)

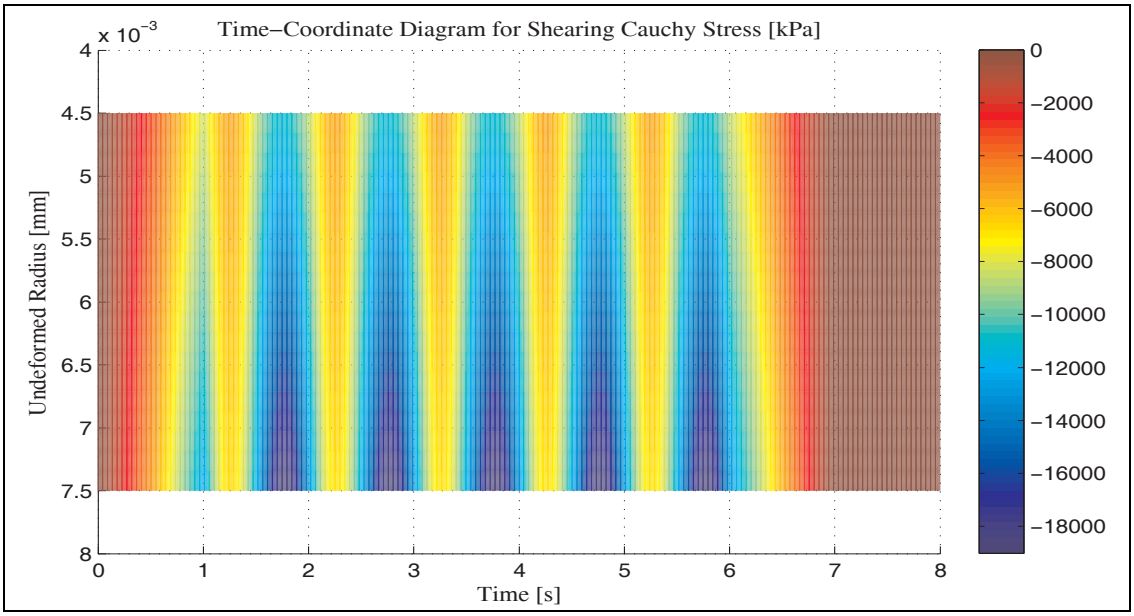

Figure A-8.1: Variation of Shear Stress with Time and within Wall Thickness under Cyclic Loading at 1Hz with Torsion using Isotropic Viscoelasticity Model with Softening Effects

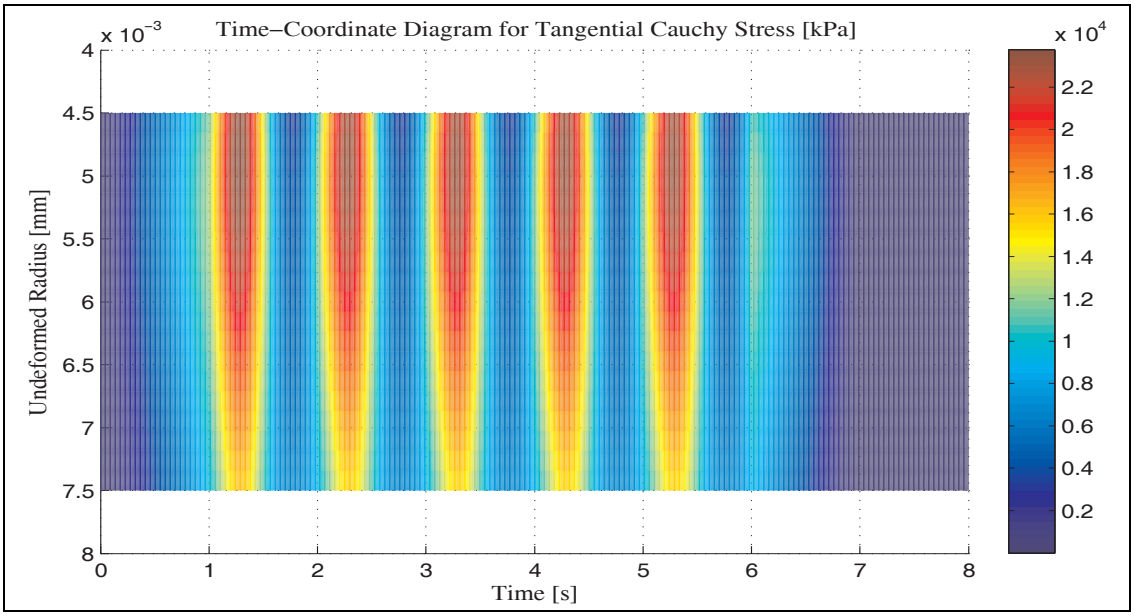

Figure A-8.2: Variation of Tangential Stress with Time and within Wall Thickness under Cyclic Loading at 1Hz with Torsion using Isotropic Viscoelasticity Model with Softening Effects"

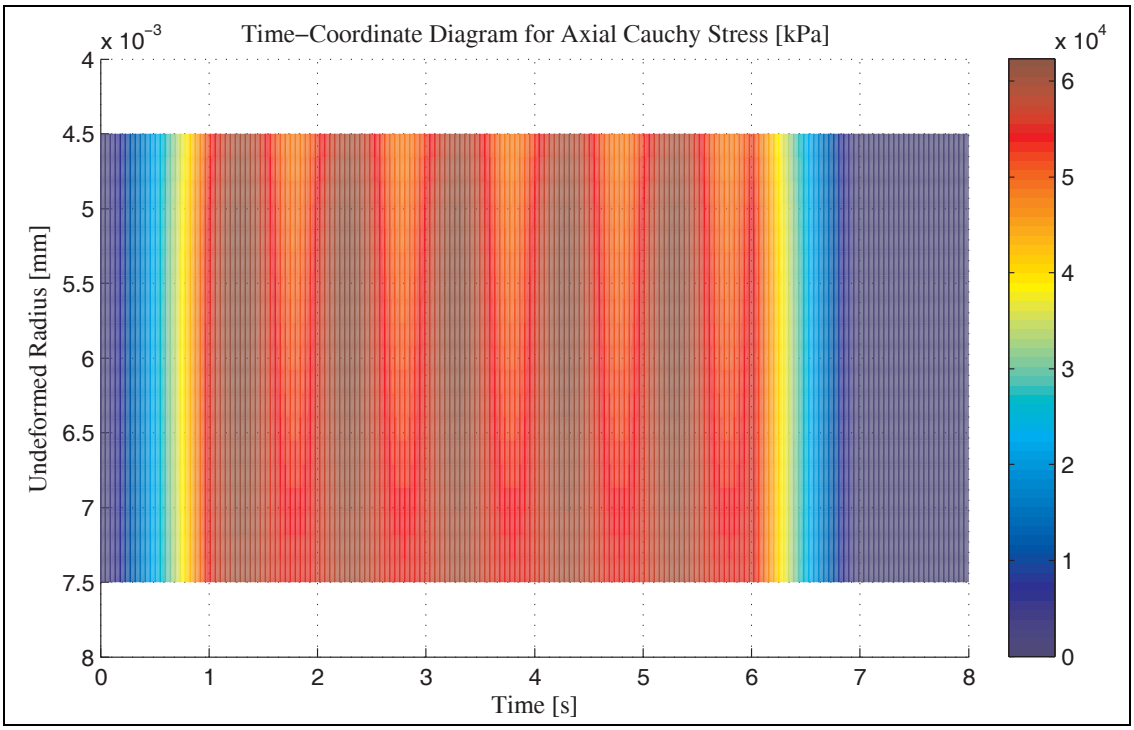

Figure A-8.3: Variation of Axial Stress with Time and within Wall Thickness under Cyclic Loading at 1Hz with Torsion using Isotropic Viscoelasticity Model with Softening Effects

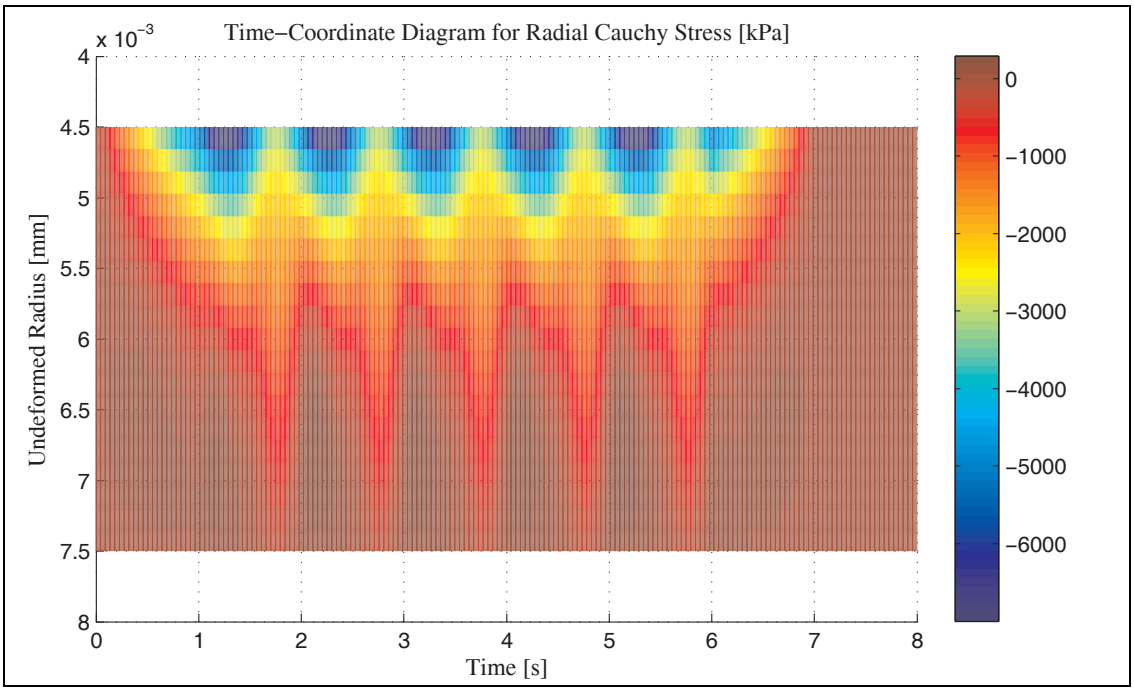

Figure A-8.4: Variation of Radial Stress with Time and within Wall Thickness under Cyclic Loading at 1Hz with Torsion using Isotropic Viscoelasticity Model with Softening Effects

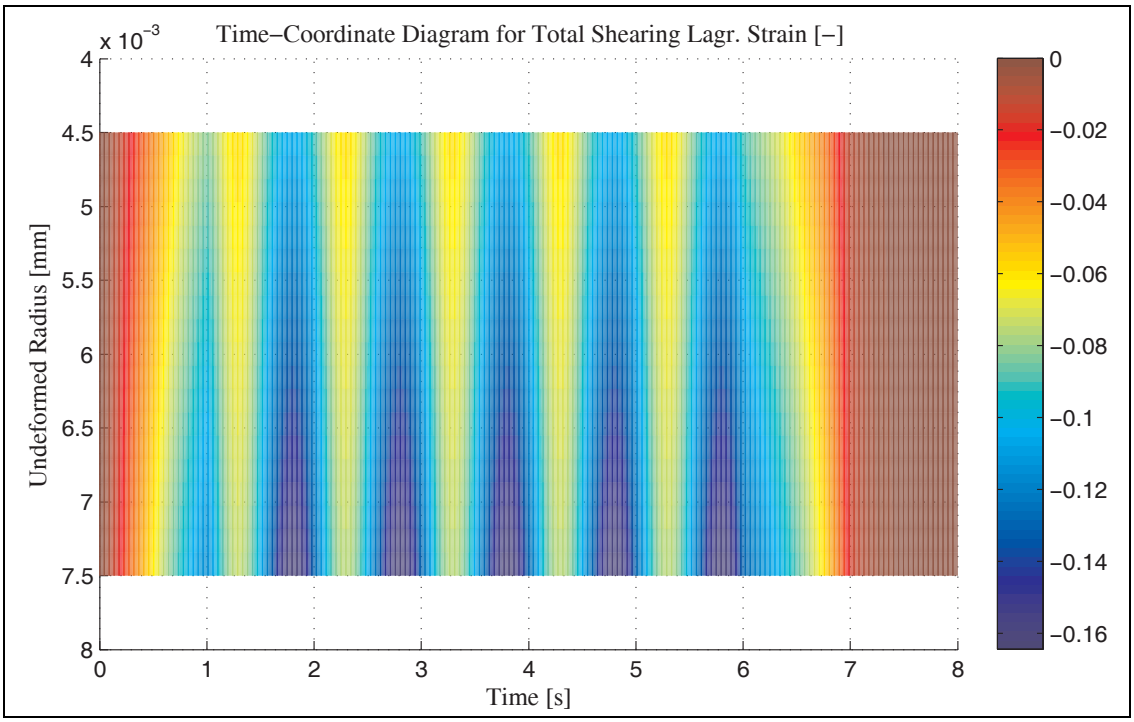

Figure A-8.5: Variation of Total Shear Strain with Time and within Wall Thickness under Cyclic Loading at 1Hz with Torsion using Isotropic Viscoelasticity Model with Softening Effects

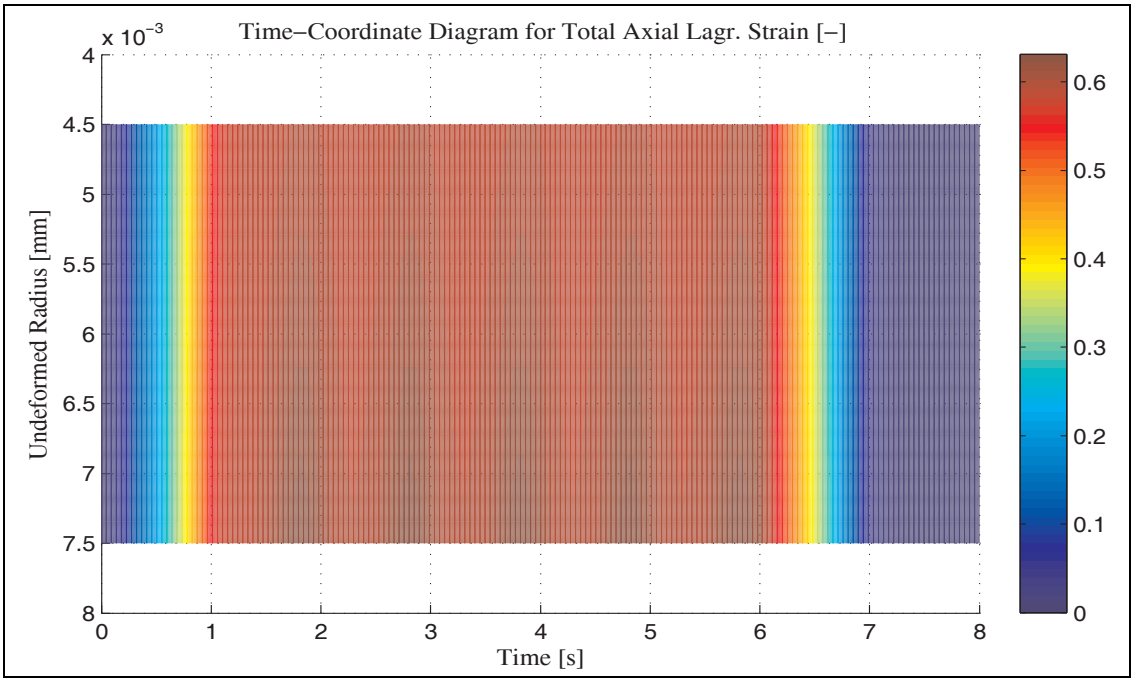

Figure A-8.6: Variation of Axial Total Strain with Time and within Wall Thickness under Cyclic Loading at 1Hz with Torsion using Isotropic Viscoelasticity Model with Softening Effects

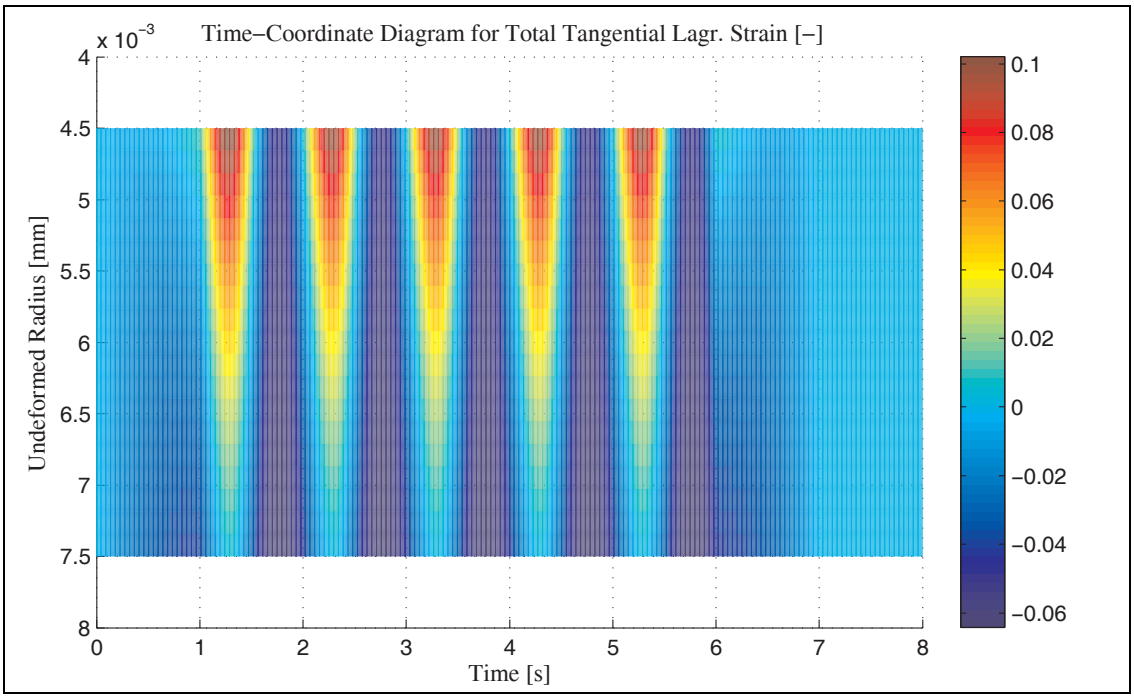

Figure A-8.7: Variation of Tangential Total Strain with Time and within Wall Thickness under Cyclic Loading at 1Hz with Torsion using Isotropic Viscoelasticity Model with Softening Effects

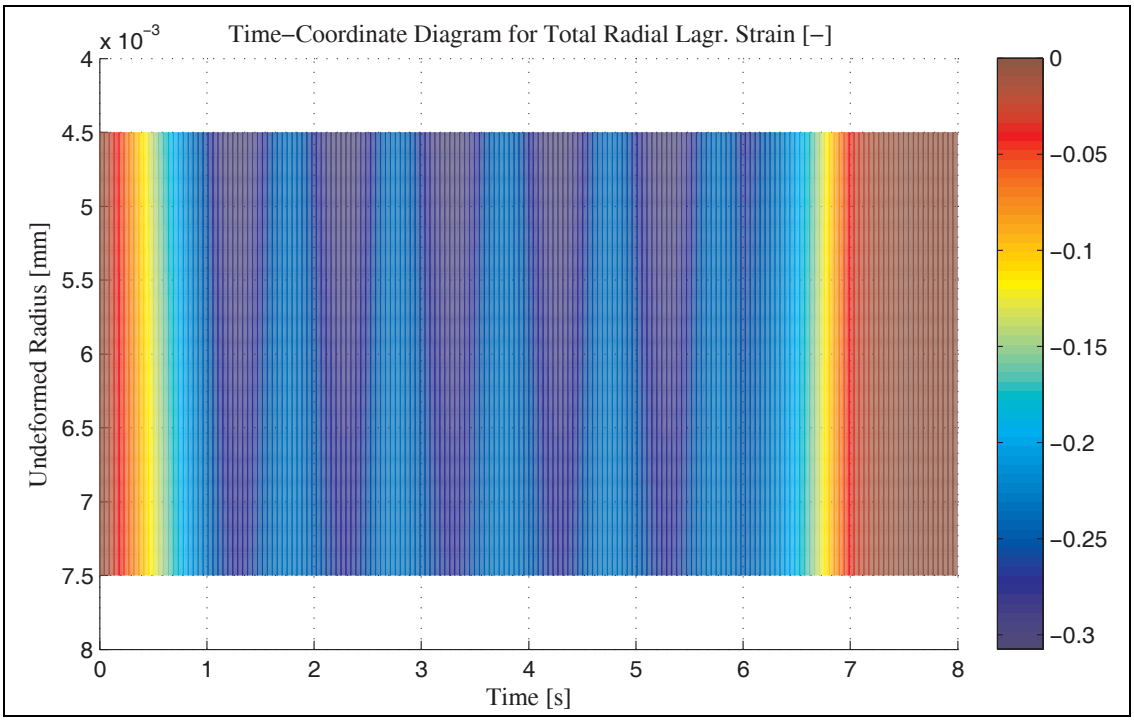

Figure A-8.8: Variation of Radial Total Strain with Time and within Wall Thickness under Cyclic Loading at 1Hz with Torsion using Isotropic Viscoelasticity Model with Softening Effects

A-9. Elastoplasticity Material Model (due to Section 11.2.1)

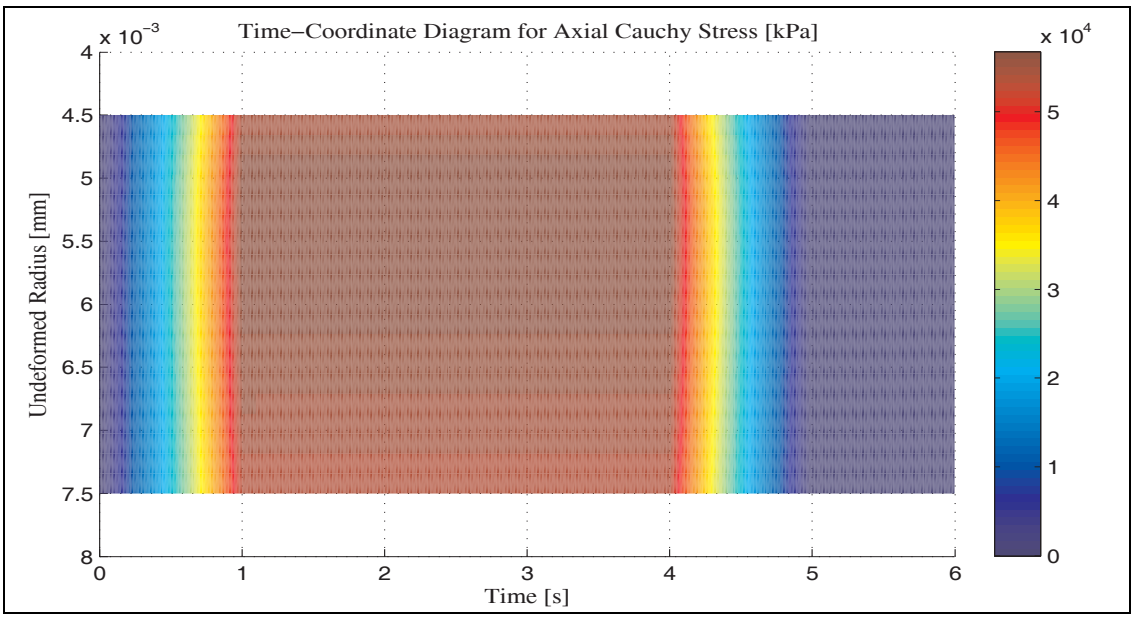

Figure A-9.1: Variation of Axial Stress with Time and within Wall Thickness During an Elastoplastic Analysis of Axisymetric Tube as to details provided Section 11.2.1

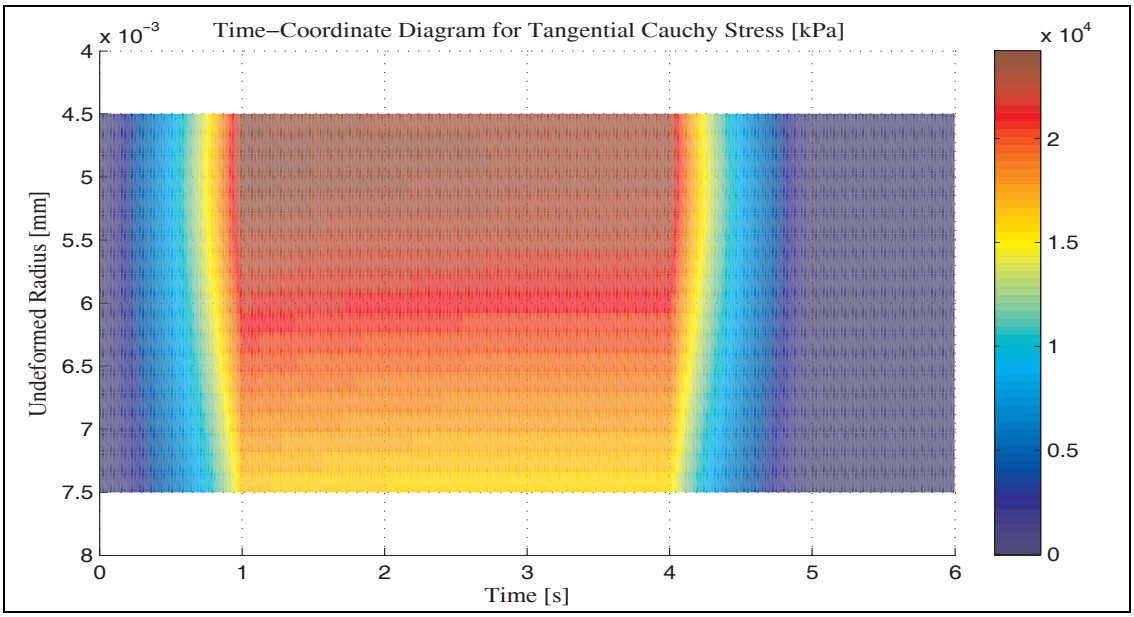

Figure A-9.2: Variation of Tangential Stress with Time and within Wall Thickness During an Elastoplastic Analysis of Axisymetric Tube as to details provided Section 11.2.1

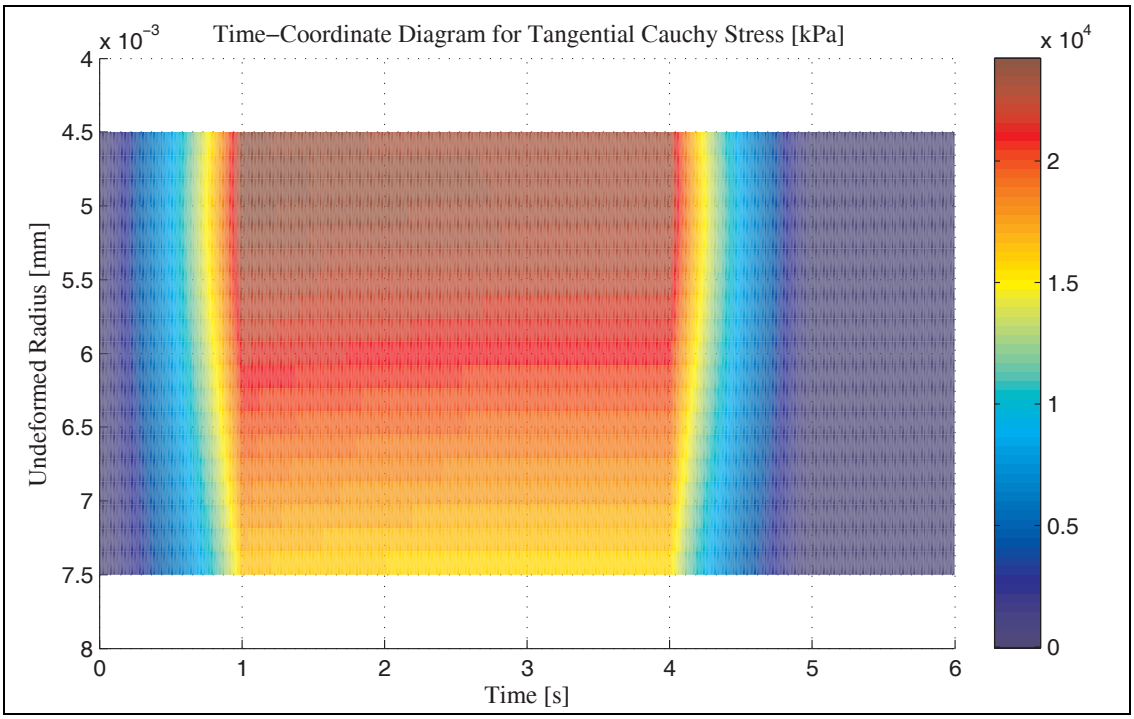

Figure A-9.3: Variation of Radial Stress with Time and within Wall Thickness During an Elastoplastic Analysis of Axisymetric Tube as to details provided Section 11.2.1

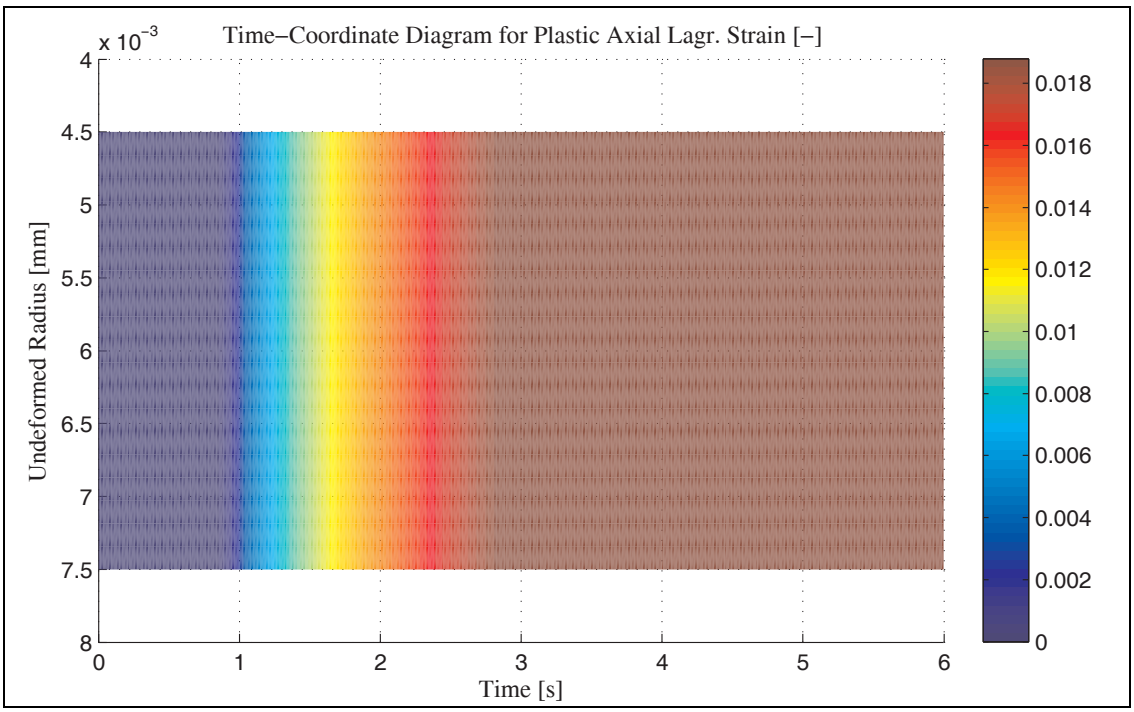

Figure A-9.4: Variation of Axial Plastic Strain with Time and within Wall Thickness During an Elastoplastic Analysis of Axisymetric Tube as to details provided Section 11.2.1

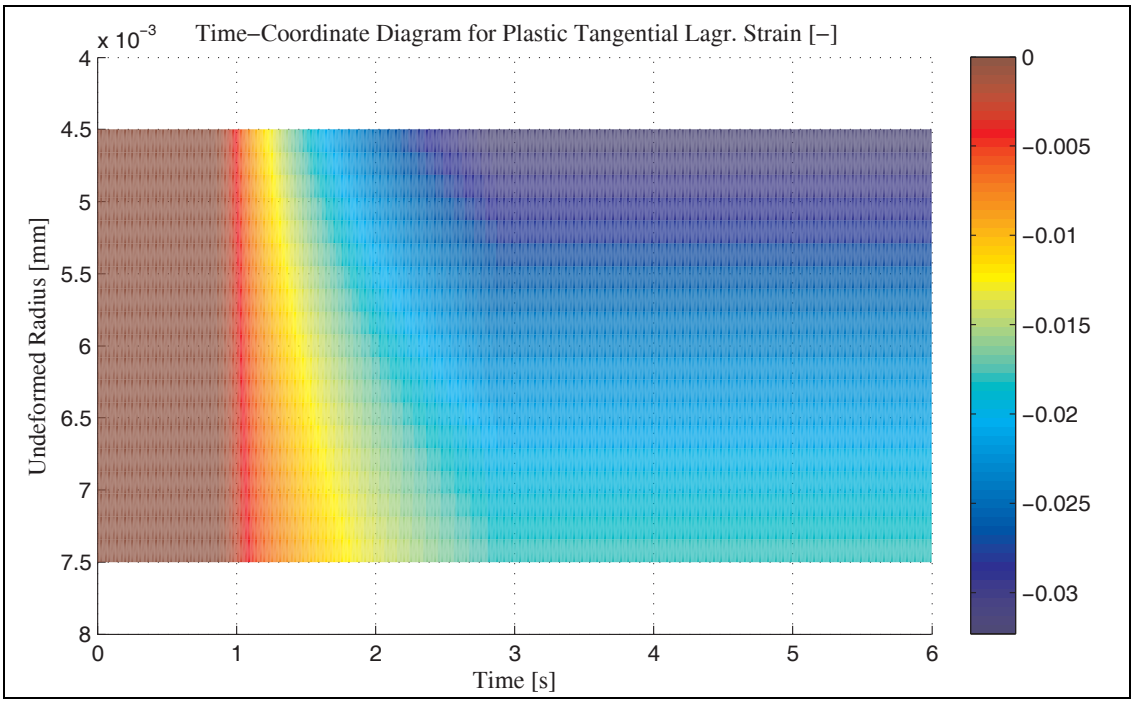

Figure A-9.5: Variation of Tangential Plastic Strain with Time and within Wall Thickness During an Elastoplastic Analysis of Axisymetric Tube as to details provided Section 11.2.1

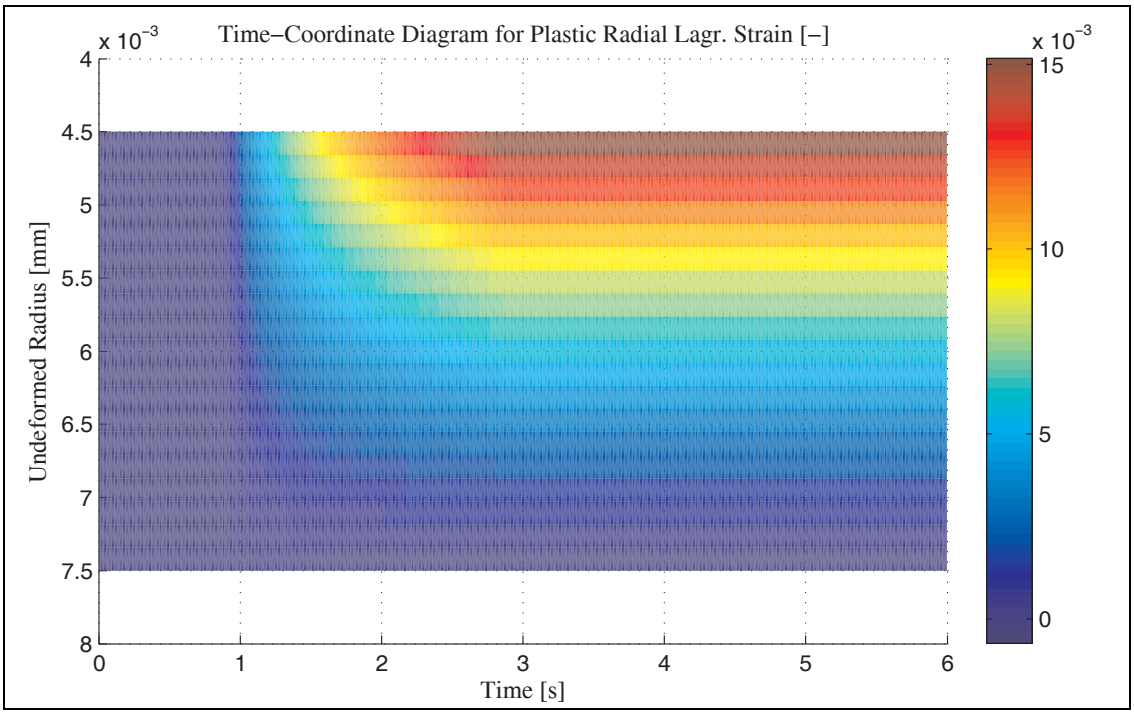

Figure A-9.6: Variation of Radial Plastic Strain with Time and within Wall Thickness During an Elastoplastic Analysis of Axisymetric Tube as to details provided Section 11.2.1

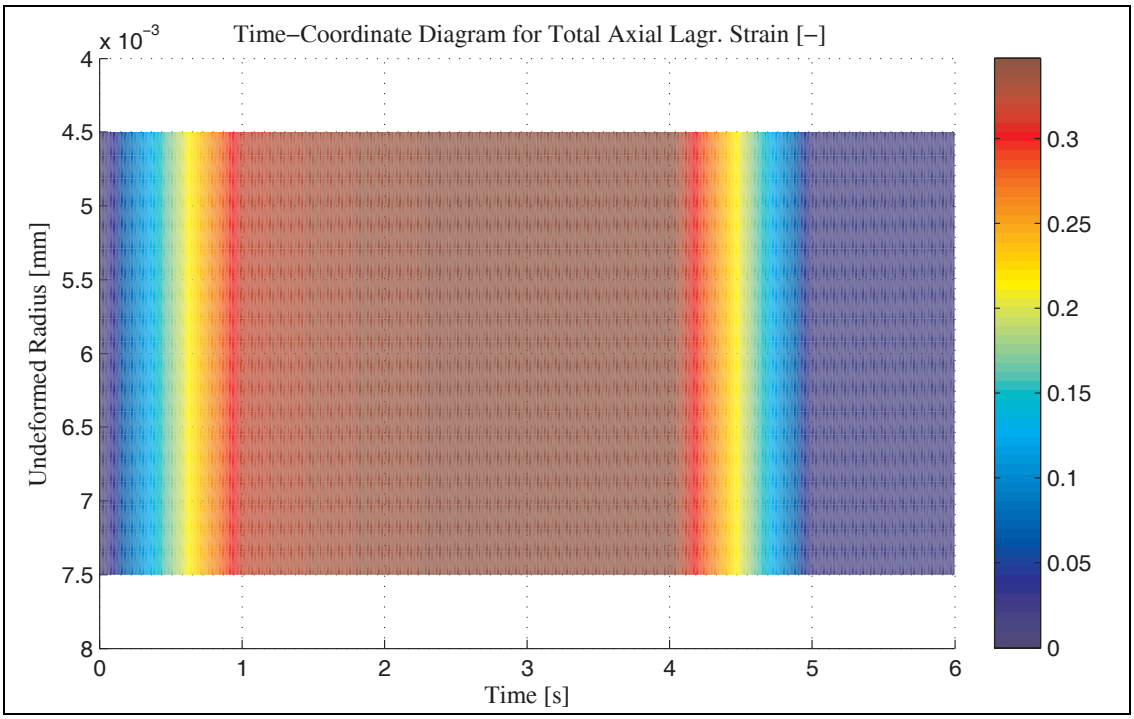

Figure A-9.7: Variation of Axial Total Strain with Time and within Wall Thickness During an Elastoplastic Analysis of Axisymetric Tube as to details provided Section 11.2.1

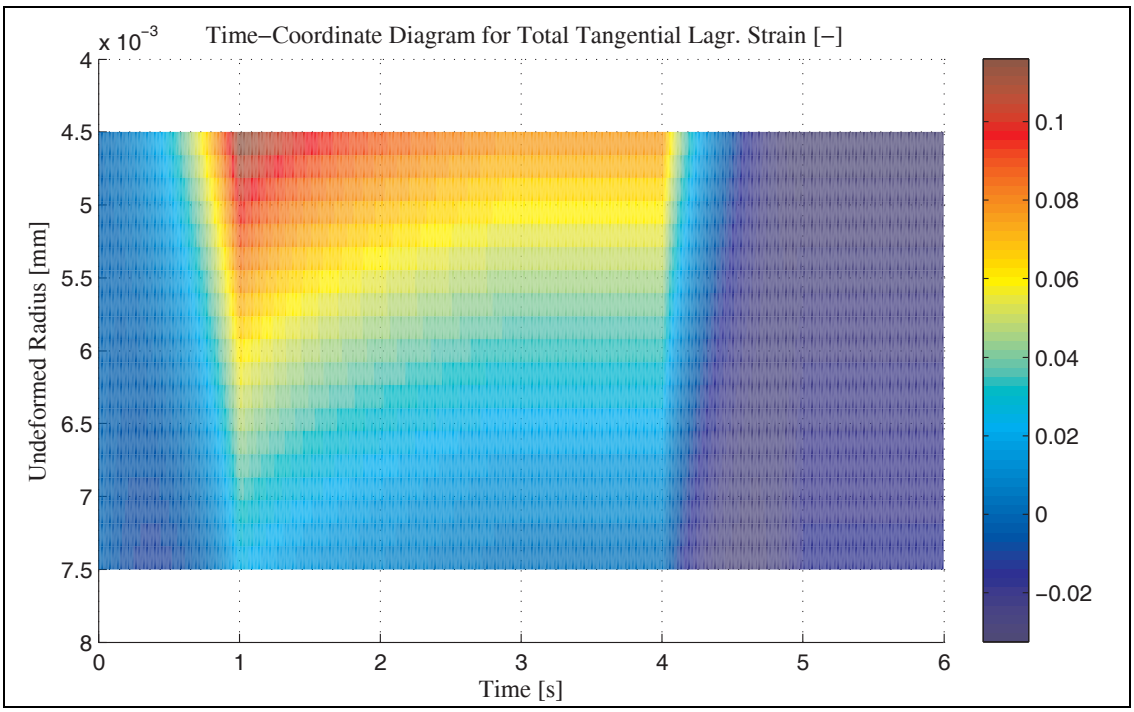

Figure A-9.8: Variation of Tangential Total Strain with Time and within Wall Thickness During an Elastoplastic Analysis of Axisymetric Tube as to details provided Section 11.2.1

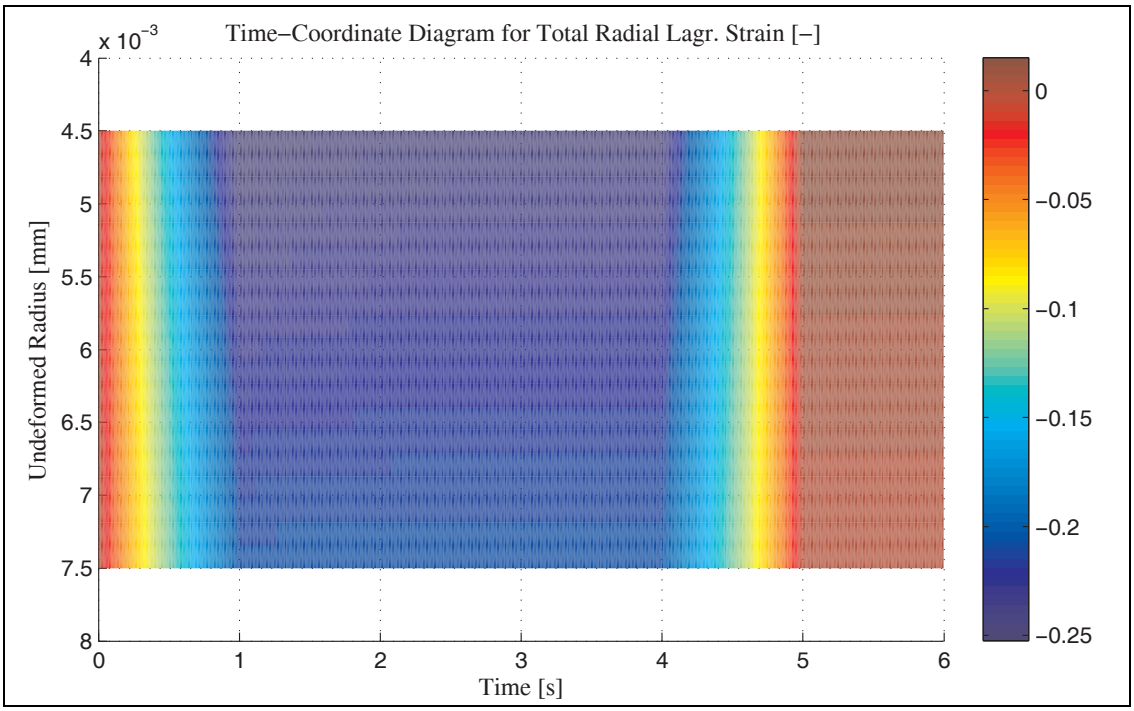

Figure A-9.9: Variation of Radial Total Strain with Time and within Wall Thickness During an Elastoplastic Analysis of Axisymetric Tube as to details provided Section 11.2.1

A-10. Viscoelastoplasticity Material Model with Isotropic Damping (due to Section 11.2.2)

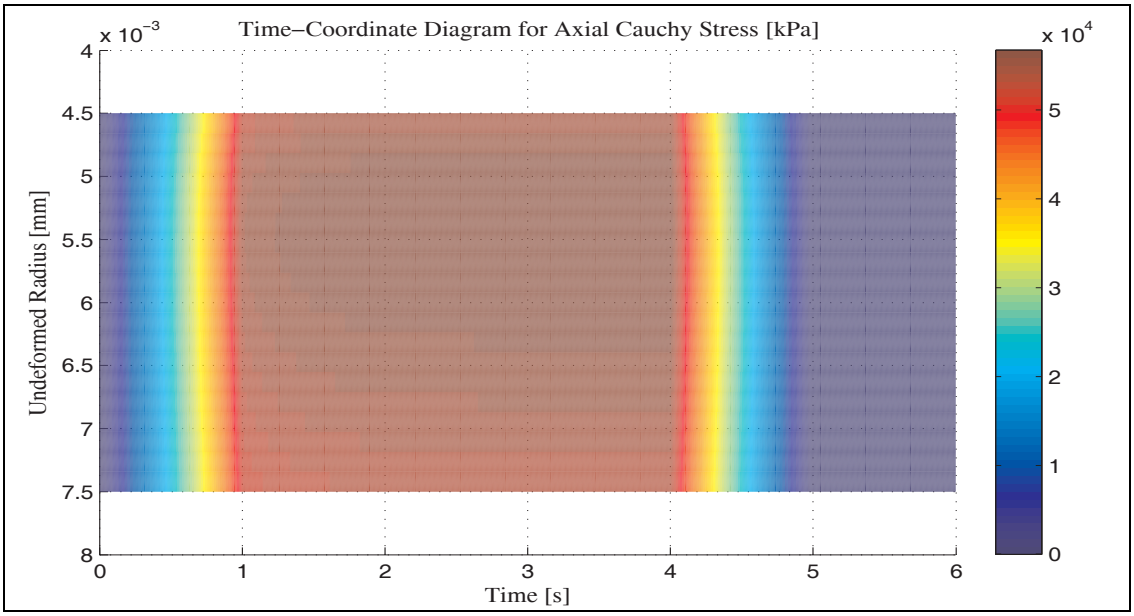

Figure A-10.1: Variation of Axial Stress with Time and within Wall Thickness During anViscoelastoplastic Analysis of Axisymetric Tube as to details provided Section 11.2.2

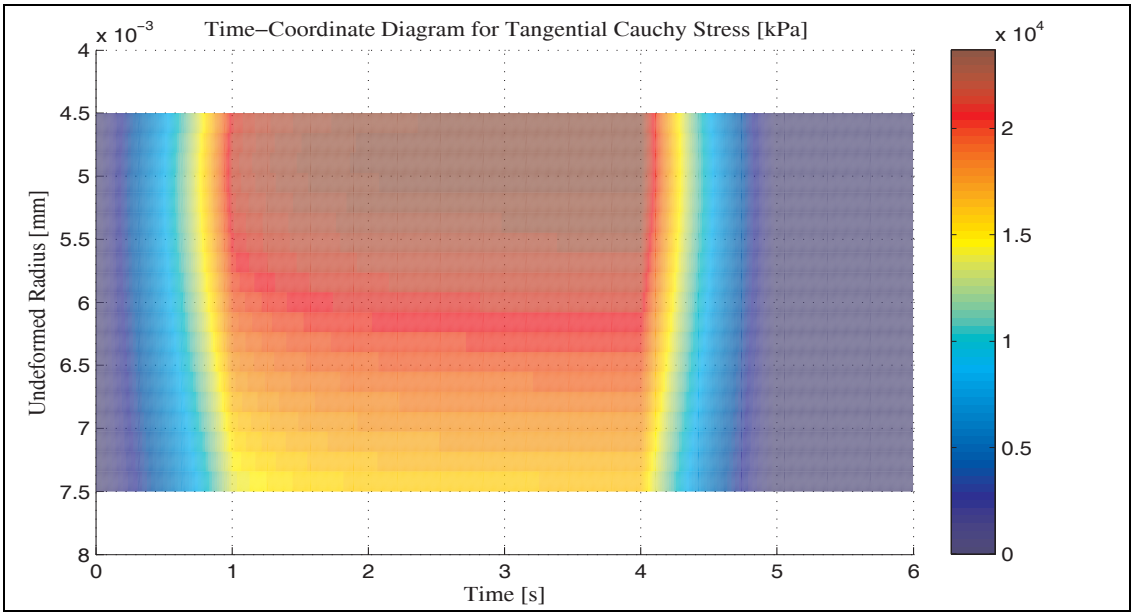

Figure A-10.2: Variation of Tangential Stress with Time and within Wall Thickness During anViscoelastoplastic Analysis of Axisymetric Tube as to details provided Section 11.2.2

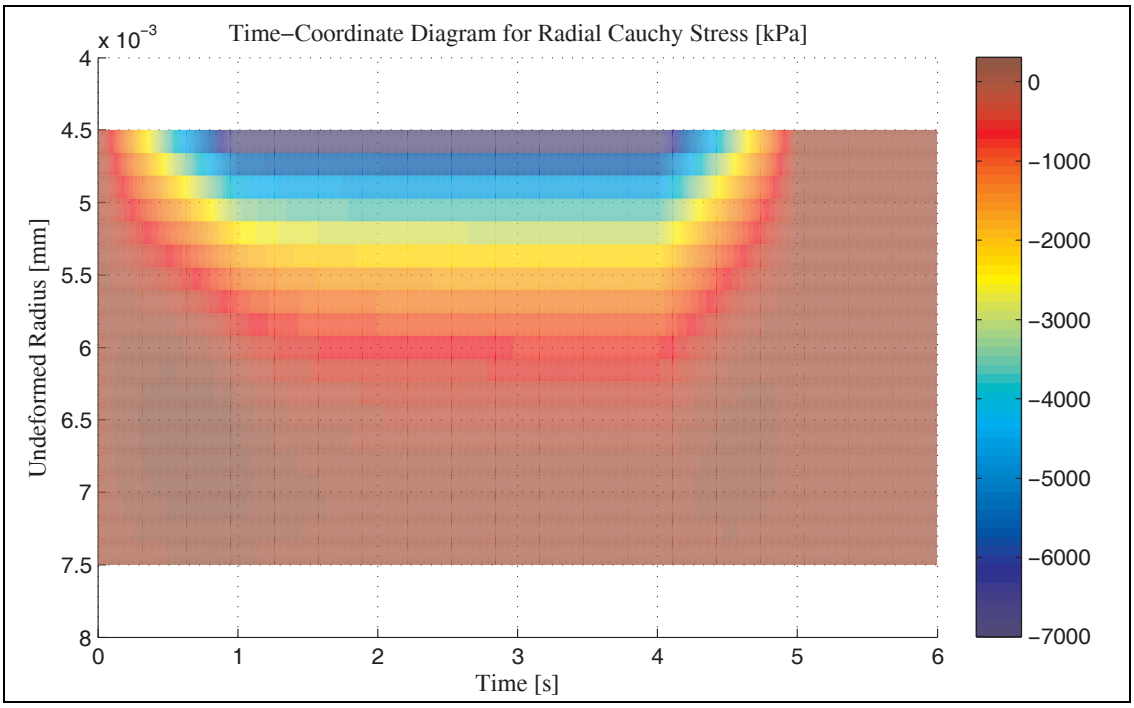

Figure A-10.3: Variation of Radial Stress with Time and within Wall Thickness During anViscoelastoplastic Analysis of Axisymetric Tube as to details provided Section 11.2.2

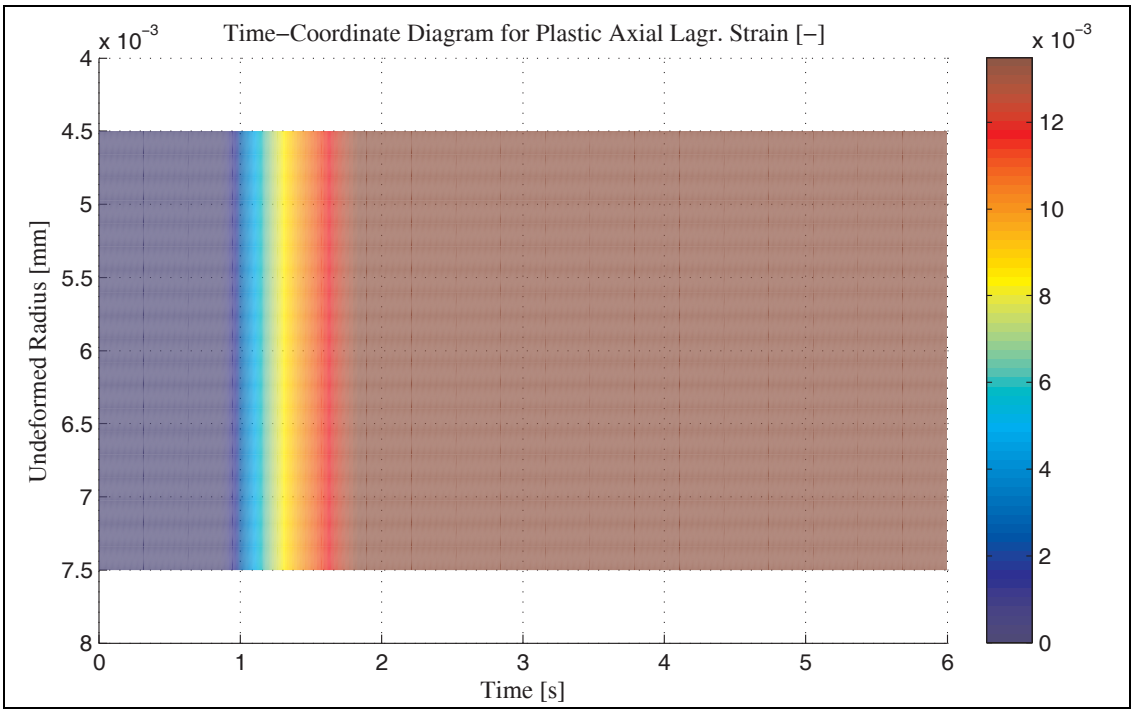

Figure A-10.4: Variation of Axial Plastic Strain with Time and within Wall Thickness During anViscoelastoplastic Analysis of Axisymetric Tube as to details provided Section 11.2.2

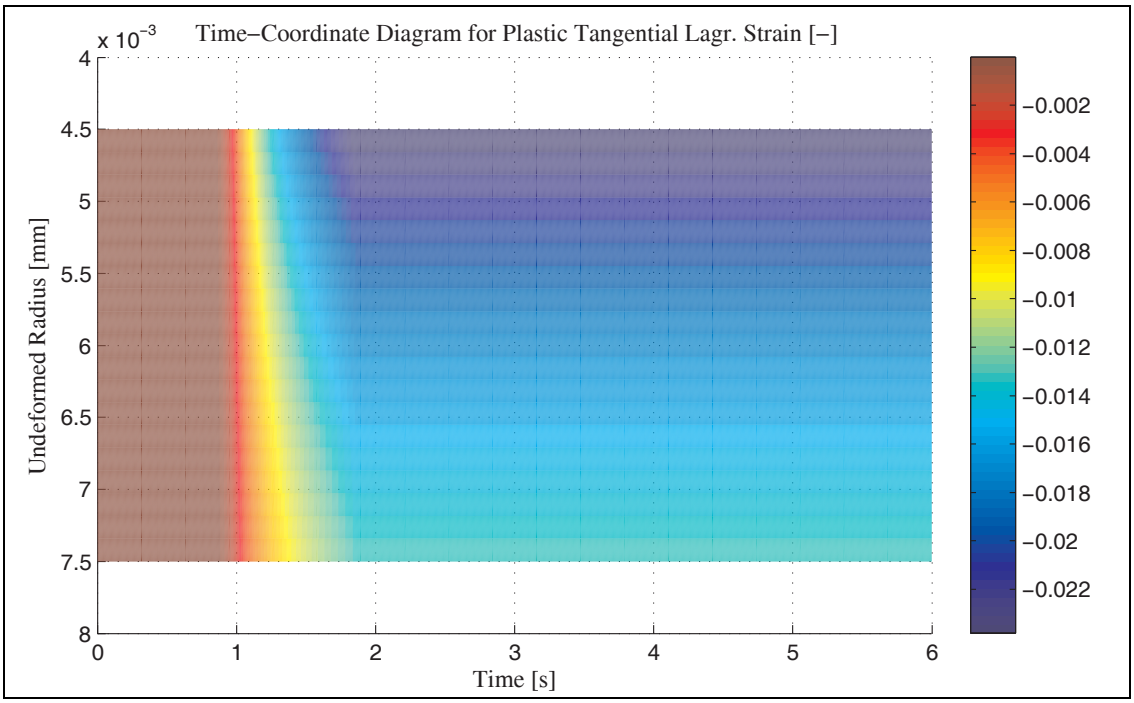

Figure A-10.5: Variation of Tangential Plastic Strain with Time and within Wall Thickness During anViscoelastoplastic Analysis of Axisymetric Tube as to details provided Section 11.2.2

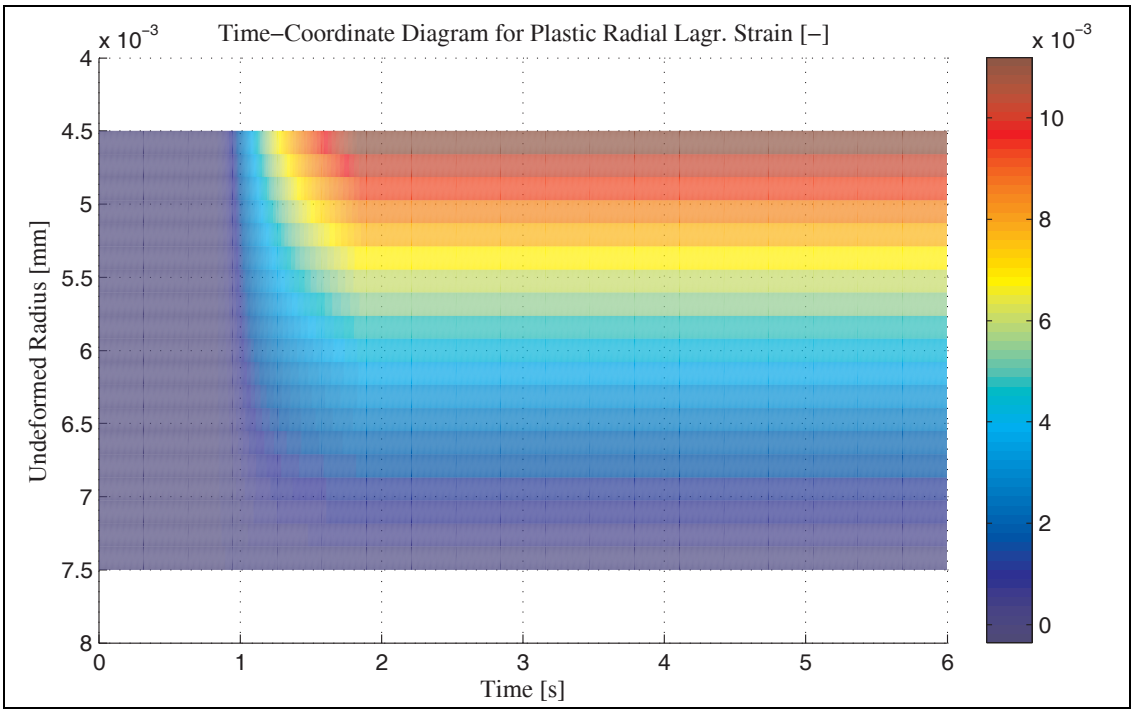

Figure A-10.6: Variation of Radial Plastic Strain with Time and within Wall Thickness During anViscoelastoplastic Analysis of Axisymetric Tube as to details provided Section 11.2.2

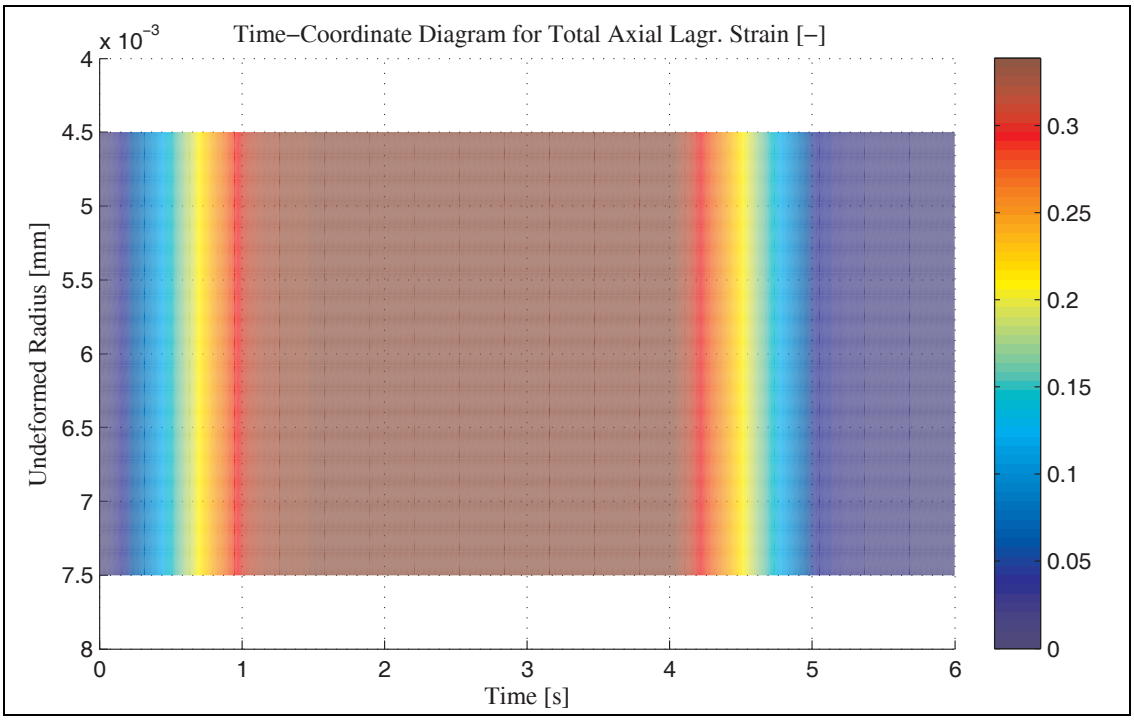

Figure A-10.7: Variation of Axial Total Strain with Time and within Wall Thickness During anViscoelastoplastic Analysis of Axisymetric Tube as to details provided Section 11.2.2

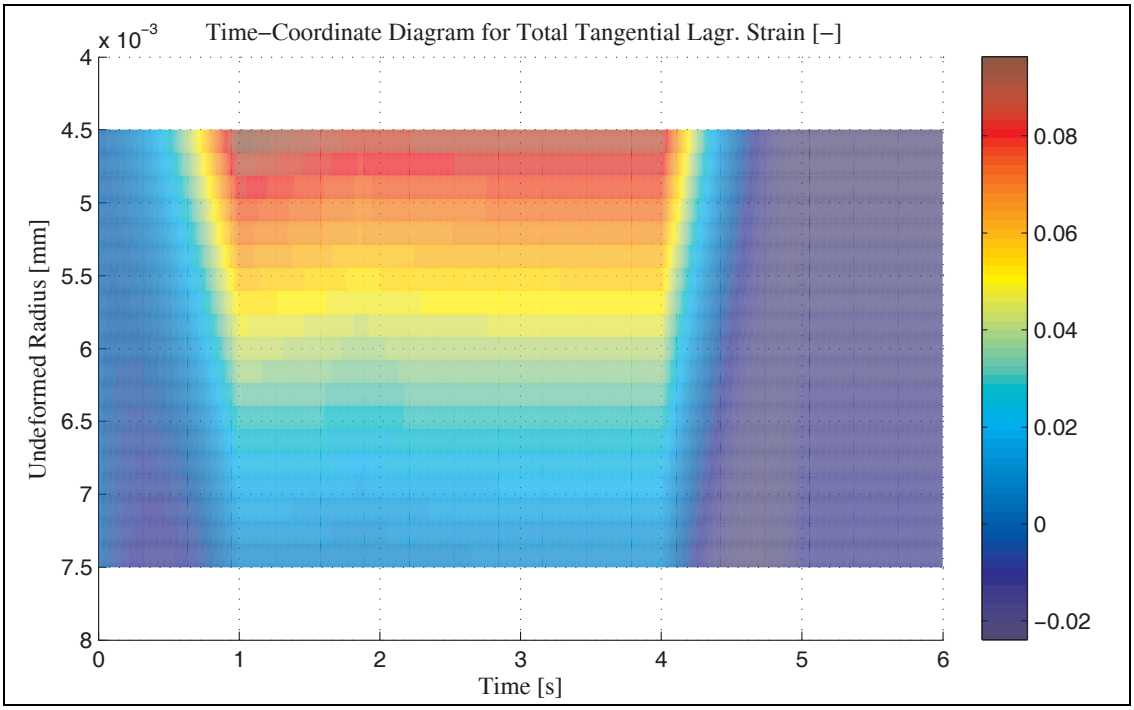

Figure A-10.8: Variation of Tangential Total Strain with Time and within Wall Thickness During anViscoelastoplastic Analysis of Axisymetric Tube as to details provided Section 11.2.2

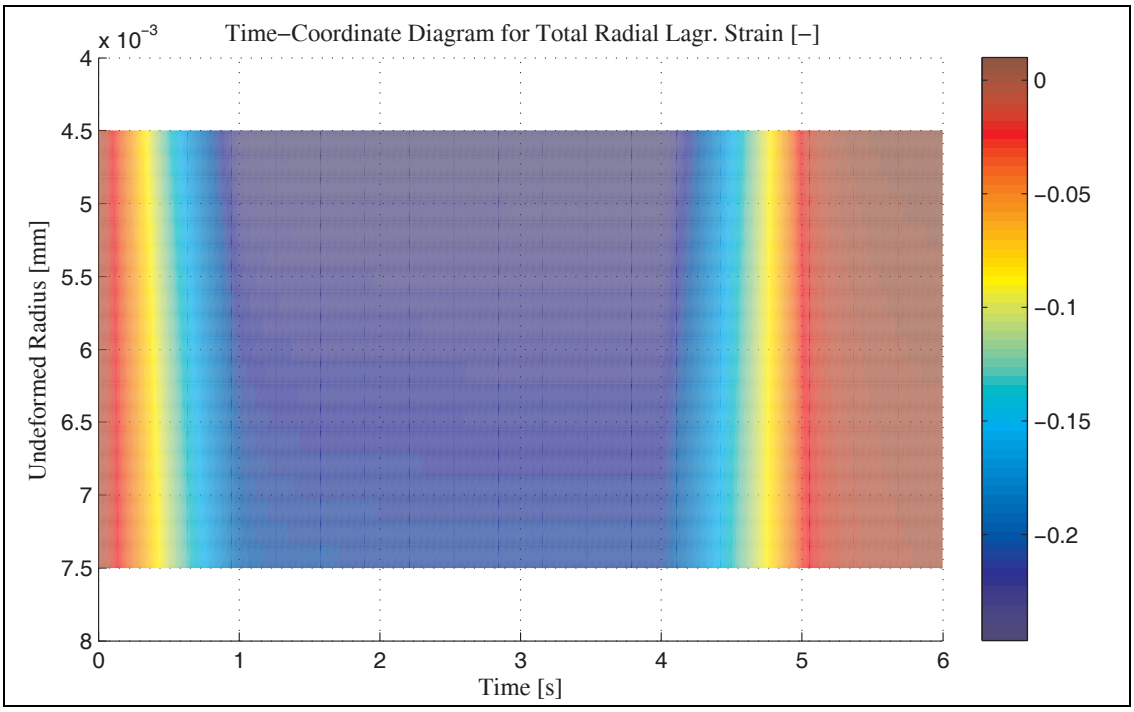

Figure A-10.9: Variation of Radial Total Strain with Time and within Wall Thickness During anViscoelastoplastic Analysis of Axisymetric Tube as to details provided Section 11.2.2

CURRICULUM VITAE

Emin SÜNBÜLOĞLU has born in 1977 in Istanbul. He has graduated from Beşiktaş Atatürk Anatolian High School in 1995, and attended to Mechanical Engineering Undergraduate Program at Istanbul Technical University, Faculty of Mechanical Engineering between 1995 and 1999. After graduation, he has taken an MBA at Boğaziçi University between 1999 and 2001. Afterwards, from 2001 to 2007 he has conducted his Ph.D. studies again at Istanbul Technical University, Institute of Science and Technology. Starting from 1999, he has been a member of Istanbul Technical University, Faculty of Mechanical Engineering as Research Assistant at the Strength of Materials Laboratory. He has completed many research studies on Biomechanics and Experimental Mechanics, as well as performing numerous concerts within the University Summer Festivals along with undergraduate students from Faculty within this time period. He has taken part in many State and TUBITAK supported projects, as well as many studies collaborated with the Industry. Emin SÜNBÜLOĞLU is still a member of Istanbul Technical University, Faculty of Mechanical Engineering.